Effects of protonation and heavy-atom substitution on the photophysics of phenothiazinium cationic dyes and related compounds: A theoretical study

Presented by:

Angela Susana Rodriguez Serrano

UNIVERSIDAD INDUSTRIAL DE SANTANDER

FACULTAD DE CIENCIAS

DOCTORADO EN QUÍMICA

BUCARAMANGA, 2014

Effects of protonation and heavy-atom substitution on the photophysics of phenothiazinium cationic dyes and related compounds: A theoretical study

Doctoral dissertation

Presented by:

Angela Susana Rodriguez Serrano

Advisors:

Dr. Martha Cecilia Daza Espinosa

Universidad Industrial de Santander

Dr. Markus Hans Oliver Doerr

Universidad Industrial de Santander

Universidad Santo Tomás

UNIVERSIDAD INDUSTRIAL DE SANTANDER

FACULTAD DE CIENCIAS

DOCTORADO EN QUÍMICA

BUCARAMANGA, 2014

To Miguel Angel and Maria Azucena. Now the time is for you.

I promise.

ACKNOWLEDGEMENTS

This thesis would have not been possible without the support of my supervisors, colleagues, family and friends who in different ways encouraged me and shared this long way. To all of you, I express my grateful acknowledgement and sincere thanks for bringing this thesis to a successful end.

First of all, I would like to thank to my supervisors Prof. Dr. Martha Cecilia Daza and Prof. Dr Markus Doerr for endowing me with this interesting project. I sincerely thank them for the confidence and for providing me with the freedom to investigate on it and for their support not only in a scientific respect. Thank you for your support and guidance over all of these years. Also I want to acknowledge all the patience from you during my two pregnancies in my studies, the time, the advices and the tears. Thanks for all your commitment during this long process. Prof. Jose Luis Villaveces, the scientific discussions with you were fantastic! To all the colleagues of the "Grupo de Bioquímica Teórica" for creating a friendly and creative atmosphere as Dr. Carlos Díaz, Andres Escorcia, Jorge Quintero and Pedro Acosta.

Part of this work has been carried out during a half-year stay at the Institute of Theoretical and Computational Chemistry of the Heinrich-Heine University in Düsseldorf, Germany. Many thanks to Prof. Dr. Christel Marian for her very kind hospitality, all the ongoing support, scientific advice and computing time at Suzi. Also I thank to the group members in Düsseldorf for all of their kind support during my visit: Dr. Vidisha Rai-Constapel, Kathleen Gollnisch, Larissa Pohler, Dr. Martin Kleinschmidt, Dr. Jörg Tatchen, Dr. Mihajlo Etinski and Dr. Oliver Weingart. Vidisha, thank you for all the patience on teaching me the calculation of intersystem crossing rate constants!

For Miguel Angel and Maria Azucena (my little kids!) all my infinite love. You teach me to be strong and to face the difficulties in this long run. To my

parents: Carla Serrano Scottpp and Jaime Rodriguez Polo, and also my sister and brother: Natalia y David, I want to also kindly acknowledge their patience and support. Thank you for being there taking part of the process.

The tremendous financial support from COLCIENCIAS ‘Programa generación bicentenario, becas Francisco José de Caldas’ (2009) is gratefully acknowledged. I Also thank the support from Fundación para la Promoción de la Ciencia y la Tecnología del Banco de la República (2630 Project) and Universidad Industrial de Santander (5169 Project) given during my doctoral studies.

Finally, I want to acknowledge the referees: Dr. Cacier Hadad Arriagada, Dr. Julio Cesar Arce Clavijo, Dr. Cristian Blanco Tirado and Dr. Gustavo Emilio Ramirez for dedicating time on revising my dissertation and for their kind suggestions.

Table of contents

List of figures

List of tables

List of abbreviations

BO = Born-Oppenheimer

COSMO = Conductor-like screening model

DFT = Density functional theory

DFT/MRCI = Density functional theory / multireference configuration interaction

FC = Franck-Condon

HF = Hartree-Fock

HT = Herzberg-Teller

IC = Internal conversion

ISC = Intersystem crossing

KS = Kohn-Sham

$^3O_2$ = Triplet ground state of molecular oxygen

$^1O_2$ = Singlet excited state ($^1\Delta_g$) of molecular oxygen

PDT = Photodynamic therapy

PES = Potential energy surface

RI-CC2 = Resolution of identity-second order approximate coupled cluster

SOME = Spin-orbit coupling matrix element

∂SOMEs = First-order derivatives of the SOMEs with respect to the normal mode coordinates

SV(P) = Split valence basis set with (d) polarization functions for non-hydrogen atoms

TDDFT = Time dependent density functional theory

TZVP = Triple-ζ basis set for valence electrons with (d,p) polarization functions

TZVPP = Triple-ζ basis set for valence electrons with a double set of (2d1f,2p1d) polarization functions

TH^+ = Monoprotonated thionine

TH_2^{2+} = Diprotonated thionine

T = Neutral thionine

TITLE: Effects of Protonation and Heavy-Atom Substitution on the Photophysics of Phenothiazinium Cationic Dyes and Related Compounds: A Theoretical Study[*]

AUTHOR: Angela Rodriguez-Serrano[†]

KEYWORDS: Intersystem crossing, phenothiazinium dyes, thionine, DFT/MRCI, TDDFT

High level quantum-chemical methods were employed for understanding the intersystem crossing mechanisms (ISC) in thionine and related compounds. In order to compete with other energy dissipation mechanisms (e.g. fluorescence), ISC have to be efficient. Based on the computed ISC rate constants (k_{ISC}) and excited-state hydration shifts, it is suggested that the efficient triplet quantum yield of thionine is primarily due to the $S_1 \rightsquigarrow T_2$ channel with a $k_{ISC} \sim 10^9 s^{-1}$, which is driven by vibronic spin-orbit coupling between $\pi \rightarrow \pi^*$ states. Remarkable effects on the ISC efficiency upon (de)protonation of thionine (TH^+) were found. ISC is more efficient at the diprotonated (TH_2^{+2}) and neutral imine (T) forms of thionine. In TH_2^{+2}, $k_{ISC} \sim 10^8 s^{-1}$ is four orders of magnitude higher than fluorescence. After photoexcitation of T, a thermally activated ISC channel is also expected to be more efficient ($k_{ISC} \sim 10^9 s^{-1}$) than fluorescence. The T_1 states of TH_2^{2+}, TH^+ and T can be populated through an equilibrium between them and transfer their excitation energy to $^3O_2$ to produce $^1O_2$. The energy transfer from the T_1 state of TH_2^{2+} to $^3O_2$ to produce $^1O_2$ is endergonic. In contrast, when occurs from the T_1 state of TH^+ and T to $^3O_2$ releases free energy, being ~4 times more exergonic for TH^+. These facts explain the experimental observation of a much smaller $^1O_2$ production in acidic aqueous solution. Moreover, we studied the internal heavy atom effects on the photophysics by substituting the sulphur of thionine by oxygen (oxonine) and selenium (selenine). In oxonine the dominant relaxation channel is fluorescence while in thionine and selenine it is ISC, which is significantly higher in selenine. This suggests that selenine-based dyes are quite efficient triplet state photosensitizers. As the excitation energy of the T_1 state of selenine is almost the same than for thionine, selenine is expected to be more efficient $^1O_2$ photosensitizer than thionine.

[*] Doctoral Dissertation

[†] Facultad de Ciencias, Escuela de química, Directora: Dra. Martha Cecilia Daza Espinosa, Director: Dr. Markus Hans Oliver Doerr

TÍTULO: Efectos de la protonación y sustitución por átomos pesados en la fotofísica de colorantes catiónicos fenotiazínicos y compuestos relacionados: Un estudio teórico[‡]

AUTOR: Angela Rodriguez-Serrano[§]

PALABRAS CLAVES: Entrecruzamiento de sistemas, colorantes fenotiazínicos, tionina, DFT/MRCI, TDDFT

En esta tesis doctoral estudiamos los procesos de entrecruzamiento de sistemas (ECS) de la tionina y análogos utilizando herramientas de la química cuántica. Los mecanismos de ECS en los cromóforos estudiados ocurren mediante acoplamiento vibrónico espín órbita. La población del conjunto de los estados triplete de tionina en agua ocurre de manera eficiente mediante un canal de relajación $S_1 \rightsquigarrow T_2$ con constante de velocidad de ECS (k_{ECS}) de $\sim 10^9 s^{-1}$. Este valor calculado es muy cercano al valor experimental ($k_{ECS}=2.8x10^9 s^{-1}$). También mostramos que la eficiencia del ESC en tionina (TH^+) cambia notoriamente debido al estado de protonación. Encontramos que el ESC es más eficiente en tionina diprotonada (TH_2^{+2}) y neutra (T) que en TH^+. En TH_2^{+2}, el ECS ($k_{ECS} \sim 10^8 s^{-1}$) es más eficiente que la fluorescencia. En T, el ESC ocurre vía un canal activado térmicamente que domina la cinética ($k_{ECS} \sim 10^9 s^{-1}$). Los estados T_1 de TH_2^{2+}, TH^+ y T pueden poblarse debido a un equilibrio ácido-base y transferir su energía de excitación al $^3O_2$ para producir $^1O_2$. La transferencia de energía entre el T_1 del TH_2^{2+} al $^3O_2$ para producir $^1O_2$ es endergónica mientras que es exergónica cuando la energía se transfiere desde los estados T_1 de TH^+ y T. Además, estudiamos el efecto de átomos pesados en la fotofísica sustituyendo el azufre de la tionina por oxígeno (oxonina) y por selenio (selenina). En oxonina el canal de relajación dominante es la fluorescencia, mientras que en tionina y selenina es el ECS, siendo mayor en selenina. Este análisis nos permite sugerir que colorantes basados en selenina pueden ser fotosensibilizadores con una alta producción del estado triplete. Como la energía de excitación del T_1 de la selenina es aproximadamente la misma que para la tionina, nosotros inferimos que selenina podría ser un fotosensibilizador más eficiente para la producción de $^1O_2$ que tionina.

[‡] Tesis doctoral

[§] Facultad de Ciencias, Escuela de química, Directora: Dra. Martha Cecilia Daza Espinosa, Director: Dr. Markus Hans Oliver Doerr

Introduction

Molecular organic photochemistry employs a number of theories and representations of the electronic structure for describing the interactions between light and organic molecules. The absorption of UV/Vis radiation by an organic chromophore populates its singlet excited state manifold ($S_0 \rightarrow S_n$). Due to a fast $S_n \rightsquigarrow S_1$ internal conversion depletion (IC), in general the first singlet excited state (S_1) is populated (Kasha's rule [1]). The most important intramolecular mechanisms for the depopulation of the S_1 state are fluorescence ($S_1 \rightarrow S_0$), radiationless IC to the ground state ($S_1 \rightsquigarrow S_0$), and intersystem crossing (ISC, $S_1 \rightsquigarrow T_n$). The fastest of these processes will dominate the overall photophysical kinetics, which defines the specific role of the photosensitizer. For example, molecules with high triplet quantum yield and triplet lifetime may serve as intermediates of photochemical transformations as the cleavage of photolabile protecting groups,[2] [2 + 2] cycloadditions [3,4] and the voltage (LOV) domains of blue-light receptors.[5,6] Molecules with small triplet quantum yields and efficiently deactivated triplet states may function as triplet quenchers and can increase, for example, the photostability of a fluorescence marker.

The lifetime of the first triplet excited state (T_1) exceeds that of the S_1 state and the molecule in these electronic states is found to react quite different than in the ground state. Once the molecule is in the T_1 state, it can undergo chemical reactions, phosphoresce ($T_1 \rightarrow S_0$), make triplet - singlet ISC ($T_1 \rightsquigarrow S_0$) or transfer its electronic excitation energy to acceptor molecules in the surrounding. The latter process is of great importance for the application of organic photosensitizers in photodynamic therapy (PDT).[3,7] PDT is an active research area nowadays where the affected living tissue is treated by a combination of a photosensitizer, visible light, and molecular oxygen ($^3O_2$).[8,9] Singlet oxygen ($^1O_2$ ($^1\Delta_g$)) is photochemically produced by triplet–triplet energy transfer from the triplet state of the sensitizer to the ground state

of molecular oxygen ($^3O_2$) present in the cellular environment. This reactive oxygen specie could efficiently photoinactivate *e. g.* tumor cells, bacteria, virus and parasites.[10]

Several families of molecules have shown singlet oxygen generating ability for PDT, for example organic xanthene dyes, porphyrins, phthalocyanines and transition metal complexes.[10] These kind of photosensitizers have exhibit properties as: *i*) a high UV-vis absorption coefficient in the spectral region of the excitation light, *ii*) a triplet state of appropriate energy (E_T > 95 kJ mol^{-1}) to allow for efficient energy transfer to the oxygen ground state ($^3O_2$), *iii*) a high triplet quantum yield (ϕ_T > 0.4), *iv*) a long triplet state lifetime (t_T > 1 μs), and *v*) a high photostability. A detailed knowledge of the electronic structure and photophysical properties of a sensitizer serves as starting point for modulating each of these characteristics for a rational design of chromophores with more efficient triplet state and singlet oxygen production. This dissertation sheds more light on the understanding of the photophysics of phenothiazinium-based photosensitizers.

The phenothiazinium family of dyes (**Fig. 1**) is a class of photobiologically active substances with many pharmaceutical applications. Due to their long wavelength light absorption at 590-660 nm within the therapeutic window and high efficiency of singlet oxygen production, thionine and its derivatives have been used in many areas such as PDT,[11,12] development of biosensors,[13-14] energy conversion,[15,16] polymerization photoinitiators,[17,18] decontamination of blood products,[19] nucleic acid probes,[20] and against bacteria,[21-25] viruses and yeasts.[26] Moreover, these compounds are also known to be active against *e. g. Plasmodium falciparum*, *Trypanosoma cruzi*,[27-28] *Staphylococcus aureus* and *Escherichia coli*.[29]

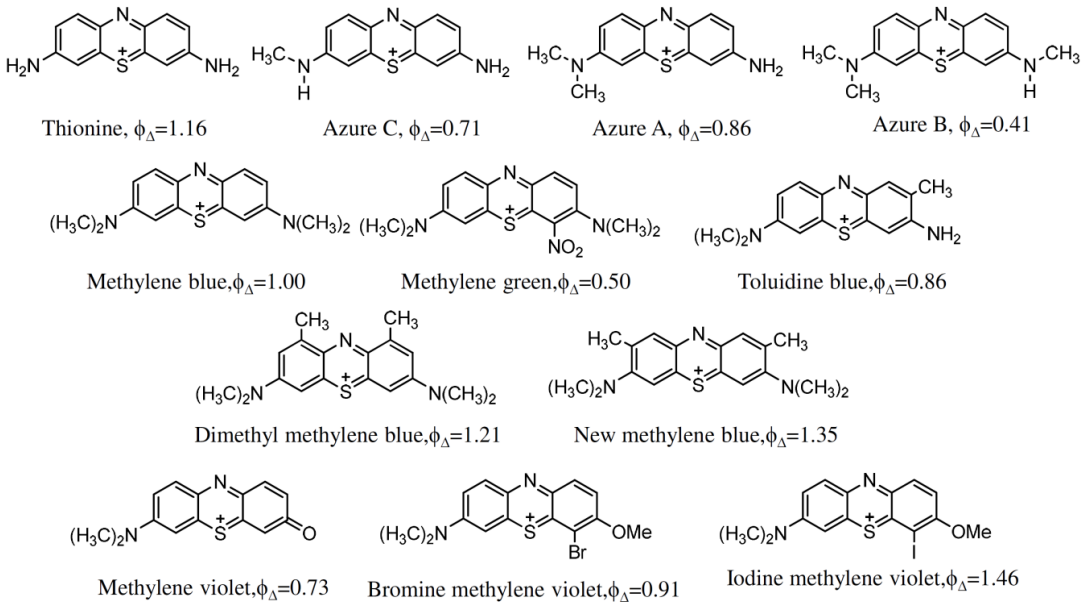

Fig. 1 Chemical structure and relative singlet oxygen quantum yields (Φ_Δ, taking methlylene blue as reference) of some cationic phenothiazinium dyes.[22]

The photodynamic action of the phenothiazinium dyes in the presence of oxygen proceeds efficiently by either involving direct excited-state reactions such as electron transfer and hydrogen abstraction,[20,30] or by the formation of singlet oxygen, **Fig. 2**.[31] The singlet oxygen quantum yields (ϕ_Δ), using methylene blue as reference (absolute ϕ_Δ = 0.44 [32])), for some phenothiazinium dyes are presented in **Fig. 1**. Changes in the structure of the parent thionine lead to dyes with increased or decreased singlet oxygen production depending on the position and the nature of the substitution. This shows that the photochemical properties of these dyes can be modulated relating the molecular structure with a desired activity and taking into account the appropriate reaction conditions (*e. g.* solvent, concentration of the dye and pH medium). For example, the ground and excited states may have different protonation states which could significantly decrease the photodynamic action via singlet oxygen production (**Fig. 2**, mechanism type II).[33,34,35,36] These pH-dependent changes are also accompanied by noticeable changes in the absorption and fluorescence spectrum of the

sensitizer due to the generation of the protonated and deprotonated species.[37-38] Moreover, aggregation processes in concentrated aqueous solution of these dyes may increase the photo-production of radicals (**Fig. 2**, mechanism Type I), decreasing the singlet oxygen production and leading to the formation of superoxide anion radical as presented in **Fig. 2** for thionine.[39] Of course, as stated above, the design of photosensitizers with high singlet oxygen production (thus, high triplet quantum yields) is desired for photobiological and PDT applications. As can be observed in **Fig. 2**, the photochemical behavior of the phenothiazinium dyes depends on how efficiently the triplet state is populated. Nevertheless, little was known about how ISC leads to an efficient population of the triplet state until the development of this thesis.

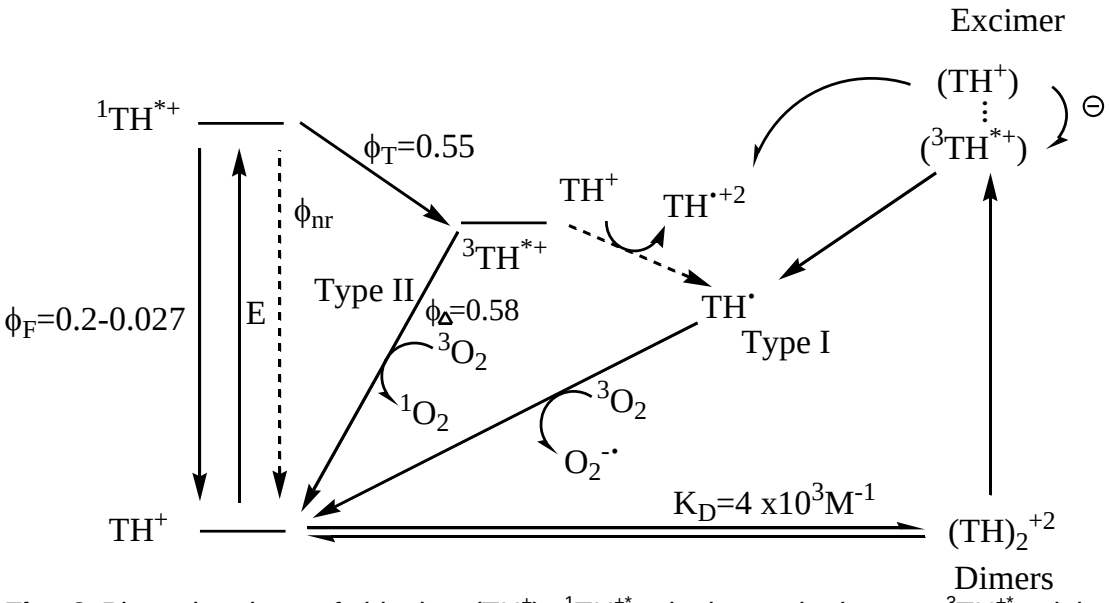

Fig. 2 Photochemistry of thionine (TH^+): $^1TH^{+*}$: singlet excited state, $^3TH^{+*}$: triplet state, $TH^\bullet$: semi-reduced radical, $TH^{\bullet+2}$: semi-oxidated radical, E: excitation energy. Type I and II refer to photodynamic action mechanism. ϕ_F: fluorescence quantum yield, ϕ_{nr}: quantum yield of non-radiative decay processes, ϕ_T: triplet state quantum yield, ϕ_Δ: singlet oxygen quantum yield. [11, modified]

Theoretical investigations have proven to be useful to improve the understanding of the photochemistry and photophysics of a variety of photosensitizers.[40-45] The aim of the present study was to understand the

mechanisms of efficient population of the triplet manifold in phenothiazinium-based chromophores by means of high level quantum mechanical methods. The 3,7-diamino-phenothiazin-5-ium, commonly called thionine (**Fig. 1**), is the representative smallest model and has been chosen as the starting point for studying the photophysics of these dyes. As the photophysics and singlet oxygen production of thionine has a marked pH-dependence,[34-35] the electronic structure and photophysical properties of the diprotonated (TH_2^{2+}) and neutral thionine (T) were studied. Understanding the effect of protonation and deprotonation on the photophysics of thionine is important for the interpretation of photo-oxidation studies in aqueous solution at different pH. It also provides additional information about the mechanism of the population and the energetics of its triplet state and, therefore, of singlet oxygen production. This knowledge contributes to a deeper understanding of their phototherapeutic actions.

Once the electronic structure and photophysics of these dyes have been elucidated, we have used this knowledge for proposing a dye with an improved ISC efficiency. The ISC efficiency can be enhanced by the inclusion of heavy atoms in the molecular structure of the dye since they increase the spin-orbit coupling. Substitution of the heteroatom of the central ring by oxygen, sulphur and selenium in tetramethylrosamine and benzo[a]phenothiazinium dyes has resulted in a significant increase in ϕ_Δ and small spectral shifts in the absorption and emission spectrum[**].[46-48] Based on this, we have investigated how such internal heavy atoms influence the photophysics of thionine. We studied the photophysical decay kinetics of two hetero-analogues of thionine: oxonine and selenine. These dyes are obtained by the replacement of the sulphur atom of thionine by oxygen and selenium.

[**] In the O-S-Se series: from 0.06 to 0.87 in the TMR dyes and from 0.005 to 0.650 in the Nile blue analogs.

The photophysics of thionine and its derivatives has been investigated in vacuum and in aqueous solution, by means of a combination of microhydration and continuum model. To this end we computed the vertical excitation spectra as well as the electronic structures at the energetic minima of the excited electronic states. In some cases also the potential energy surfaces (PESs) between these minima were explored. Molecular geometries were obtained using (time-dependent) density functional theory (TD-DFT).[49,50] The electronic structure at these geometries was calculated using the combined density functional theory/configuration interaction method (DFT/MRCI) of Grimme and Waletzke.[51] In this method, the major part of dynamic electron correlation is captured by the DFT treatment, and static correlation effects are introduced by the MRCI technique which is also flexible enough to properly describe states with double excitation character. A statistical benchmark of the DFT/MRCI and TDDFT (with the BP86, B3LYP and BHLYP functionals) excitation energies [52] shows that lowest deviations are found for DFT/MRCI and are ≈ 0.24 eV for valence states. These methods have been applied for studying the photophysics of several dyes of medium (such as phenalenone [53] and psolarens [54]) and large size (such as phorphyrins [55]) obtaining results very close to the experimental data.

The rate constants for the concurrent radiative (fluorescence and phosphorescence) and radiationless (ISC) processes have been computed and their implications on the photophysics are discussed. The fluorescence and phosphorescence rate constants were calculated from the minima of the S_1 and T_1 states, respectively. The ISC rate constants for the individual channels have been computed in the framework of the Fermi's golden rule. The performance of two methodologies for calculating the ISC rate constants has been evaluated: the time-independent[54] and time-dependent approaches.[56-57] The former is based on the direct evaluation of normal mode wavefunction integrals in a selected energy interval (2η) around the initial state which has to be the lowest vibrational state (for details see Ref.

[54]). In the latter method the ISC rate constant is calculated as the integral of the time correlation function.[56-57] The required data about spin-orbit coupling strengths between initial (singlet) and target (triplet) states for the correlated DFT/MRCI wave functions was obtained from high level multireference spin-orbit coupling interaction configuration (MRSOCI) calculations and using a one-center mean-field approximation to the Breit-Pauli Hamiltonian.[58-61] The mechanism of ISC in thionine and its analogs was studied in vacuum and taking into account the hydration shifts to the adiabatic excitation energies ("aqueous solution"). Depending on the character of the states involved, the ISC will be driven by two particular "types" of spin-orbit coupling which are denoted as *direct* and *vibronic* spin-orbit coupling.[62][††] According to El-Sayed,[63] ISC is very efficient if the radiationless transition involves a change of type of the molecular orbitals involved in the excitation. Spin-orbit coupling between π→π* and *n*→π* states are in general much larger than between two π→π* states. Thus, in the framework of *direct* spin-orbit coupling, the ISC rate constants for (π→π*) ⇝ (*n*→π*) processes will be in general larger than for (π→π*) ⇝ (π→π*). As recent studies have shown,[54-55,64] *vibronic* spin-orbit coupling may enhance the ISC constants between two π→π* states taking into account a Herzberg-Teller type expansion of the spin-orbit coupling. Vibrational excitations occur simultaneously to the electronic transitions where the population of *out-of-plane* modes breaks the symmetry of the molecule. Therefore the excited (*e. g.* a π→π*) state electronic wavefunction could mix with the other excited (*e. g.* a *n*→π*) state wavefunctions. The enhancement of the efficiency of an ISC channel that couples two π→π* states can be seen as an intensity borrowing from the much faster (π→π*) ⇝ (*n*→π*) / (*n*→π*) ⇝ (π→π*) processes. Since we

[††] Direct and vibronic spin-orbit coupling follows the nomenclature introduced by Henry and Siebrand et al. [62].

found that direct spin-orbit coupling does not explain the high triplet quantum yield in the systems under investigation, this study focus on the ISC driven by vibronic spin-orbit coupling.

This doctoral dissertation is organized as follows. **Chapter 1**: an overview of quantum chemical methods employed. **Chapter 2**: theoretical background of the most common photophysical processes and includes details about the calculation of the fluorescence, phosphorescence and ISC rate constants. **Chapter 3**: state of art of the photochemistry of thionine and its derivatives. **Chapter 4**: description of the computational methodology used to obtain the ground and excited state minima, electronic structure, excitation energies, decay rate constants and hydration effects. The following three chapters address the results and discussion. **Chapter 5**: study of the electronic structure of thionine and ISC decay mechanisms. **Chapter 6**: influence on the degree of protonation in the protophysics of thionine. **Chapter 7**: internal heavy atom effects on the photophysics of thionine. **Chapter 8**: general conclusions.

List of papers

Articles published:

1) Rodriguez-Serrano A.; Daza, M. C.; Doerr, M.; Marian, C. M. "A quantum chemical investigation of the electronic structure of thionine" Photochem. Photobiol. Sci. (2012) 11, 397-408.

2) Rodriguez-Serrano A.; Rai-Constapel, V.; Daza, M. C.; Doerr, M.; Marian, C. M. "A theoretical study of thionine: Spin-orbit coupling and intersystem crossing" Photochem. Photobiol. Sci. (2012) 11, 1860-1867.

3) Rodriguez-Serrano A.; Daza, M. C.; Doerr, M.; Villaveces, J. L. "Proton transfer from 1,4-pentadiene to superoxide radical anion: a QTAIM analysis", Rev. Colomb. Quim. accepted in 2012, to be published in "Vol. 41 (3)".

Manuscript drafts:

1) Rodriguez-Serrano A.; Rai-Constapel, V.; Daza, M. C.; Doerr, M.; Marian, C. M. "Internal Heavy Atom Effects on Phenothiazinium Dyes: Enhancement of Intersystem Crossing by Vibronic Spin-Orbit Coupling". Submitted to J. Phys Chem. A.

2) Rodriguez-Serrano A.; Daza, M. C.; Doerr, M.; Rai-Constapel, V.; Marian, C. M. "Protonation and hydration effects on the photophysics of thionine: A theoretical study". In preparation.

Participation in conferences

1) Rodriguez-Serrano A.; Daza, M. C.; Doerr, M. "Computational study of the electronic structure of thionine" Ninth Triennial Congress of the World Association of Theoretical and Computational Chemists (WATOC), July 17th - 22nd, Santiago de Compostela, Spain, 2011.

2) Rodriguez-Serrano A.; Daza, M. C.; Doerr, M. "Theoretical study of the effect of methylation on the electronic structure of thionine" IUPAC 2011 World Chemistry Congress, July 30th to August 7th, San Juan, Puerto Rico, 2011.

3) Rodriguez-Serrano A.; Rai-Constapel, V.; Daza, M. C.; Doerr, M.; Marian, C. M. " A theoretical study of thionine: Spin-orbit coupling and intersystem crossing". 14th International Congress of Quantum Chemistry, June 25th-30th, Boulder, United States of America, 2012.

4) Rodriguez-Serrano A.; Daza, M. C.; Doerr, M. "Efecto de la sustitución del azufre intraanular por oxígeno y selenio en la fotofísica de la tionina" I Congreso latinoamericano de estudiantes de química pura y aplicada. XIV Encuentro nacional de estudiantes de química UIS, November 6th - 9th, Bucaramanga, Colombia, 2012.

Chapter 1. Conceptual framework: Quantum chemical methods

1.1. Overview

In this Chapter, the conceptual framework of molecular quantum mechanics is outlined. We restrict to the introduction of general aspects, concepts and notions in quantum chemistry specific to this work which will not be extended beyond fundamental aspects. For a consistent overview over the basic aspects in the field of theoretical chemistry, the reader is encouraged to refer to the literature, *e. g.* Ref. [65].

1.2. The spin-free Schrödinger equation and the Born-Oppenheimer approximation

According to the principles of quantum mechanics, the wave function $\left(\Psi(\mathrm{R},\mathrm{r})\right)$ of any atomic or molecular system is a mathematical function that contains all the information that is necessary to determine any measurable property, static or dynamic, of the atomic or molecular system by performing appropriate mathematical operations on the function to produce a solution that includes the value of the property of interest. Once the wave function is available, all the properties of the molecule can in principle be computed. This wave function is produced by solving the Schrödinger equation (**Eq 1**):

$$\textbf{Eq 1. } \widehat{\boldsymbol{H}}\boldsymbol{\Psi}(\mathbf{R},\mathbf{r}) = \mathbf{E}\boldsymbol{\Psi}(\mathbf{R},\mathbf{r})$$

where H is the complete Hamiltonian and corresponds to the mathematical operator for the possible energies (E) associated with each wave function $\Psi(\mathrm{R},\mathrm{r})$. In order to describe molecular processes it is of fundamental importance to specify a molecular Hamiltonian. The complete molecular Hamiltonian, **Eq 2**, contains three space and one spin degree of freedom per particle (an electron or a nucleus):

Eq 2. $\widehat{\boldsymbol{H}} = \widehat{\boldsymbol{T}} + \widehat{\boldsymbol{V}} + \widehat{\boldsymbol{H}}_{\boldsymbol{es}} + \widehat{\boldsymbol{H}}_{\boldsymbol{hfs}}$

Here, the first term $\hat{T}$ is the kinetic energy operator, $\hat{V}$ is an electrostatic potential operator due to Coulomb interaction between nuclei, electrons, and between electrons and nuclei. $\widehat{H}_{es} = \widehat{H}_{SO} + \widehat{H}_{sr} + \widehat{H}_{ss}$ is a Hamiltonian related to the interaction of each electron's spin magnetic moment with the magnetic moments generated by the orbital motion of electron, the magnetic moments generated by the orbital motions of the nuclei $\left(\widehat{H}_{sr}\right)$ and the spin magnetic moments of the other electrons $\left(\widehat{H}_{ss}\right)$. The interaction with its own orbital moment is called spin-same orbit interaction and is part of the total spin-orbit interaction $\widehat{H}_{SO}$. In this thesis, only the spin-orbit Hamiltonian $\widehat{H}_{es} = \widehat{H}_{SO}$ will be considered. In this section we will first consider the spin-free part of the Hamiltonian. The influence of the electronic spin will be taken into account in the framework of Fermi´s golden rule (time-dependent perturbational theory) for treating spin-forbidden radiationless transitions, described in section **2.5.2.1**. The last term in **Eq 2** is related to the interaction of the magnetic and electric moments of the nuclei with the other electric and magnetic moments in the molecule. Because its contribution is very small compared to the other terms, it is neglected in the present context.

A big problem concerning the description of the electronic and nuclear motion lies in the fact that electronic and nuclear degrees of freedom are coupled mutually through their interaction. Hence, the first step in the solution of the molecular Schrödinger equation is the separation of electronic and nuclear motions. Labeling *n* as nuclei, *e* as electrons, $\hat{T}$ as kinetic energy operator and $\hat{V}$ as potential energy operator, the spin-free Schrödinger equation can be, then, be written as:

Eq 3. $\left(\widehat{\boldsymbol{T}}_{\boldsymbol{n}}(\mathbf{R}) + \widehat{\boldsymbol{T}}_{\boldsymbol{e}}(\mathbf{r}) + \widehat{\boldsymbol{V}}_{\boldsymbol{nn}}(\mathbf{R}) + \widehat{\boldsymbol{V}}_{\boldsymbol{ne}}(\mathbf{R},\mathbf{r}) + \widehat{\boldsymbol{V}}_{\boldsymbol{ee}}(\mathbf{r})\right)\boldsymbol{\Psi}(\mathbf{R},\mathbf{r}) = \mathbf{E}\boldsymbol{\Psi}(\mathbf{R},\mathbf{r})$

In a simple picture, the absorption of light generates a change in the electronic configuration which, as a consequence, promotes a change in the

configuration of the nuclei. An electronic transition can be considered to take place instantaneously (10^{-15}-10^{-16} s^{-1}) in comparison to the timescale of nuclear motions (10^{-12}-10^{-13} s^{-1}). Hence, when electrons move, the nuclei can be regarded as stationary. On the other hand, when the nuclei rearrange the electronic structure adjusts instantaneously. This is the basic idea behind the Born-Oppenheimer (BO) approximation. This approximation allows to treat electronic motion described by a wave function $\psi_i(\mathrm{R};\mathrm{r})$) and nuclear motions (described by a wave function $\chi_i(\mathrm{R})$) independently), **Eq 4**.

$$\textbf{Eq 4. } \boldsymbol{\Psi(\mathbf{R},\mathbf{r}) = \chi_i(\mathbf{R})\psi_i(\mathbf{R};\mathbf{r})}$$

The electronic wave function $\psi_i(\mathrm{R};\mathrm{r})$ depends on the electron coordinates and parametrically on the nuclear coordinates and is a solution of the electronic Schrödinger, **Eq 5**.

$$\textbf{Eq 5. } \boldsymbol{\left(\hat{T}_e(\mathbf{r}) + \hat{V}_{ne}(\mathbf{R},\mathbf{r}) + \hat{V}_{ee}(\mathbf{r})\right)\psi_i(\mathbf{R};\mathbf{r}) = \mathbf{E_i}\psi_i(\mathbf{R};\mathbf{r})}$$

This greatly simplifies the solution of **Eq 1** because it allows to compute the electronic wave function for any selected static nuclear framework. The nuclei, in principle, can be arranged in all possible configurations and the electronic energies $E_i(r)$ can be computed for each of them. This introduces the potent paradigm of potential energy (hyper)surfaces. However, this approximation breaks down when two PESs come close.

1.3. The Hartree-Fock approximation

Hartree–Fock (HF) method is a method of approximation for the determination of the wave function and the energy of a quantum many-body system in a stationary state. It is the most elementary way for obtaining a molecular orbital basis while taking into account the Pauli exclusion principle. The two-particle Coulomb interaction is substituted with an effective one-particle interaction. The electrons move in their spin orbitals independently of

each other. The effective interaction represents an average field created by all other electrons and nuclei that interact with a given electron.

The HF method is typically used for solving the time-independent Schrödinger equation for a multi-electronic systems. Since there are no known solution for many-electron systems, the problem is solved numerically. Due to the nonlinearities introduced by the HF approximation, the equations are solved using a nonlinear method, the "self-consistent field method" (SCF). The HF method makes five simplifications: *i*) the BO approximation is inherently assumed, *ii*) tipically relativistic effects are neglected (therefore, the momentum operator is assumed to be completely non-relativistic), *iii*) the variational solution is assumed to be a linear combination of a finite number of basis functions, which are usually chosen to be orthogonal, *iv*) each energy eigenfunction is assumed to be describable by a single Slater determinant and *v*) the mean field approximation is implied. Effects arising from deviations from the latter assumption, known as electron correlation, are completely neglected for the electrons of opposite spin, but are taken into account for electrons of parallel spin.

In the HF approximation, a product of one-electron wave functions (called orbitals) is used to approximate the electronic wavefunction $\psi_i(\mathrm{R};\mathrm{r})$. For a two particle system, the wavefunction can be written in the form of a Hartree product which is given as in **Eq 6**.

Eq 6. $$\boldsymbol{\psi_i}(\mathbf{R};\mathbf{r}) = \boldsymbol{\psi_i}(\boldsymbol{e_1}, \boldsymbol{e_2}) = \boldsymbol{\psi_1}(\boldsymbol{e_1})\,\boldsymbol{\psi_2}(\boldsymbol{e_2})$$

A linear combination of Hartree product functions form the Slater determinant that satisfies the antisymmetry principle. Therefore, electronic wavefunction is then represented as an antisymmetrized product of one-electron wavefunctions (spin orbitals, $\psi_i(\boldsymbol{e}_i)$) . The orbitals which optimally represent the many-electron wavefunction are the orbitals that minimize the total electronic energy. The wavefunction in the Slater determinant form for n electrons is given below:

Eq 7. $\boldsymbol{\psi_i(e_1, e_2, \ldots, e_i) = \frac{1}{\sqrt{N!}} \begin{vmatrix} \psi_1(e_1) & \psi_2(e_2) & \ldots & \psi_i(e_i) \\ \psi_1(e_1) & \psi_2(e_2) & \ldots & \psi_i(e_i) \\ \vdots & \vdots & \ddots & \ddots \\ \psi_1(e_1) & \psi_2(e_2) & \ldots & \psi_i(e_i) \end{vmatrix}}$

where $\psi_i(e_i)$ is the *n*th molecular spin orbital and e_i is the *i*th electron.

The energy is determined by using the variational principle, which leads to the HF equations, **Eq 8**.

Eq 8. $\boldsymbol{\hat{F}\psi_i = \varepsilon_i \psi_i}$

Where $\hat{F}$ is the Fock operator, ε_i is the energy of the molecular orbital ψ_i. The Fock operator is an effective one-electron operator which has the form:

Eq 9. $\boldsymbol{\hat{F} = -\frac{1}{2}\nabla_i^2 - \sum_{A=1}^{M} \frac{Z_A}{r_{iA}} + v^{HF}(i)}$

where $\boldsymbol{v^{HF}}$ is the average potential experienced by the *i*-th electron due to the presence of the other electrons. Since the $\hat{F}$ depends on ψ_i, the initial orbitals are guessed and then refined iteratively. Therefore, the HF equations (**Eq 8**) must be solved iteratively SCF method. First, an initial guess for the wavefunction is made, followed by the formation of the Fock operator, which is then used to generate the improved wavefunction. This procedure is iterated until self-consistency is reached. The main drawback of the HF method is that it does not account for the instantaneous electron-electron correlation (explicit electron-electron interaction) because the electrons are in the average field of all the other (N-1) electrons and the nuclei. Due to the neglect of the electron correlation, the HF method gives an upper limit to the exact energy and the difference between the exact and the HF energy is called the electron correlation energy. The correlation energy represents the energy due to instantaneous electron interactions in the molecule. Usually, it is divided into dynamic and static. The dynamic correlation energy is a consequence of the fact that the Fock operator does not represent the complete electronic Hamiltonian which differ due to a fluctuating potential. It

produces virtual excitations from occupied to unoccupied orbitals. The static correlation energy is a consequence of the inadequacy of the one Slater determinant to represent the electronic wavefunction and is usually considered as a long-range effect. Approaches to solve the correlation energy problem are divided into single and multi-reference methods. Single-reference methods account primary to dynamic correlation and are based on one Slater determinant for subsequent perturbational or variational treatments. Multi-reference methods address to both static and dynamic correlation energy and are based on a linear combination of several Slater determinants.

In practice, the HF equations are solved by introducing a finite set of spatial basis functions. The wavefunction is expressed in the form of a linear combination of atomic orbitals (LCAO) as given in **Eq 10**:

$$\textbf{Eq 10. } \boldsymbol{\psi_i = \sum_{\mu}^{N} C_{\mu i} \chi_{\mu} \;\; i = 1, 2, 3, \ldots, N}$$

$C_{\mu i}$ are the MO expansion coefficients, N is the number of basis functions and $\{\chi_{\mu}\}$ are a set of K known basis functions. If the set $\{\chi_{\mu}\}$ was complete, this would be an exact expansion and any complete set $\{\chi_{\mu}\}$ could be used. Unfortunately, for practical computational reasons this expansion is always truncated to a finite set of N basis functions. As such, it is important to choose a basis set that provide as far as possible a reasonably accurate expansion for the exact molecular orbitals, particularly for those molecular orbitals which are occupied and determine the ground state energy. There are many basis sets defined for polyatomic calculations like the split-valence Pople type basis sets,[66] Dunning's correlation-consistent basis sets,[67] split-valence basis sets of Ahlrichs and coworkers[68] are some of the most popular.

1.4. Density functional theory (DFT)[‡‡]

The time-dependent density functional theory (TDDFT) is an evolution of some ground state of a given system. This means that TDDFT is an initial value problem that can only be solved in the presence of some initial ground state. For this reason, the ground state density functional theory (DFT) is briefly reviewed in this section. For further details and derivations the reader is referred to books [69-70] and reviews.[71,72-73]

DFT is a reformulation of the ground state quantum mechanics in terms of the electron density rather than the many body wavefunction ($\Psi(r)$) which is very difficult to work with in most of real life systems: for an N-particle system, the many body wavefunction has 3N degrees of freedom (excluding spin), while the single particle density has only three degrees of freedom. The basic foundation of DFT is the Hohenberg-Kohn (HK) theorem,[74] which states that the external potential is a functional of the ground-state density. In other words, the density (an observable in 3D space) is used to describe the physics behind the interactions between electrons and, therefore, determines everything about the system: [75]

i) there is a one-to-one correspondence between the ground state density $\rho(\mathbf{r})$ of a non-relativistic quantum system and its external potential $v(\mathbf{r})$, and

ii) if a universal energy functional (in terms of the density) that is valid for any external potential is defined, then for a particular potential, the exact ground state energy of the system is the global minimum of this universal energy functional and the corresponding density that minimizes this functional is the ground state density of the system.

The HK theorem tells us that we can determine everything about a given system solely from its density but it does not tell us how to get this density.

[‡‡] This section closely follows references [71-72].

Kohn and Sham [76] (KS) proposed that the ground state density could be determined by mapping the fully interacting problem onto a fictitious non-interacting problem whose density is equal to that of the interacting problem. That means, the potential of the non-interacting problem should be chosen in such a way that give the correct ground state density of the fully interacting problem. In KS theory, this is formulated as a simple expression for the ground state energy, **Eq 11**:

$$\textbf{Eq 11. } \boldsymbol{E[\rho] = T_s[\rho] + V_{ne}[\rho] + J[\rho] + E_{xc}[\rho]}$$

where the forms of some of the functionals are explicitly known and presented in the following. The kinetic energy for the KS non-interacting reference system ($T_s[\rho]$) is given by **Eq 12** in terms of {ϕ_i}, the set of one electron KS orbitals.

$$\textbf{Eq 12. } \boldsymbol{T_s[\rho] = \sum_i \left\langle \phi_i \left| -\frac{1}{2}\nabla^2 \right| \phi_i \right\rangle}$$

The electron density of the KS reference system ($\rho(\mathbf{r})$) is given by:

$$\textbf{Eq 13. } \boldsymbol{\rho(\mathbf{r}) = \sum_i |\phi_i(\mathbf{r})|^2}$$

The nucleus-electron potential energy ($V_{ne}[\rho]$) is expressed in terms of the external potential due to the nuclei, $v[\mathbf{r}] = -\sum_A (Z_A/|\mathbf{r} - \mathbf{R}_A|)$:

$$\textbf{Eq 14. } \boldsymbol{V_{ne}[\rho] = \int \rho(\mathbf{r})\, v(\mathbf{r}) \mathbf{dr}}$$

And, finally the classical electron-electron repulsion Coulomb energy ($J[\rho]$):

$$\textbf{Eq 15. } \boldsymbol{J[\rho] = \frac{1}{2}\iint \frac{\rho(\mathbf{r})\rho(\mathbf{r}')}{|\mathbf{r}-\mathbf{r}'|} \mathbf{dr dr}'}$$

Much is known about the key remaining term, the exchange-correlation functional $E_{xc}[\rho]$, although no explicit form is available. It can be expressed in the constrained search formulation for density functionals: [77]

$$\textbf{Eq 16. } \boldsymbol{E_{xc}[\rho] = \min_{\Psi\to\rho} \langle \Psi | T + V_{ee} | \Psi \rangle - T_s[\rho] - J[\rho] = (T[\rho] - T_s[\rho]) + (V_{ee}[\rho] - J[\rho])}$$

where Ψ is a correctly antisymmetrized electron wavefunction, the minimization of the kinetic and electron-electron repulsion energies is done over all such wavefunctions that yield the density $\rho(\mathbf{r})$.

The E_{xc} energy is usually split into an exchange piece, E_x, and a correlation energy:

$$\textbf{Eq 17. } \boldsymbol{E_{xc} \equiv E_x - E_c}$$

Exchange can be defined in a HF-like way in terms of the KS spin orbitals $\phi_{i\sigma}(\mathbf{r})$ as in **Eq 18**:

$$\textbf{Eq 18. } \boldsymbol{E_x = -\frac{1}{2}\sum_{i,j,\sigma}^{occ} \iint \frac{\phi^*_{i\sigma}(\mathbf{r})\phi^*_{j\sigma}(\mathbf{r}')\phi_{i\sigma}(\mathbf{r}')\phi_{j\sigma}(\mathbf{r})}{|\mathbf{r}-\mathbf{r}'|}\mathbf{dr}\mathbf{dr}'}$$

To perform the self-consistent calculations in the noninteracting system, we need the functional derivative of the E_{xc} energy,

$$\textbf{Eq 19. } \boldsymbol{v_{xc}[\rho](\mathbf{r}) = \frac{\delta E_{xc}[\rho]}{\delta \rho(\mathbf{r})}}$$

This is called the exchange-correlation potential $v_{xc}[\rho](\mathbf{r})$, and it is the essential part of the multiplicative KS potential $v_s[\rho](\mathbf{r})$, part of the set of one-particle KS equations:

$$\textbf{Eq 20. } \boldsymbol{\left(-\frac{1}{2}\nabla^2 + v_s[\rho](\mathbf{r})\right)\phi_i(\mathbf{r}) = \varepsilon\phi_i(\mathbf{r});\ \ v_s[\rho](\mathbf{r}) = V_{ne}[\rho] + J[\rho] + v_{xc}[\rho]}$$

One can imagine smoothly connecting the interacting and non-interacting systems by multiplying the electron-electron repulsion term by λ, called the coupling-constant. Changing λ varies the strength of the interaction, and if we simultaneously change the external potential to keep the density fixed, we have a family of solutions for various interaction strengths. This makes all quantities (besides the density) functions of λ. When λ = 0, one has the non-interacting KS system, and when λ = 1, one has the fully interacting system. Thus, the exchange-correlation functional $E_{xc}[\rho]$ can also be expressed through the adiabatic connection by using the Hellmann-Feynman theorem: [78-79]

Eq 21. $$E_{xc}[\rho] = \int_0^1 \langle \Psi_\lambda | V_{ee} | \Psi_\lambda \rangle \, d\lambda - J[\rho]$$

In practice, the KS potential $v_s[\rho](\mathbf{r})$ is not known exactly. Many kinds density functional approximations have been developed for practical applications. DFT calculations use approximations to $E_{xc}[\rho]$, whose derivative yields an approximation to $v_{xc}[\rho](\mathbf{r})$. Also, many approximate xc-energy functionals have developed since the start of DFT. In the simplest local density approximation (LDA), the xc-energy at a point r' is calculated as if it were in a uniform gas. This approximation is useful in solids and other bulk materials where the electrons almost look like a uniform gas.[76] It is improved by including the gradient of the density, leading to the generalized gradient approximation (GGA). Some popular GGAs are BLYP (B88 [80] for exchange and LYP [81] for correlation) and PBE.[82] Hybrid potentials are popular among chemists because of their improved accuracy for main-group thermochemistry and transition-state barriers. These hybrid functionals mix in some fraction of exact exchange with GGA. They have an exchange energy which is a mixture of GGA and HF, which attempts to get the best of both worlds:

Eq 22. $$E_{xc}^{hyb}[\rho] = E_{xc}^{GGA} + a(E_x - E_x^{GGA})$$

The most widely used hybrid B3LYP, contains 3 experimentally fitted parameters [81,83,84] whereas PBE is derived from general principles of quantum mechanics.[82]

1.5. Methods for modeling electronically excited states

The phenothiazinium dyes contain an extended π-system with different types of low-lying excited states. Dynamic and static electron correlation have to be accounted for modeling the electronic structure of these states. The complete active space second order perturbation theory (CASPT2) is one of the well established *ab initio* treatments that includes both effects. Nevertheless, the application of this method is still limited to rather small molecules, and there is

still a need for methods that can accurately deal with larger systems. Over the past decade, the time-dependent density functional theory (TDDFT) [49] has emerged as a very common tool for studying electronically excited states of molecules of medium and large size.[50] The major advantage of TDDFT is its low computational cost,[85] roughly comparable with single excitation theories based on the Hartree-Fock (HF) ground state such as, *e. g.*, configuration interaction singles (CIS). Since the commonly used adiabatic approximation represents the response of a molecule in terms of single excitations (linear response), TDDFT is best suited for excited states that are dominated by single excitations and is not suited for the description of states with strong multireference and double excitation character.

The combined DFT/multi-reference configuration interaction (DFT/MRCI) of Grimme and Waletzke [51] constitutes an efficient alternative for the study of the electronic structure of dyes. In this method, the major part of dynamic electron correlation is captured by the DFT treatment, and static correlation effects are introduced by the MRCI technique which is also flexible enough to properly describe states with double excitation character. In short, the MRCI expansion is built up from Kohn-Sham (KS) determinants. The DFT/MRCI configuration state functions (CSFs) are built from KS rather than HF orbitals. An statistical benchmarking of the DFT/MRCI and several TDDFT (with the BP86, B3LYP and BHLYP functionals) methods [52] shows that lowest deviations are found for DFT/MRCI ≈ 0.24 eV for valence states. The method has been tested for a number of organic chromophores [86] and applied to the computation of UV-Vis spectra and dark states (see for example [40-45,87-95]), calculation of ISC rates and singlet-triplet coupling,[144,53,96-100] fluorescence [101-102] and circular dicrohism spectra.[103] Nevertheless, as can be seen in the cited literature, DFT/MRCI gradients are not available for excited states optimization of sizeable molecules and the electronically excited state minima should be obtained with another method for which the topology of the PES is similar to the one obtained with

DFT/MRCI. Excited state geometries have been shown to be predicted reliably using TDDFT and, combined with DFT/MRCI, the study of the photophysics of several dyes of medium (such as psolarens [54]) and large (such as porphyrins [55]) size has been accurately performed obtaining results very close to the experimental data.

1.5.1. Time-dependent density functional theory (TDDFT)[§§]

An overview of the basics of time-dependent density functional theory (TDDFT) is presented. For a more in-depth review, we refer to ref. [104,105, 106-108], and references therein.

Just like ground-state DFT where the HK and KS theorems prove a one-to-one correspondence between ground-state densities and potentials, there is a similar principle for TDDFT: The Runge-Gross (RG) theorem.[109] Consider N non-relativistic electrons, mutually interacting via the Coulomb repulsion, in a time-dependent external potential. The RG theorem states that the densities $\rho(\mathbf{r},\mathrm{t})$ and $\rho'(\mathbf{r},\mathrm{t})$ evolving from a common initial state $\Psi_0 = \Psi(t = 0)$ under the influence of two external potentials $v_{ext}[\rho](\mathbf{r},\mathrm{t})$ and $v_{ext}{}'[\rho](\mathbf{r},\mathrm{t})$ (both Taylor expandable about the initial time 0) are always different provided that the potentials differ by more than a purely time-dependent (**r**-independent) function:

$$\textbf{Eq 23. } \Delta\boldsymbol{v_{ext}}(\mathbf{r},\boldsymbol{t}) \neq \boldsymbol{c}(\boldsymbol{t}),$$

where

$$\textbf{Eq 24. } \Delta\boldsymbol{v_{ext}}(\mathbf{r},\boldsymbol{t}) = \boldsymbol{v_{ext}}(\mathbf{r},\boldsymbol{t}) - \boldsymbol{v_{ext}}'(\mathbf{r},\boldsymbol{t})$$

There is a one-to-one mapping between densities and potentials. Thus, this theorem states that, the time-dependent potential (and all other properties) is a functional of the time-dependent density (and the initial state).

[§§] The derivation outlined here follows reference [105].

The time-dependent Kohn–Sham (TDKS) equations are then defined in analogy to one-particle KS equations (**Eq 25**):

$$\textbf{Eq 25. } \left(-\frac{1}{2}\nabla^2 + v_s[\rho](\mathbf{r},t)\right)\phi_i(\mathbf{r},t) = i\frac{\partial}{\partial t}\phi_i(\mathbf{r},\mathrm{t}); \quad \phi_i(\mathbf{r},0) = \phi_i(\mathbf{r})$$

These set of equations describe a system of non-interacting electrons that evolve in a TDKS potential $v_s[\rho](\mathbf{r},\mathrm{t})$ and produce the same time-dependent density ($\rho(\mathbf{r},t)$) in **Eq 26** as that of the interacting system of interest. Thus, it replaces the interacting problem with a much simpler non-interacting one, as in the ground-state DFT.

$$\textbf{Eq 26. } \rho(\mathbf{r},\mathrm{t}) = \sum_i |\phi_i(\mathbf{r},t)|^2$$

Then, the TDKS effective potential $v_s[\rho](\mathbf{r},\mathrm{t})$, equation (**Eq 27**):

$$\textbf{Eq 27. } v_s[\rho](\mathbf{r},t) = v_{ext}[\rho](\mathbf{r},t) + v_H[\rho](\mathbf{r},t) + v_{xc}[\rho](\mathbf{r},t)$$

is decomposed to extract: *i*) the external potential of the system $v_{ext}[\rho](\mathbf{r},t)$ due to the ions in the system and any other external electromagnetic field such an external laser field, *ii*) the time-dependent Hartree potential $v_H[\rho](\mathbf{r},t)$ acording to **Eq 28** and *iii*) the remaining time-dependent exchange-correlation potential $v_{xc}[\rho](\mathbf{r},\mathrm{t})$.

$$\textbf{Eq 28. } v_H[\rho](\mathbf{r},t) = \int \frac{\rho(\mathbf{r},t)}{|\mathbf{r}-\mathbf{r}'|}\mathbf{d}^3\mathbf{r}$$

Then, a time-dependent xc-potential $v_{xc}[\rho](\mathbf{r},t)$ should be defined (and approximated). In contrast to the ground-state problem, the XC potential depends not only on the density but on the initial wavefunction Ψ(0) and KS Slater determinant ϕ(0). This means that it is a functional of the entire history of the densities $\rho(\mathbf{r},t)$, the initial interacting wavefunction and KS wavefunction. If both are non-degenerate ground states, it becomes a simple functional of $\rho(\mathbf{r},t)$ alone. This more complicated dependence comes about because two different wavefunctions, which are chosen to have the same density for all time, can come from completely different external potentials

which the xc-potential accounts for. As the density evolves, the xc-potential is determined not solely by the present density $\rho(\mathbf{r},t)$, but also by the history $\rho(\mathbf{r},t')$ for 0 ≤ t' < t. In practical calculations, many approximations exist for $v_{xc}[\rho](\mathbf{r},t)$ as a functional of the density and modifications of traditional time-dependent Schrödinger equation schemes have been evaluated for the propagation.[110] For example, it is useful to break the xc-potential up into two pieces: an adiabatic part which only depends on the present density and a dynamic one which incorporates the memory dependence:

Eq 29. $$\boldsymbol{v_{xc}[\rho;\Psi(0),\phi(0)](\mathbf{r},t) = v_{xc}^{dyn}[\rho;\Psi(0),\phi(0)](\mathbf{r},t) + v_{xc}^{adia}[\rho](\mathbf{r},t)}$$

The adiabatic piece of the potential (v_{xc}^{adia} in **Eq 29**) is the xc-potential for electrons as if their instantaneous density were a ground state, **Eq 30**. In the spirit of DFT, the dynamic piece is everything else.

Eq 30. $$\boldsymbol{v_{xc}^{adia}[\rho](\mathbf{r},t) = \left.\frac{\delta E_{xc}[\rho]}{\delta\rho(\mathbf{r})}\right|_{\rho(t)}}$$

More practical TDDFT calculations use linear response theory. Within linear response theory, the TDDFT equations simply reduce to an eigenvalue equation [111]

Eq 31. $$\boldsymbol{\Omega^{(\pm)}\mathbf{F}_i^{(\pm)} = \omega_i^2\mathbf{F}_i^{(\pm)}}$$

where the ω_i are the excitation energies of the system. The superscript $\pm$ means that there are two sets of equations, *e. g.* singlet and triplet state energies. The diagonalization of $\boldsymbol{\Omega}^{(\pm)}$ matrix immediately yields the transition frequencies ω_i:

Eq 32. $$\boldsymbol{\Omega_{ia,jb}^{(\pm)} = \delta_{ab}\delta_{ij}(\varepsilon_a-\varepsilon_i)^2 + 2\sqrt{\varepsilon_a-\varepsilon_i}\left(K_{ia,jb}^{\uparrow\uparrow} \pm K_{ia,jb}^{\uparrow\downarrow}\right)\sqrt{\varepsilon_b-\varepsilon_j}}$$

where the $\varepsilon_{i,j}$ are occupied and $\varepsilon_{a,b}$ are unoccupied KS orbital energies, ↑ and ↓ specify the spin orientation and the **K** matrix elements are discussed below. The KS orbitals correspond to a system of non-interacting electrons, the sum of whose squares the true density of the system (in an exact DFT

formulation). The first term of the $\boldsymbol{\Omega}^{(\pm)}$ matrices is the KS transition energy. The second term corrects the KS result to give the true interacting result, the singlet and triplet transition energies.

The **K** matrix elements given in **Eq 32** are given by **Eq 33**:

Eq 33.

$$\boldsymbol{K}_{\boldsymbol{ia,jb}}^{\boldsymbol{\sigma\sigma'}}(\boldsymbol{\omega}) = \iint \frac{\boldsymbol{\phi}_{i\sigma}(\mathbf{r})\boldsymbol{\phi}_{a\sigma}(\mathbf{r})\boldsymbol{\phi}_{b\sigma'}(\mathbf{r}')\boldsymbol{\phi}_{j\sigma'}(\mathbf{r}')}{|\mathbf{r}-\mathbf{r}'|}\mathbf{dr}\mathbf{dr}' + \iint \boldsymbol{\phi}_{i\sigma}(\mathbf{r})\boldsymbol{\phi}_{a\sigma}(\mathbf{r})\boldsymbol{f}_{xc}^{\sigma\sigma'}(\mathbf{r},\mathbf{r}',\boldsymbol{\omega})\boldsymbol{\phi}_{b\sigma'}(\mathbf{r}')\boldsymbol{\phi}_{j\sigma'}(\mathbf{r}')\mathbf{dr}\mathbf{dr}'$$

where we used σ, σ' to generically indicate spins, *i,j* indicate occupied orbitals and *a,b* virtual orbitals. The first term in this equation is the Hartree term, which is only dependent on the ground-state KS orbitals. From **Eq 32** for $\boldsymbol{\Omega}_{ia,jb}^{(\pm)}$ we see that this term cancels in the triplet case in the minus combination. The second term contains the xc-kernel, **Eq 34**:

$$\textbf{Eq 34. } \boldsymbol{f}_{xc\sigma\sigma'}(\mathbf{r},\mathbf{r}',\boldsymbol{t}-\boldsymbol{t}') = \frac{\boldsymbol{\delta v}_{xc\sigma}(\mathbf{r},\mathbf{t})}{\boldsymbol{\delta\rho}_{\sigma'}(\mathbf{r}',\mathbf{t}')}$$

whose Fourier transform is simply $f_{xc}^{\sigma\sigma'}(\mathbf{r},\mathbf{r}',\omega)$. The xc-kernel is the only part in this expression that needs to be approximated, after the ground-state calculation has been performed. There exist many different kinds of xc-kernels such as: the adiabatic local density approximation (ALDA, [112]), the "exact" adiabatic approximation (AA, [113]), the Gross-Kohn (GK, [114]) approximation, the Vignale-Kohn (VK, [115]) and the exact exchange (EE, [116-117]) methods.

1.5.2. Density functional theory/multireference configuration interaction (DFT/MRCI)

Another DFT-based method for describing electronically excited states is the combination of DFT and configuration interaction (CI). S. Grimme [118] initially proposed such a combination with a CIS treatment involving only single excitations. This was later extended and generalized to a

multireference singles and doubles CI treatment (DFT/MRCI) [51,119] which is briefly outlined in the following.

The general idea behind the DFT/MRCI method is to capture dynamic electron correlation by standard DFT and the non-dynamical effects by a rather small CI expansion. Considering the fact that the electronic Hamiltonian in a CI method can be written in terms of a one-electron Fock operator and the SCF energy of a particular parent configuration, any matrix element can be formulated in terms of its difference from the SCF result.[118] Denoting the occupation number of the *i*th MO in the parent configuration by $\bar{n}_i$, the Fock operator, the Hartree-Fock (HF) energy, and the Hamiltonian are given by:

Eq 35. $$\widehat{\boldsymbol{F}}_{\boldsymbol{ij}}^{\mathbf{HF}} = \widehat{\boldsymbol{h}}_{\boldsymbol{ij}} + \sum_{\boldsymbol{k}} \bar{\boldsymbol{n}}_{\boldsymbol{k}} \left[(\boldsymbol{ij}|\boldsymbol{kk}) - \mathbf{1/2}(\boldsymbol{ik}|\boldsymbol{jk})\right]$$

Eq 36. $$\boldsymbol{E}^{\mathbf{HF}} = \sum_{\boldsymbol{i}} \bar{\boldsymbol{n}}_{\boldsymbol{i}} \widehat{\boldsymbol{F}}_{\boldsymbol{ii}}^{\mathbf{HF}} - \frac{\mathbf{1}}{\mathbf{2}} \sum_{\boldsymbol{ij}} \bar{\boldsymbol{n}}_{\boldsymbol{i}} \bar{\boldsymbol{n}}_{\boldsymbol{j}} [(\boldsymbol{ii}|\boldsymbol{jj}) - \mathbf{1/2}(\boldsymbol{ij}|\boldsymbol{ij})]$$

Eq 37.

$$\widehat{\boldsymbol{H}} = \sum_{\boldsymbol{ij}} \boldsymbol{F}_{\boldsymbol{ij}}^{\mathbf{HF}} \widehat{\boldsymbol{E}}_{\boldsymbol{i}}^{\boldsymbol{j}} - \sum_{\boldsymbol{ijk}} [(\boldsymbol{ij}|\boldsymbol{kk}) - \mathbf{1/2}(\boldsymbol{ik}|\boldsymbol{jk})] \bar{\boldsymbol{n}}_{\boldsymbol{k}} \widehat{\boldsymbol{E}}_{\boldsymbol{i}}^{\boldsymbol{j}} + \frac{\mathbf{1}}{\mathbf{2}} \sum_{\boldsymbol{ijkl}} (\boldsymbol{ij}|\boldsymbol{kl}) \left[\widehat{\boldsymbol{E}}_{\boldsymbol{i}}^{\boldsymbol{j}} \widehat{\boldsymbol{E}}_{\boldsymbol{k}}^{\boldsymbol{l}} - \boldsymbol{\delta}_{\boldsymbol{jk}} \widehat{\boldsymbol{E}}_{\boldsymbol{i}}^{\boldsymbol{l}}\right]$$

where the two-electron integrals are written in Mulliken notation and $\hat{E}_k^l$ is the single-particle (de)excitation operator. Defining the occupation number vector υ for the space part and the spin-specific coupling pattern *w*, the Hamiltonian matrix elements between two CSFs $\langle wv|\hat{H}|w'v'\rangle$ can be divided into four classes: [119]

- Ia Same space part, same spin-coupling (diagonal);
- IIa Same space part, different spin-coupling (off-diagonal);
- Ib Space part differs by one-electron excitation (off-diagonal);
- IIb Space part differs by two-electron excitation (off-diagonal).

The key approximation of the DFT/MRCI method is to introduce empirical corrections of the exact Kohn-Sham matrix elements and scaled two-electron integrals, to avoid double counting of correlation effects and to be able to tune

the results. The diagonal elements of the effective DFT/CI Hamiltonian $\widehat{H}^{\mathrm{DFT}}$ have the form:

$$\textbf{Eq 38. } \langle \boldsymbol{wv}|\widehat{\boldsymbol{H}}^{\mathbf{DFT}} - \boldsymbol{E}^{\mathbf{DFT}}|\boldsymbol{wv}\rangle = \langle \boldsymbol{wv}|\widehat{\boldsymbol{H}} - \boldsymbol{E}^{\mathbf{DFT}}|\boldsymbol{wv}\rangle - \sum_{\boldsymbol{c}}^{\boldsymbol{n_{exc}}}(\boldsymbol{F}_{\boldsymbol{cc}}^{\mathbf{HF}} - \boldsymbol{F}_{\boldsymbol{cc}}^{\mathbf{KS}})$$

$$+ \sum_{\boldsymbol{a}}^{\boldsymbol{n_{exc}}}(\boldsymbol{F}_{\boldsymbol{aa}}^{\mathbf{HF}} - \boldsymbol{F}_{\boldsymbol{aa}}^{\mathbf{KS}}) + \frac{\mathbf{1}}{\boldsymbol{n_{exc}}}\sum_{\boldsymbol{a}}^{\boldsymbol{n_{exc}}}\sum_{\boldsymbol{c}}^{\boldsymbol{n_{exc}}}\boldsymbol{p_J}\,(\boldsymbol{aa}|\boldsymbol{cc}) - \boldsymbol{p}[\boldsymbol{N_o}](\boldsymbol{ac}|\boldsymbol{ac})$$

where F_{ij}^{KS} is a matrix element of the Kohn-Sham Fock operator of the parent state and E^{DFT} is the pure DFT energy of the parent determinant $|\overline{wv}\rangle$. The indices c and a refer to creation and annihilation operators, and n_{exc} is the excitation level with respect to the space part of the parent determinant. $p[N_o]$ has different forms for singlet and triplet states: ${}^1p[N_o] = p[0] + N_0^1\alpha$ and ${}^3p[N_o] = N_0^3\alpha$. The off-diagonal elements are obtained by an appropriate scaling of the exact matrix elements:

$$\textbf{Eq 39. } \langle \boldsymbol{wv}|\widehat{\boldsymbol{H}}^{\mathbf{DFT}}|\boldsymbol{w'v'}\rangle = \langle \boldsymbol{wv}|\widehat{\boldsymbol{H}}|\boldsymbol{w'v'}\rangle \boldsymbol{p_1 e^{-p_2 \Delta E_{ww'}^4}}$$

where p_1 and p_2 are scaling factors and $\Delta E_{ww'}$ is the energy difference between the diagonal elements of the two CSFs. This damping is necessary to avoid an overestimate of electron correlation effects, which are already partly included in the diagonal term. The parameters p_J , p[0] and α are obtained by a least-squares fit of calculated excitation energies against experimental data of selected reference molecules, using BHLYP [50,60-61] as DFT functional. The final DFT/MRCI parameters are shown in **Table 1**.

Table 1 DFT/MRCI parameters for BH-LYP functional for singlet and triplet states, taken from Ref. [119].

Multiplicity	Parameter				
	p_1	p_2	p_J	p[0]	α
Singlet	0.619	3.27	0.510	0.595	0.106
Triplet	0.619	3.27	0.493	-	0.056

1.5.3. The CC2 method[***]

This section provides a brief general description of coupled-cluster (CC) theory and the CC2 method. Details of the methodology could be found in the original publications [120,121,122]. The CC method is a single-reference method that successfully solves the problem of dynamic electron correlation. Dynamic correlations due to the fluctuating potential manifest themselves as virtual excitations from occupied to unoccupied orbitals. Excitations are divided into single (S), double (D), triple (T), etc… according to the number of excitations to virtual orbitals. These excitations have a certain amplitude and associated probability to occur. The Rayleigh-Schrödinger perturbation theory accounts only for excitations up to a given order, where the fluctuating potential is a perturbation. The second-order perturbation produces double excitations from the occupied orbitals to unoccupied orbitals but the perturbation expansion converges slowly. It is possible to use an exponential ansatz for the wavefunction for speeding up convergence:

$$\textbf{Eq 40. } |\boldsymbol{\Psi_{CC}}\rangle = \boldsymbol{e^{\hat{T}}}|\boldsymbol{\Phi_{HF}}\rangle$$

where $|\Phi_{HF}\rangle$ denotes de Hartree-Fock reference wavefunction and $\hat{T}$ is the cluster operator which is a sum of operators that produce single ($\hat{T}_1$), double ($\hat{T}_1$), and higher excitations:

$$\textbf{Eq 41. } \boldsymbol{\hat{T} = \hat{T}_1 + \hat{T}_2 + \hat{T}_3 + \cdots + \hat{T}_n = \sum_{i=1}^{n} \sum_{\mu_i} t_{\mu_i} \tau_{\mu_i}}$$

where n is the number of electrons of the system. Excitation operators in the second quantization are written as $a_A^\dagger a_I$ for single excitations and $a_A^\dagger a_I a_B^\dagger a_J$ for double excitations which can be denoted by τ_{μ_i} for *i*-tuple excitations. Thus the index *i* corresponds the level of excitation and *μ* stands for a particular index set, for example:

[***] This section follows references [151] and [122].

Eq 42. $\hat{\boldsymbol{T}}_{\mathbf{1}} = \sum_{AI} \boldsymbol{t}_{\boldsymbol{I}}^{\boldsymbol{A}} \boldsymbol{a}_{\boldsymbol{A}}^{\dagger} \boldsymbol{a}_{\boldsymbol{I}}$; $\hat{\boldsymbol{T}}_{\mathbf{2}} = \sum_{\boldsymbol{A>B,I>J}} \boldsymbol{t}_{\boldsymbol{IJ}}^{\boldsymbol{AB}} \boldsymbol{a}_{\boldsymbol{A}}^{\dagger} \boldsymbol{a}_{\boldsymbol{I}}\, \boldsymbol{a}_{\boldsymbol{B}}^{\dagger} \boldsymbol{a}_{\boldsymbol{J}}$

where the indices *I* and *J* are used for occupied orbitals and *A* and *B* for unoccupied orbitals. t_I^A and t_{IJ}^{AB} are cluster amplitudes for single and double excitations, respectively. When the CC wavefunction is introduced into the time-independent Schrödinger equation and pre-multiplied with $e^{-\hat{T}}$ one obtains:

Eq 43. $\boldsymbol{e^{-\hat{T}} \hat{H} e^{\hat{T}} \left|\Phi_{HF}\right\rangle = E_{CC} \left|\Phi_{HF}\right\rangle}$

The expression for the CC energy can be obtained by projecting on the Hartree-Fock reference space (**Eq 44**) since the $e^{-\hat{T}}$ operator vanishes due to the condition: $\tau_{v_i} \left|\Phi_{HF}\right\rangle = 0$.

Eq 44. $\boldsymbol{E_{CC} = \left\langle \Phi_{HF} \right| \hat{H} e^{\hat{T}} \left| \Phi_{HF} \right\rangle}$

These are the central equations of CC theory. Retaining only certain classes of excitations creates a hierarchy of approximations. The ansatz for coupled-cluster singles (CCS) contains only the $\hat{T}_1$ operator, for singles and doubles (CCSD) it contains $\hat{T}_1 + \hat{T}_2$, for singles, doubles and triples (CCSDT) it contains $\hat{T}_1 + \hat{T}_2 + \hat{T}_3$. One can derive approximate approaches that include higher excitations via a perturbative framework, and thus reduce the scaling of the computational effort with respect to the number of orbitals, without significant loss of accuracy. The most popular of such methods for treating excited states by CC theory is CC2.

The CC2 method is an approximation to CCSD where the singles equations are treated in the same manner as CCSD. The double excitation equations for the nonlinear ground-state amplitudes and linear response are approximated by the first-order terms only. The $\hat{T}_1$ operator is treated as zeroth order, since the response of the single excitations to an external one-electron perturbation is of zeroth order too (such as electromagnetic radiation). The equations for the ground-state doubles amplitudes are similar

to the expressions of the MP2 method, apart from the fact that the two-electron integrals are transformed with $\hat{T}_1$. Concerning excited electronic states, single excitations are corrected through second order and pure double excitations are only correct to zeroth order. Furthermore, the CC2 method is usually employed in combination with the resolution-of-identity (RI) approximation. This approximation simplifies the calculation of the two-electron integrals in an atomic basis. The particularly computationally demanding are four-index integrals. They are substituted by three-center integrals using an auxiliary basis set in the RI method. Products of the atomic orbitals are expanded in the auxiliary basis set of atom-centered Gaussian functions.

1.6. Conductor-like screening model (COSMO) for solvent effects

The Conductor-like Screening Model (COSMO) [123,124] is a continuum solvation model, the solvent is not represented explicitly, but rather by a structureless continuous medium which is polarized by the solute. The solute molecule forms a cavity within the dielectric continuum of permittivity ε that represents the solvent. The charge distribution of the solute polarizes the dielectric medium. The response of the medium is described by the generation of screening charges on the cavity surface. Continuum solvation models usually require the solution of the rather complicated boundary conditions for a dielectric in order to obtain the screening charges. COSMO uses a simple boundary condition of vanishing electrostatic potential for a conductor to obtain the screening charges:

$$\textbf{Eq 45. } \boldsymbol{\Phi}^{\mathbf{tot}} = \mathbf{0}$$

This represents an electrostatically ideal solvent with ε = ∞ The vector of total electrostatic potential on the cavity surface segments is determined by the solute potential Φ^{sol},

$$\textbf{Eq 46. } \boldsymbol{\Phi}^{\mathbf{tot}} = \boldsymbol{\Phi}^{\mathbf{sol}} + \mathbf{A}\boldsymbol{q} = \mathbf{0}$$

which consist of the electronic and the nuclear part, and the vector of screening charges $\mathbf{q}$. $\mathbf{A}$ is the Coulomb matrix of the screening charge interactions. For a conductor, the boundary condition $\Phi^{\mathrm{tot}} = 0$ defines the screening charges as:

$$\textbf{Eq 47. } \mathbf{q} = -\mathbf{A}^{-1}\boldsymbol{\Phi}^{\mathbf{sol}}$$

To take into account the finite permittivity of real solvents, the screening charges are scaled by a factor $\mathrm{f}(\varepsilon)$.

$$\textbf{Eq 48. } \mathbf{f}(\boldsymbol{\varepsilon}) = \frac{\boldsymbol{\varepsilon}-\mathbf{1}}{\boldsymbol{\varepsilon}+\frac{\mathbf{1}}{\mathbf{2}}}$$

Therefore:

$$\textbf{Eq 49. } \mathbf{q}^{*} = -\mathbf{f}(\boldsymbol{\varepsilon})\mathbf{q}$$

The deviations of this COSMO approximation from the exact solution are rather small. For strong dielectrics like water they are less than 1%, while for non-polar solvents with $\varepsilon \approx 2$ they may reach 10% of the total screening effects. However, for weak dielectrics, screening effects are small, and the absolute error therefore typically amounts to less than one kcal/mol. The dielectric energy, i.e. the free electrostatic energy gained by the solvation process, is half of the solute-solvent interaction energy.

$$\textbf{Eq 50. } \mathbf{E}_{\mathbf{diel}} = \frac{\mathbf{1}}{\mathbf{2}}\mathbf{f}(\boldsymbol{\varepsilon})\mathbf{q}^{\dagger}\boldsymbol{\Phi}^{\mathbf{sol}}$$

The total free energy of the solvated molecule is the sum of the energy of the isolated system calculated with the solvated wave function and the dielectric energy. A COSMO energy calculation starts with the construction of the cavity surface grid. Within the SCF procedure, the screening charges are calculated in every cycle and the potential generated by these charges is included into the Hamiltonian. This ensures a variational optimization of both the molecular orbitals and the screening charges, which then also allows the evaluation of analytic gradients.

Chapter 2. Photophysical processes of electronically excited states of organic chromophores

2.1. Overview

Absorption of UV-Vis radiation by an organic chromophore creates excited electronic states ($S_0 \rightarrow S_n$), see **Fig. 3**. Compared to the electronic ground state, the lifetime of these excited states is rather short. Moreover, light absorption triggers a multitude of processes that compete for the dissipation of the excess of energy in the excited states. After photoexcitation, experience has shown that the fastest primary intramolecular process is IC (energy loss in absence of light emission) to a low-lying singlet excited state, commonly the first singlet state ($S_n \dashrightarrow S_1$). Photochemical and photophysical processes can drive the subsequent depopulation of the S_1 state.

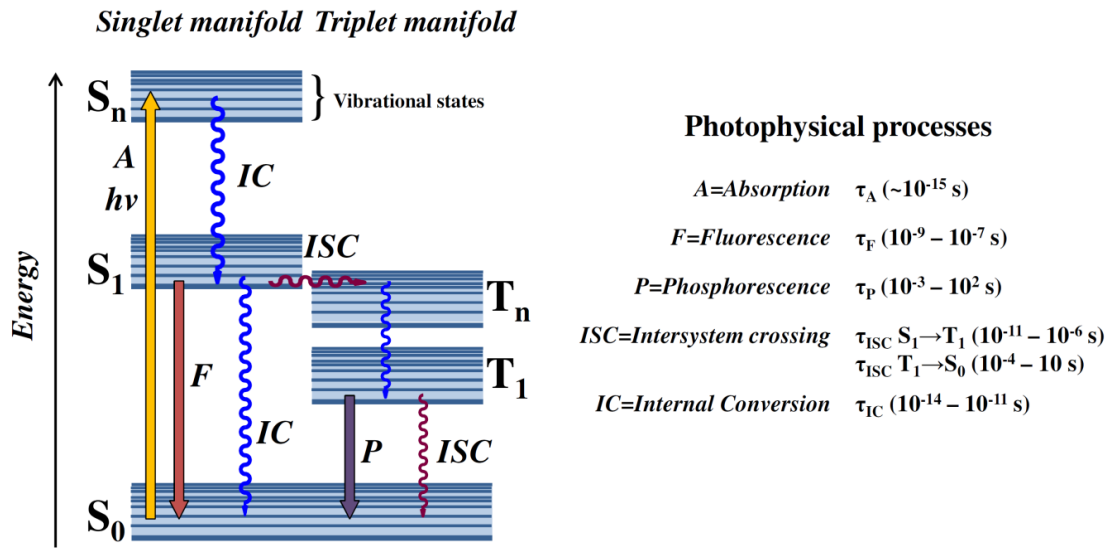

Fig. 3 Jablonski diagram representing the radiative and radiationless photophysical processes. Their time scales (s) are presented in the right [125]. This diagram is representative for organic chromophores that typically exhibit a closed-shell singlet excited state. The radiative processes are shown in straight arrows and radiationless processes in curly arrows.

In photochemical processes, the electronically excited molecule undergoes chemical reactions in order to form new species. Collisions with other molecules can cause energy transfer which may result in quenching of the excited electronic state. On the other hand, photophysical (unimolecular) processes are defined as transitions that interconvert excited states to each other or that interconvert excited states to the ground state. The final result of these processes is the initial molecular specie. The photophysical decay of excited electronic states can be a radiative (see Section **2.4**) or radiationless process (see Section **2.5**) as is depicted in **Fig. 3**. Which process dominates the deexcitation depends mainly on how fast these competing processes occur. The relative rates of the transitions from a given state determine the probability of the various plausible processes that can occur. The values of these rates are available if the rate constants (*k*) for the various processes can be estimated from experiment or through computation. Moreover, these rates depend on a number of structural and energetic factors. The main purpose of this proposal is to study the mechanisms involved in the photophysical decay of thionine and its derivatives upon absorption of light. Therefore this Chapter outlines the generally most important photophysical processes and gives an overview of the theoretical framework of the calculation of the deactivation rates that will be employed in this work. For further detailed information, see Ref. [125] for photochemistry topics.

2.2. Light absorption

The absorption of light by a molecule occurs on an ultrafast timescale (≈ 10^{-15} s^{-1}) in discrete amounts of energy, termed photons ($E = hv$) and corresponds to excitation of the molecule from the ground state to an excited state. This process occurs due to an interaction of the oscillating electric field vector of the light wave with charges (electrons) in the molecule, and can only occur with incident light of specific wavelengths. If the energy of the photon is insufficient to promote an electronic transition, no absorption occurs. If the

absorbed photon contains more energy than is necessary for a simple electronic transition, the excess energy is usually converted into vibrational and rotational energy. Because excitation of an organic molecule by light absorption normally occurs without a change of the electronic spin, the excited state also has singlet multiplicity.

With UV or visible light, dyes are usually excited to higher vibrational levels of excited electronic states. Irradiation with a wide spectrum of wavelengths will generate an entire range of allowed transitions that populate the various vibrational energy levels of these excited states. Some of these transitions will have a much higher probability than others, and all absorptions constitute the absorption spectrum of the molecule. The various energy levels involved in the absorption and emission of light are treated in this proposal in the framework of the spin-free Born-Oppenheimer approximation, which defines the vibronic states (see Section **1.2**). These vibronic states are products $\chi_m(R)\psi_n(r;R)$ of nuclear and electronic wavefunctions. The vibronic density of states is lowest in the vicinity of the first vibrational level of the electronic ground state. At vibrational higher energies, the vibronic density of states increases rapidly, which facilitates many relaxation processes after light absorption.

2.3. The Franck-Condon (FC) principle

The Frank-Condon (FC) principle is a powerful means for understanding the shape and intensity distribution of an absorption (and emission) band. It is based on the separation of nuclear and electronic degrees of freedom as was introduced in section **1.2**. In this case, the electronic transition between the initial state ($\langle i| = \langle i_e i_n|$, *e* denote electrons and *n* nucleus) and the final state ($|f\rangle = |f_e f_n\rangle$) is vertical (*i. e.* it occurs so fast that the nuclei do not change their positions during the electronic transition). The probability of a transition between the two states is proportional to the square of the corresponding electronic transition moment matrix element $\mathbf{R}$:

$$\textbf{Eq 51. } \mathbf{R} = \langle \boldsymbol{i} | \widehat{\boldsymbol{M}} | \boldsymbol{f} \rangle \; ; \; \widehat{\boldsymbol{M}} = \widehat{\boldsymbol{M}}_{\boldsymbol{e}}(\boldsymbol{R}; \boldsymbol{r}) + \widehat{\boldsymbol{M}}_{\boldsymbol{n}}(\boldsymbol{R})$$

where $\widehat{M}$ is the transition moment vector operator, here given in the dipole approximation, which can be separated into one part depending on the electrons ($\widehat{M}_e$, electronic dipole moment operator) and one depending on the nuclei ($\widehat{M}_n$, nuclear dipole moment operator). Substituting $\widehat{M}$ and separating the electronic terms on $\widehat{M}_n$ we obtain **Eq 52**:

$$\textbf{Eq 52. } \mathbf{R} = \langle \boldsymbol{i_e i_n} | \widehat{\boldsymbol{M}}_{\boldsymbol{e}}(\boldsymbol{R}; \boldsymbol{r}) | \boldsymbol{f_e f_n} \rangle \; + \langle \boldsymbol{i_n} | \widehat{\boldsymbol{M}}_{\boldsymbol{n}}(\boldsymbol{R}) | \boldsymbol{f_n} \rangle \, \langle \boldsymbol{i_e} | \boldsymbol{f_e} \rangle$$

The integral over the electron coordinates in the final term is zero because the electronic states are orthogonal to one another for each selected value of R ($\langle i_e | f_e \rangle = \delta_{if} = 0$). $\widehat{M}_e(R; r)$ in **Eq 52** is the electronic dipole moment for the transition when the nuclei have the coordinates R. To a reasonable first approximation, this transition moment is independent of the locations of the nuclei as long as they are not displaced by a large amount from the minimum on the PES. Therefore, the overall transition dipole moment is: [65]

$$\textbf{Eq 53. } \mathbf{R} = \langle \boldsymbol{i_e} | \widehat{\boldsymbol{M}}_{\boldsymbol{e}}(\boldsymbol{R}) | \boldsymbol{f_e} \rangle \, \langle \boldsymbol{i_n} | \boldsymbol{f_n} \rangle$$

The first term in **Eq 53** is called electronic transition moment, and is also commonly denoted $\mu_{el}(i, f)$. In the Born-Oppenheimer approximation this matrix element does not depend directly on the position of the nuclei, but indirectly via the parametric dependence of the electronic eigenfunctions on the nuclear coordinates. If the electronic transition takes place instantaneously, the nuclei will not move during the transition. Therefore, this matrix element will not change and can be treated as constant. In section **2.5.2**, we will see that for ISC processes there are some cases where the description of the transition matrix element has to be extended beyond this zero-order term.

A schematic illustration of this principle is presented in **Fig. 4**. In the FC approximation, the transition occurs vertically between the zeroth vibrational

level of the initial state ($\Psi_i, \mathrm{v} = 0$) and the vibrational levels of the final state ($\Psi_f, \mathrm{v}' = \{0,1,2 \ldots\}$). The shape of the absorption band does not only depends on the form of PESs of initial and final state and the vibrational wave functions, but also on the displacement between the geometries of the two states. Three cases can be distinguished, see **Fig. 4**:

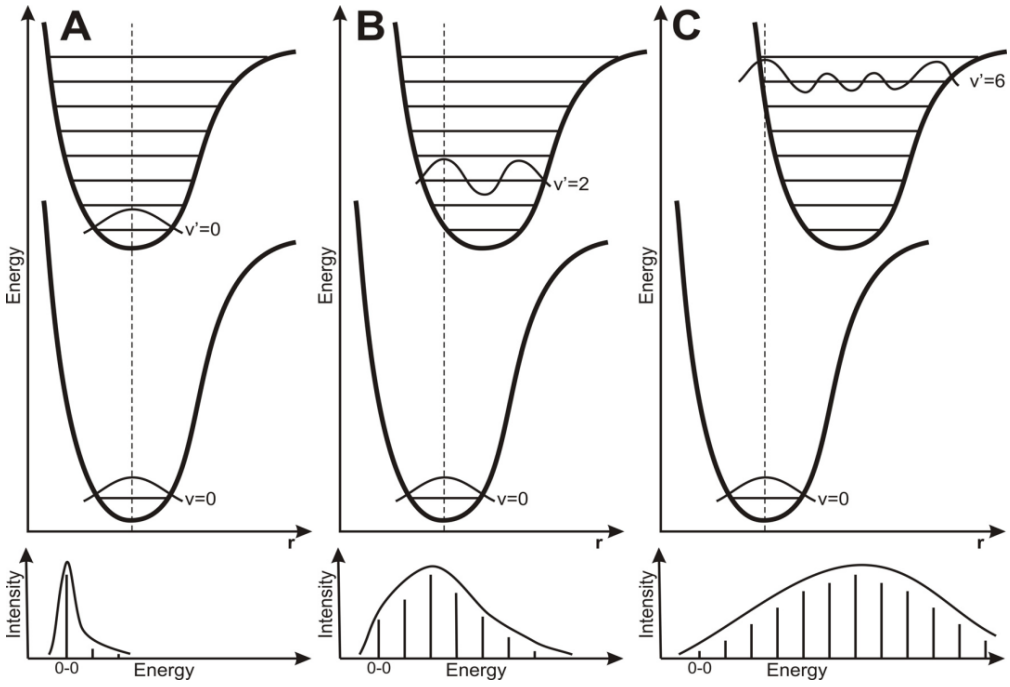

Fig. 4 Upper part: Potential energy curves explaining the intensity distribution in absorption spectra according to the FC principle for three different cases. The electronic transition is represented by the dashed vertical line. The equilibrium geometries of initial and final states are: (A) the same, differ by a small amount (B) and differ by a large amount (C). Bottom: intensity distributions and resulting shape of the absorption band.[Source, Ref. 126]

A) The nuclear coordinates of initial and final state minima are identical and no other transitions are observable (due to the orthogonality of the vibrational eigenfunctions). The most intense absorption is obtained for the 0-0 transition and transitions to higher-lying vibrational levels are nearly forbidden.

B) The initial and final state minima are similar: In this case the 0-0 transition is no longer the most probable transition but can still be present. Instead, the

largest overlap between the eigenfunctions occurs between v = 0 and a low-lying vibrational level (for example, v = 2 in **Fig. 4**).

C) When the initial and final state minima are (very) different, the 0-0 transition may appear as a very small absorption and the most probable transition occurs between v = 0 and a high-lying vibrational level (for example, v = 6 in **Fig. 4**). The shape of the resulting absorption band is wide.

2.4. Radiative decay processes

Radiative decay processes are mechanisms in which the excess of excitation energy is discarded as a photon. In the Jablonski diagram (**Fig. 3**) these processes are indicated as straight arrows. During the electronic relaxation the total electronic spin may change. Therefore, the radiative processes are in organic chromophores can be classified as:

- ✓ Spin-allowed singlet-singlet emission of photons $S_1 \rightarrow S_0 + h\nu$, called *fluorescence* and characterized by a rate constant k_F
- ✓ Spin-forbidden triplet-singlet emission of photons $T_1 \rightarrow S_0 + h\nu$, called *phosphorescence* and characterized by a rate constant k_P

2.4.1. Fluorescence

Fluorescence processes consist of *i*) photoexcitation of the molecule to the higher vibrational levels of the excited singlet state, followed by subsequent relaxation to its lowest vibrational level, *ii*) photon emission to an excited vibrational level of the electronic ground state, and *iii*) finally relaxation to the lowest vibrational level of the electronic ground state. According to Kasha's rule [1], only the lowest excited electronic state S_1 exhibits detectable emission but there are exceptions. An example is azulene where the second excited state emits. The lifetime of a singlet excited state is approximately 10^{-9} - 10^{-7} s and therefore the decay in a fluorescence process is of the same order of magnitude. The fluorescence emission also occurs in accordance

with the Frank-Condon principle and the emission spectrum will show the vibrational structure characteristic of the electronic ground state. For most molecules, the equilibrium geometry of the ground state and the excited state are different. This results in a redshift of the emission maximum with respect to the absorption maximum, called Stokes' shift. In condensed phase, various intermolecular interactions in the ground and excited states cause a separation of the 0-0 transitions of absorption and emission. This phenomenon is referred to as anomalous Stokes' shift and can be seen as a measure of the interaction between solvent and molecule.

2.4.2. Phosphorescence

The transitions leading to phosphorescence are also illustrated in **Fig. 3**. Here the emission of the photon occurs in a sequence of steps that involves the change in multiplicity which in the spin-free and non-relativistic Born-Oppenheimer treatment is a forbidden process. However, in a relativistic treatment this is not the case. In a simple picture, spin-orbit coupling (see Section **2.5.2.3**) mixes the singlet and triplet states which results in non-vanishing transition probabilities between these states.

After light absorption, vibrational relaxation and radiationless transitions within the electronic excited states occur and, if this is not too fast, the spin-orbit coupling in the molecule may succeed in causing ISC to the triplet manifold (see Section **2.5.2**). The repopulation of the singlet manifold from a triplet state (T_1) has been found to be highly improbable if the difference in energy between the $T_1(v = 0)$ and the $S_1(v = 0)$ state is large compared to the thermal energy. Finally the system can slowly relax to the ground state because spin-orbit coupling enables this transition with a decay rate in the range of 10^{-2} to 10^4 s^{-1}.[125] Phosphorescence is therefore much slower than fluorescence, at least in molecules composed of light elements as many organic molecules.

2.4.3. Calculation of radiative rate constants

The radiative rate constant depends on the transition dipole moment $\mu_{el}(i,f)$ between the initial state *i* and the final electronic state *f* and the vertical energy gap $\Delta E_{i,f}$ between the two states. It can be estimated using **Eq 54**: [†††]

$$\textbf{Eq 54. } \boldsymbol{k_{rad}(i \rightarrow f) = \frac{4e^2}{3c^3\hbar^4} \Delta E_{i,f}^3 \, \mu_{el}^2(i,f)}$$

For fluorescence, the determination of $\mu_{el}(i,f)$ is possible in the framework of non-relativistic theory, **Eq 55**, and the rate constants (k_{rad} = k_F) can be computed directly using **Eq 54**:

$$\textbf{Eq 55. } \boldsymbol{\mu_{el}(i,f) = \langle i_e | \hat{M}_e(R) | f_e \rangle \; ; \; \hat{M}_e = \sum_g e\vec{r}_g}$$

where $\vec{r}_g$ is the position vector of the gth electron.

However, this is not the case for calculation of the phosphorescence rate constants (k_{rad} = k_P). Here, spin-orbit coupling must be taken into account in the calculation of $\mu_{el}(i,f)$. To this end, a procedure based in perturbational theory has been formulated: the Hamiltonian is split into a spin-free (SF) part (as the unperturbed Hamiltonian) $\hat{H}^0 = \hat{H}_{SF}$ and the spin-dependent perturbation as the spin-orbit Hamiltonian $\hat{H}^{(1)} = \hat{H}_{SO}$. In this approach $\mu_{el}(i,f)$ between the T_x sublevel (the *x* refers to the cartesian component) of the excited triplet state $i_x = {}^3\Psi_a$ and the electronic ground state $f = {}^3\Psi_X$ is given by **Eq 56**:

$$\textbf{Eq 56.}$$

$$\boldsymbol{\mu_{el}(a_x, X) =}$$

$$\boldsymbol{\sum_j^{sing.} a_j \left\langle {}^1\Psi_X^{(0)} \middle| \sum_g^N e\vec{r}_g \middle| {}^1\Psi_j^{(0)} \right\rangle + \sum_j^{trip.} b_j^* \left\langle {}^3\Psi_j^{(0)}, T_x \middle| \sum_g^N e\vec{r}_g \middle| {}^3\Psi_a^{(0)}, T_x \right\rangle}$$

[†††] Expressing k_F in units of s^{-1}, $\Delta E_{i,f}$ in cm^{-1} and $\mu_{el}(i,f)$ in atomic units (ea_0), the numerical prefactor becomes 2.0261×10^{-6}.

The abbreviation *sing*. refers to singlets and *trip*. refers to triplets. Similar expressions can be obtained for the T_y and T_z sublevels (for further details see Ref. [64]). The coefficients a_j and b_j^* are obtained by diagonalizing H_{SO} in the basis of unperturbed wavefunctions. Therefore, results will depend on the way how the secular equation $\widehat{H} = \widehat{H}_{SF} + \widehat{H}_{SO}$ is solved. Several treatments such as quasi-degenerate perturbational theory (QDPT),[64] two step spin-orbit CI,[127] or LS-contracted spin-orbit CI [128] have been also proposed for calculating $\mu_{el}(i,f)$. Nevertheless, the evaluation of phosphorescence rates using perturbational expressions converges very slowly with the number of zero-order states employed in the expansion of the first-order perturbed wavefunction.[129] The MRSOCI (multireference spin-orbit configuration interaction) methodology is an alternative way where spin-orbit coupling is included variationally. In this case, $\widehat{H} = \widehat{H}_{SF} + \widehat{H}_{SO}$ is solved in the basis of configurational state functions (CSFs). Due to the large dimensions of the secular problem, a complete diagonalization cannot be carried out. Instead the solutions are determined iteratively by a modified Davidson scheme that has been extended to complex-valued matrices. The convergence of the Davidson procedure is accelerated by using spin-orbit coupled QDPT wavefunctions to start up the iteration. For further details see Ref. [58] and Ref. [130].

2.5. Radiationless decay processes

Radiationless transitions between electronic states are a form of electronic relaxation in which the electronic energy is converted into kinetic energy associated with nuclear vibrational motion. These processes can be spin-allowed or spin-forbidden and are represented by wavy arrows in **Fig. 3**:

- ✓ Spin-allowed radiationless transitions between states of the same spin: $S_1 \rightarrow S_0$ + heat, $S_n \rightarrow S_1$ + heat and $T_n \rightarrow T_1$ + heat are called *internal conversion* (IC) and are characterized by a rate constant k_{IC}.

- ✓ Spin-forbidden radiationless transitions between excited states of different multiplicity $S_1 \rightarrow T_n$ + heat are called *intersystem crossing* (ISC) and are characterized by a rate constant k_{ISC}.
- ✓ Spin-forbidden radiationless transitions between the first triplet state and the ground state $T_1 \rightarrow S_0$ + heat are also called *intersystem crossing* (ISC) and are characterized by a rate constant k_{TS}.

2.5.1. Internal conversion (IC) and vibrational relaxation (VR)

Internal conversion (IC) is an isoenenergetic radiationless transition between two electronic states of the same multiplicity. When the transition results in a vibrationally excited molecular entity in the lower electronic state, the molecule could undergo deactivation to its lowest vibrational level. The rate of IC between different states is fast when the adiabatic energy separation between the two states is small. Usually, $S_n \rightarrow S_1$ and $T_n \rightarrow T_1$ ICs are substantially faster than $S_1 \rightarrow S_0$ IC (sometimes even faster than the period of a molecular vibration), since the adiabatic energy differences among the electronically excited states are much smaller than the S_1 - S_0 gap. Experimental observations show an exponential dependence of the $S_1 \rightarrow S_0$ IC rate constant on the energy gap between the two states. Commonly, this relation is referred to as the energy-gap law.[131] $S_1 \rightarrow S_0$ IC can be ultra-fast when a barrierless conical intersection between these states is found (pentacene Φ_{IC} = 0.75 [132] and azulene $k_{IC} \approx 10^{12}$ s^{-1} [133-134]). One consequence of the very fast $S_n \rightarrow S_1$ and $T_n \rightarrow T_1$ ICs in the vast majority of molecules is that fluorescence and phosphorescence are observed from the S_1 and the T_1 excited states, known as Kasha's rule.[1] For instance, due to the very fast $S_n \rightarrow S_1$ + heat and $T_n \rightarrow T_1$ + heat IC processes, the particular photophysics of a dye will depend on the lifetime and reactivity of the S_1 and the T_1 excited states.

In the condensed phase it is possible to observe vibrational relaxation (VR) as a consequence of collisions with solvent molecules. In the low-pressure

gas phase the total energy of the molecule remains conserved for a long time. Internal vibrational redistribution (IVR) represents an energy flow between normal modes due to anharmonicity. The advent of pulsed picosecond and femptosecond laser spectroscopy has allowed the direct measurement of electronic and vibrational relaxation processes which occur in this time range in fluid solutions at room temperature. For a variety of organic molecules,[135-136] values for the rate constant of vibrational relaxation are typically $\approx 10^{12} - 10^{14}$ s^{-1}. The reason why this transfer of excess vibrational energy to the environment is so fast is that the vibrations within a molecule and the vibrations of the molecules in the environment have the ability to rapidly accept the energy of nuclear motion of a molecule (in both its ground and excited state) and convert it into many different degrees of vibrational motion. Because the vibrational, rotational and translational energy levels of the solvent environment of an excited state form a continuous, these energy levels may serve as a classical heat bath capable of taking up any amount of vibrational energy that the excited molecule needs to dispose.[136] This represents nowadays a difficulty for modeling solvation effects on the photophysics of dyes because the current quantum chemical optimization methods do not simulate the response of the molecule and the surrounding solvent when the system is photoexcited. Nevertheless, a qualitative picture of the subsequent deactivation processes and photophysics of a photosensitizer can be obtained by calculating the spectroscopic solvation shifts at the ground state geometry or by optimizing the desired excited states using solvation models, see Sections **1.6** and **4.4**.

2.5.2. Intersystem crossing (ISC)

The spin-forbidden ISC process is a radiationless transition promoted by spin-orbit coupling in organic molecules. In the Born-Oppenheimer approximation, there is no mechanism for ISC resulting from the artificial separation of the electronic and spin motions. In this framework, if a molecule is in a singlet

state, it will stay forever in the singlet state even if a reaction coordinate exists such that a crossing of the singlet and triplet PESs occurs. The interaction of the electron spin magnetic moment with the magnetic moment due to the orbital motion of electrons, called *spin-orbit coupling*, mixes zero-order states of different multiplicity. Then, if spin orbit-coupling is present, a mixing of singlet and triplet states at a nearby crossing point of the corresponding PESs may occur and ISC will be partially allowed if certain conditions are met: (*i*) The singlet and triplet states involved should be close in energy, (*ii*) their spin-orbit coupling interaction should be of reasonably strength, and (*iii*) the density of vibrational levels should be high in the accepting state. Let us open this discussion in some detail in the following sections.

2.5.2.1. The Fermi's golden rule

Fermi's golden rule provides the rate at which electronic transitions take place between two given states. It applies to a wide range of optical and electronic processes. The rates are calculated from probabilities determined by transition matrix elements in quantum mechanical, first-order perturbation theory. This rule is valid when the initial state has not been significantly depleted by scattering into the final states. The most common way to derive the equation is to start with time-dependent perturbation theory and to take the limit for absorption under the assumption that the time of the measurement is much larger than the time needed for the transition. The derivation presented in this section follows Ref. [137-151].

Here, the Wigner-Weisskopf model for irreversible decay will be explained for deriving the Fermi's golden rule.[138-139] Let's assume an initial level $|s\rangle$ which is prepared at t=0 and is coupled to a set of levels $|\{l\}\rangle$. The coupling V_{sl}, which couples the $|s\rangle$ and $|\{l\}\rangle$ levels is not an eigenstate of the total Hamiltonian. Moreover, if there is a sufficient density of $\{l\}\rangle$-levels, the population transfer from $|s\rangle$ to $|\{l\}\rangle$ is considered irreversible. Otherwise the population oscillate back and forth. The Hamiltonian for the model is:

Eq 57. $\widehat{\mathbf{H}} = \widehat{\mathbf{H}}_{\mathbf{0}} + \widehat{\mathbf{V}} = \mathbf{E}_{\boldsymbol{s}}|\boldsymbol{s}\rangle\langle\boldsymbol{s}| + \sum_{\boldsymbol{l}} \mathbf{E}_{\boldsymbol{l}}|\boldsymbol{l}\rangle\langle\boldsymbol{l}| + \sum_{\boldsymbol{l}} \mathbf{V}_{\boldsymbol{sl}}(|\boldsymbol{s}\rangle\langle\boldsymbol{l}| + |\boldsymbol{l}\rangle\langle\boldsymbol{s}|)$

It is sufficient to consider only the time-independent Schrödinger equation since all couplings in the model are time-independent:

Eq 58. $\left(\mathbf{E} - \widehat{\mathbf{H}}\right)|\boldsymbol{\psi}\rangle = \mathbf{0}$

The Green function for this equation is defined as:

Eq 59. $\left(\mathbf{E} - \widehat{\mathbf{G}}(\mathbf{E})\right)|\boldsymbol{\psi}\rangle = \mathbf{0}$

Eq 60. $\widehat{\mathbf{G}}(\mathbf{E}) = \frac{\mathbf{1}}{\boldsymbol{E} - \widehat{\mathbf{H}} + \mathbf{i}\boldsymbol{\epsilon}}$

The Green function for the zero-order Hamiltonian $\widehat{\mathrm{H}}_0$ is:

Eq 61. $\widehat{\mathbf{G}}_{\mathbf{0}}(\mathbf{E}) = \frac{\mathbf{1}}{\boldsymbol{E} - \widehat{\mathbf{H}}_{\mathbf{0}} + \mathbf{i}\boldsymbol{\epsilon}}$

Setting $\widehat{\mathbf{A}} = E - \widehat{\mathrm{H}} + \mathrm{i}\epsilon$ and $\widehat{\mathbf{B}} = E - \widehat{\mathrm{H}}_0 + \mathrm{i}\epsilon$, we can use the identity **Eq 62** for obtaining the Dyson equation **Eq 63**:

Eq 62. $\frac{\mathbf{1}}{\widehat{\mathbf{A}}} = \frac{\mathbf{1}}{\widehat{\mathbf{B}}} + \frac{\mathbf{1}}{\widehat{\mathbf{B}}}\left(\widehat{\mathbf{B}} - \widehat{\mathbf{A}}\right)\frac{\mathbf{1}}{\widehat{\mathbf{A}}}$

Eq 63. $\widehat{\mathbf{G}}(\mathbf{E}) = \widehat{\mathbf{G}}_{\mathbf{0}}(\mathbf{E}) + \widehat{\mathbf{G}}_{\mathbf{0}}(\mathbf{E})\widehat{\mathbf{V}}\widehat{\mathbf{G}}(\mathbf{E})$

The time development of the population of the $|s\rangle$ state:

Eq 64. $\mathbf{P}_{\mathbf{s}}(\boldsymbol{t}) = \left|\left\langle \mathbf{s}\middle|\widehat{\mathbf{G}}(\boldsymbol{t})\middle|\mathbf{s}\right\rangle\right|^{\mathbf{2}}$

where $\widehat{\mathrm{G}}(t)$ is the Fourier transform of $\widehat{\mathrm{G}}(\mathrm{E})$, $\widehat{\mathrm{G}}(t) = \frac{1}{2\pi}\int_{-\infty}^{\infty} \mathrm{e}^{\mathrm{iE}t}\widehat{\mathrm{G}}(\mathrm{E})\mathrm{d}t$. Hence, inserting the Dyson equation between $|s\rangle, \langle\boldsymbol{s}|$ and $|\boldsymbol{s}\rangle, \langle\boldsymbol{l}|$:

Eq 65. $\mathbf{G}_{\boldsymbol{ss}}(\mathbf{E}) = \frac{\mathbf{1}}{\boldsymbol{E} - \boldsymbol{E_s} + \boldsymbol{i\epsilon}} + \frac{\mathbf{1}}{\boldsymbol{E} - \boldsymbol{E_s} + \boldsymbol{i\epsilon}}\sum_{\boldsymbol{l}} \boldsymbol{V_{sl}}\boldsymbol{G_{ls}}(\boldsymbol{E})$

Eq 66. $\mathbf{G}_{\boldsymbol{ls}}(\mathbf{E}) = \frac{\mathbf{1}}{\boldsymbol{E} - \boldsymbol{E_l} + \boldsymbol{i\epsilon}}\boldsymbol{V_{ls}}\boldsymbol{G_{ss}}(\boldsymbol{E})$

Substituting **Eq 66** into **Eq 65**, we obtain:

Eq 67. $\mathbf{G}_{\boldsymbol{ss}}(\mathbf{E}) = \frac{\mathbf{1}}{\boldsymbol{E} - \boldsymbol{E_s} + \sum(\boldsymbol{E})}$

where $\sum(E)$ is the self energy:

$$\textbf{Eq 68. } \sum(\boldsymbol{E}) = \sum_{\boldsymbol{l}} \frac{|\boldsymbol{V_{sl}}|^2}{\boldsymbol{E}-\boldsymbol{E_l}+\boldsymbol{i\epsilon}}$$

Which has a real and an imaginary part:

$$\textbf{Eq 69. } \sum(\boldsymbol{E}) = \boldsymbol{\Delta_s}(\boldsymbol{E}) - \boldsymbol{i\Gamma_s}(\boldsymbol{E}) = \boldsymbol{P}\sum_{\boldsymbol{l}} \frac{|\boldsymbol{V_{ls}}|^2}{\boldsymbol{E}-\boldsymbol{E_l}} - \boldsymbol{2i\pi}\sum_{\boldsymbol{l}}|\boldsymbol{V_{ls}}|^2\boldsymbol{\delta}(\boldsymbol{E}-\boldsymbol{E_l})$$

P denotes the principal value of the integral, $\boldsymbol{\Delta_s}(\boldsymbol{E})$ is the level shift due to coupling, and $\boldsymbol{\Gamma_s}(\boldsymbol{E})$ is the resonance width. The energy dependence of $\sum(\boldsymbol{E})$ can be complicated. Assuming that the coupling constants $\boldsymbol{V_{ls}}$ do not strongly depend on the energy levels $|\{l\}\rangle$ then the variation of $\sum(\boldsymbol{E})$ in the vicinity of $\boldsymbol{E} = \boldsymbol{E_s}$ will be small. The frequency dependence is dominated by the resonance at $\boldsymbol{E} = \boldsymbol{E_s}$ and the energy dependence of $\sum(\boldsymbol{E})$ can be replaced with the value of $\sum(\boldsymbol{E_s})$.

The population of the energy level $|s\rangle$ is given by:

$$\textbf{Eq 70. } \mathbf{P_s}(\boldsymbol{t}) = \left|\frac{\mathbf{1}}{\mathbf{2\pi}}\int_{-\infty}^{\infty} \mathbf{e}^{\mathbf{iEt}}\widehat{\mathbf{G}}_{\boldsymbol{ss}}(\mathbf{E})\mathbf{dt}\right|^2 = \left|\frac{\mathbf{1}}{\mathbf{2\pi}}\int_{-\infty}^{\infty} \mathbf{e}^{\mathbf{iEt}}\frac{\mathbf{1}}{\mathbf{E}-(\mathbf{E_s}+\boldsymbol{\Delta_s}(\mathbf{E_s}))+\boldsymbol{i\Gamma_s}(\mathbf{E_s})}\mathbf{dt}\right|^2 = \mathbf{e}^{\boldsymbol{\Gamma t}}$$

where the rate of the decay is:

$$\textbf{Eq 71. } \boldsymbol{\Gamma} = \mathbf{2\pi}\sum_{\boldsymbol{l}}|\boldsymbol{V_{ls}}|^2\boldsymbol{\delta}(\boldsymbol{E_s}-\boldsymbol{E_l})$$

The **Eq 71** is the Fermi golden rule of quantum mechanics which describes how the population of a initially excited vibronic level decays exponentially with the rate constant Γ.

2.5.2.2. Energy gap law

Jortner and coworkers [140-141] have differentiated between two cases for the probabilities of radiationless transitions in large molecules: weak coupling and strong coupling. In the weak coupling limit, the transition probability depends exponentially on the adiabatic energy difference ΔE upon small displacements along the vibrational normal modes. Thus, the smaller the

energy gap, the larger the transition probability, which is commonly referred to as the energy gap law. However, this qualitative rule applies only for a pair of nested states.

The strong coupling case is characterized by large relative displacements in some coordinates so that an intersection of PESs could be expected. The probability of a radiationless transition exhibits a Gaussian dependence on the energy parameter $\Delta E\text{-}E_M$, where E_M is the molecular rearrangement energy, which corresponds to half of the Stokes shift for the two electronic states involved in the transition. Taking temperature effects into account within a Boltzmann distribution, the analysis of the strong coupling limit for the displaced PES resulted in a generalized activated rate equation similar to Marcus theory.[142] As a consequence, a straightforward rule could not be enounced and there are cases where either a direct [143-144] or an inverse relationship between the transition probability and ΔE could be observed.

2.5.2.3. Spin-orbit coupling

The electron spin is a relativistic effect. The first theory that successfully explained the origin of the electron spin is Dirac's fully relativistic one-particle theory. In this theory, the electron spin and angular momentum are not conserved separately but the resulting total angular momentum is conserved. A fully relativistic two-body equation for electrons is unknown. Hence, approximate equations are used for relativistic electronic structure calculations (details can be found in Ref. [64]). Usually the starting point for further approximations is a four-component Dirac-Coulomb-Breit Hamiltonian that contains a sum of Dirac-like terms (kinetic energy and one-electron interaction), the Coulomb and Breit interaction (retardation effect for the Coulomb interaction and magnetic interactions). This is reduced to two components and split into separate spin-independent and spin-dependent parts in order to obtain the spin-orbit Hamiltonian. The most important transformations are the Foldy-Wouthuysen and Douglas-Kroll

transformations. Using the Foldy-Wouthuysen transformation, one can derive the Breit-Pauli spin-orbit Hamiltonian ($\widehat{H}_{SO}^{BP}$):

Eq 72. $$\widehat{\boldsymbol{H}}_{\boldsymbol{SO}}^{\boldsymbol{BP}} = \frac{e^2\hbar}{2m^2c^2}\left(\sum_i \sum_A \boldsymbol{Z_A s_i}\left(\frac{\boldsymbol{R_{iA}}}{\boldsymbol{R_{iA}^3}} \times \boldsymbol{p_i}\right) - \sum_{i \neq j}\left(\frac{\boldsymbol{r_{ij}}}{\boldsymbol{r_{ij}^3}} \times \boldsymbol{p_i}\right) \cdot \left(\boldsymbol{s_i} + \boldsymbol{2s_j}\right)\right)$$

$$= \sum_{\boldsymbol{i}} \widehat{\boldsymbol{H}}_{\boldsymbol{SO}}\,(\boldsymbol{i}) + \sum_{\boldsymbol{i,j}} \widehat{\boldsymbol{H}}_{\boldsymbol{SO}}(\boldsymbol{i,j})$$

Here, Z_A is the charge of the *A*-th nucleus, $\boldsymbol{R}_{iA}$ is the position vector between electron *i* and nucleus A, $\boldsymbol{r}_{ij}$ is the position vector between electrons *i* and *j*, $\boldsymbol{s}_i$ is the spin of the *i*-th electron and $\boldsymbol{p}_i$ is its linear momentum. In the simplified notation of **Eq 72**, it can be seen that the Breit-Pauli Hamiltonian is the sum of one- and two-electron terms. The one-electron term ($\widehat{H}_{SO}(i)$) corresponds to the one-electron interaction that each electron samples by "revolving" about all nuclei. The two-electron term ($\widehat{H}_{SO}(i,j)$) simulate the interaction of the angular momentum of an electron with the spins of other electrons. The calculation of the spin-orbit integrals in the basis of molecular orbitals can be performed using the mean-field spin-orbit Hamiltonian defined by Heβ et al.[61]. This represents a way of incorporating the two electron contributions in an average way by performing a mean-field summation over the two-electron interactions, similar to the Coulomb and exchange operators in Hartree-Fock theory as given by **Eq 73**:

Eq 73. $$\widehat{\boldsymbol{H}}_{\boldsymbol{ij}}^{\boldsymbol{SO}} = \langle \boldsymbol{i}|\boldsymbol{H}^{\boldsymbol{SO}}(\boldsymbol{1})|\boldsymbol{j}\rangle$$

$$+\frac{\boldsymbol{1}}{\boldsymbol{2}}\sum\nolimits_{\boldsymbol{k,fixed}\,\{\boldsymbol{n_k}\}} \boldsymbol{n_k}\left(\langle \boldsymbol{ik}|\boldsymbol{H}^{\boldsymbol{SO}}(\boldsymbol{1,2})|\boldsymbol{jk}\rangle - \langle \boldsymbol{ik}|\boldsymbol{H}^{\boldsymbol{SO}}(\boldsymbol{1,2})|\boldsymbol{kj}\rangle - \langle \boldsymbol{ki}|\boldsymbol{H}^{\boldsymbol{SO}}(\boldsymbol{1,2})|\boldsymbol{jk}\rangle\right)$$

where *k* runs over the core and selected valence spin orbitals (*i* and *j*) and n_k stands for the occupation of orbital *k*. The occupation numbers of the core shells are always 2, while the occupation numbers of the valence shells may vary between 0 and 2, depending on the reference determinant. In this way the two-electron contributions of the valence shells are averaged. Averaging

over the spin component is done as well. This approximation works well for one- and many-center terms. A further approximation can be obtained by replacing the molecular mean-field by a sum of atomic mean fields. In this way, only the two-electron integrals for basis functions located at the same center have to be evaluated.

2.5.2.4. Time-independent formalism for the calculation of ISC rate constants[‡‡‡]

In typical organic molecules, the spin-orbit interaction of two states is small compared to their adiabatic energy difference and the density of final vibrational states at the energy of the initial state is high. Within the framework of time-dependent perturbation theory an expression using Fermi's golden rule (Section **2.5.2.1**) can be employed to determine ISC rates k_{ISC}^{TI}:

$$\textbf{Eq 74. } \boldsymbol{k_{ISC}^{TI} = \frac{2\pi}{\hbar}\sum_{\{|f\rangle\}}\left|\langle i,\{v_{ij}\}|\widehat{H}'|f,\{v_{fk}\}\rangle\right|^2\delta\left(E_i^0 - E_f^0\right)}$$

Here, $\widehat{H}'$ is the perturbation operator that corresponds to the spin-orbit coupling Hamiltonian $\widehat{H}_{SO}$ that couples the two vibronic states ($|S_i\{v_{ij}\}\rangle = i,\{v_{ij}\}$ and $|T_f\{v_{fk}\}\rangle = f,\{v_{fk}\}$) and the δ function is the density of levels and ensures the conservation of the molecular energy for the non-radiative transition. In order to obtain k_{ISC}^{TI} from **Eq 74** (time-independent approach), several modifications are necessary. According to Toniolo and Persico [145-146], it is possible to approximate this expression by a summation over rates of transitions in an energy interval of width 2η around the energy of the zeroth level of the initial state *i* (E_i,*v* = 0). This means that instead of treating a strictly isoenergetic transition, an interval of final states is considered taking into account all final states within ±η of the vibronic energy of the initial level. Consequently, the results depend on the choice of η: it should be as small as possible because the transition *i* → *f* should be isoenergetic, but large enough

[‡‡‡] This section closely follows references [54] and [64].

to cover a sufficient number of acceptor states. If we denote the coupling matrix elements driving the radiationless transition by $H^{SO}_{\mathbf{v}=0,\mathbf{v}'}$, the rate constant is obtained as:

$$\textbf{Eq 75. } k_{ISC}^{TI} = \frac{2\pi}{\hbar\eta}\sum_{\left|E_{f,\{v_{fk}\}}-E_{i,v=0}\right|<\eta}\left|H^{SO}_{v=0,\{v_{fk}\}}\right|^2$$

Note that the vectors $\{v_{ij}\}$ and $\{v_{fk}\}$ represent sets of vibrational quantum numbers in all normal modes of the initial (*i*) and final (*f*) electronic states. Only those levels of the final state contribute, which lie in a chosen interval of width 2η centered around the energy $E_{i,v=0}$ of the initial state.

In order to get the coupling matrix elements needed in **Eq 75**, a cumbersome integration over both the electronic and the nuclear degrees of freedom has to be performed. The $H^{SO}_{\mathbf{v}=0,v_{fk}}$ term can be expanded into a power series in the variables $\{q_m\}$ around some reference configuration $\mathbf{q}_0$ [62] which can be chosen to coincide with the minimum of the initial state, **Eq 76**. For more background regarding to this derivation we refer the reader to references [54], [147] and [148].

Eq 76.

$$H^{SO}_{v=0,v_{fk}} =$$

$$\langle i|\hat{H}_{SO}|f\rangle|_{\mathbf{q}_0=0}\langle v=0|v_{fk}\rangle + \sum_m\left(\frac{\partial}{\partial q_m}\langle i|\hat{H}_{SO}|f\rangle\right)\Big|_{\mathbf{q}_0=0}\langle v=0|q_k|v_{fk}\rangle + \cdots$$

The first term on the right-hand side of **Eq 76** is a purely electronic matrix element within the Condon approximation and is denominated as *direct* spin-orbit coupling in the following. Whereas, the second term represents the first order derivative or Herzberg-Teller type coupling and is denoted as *vibronic* spin-orbit coupling.

For molecules with more than one internal degree of freedom, the normal modes of the ground and excited states are not identical (Duschinsky effect). Thus, for the calculation of the multidimensional integrals generated by the

combination of **Eq 75** and **Eq 76** it is necessary to describe the excited state normal modes in the basis of the ground state normal modes taking into account the different minimum geometries. This is achieved by the following Duschinsky-transformation [149]:

$$\textbf{Eq 77. } \mathbf{Q}_f = \mathbf{J}\mathbf{Q}_i + \mathbf{D}$$

where $\mathbf{Q}_f$ and $\mathbf{Q}_i$ are the mass-weighted normal coordinates of the final and initial states, $\mathbf{J}$ is the Duschinsky matrix that accounts for coordinate rotations and $\mathbf{D}$ corresponds to the displacement vector that expresses the geometry change between two potentials.

The implications of direct spin-orbit coupling are also known as El-Sayed's rule [63]: k_{ISC}^{TI} is relatively large if the radiationless transition involves a change of orbital type. In the framework of organic molecules, the spin-orbit coupling matrix elements (SOMEs) between π→π* and *n*→π* states are in general much larger than SOMEs between two π→π* states. Thus, if only direct spin-orbit coupling is considered (Condon approximation), ISC rate constants are much slower for π→π* ⇝ π→π* processes than for π→π* ⇝ *n*→π* processes. These rules can easily be deduced from the mathematical structure of the spin-orbit coupling operator.[64] One example of an El-Sayed type system is phenalenone, a photosentitizer which is known to efficiently populate the triplet manifold after photoexcitation (ϕ_T = 1.00) at a calculated ISC rate in the order of ≈ 2 x 10^{10} s^{-1} for the $S_1(n\rightarrow\pi^*)\rightarrow T_1(\pi\rightarrow\pi^*)$ transition.[53] In the Condon approximation, the vibrational part of the rate is easily obtained by summing over the FC factors ($\langle\{\mathrm{v}_{aj}\}|\{\mathrm{v}_{bk}\}\rangle$) of all vibrational states v' in the interval η:

$$\textbf{Eq 78. } k_{ISC}^{TI}[\mathbf{direct}] = \frac{2\pi}{\hbar\eta}\sum_{\left|E_{f,v_{fk}}-E_{i,v=0}\right|<\eta}\left|\langle i|\hat{H}_{SO}|f\rangle\right|_{\mathbf{q_0}=\mathbf{0}}^{2}\times\left|\langle v=0|v_{fk}\rangle\right|^{2}$$

El-Sayed forbidden ISC can be considerably accelerated by vibronic interactions between π→π* and *n*→π* states. In this case, *out-of-plane*

distortions along the vibrational normal modes cause a mixing of π→π* and *n*→π* states. One explanation for the dependence of k_{ISC} on vibrational excitations which occur simultaneously to the electronic transition is that displacements along the normal modes break the symmetry of the molecule. Therefore a mixing of the excited (*e. g.* a π→π*) state electronic wave function with the other excited (*e. g.* a *n*→π*) state wavefunctions occurs. Thus, the enhancement of k_{ISC}^{TI} between two π→π* states can be seen as an intensity borrowing from the much faster π→π* ⇝ *n*→π* / *n*→π* ⇝ π→π* processes. As recent studies have shown, vibronic spin-orbit coupling is a mechanism found in many organic chromophores [54,148].

When vibronic spin-orbit coupling effects are accounted for in the calculation of k_{ISC}^{TI}, the binomial product shown in **Eq 79** has to be solved and two more contributions are obtained: one which includes a cross term that contains FC- and HT-like expressions and a term that stems exclusively from the derivative (HT) couplings.

Eq 79.

$$\boldsymbol{k_{ISC}^{TI} = \frac{2\pi}{\hbar\eta} \sum_{\left|E_{f,v_{fk}} - E_{i,v=0}\right| < \eta} \left| \langle i|\hat{H}_{SO}|f\rangle\big|_{q_0=0} \langle v=0|v_{fk}\rangle + \sum_m \left(\frac{\partial}{\partial q_m}\langle i|\hat{H}_{SO}|f\rangle\right)\Big|_{q_0=0} \langle v=0|q_m|v_{fk}\rangle \right|^2}$$

The multidimensional FC integrals are evaluated analytically using the recursive method of Doctorov et al. which is relatively time consuming and may readily become computationally impossible for large energy gaps or due to system size. Tatchen et al.[54,147] implemented the time-independent method for the calculation of the zero-temperature ISC rates taking into account direct and vibronic spin-orbit coupling. The mixed direct-vibronic coupling term was not taken into account:

Eq 80.

$$k_{ISC}^{TI}[\mathbf{vibronic}] = \frac{2\pi}{\hbar\eta} \sum_{\left|E_{f,v_{fk}} - E_{i,v=0}\right| < \eta} \left| \sum_{m} \left(\frac{\partial}{\partial q_m} \langle i | \hat{H}_{SO} | f \rangle \right) \Big|_{q_0=0} \langle v = 0 | q_m | v_{fk} \rangle \right|^2$$

One complication is that the SOMEs may be complex valued so that, depending on the relative phase of the coupling matrix elements, the off-diagonal contributions to the rate could be positive or negative. For further explanations of how this difficulty can be solved in practice, see Section **4.8**. There are several strategies for calculating ISC rate constants within this approach for speeding up the computation of the FC integrals. For example, the selection of the most important coupling and accepting modes, the number of quanta applied and small η values are some of them. Nevertheless, it is important to perform several test calculations for finding the optimal technical parameters and analyze their influence in the ISC rate constant in order to obtain reasonable values.

2.5.2.5. Time-dependent formalism for the calculation of ISC rate constants[§§§]

The time-dependent formalism can easily handle non-radiative transitions in molecular systems with many vibrational degrees of freedom. Let us explain what is the meaning of time in the time-dependent approach. In quantum mechanics there are different ways to deal with time dependence: Schrödinger and Heisenberg pictures. In the Schrödinger picture, the state vectors are time dependent but operators do not necessarily carry time dependence. Time-dependent approaches for the calculation of decay rates are based on a transformation of the golden rule into a Heisenberg picture.[150] This means that the time dependence of the expectation value of some operator $\hat{A}$, $\langle \hat{A} \rangle(t) = \langle \psi(t) | \hat{A} | \psi(t) \rangle$ can also be obtained by using the

[§§§] This section closely follows Refs. [56], [64] and [151]

unitary transformation $e^{-it\hat{H}}$. In that case, the expectation value becomes $\langle\hat{A}\rangle(t) = \langle\psi(0)|e^{it\hat{H}}\hat{A}e^{-it\hat{H}}|\psi(0)\rangle$. Now the operator is time dependent $\hat{A}(t) = e^{it\hat{H}}\hat{A}e^{-it\hat{H}}$ and the state vector $|\psi(0)\rangle$ is time independent. The time dependence of the spin-orbit operator in the Heisenberg picture naturally introduces the correlation function into the expression for the golden rule. Using a closed form expression for the sum of the Hermite polynomials, an exact expression for the rate could be derived. This approach is attractive because it completely avoids the explicit calculation of FC integrals without resorting to the estimated values for the density of states at the energy of the initial state.

Let us first introduce the Fermi golden rule for the decay from a manifold of thermally populated singlet vibronic states $|S_a, \{v_{ij}\}\rangle = \boldsymbol{i}, \{v_{ij}\}$ to a quasi-continuum of triplet vibronic states $|T_b, \{v_{ij}\}\rangle = \boldsymbol{f}, \{v_{fk}\}$:

Eq 81. $$\boldsymbol{k_{ISC}^{TD}} = \frac{\mathbf{2\pi}}{\mathbf{Z}} \sum_{\mathbf{j,k}} \mathbf{e}^{-\boldsymbol{\beta}\mathbf{E_j}} \left|\langle \boldsymbol{i}, \{\boldsymbol{v_{ij}}\}|\widehat{\boldsymbol{H}}_{\boldsymbol{SO}}|\boldsymbol{f}, \{\boldsymbol{v_{fk}}\}\rangle\right|^{\mathbf{2}} \boldsymbol{\delta}(\boldsymbol{E_{ij}} - \boldsymbol{E_{fk}})$$

where $Z = \sum_j \mathrm{e}^{-\beta \mathrm{E_j}}$ is a canonical partition function for vibrational motion in the singlet electronic state, β is the inverse of the temperature and $\mathrm{E_j}$ is the energy of the vibrational level in the singlet electronic state.

As also explained above in the previous section, in the linear Herzberg-Teller approximation, the ISC rate constant is a sum of three contributions due to a direct term, a mixed direct-vibronic term and a vibronic term where these rates are given by:

Eq 82. $$\boldsymbol{k_{ISC}^{TD}}[\mathbf{direct}] = \frac{\mathbf{2\pi}}{\mathbf{Z}} \left(\left|\langle \boldsymbol{i}|\widehat{\boldsymbol{H}}_{\boldsymbol{SO}}|\boldsymbol{f}\rangle\right|^{\mathbf{2}}_{\mathbf{q_0}}\right) \sum_{\mathbf{j,k}} \mathbf{e}^{-\boldsymbol{\beta}\mathbf{E_j}} \left|\langle\{\boldsymbol{v_{ij}}\}|\{\boldsymbol{v_{fk}}\}\rangle\right|^{\mathbf{2}} \boldsymbol{\delta}(\boldsymbol{E_{ij}} - \boldsymbol{E_{fk}})$$

Eq 83.

$$\boldsymbol{k_{ISC}^{TD}}[\mathbf{mixed}] =$$

$$\frac{\mathbf{4\pi}}{\mathbf{Z}} \left|\langle \boldsymbol{i}|\widehat{\boldsymbol{H}}_{\boldsymbol{SO}}|\boldsymbol{f}\rangle\right|_{\mathbf{q_0}} \sum_{\mathbf{j,k}} \mathbf{e}^{-\boldsymbol{\beta}\mathbf{E_j}} \langle\{\boldsymbol{v_{ij}}\}|\{\boldsymbol{v_{fk}}\}\rangle \left\langle\{\boldsymbol{v_{ij}}\}\right| \frac{\boldsymbol{\partial}}{\boldsymbol{\partial q_m}} \langle \boldsymbol{i}|\widehat{\boldsymbol{H}}_{\boldsymbol{SO}}|\boldsymbol{f}\rangle \left|\{\boldsymbol{v_{fk}}\}\right\rangle \boldsymbol{\delta}(\boldsymbol{E_{ij}} - \boldsymbol{E_{fk}})$$

Eq 84. $k_{ISC}^{TD}[\mathbf{vibronic}] = \frac{2\pi}{Z}\sum_{j,k} e^{-\beta E_j} \left| \left\langle \{v_{ij}\} \right| \frac{\partial}{\partial q_m} \langle i|\hat{H}_{SO}|f\rangle \left| \{v_{fk}\} \right\rangle \right|^2 \delta(E_{ij} - E_{fk})$

For evaluating these expressions, it is necessary to employ a Fourier transform representation of the delta function.[56,151-152]

Eq 85. $\delta(E_{ij} - E_{fk}) = \frac{1}{2\pi}\int_{-\infty}^{+\infty} e^{it(E_{ij}-E_{fk})} dt$

Substituting Eq 85 back in **Eq 82** - **Eq 84** and slightly rearranging the square of the spin-orbit matrix elements, we find:

Eq 86. $k_{ISC}^{TD}[\mathbf{direct}] = \frac{1}{Z}\left|\langle i|\hat{H}_{SO}|f\rangle\right|_{q_0}^2 \int_{-\infty}^{\infty} G_1(t) e^{it\Delta E_{if}}\, dt$

Eq 87. $k_{ISC}^{TD}[\mathbf{mixed}] = \frac{1}{Z}\langle i|\hat{H}_{SO}|f\rangle\big|_{q_0} \int_{-\infty}^{\infty} G_2(t) e^{it\Delta E_{if}}\, dt$

Eq 88. $k_{ISC}^{TD}[\mathbf{vibronic}] = \frac{1}{Z}\int_{-\infty}^{\infty} G_3(t) e^{it\Delta E_{if}}\, dt$

where,

Eq 89. $G_1(t) = \sum_{j,k} e^{-\beta E_j} \left|\langle \{v_{ij}\}|\{v_{fk}\}\rangle\right|^2 e^{it\Delta E_{jk}}$

Eq 90. $G_2(t) = 2\sum_{j,k} e^{-\beta E_j} \langle \{v_{ij}\}|\{v_{fk}\}\rangle \left\langle \{v_{ij}\} \right| \frac{\partial}{\partial q_m} \langle i|\hat{H}_{SO}|f\rangle \left| \{v_{fk}\} \right\rangle e^{it\Delta E_{jk}}$

Eq 91. $G_3(t) = \sum_{j,k} e^{-\beta E_j} \left| \left\langle \{v_{ij}\} \right| \frac{\partial}{\partial q_m} \langle i|\hat{H}_{SO}|f\rangle \left| \{v_{fk}\} \right\rangle \right|^2 e^{it\Delta E_{jk}}$

are generating functions in terms of the harmonic oscillator eigenfunctions for the normal modes in the singlet and triplet electronic states. Normal modes of the triplet and singlet states are related through a Duschinsky transformation. Then, it is possible to find the analytic forms of the generating functions. To this end, Mehler's formula[153,154] for Hermite polynomials is applied. For details regarding to the complete derivation of each of the terms, the reader is referred to the forthcoming publication of Etinski et al.[57] Within this implementation, the calculated intersystem crossing rate constant is a sum of the three terms of the rate, where the mixed direct-vibronic terms are taken

into account. Moreover, this formulation is applicable to zero and finite temperature cases.

In the case of low temperatures or small number of normal modes, the generating functions will exhibit many recurrences that make the integration of the generation functions (also called time-correlation function) more difficult. To ensure convergence of the time-integration, a Gaussian damping function is introduced. This means that the damping function ensures the generation function decays to zero in a selected time interval. From a fundamental point of view, this damping is consistent with a dephasing of the correlation function due to the interaction with a bath (solution phase) or the redistribution of vibrational energy (gas-phase molecules). Its physical role is to include all possible additional dampings that the vibronic states may experience, such as radiative damping or damping due to vibrational relaxation. The calculated rate will depend, of course, on the choice of the damping parameter. The damping η is expressed in energy units in order to correlate its value with the width of the window function in the time-independent approach for the calculation of ISC rate constants discussed in the previous section. Extensive tests on ISC transitions in thymine, flavone, phenalenone, and free-base porphyrin have shown that the calculated ISC rate constants depend only slightly on the particular width of the damping function as long as the density of final vibrational states is sufficiently high.[56] On the other hand, the appropriate time interval for the integration (in fs) and the number of grid points for the integration have to be tested in addition to the width of the damping function. The time interval should be sufficiently large to ensure that the values of the correlation function is almost completely damped at the interval boundary. Also, the number of the integration points should be sufficiently enough to guarantee numerical accuracy.

Chapter 3. Photochemistry of thionine

3.1. Overview

As stated in the Introduction, the photodynamic action of thionine and its derivatives in the presence of oxygen proceeds efficiently by either involving direct excited-state reactions such as electron transfer and hydrogen abstraction,[20,30] or by the formation of singlet oxygen.[155] Both mechanisms proceed via a triplet state of the dye. The 3,7-diamino-phenothiazin-5-ium, commonly called thionine (**Fig. 1**), is the representative smallest model and has been chosen as the starting point for studying the photophysics of the phenothiazinium family of dyes. Thus, in the following sections the experimental background on the spectral photophysical and photochemical properties of thionine are described.

3.2. The absorption spectrum of thionine (TH^+)

In dilute aqueous solution, thionine has a strong absorption at 597 nm (2.08 eV) with a maximum molar absorptivity of 5.52×10^4 dm^3 mol^{-1} cm^{-1},[37] which is found to be redshifted to 603 nm (2.06 eV) in pure ethanol [156] and to 614 nm (2.02 eV) in pyridine.[157] This absorption band has been attributed to the presence of the thionine monomer with a positive resonance charge.[158-160] It is accompanied by a vibrational sideband which appears as a shoulder at ≈ 560 nm and which has been assigned to the 1←0 vibronic transition.[159-160] In addition a weak absorption band is observed in the ultra-violet region at 281 nm (4.42 eV) (molar absorptivity 4.06×10^4 dm^3 mol^{-1} cm^{-1}) in water,[37] which is also found in ethanolic solution.[39]

In aqueous solution, the absorption spectrum of thionine is concentration-dependent due to the formation of aggregates in concentrated solution. As the thionine concentration is increased, a second absorption band on the longer-wavelength side of the 597 nm absorption band appears and becomes

the major absorption band when the thionine concentration is higher than 10^{-3} *M*. Below concentrations of 8×10^{-4} *M* a monomer-dimer model is adequate to describe aqueous solution of thionine and a dimerization constant of $k_D \sim 4 \times 10^3\ M^{-1}$ has been determined.[39] Even higher aggregates than dimers are observed at very high concentrations. Additionally, aggregation is also directly related to the chemical nature of the solvent.[160] The presence of aggregates in the dye solution may influence considerably their unique photo-physical behavior. For example, the molecular associations cause a decreasing emission (fluorescence) quantum yield and life-time of the first singlet excited state of the dye, and therefore, weaker laser efficiency can be expected.

Using the current time-(in)dependent ISC treatments is computationally not possible for an appropriate description of the photophysics of the dimers and the concurrent photo-processes (this should be done in the framework of the Exciton Theory [161]) due to large size of the system. The consideration of aggregation processes involved in concentrated aqueous solution and its photophysics is therefore out of the scope of this dissertation.

Surprisingly, in contrast to the wealth of experimental data which is available for this family of dyes, before the development of this research, only a few theoretical studies were performed on the electronic structure of these systems. In an early computational work, Sommer and Kramer [162] examined the $\pi \rightarrow \pi^*$ electronic excitation energies of thionine employing a semi-empirical configuration interaction (CI) method. More recently Homem-de-Mello *et al.* [163-164] investigated the electronic spectra of monomeric and dimeric phenothiazinium dyes employing a combination of density functional theory (DFT) and the semi-empirical ZINDO method.

3.3. Fluorescence and the singlet state of thionine (TH^+)

The fluorescence of thionine can readily be detected although its quantum yield is quite low. The emission maximum shows up at λ = 610 - 625 nm whose position does not depend on the nature of the solvent.[165-166] Nevertheless, the relative fluorescence yield changes slightly as a function of the solvent. For example, in ethanol the fluorescence yield of thionine is nearly concentration-independent ($\varphi_F \approx 0.20$), while it decreases from 0.10 to 0.027 with increasing concentration (2.5×10^{-5} to 2.5×10^{-3} *M*) in aqueous solution. This is primarily a result of aggregation because only the monomeric form is weakly fluorescent (ϕ_F = 0.047 at pH 2.5).[160,167-168] From time-resolved experiments in diluted aqueous solution at pH 2.5 the singlet state lifetime of 360 ps and a fluorescence rate of $1.31 \times 10^8\ s^{-1}$ have been determined.[169] In ethanolic solution, a singlet lifetime of 450 ps has been obtained from a time-resolved transient spectrum (532 nm laser pulse and 18 ps pulse duration) of the singlet excited state of thionine ($^1TH^+$) $S_1 \rightarrow S_n$ which shows an absorption maximum at 460 nm and a shoulder around 500 nm.[170] Based on its spectroscopic properties the S_1 state has been described to be essentially of $\pi \rightarrow \pi^*$ character.[162]

3.4. The triplet state of thionine (TH^+)

Upon excitation to a singlet state S_n, thionine can undergo IC to a low-lying singlet state, followed by efficient ISC ($k_{ISC} = 2.8 \times 10^9\ s^{-1}$ [171]) with a triplet quantum yield ϕ_T = 0.55 (water, dilute solution, pH 7.2).[172] Then two major photochemical pathways are observed as shown in Fig. 2: (a) type I where reducing agents donate an electron to the thionine triplet excited state yielding the semireduced radical, (b) type II where singlet oxygen ($^1O_2$) is generated by energy transfer from the triplet excited state to a ground state oxygen molecule ($^3O_2$) with moderate quantum yield (ϕ_Δ = 0.58 in aqueous

solution).[173] On the basis of experimental evidence, the first triplet excited state of thionine has been characterized as a $\pi \rightarrow \pi^*$.[162]

3.5. The protonation of thionine (TH^+): the diprotonated (TH_2^{2+}) and neutral dyes (T)

The absorption spectrum of thionine also shows a marked pH-dependence. Depending on the pH, thionine can exist in the following protonation states: neutral thionine (T), monoprotonated (TH^+) and diprotonated thionine (TH_2^{2+}) as shown in **Fig. 5**.

The absorption maxima and the extinction coefficients corresponding to each protonation state of thionine are presented in **Table 2**. At pH between 2 and 10, the monocationic thionine (TH^+) is the stable species, which is only protonated in strongly acidic solution (pK_a in water is -0.3).[20,30] As the pH decreases below 2, the intensity of the 597 nm absorption band decreases and simultaneously a new absorption band at 673 nm appears.[37] This behavior has been explained by the protonation of thionine (TH^+) forming the diprotonated thionine (TH_2^{2+}), where the proton is located at the heterocyclic (ring-) N atom (See **Fig. 5**). Neutral thionine (T) has been found in alkaline aqueous solution (pH above 8) and has an maximum absorption wavelength at 510 - 520 nm.[37-38] A triply protonated state of thionine (TH_3^{+3}) is known to exist but is rarely formed, only at acid strengths greater than 15 mol dm^{-3} which will not be under consideration in this work.

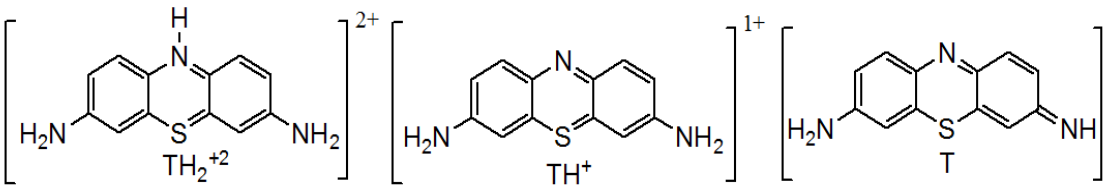

Fig. 5 Different protonation states of thionine.

Table 2 Absorption spectra (λ_{max}, nm) and extinction coefficients (ε, $dm^3mol^{-1}cm^{-1}$) of the protonated states of thionine. Data obtained from Ref. [37]

	λmax	ε	λmax	ε	λmax	ε	λmax	ε
T	515	1.42×10^{-4}	-	-	268	1.67×10^{-4}	-	-
TH^+	597	5.52×10^{-4}	-	-	281	4.06×10^{-4}	-	-
TH_2^{+2}	673	3.87×10^{-4}	405	0.34×10^{-4}	279	2.96×10^{-4}	245	1.72×10^{-4}

On the other hand, thionine (TH^+) is a compound in which the pK_a in the triplet state ($^3TH^+$) is very different from the value observed for the ground state as depicted in **Fig. 6**. Thus, after photoexcitation and ISC of monocationic thionine (TH^+), the subsequent formation of the different triplet states species ^3T, $^3TH^+$, and $^3TH_2^{+2}$ can occur depending of the pH of the solution. The chemical structures of these protonated triplet states of thionine are analogs of those presented in **Fig. 5**. At pH values close to neutral the triplet state may exist in diprotonated ($^3TH_2^{+2}$) and monoprotonated ($^3TH^+$) forms that can be distinguished by their absorption spectra and have very different lifetimes.[33] A pK_a value of 7.0 ± 0.1 in methanolic solution and of 6.3 in water has been measured for the $^3TH_2^{+2} \rightleftharpoons {}^3TH^+$ equilibrium, where the protonation process occurs at a very high rate (≈ 10^{10} M^{-1} s^{-1}, tested in different media: details in Ref. [35]).[33,174-175] The lifetime of $^3TH_2^{2+}$ is 8.5 μs while $^3TH^+$ has a much longer lifetime of 12 μs in buffered aqueous solution [176] (in pure aqueous solution it has been determined as 60 μs for $^3TH^+$ [177]). This has consequences for the reactivity of the triplet state. For example, Bonneau et al have examined the elementary steps of the photoreduction mechanism of thionine by EDTA. They found that the variations in the apparent reactivity of thionine triplet state follow closely variations of percentage of the protonated triplet $^3TH_2^{2+}$ form, concluding that this acid form of the triplet dye is much more reactive through photoreduction than the basic form ($^3TH^+$).[178]

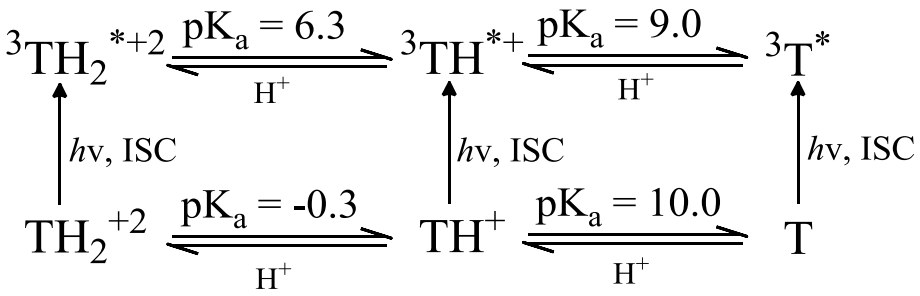

Fig. 6 Protonation of the ground and triplet excited states of thionine and its protonated species in aqueous solution.

One of the earliest studies investigated the effect of pH on the oxygen-dependent photophysics of thiazine dyes, in particular thionine (TH^+) and methylene blue (MB^+). The production of singlet oxygen (measured by the rate of photooxidation of tryptophan) was found to be very sensitive to changes of pH in the range 5 - 9.[34] Upon acidification, a decrease in the quantum yield of singlet oxygen in more acidic solution was correlated to the observation that the rate constant of oxygen quenching of the triplet state of the protonated dye ($^3TH_2^{+2}$) was significantly smaller than that for the monocationic triplet state ($^3TH^+$), see **Table 3**. This difference in the rate constants was interpreted to reflect differences in the energies of the corresponding triplet states $E(^3TH_2^{+2}) < E(^3TH^+)$, with $E(^3TH_2^{+2})$ being estimated to be very close to the excitation energy of singlet oxygen ($E(^1O_2\Delta_g) = 0.97$ eV, $E(^3TH^+) = 1.69$ eV and $E(^3TH_2^{+2}) = 1.28$ eV).[30,34] It was argued that reversible energy transfer from the already formed singlet oxygen to the sensitizer could be manifested by a smaller rate constant for quenching by oxygen. For methylene blue (an amine methylated derivative of thionine) it has been found that the $^1O_2$ production is approximately five times more efficient in basic than in acidic medium.[34]

Evidence of a equilibrium between the neutral ^3T and monoprotonated $^3TH^+$ forms has been also studied ($pK_a = 8.9$ [36], see **Fig. 6**) in basic aqueous solution. In this case, the pK_a of the corresponding equilibrium at the ground state ($pK_a = 11$ [36], see **Fig. 6**) is higher than between the triplet excited

states. The photoreduction of thionine by EDTA shown a interesting trend in the oxidizing properties of the protonation forms of the triplet state: the neutral ^3T state as least 100 less reactive than the $^3TH^+$ which is itself approximately 20 times less reactive than the $^3TH_2^{2+}$ state [36]. In pyridine (aprotic solvent and alkaline solution), Eipper et al found a deactivation pathway of the thionine triplet ($^3TH^+$) via the neutral triplet form (^3T).[157] In this medium, the electronic relaxation of the triplet $^3TH^+$ occurs via protolytic dissociation to the triplet ^3T (deprotonation occurs with a rate of $2 \times 10^5\ s^{-1}$) which, after radiationless decay to the ground state T, is rapidly reprotonated to TH^+. This means that this deactivation pathway represents a complete Förster cycle which was followed by microsecond flash spectroscopy. The energy of the triplet state ^3T was estimated to be 1.55 eV in this media and the rate constant of singlet oxygen production was found to be $2 \times 10^9\ M^{-1}\ s^{-1}$ (**Table 3**).[157]

Table 3 Reported quenching rate constants of the triplet protonated states of thionine by oxygen (k_{ox}, $M^{-1}\ s^{-1}$) and the reported values for the triplet state energies (E_T, eV).

Dye species	k_{ox}	pH	E_T
^3T	2.0×10^9	Piridine slightly basic media [157]	1.55
$^3TH^+$	2.7×10^9	7.5 (aqueous solution) [34]	1.69
$^3TH_2^{+2}$	1.5×10^9	3 (aqueous solution) [34]	1.28

As can be seen, protonation has a direct effect on the photophysics of the thionine: It changes its electronic structure, which means that it also has noticeable effects on the absorption and fluorescence spectra, as well as on the ISC rate for the production of thionine triplet. Furthermore, the pH can influence the extent to which the system can be incorporated and retained in a cell: protonation changes the charge of the system, which could influence where it is localized in specific subcellular domains (*e. g.*, hydrophilic *vs* hydrophobic domains). As singlet oxygen in cells is produced in or near the mitochondria and the spatial domains around cancer cells are characterized by unique pH gradients [179], where protonated forms of thionine and its

derivates could be present, such local differences in proton concentration can certainly influence the effectiveness of thionine and its derivates administered as drugs in photodynamic therapy.

3.6. Internal heavy atom effect: selenine and oxonine dyes

Spin-orbit coupling between electronic states plays an important part in the photophysical deactivation of molecules as they make radiationless spin-forbidden processes possible (k_{ISC} is proportional to the square of the corresponding spin-orbit coupling matrix elements as described in Section **2.5.2**). The incorporation of heavy atoms into molecular systems leads to changes in the photophysical behavior, enhancing singlet-triplet transitions (intercombination transitions in general), which is known as "heavy-atom effect". From the spin-orbit coupling operator (**Eq 72**) it is clear that the effect strongly depends on the atomic number, making it possible to emphasize the role of "heavy" atoms. The effect has been referred to as "internal", when the heavy atoms are part of the molecule and "external" when they belong to the surrounding (*e. g.* solvent). The enhancement of radiative and nonradiative intercombination transitions under the heavy-atom effect is responsible for fluorescence quenching and the shortening of the phosphorescence life time. Photophysical investigations show that the corresponding transition probabilities in different channels of excited-state deactivation exhibit specific dependence on the molecular structure. It is significant that fluorescence quenching is directly related to the population of the lowest triplet electronic state, therefore, an enhancement of the corresponding spin-forbidden processes.[180]

The heavy-atom effect in molecules can be position dependent. Hamanoue et al.[181] showed that a chlorine or bromine β-substitution in anthraquinone has a weak effect on phosphorescence (77 K), which belongs to the $^3(n\rightarrow\pi^*)\rightarrow S_0$ type (the weak effect of heavy atoms on the $n\rightarrow\pi^*$ phosphorescence has long been recognized). In contrast, in the case of the

α-substitution by one or two chlorine or bromine atoms (including a mixed chlorine - bromine substitution), the phosphorescence is quenched and the fluorescence quantum yield is decreased by a factor of 100. The authors attribute these changes to the nonplanarity arising from steric interactions between the oxygen and the halogen atoms. As well, the intra-annular heavy-atom effect[****] in the spectral-luminescent properties of dibenzoperylene, benzo- and dibenzoderivatives of furan, thiophene, selenophene, and tellurophene compounds show a pronounced increase in the ISC rate and a quenching of the radiative processes has been clearly observed.[180] Concerning to photobiologically active dyes, the replacement of the furan oxygen with sulfur or selenium in the widely known psoralens has been shown to increase the triplet quantum yields giving rise to compounds having highly improved photoactivity.[182]

Regarding the family of dyes under investigation in this dissertation, several investigations about the effect of structural modification of the phenothiazinium core on the photochemical/physical properties (such as maximum absorption wavelength, singlet oxygen production, or the lipophilicity) have revealed the interesting interplay between the structure and photoactivity of the members of this family. For example, methylation of the amine-groups (see **Fig. 7**), methylene blue (MB), decreases the singlet oxygen quantum yield (ϕ_{Δ}) with respect to thionine.[173,183] Methylation on the tricyclic system combined with dimethylation of the amine-groups leads to increased singlet oxygen production, *i. e.*, new methylene blue and dimethyl methylene blue.[183] Other alkyl and aryl derivatives[184-187] and variations of the structure beyond simple modifications[188] have shown smaller ϕ_{Δ} yields, with no significant variation in toxicity between the derivatives and methylene blue.

[****] The effect on the photophysics exerted by a heavy atom incorporated into the cycle of a heteroaromatic molecule.

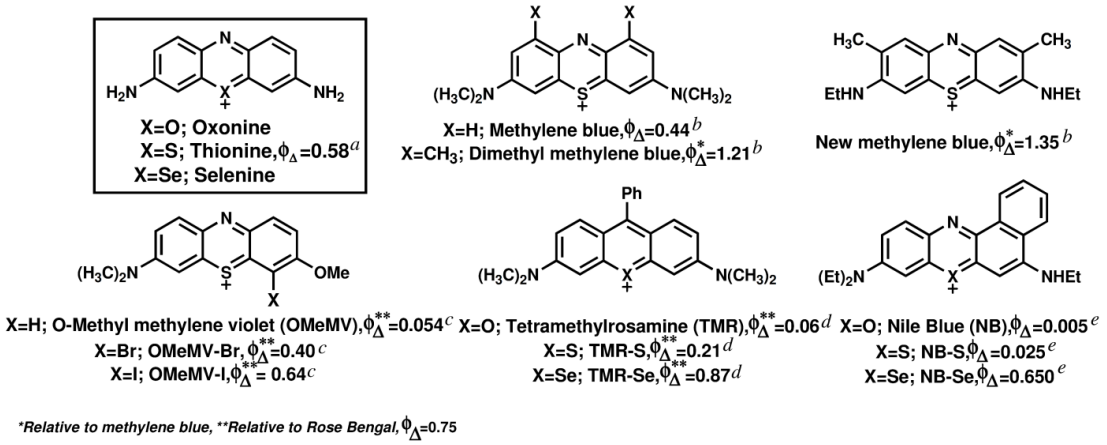

Fig. 7 Singlet oxygen quantum yield (ϕ_Δ) of thionine and some of its heteroanalogues. [a]Ref [183]. [b]Ref [183]. [c]Ref [189]. [d]Ref [46]. [e]Ref [48].

A necessary condition for a high singlet oxygen quantum yield is a high triplet quantum yield of the sensitizer. The triplet quantum yield is high, if the ISC is faster than the other competing photophysical processes. As it was explained above, the ISC efficiency can be enhanced by the inclusion of heavy atoms since they increase the spin-orbit coupling. The peripheral inclusion of bromine or iodine in the O-methyl methylene violet chromophore results in a significant rise of ϕ_Δ from bromine to iodine as can be seen in **Fig. 7**.[189] However, halogen substitution of the phenothiazinium core was not explored further as this results in a considerable decrease in its solubility in water.[19,190] Substitution of the heteroatom of the central ring by oxygen, sulphur and selenium in tetramethylrosamine and benzo[a]phenothiazinium dyes has resulted in a significant increase in ϕ_Δ (**Fig. 7**) and small spectral shifts in the absorption and emission spectrum.[46,48,191-195] Based on these observations, it has been of interest in this thesis to investigate how such internal heavy atom effects influence the photophysics of the parent phenothiazinium chromophore thionine.

The replacement of the central ring sulphur atom of thionine (X = S) by oxygen and selenium gives oxonine (X = O) and selenine (X = Se) (see **Fig. 7**). These three compounds show similar spectral properties in the ground

and in the triplet state.[174,196] The increasing spin-orbit coupling of the heteroatom can be seen in the fluorescence quantum yields, the triplet lifetimes and the zero-field splitting parameters of the electronic paramagnetic resonance triplet spectra.[197] Oxonine (also known as oxazine 118) has an absorption maximum at 578 nm [198] and a triplet transient absorption band at 780 nm [199] in aqueous solution, while the corresponding maxima for thionine are located at ~ 600 nm and 780-800 nm.[171] Also the pK_a values of these molecules in their ground states differ only slightly. The substitution of sulphur by oxygen leads to an increased fluorescence yield (τ_F = 3.2 ns and ϕ_F = 1.00 in water, τ_F = 3.1 ns and ϕ_F = 0.61 in ethanol)[200,198] due to the strongly decreased ISC ($k_{ISC} = 7.2 \pm 2.2 \times 10^5\ s^{-1}$, $\phi_T = 1.7 \pm 0.4 \times 10^{-3}$).[199] These photophysical properties of the oxazinium fluorophores make them suitable as laser dyes and optical sensors.[200-201] Although this trend is known for the X =O, S pair, similar experimental observations for selenine are not available.

Chapter 4. Methodology

This chapter collects all the computational details for obtaining the electronic state minima of the dyes under investigation as well as for computing the fluorescence, phosphorescence and the ISC rates within the time-independent and time-dependent approaches. Furthermore, other information regarding the details for the optimization of the electronic states, DFT/MRCI excitation spectra and spin-orbit coupling matrix elements using the one-center mean-field approximation to the Breit-Pauli Hamiltonian are also presented.

4.1. Geometry optimization and vibrational frequencies in vacuum

The geometry of the electronic ground states has been optimized using the B3LYP functional [81-83] as implemented in the Turbomole 6.1 program package.[202] According to our experience this functional yields reliable geometries as long as no charge-transfer states are involved. Furthermore, this functional has yielded reasonable excitation energies comparable to other popular functionals such as PBE0, and somewhat better than long-range corrected functionals such as LC-BLYP and CAM-B3LYP.[203] TDDFT[49] has been employed for the optimization of all electronically excited singlet and triplet states. The optimized structures were proven to be minima on the PES by calculating vibrational frequencies. For the ground state these frequencies were calculated analytically using the aoforce module from the Turbomole package. Frequencies of the excited states were calculated from numerical derivatives of analytic gradients using the NumForce script and the SNF program.[204] Zero-point vibrational energies (ZPVE) were scaled by a factor of 0.9614 as recommended for the B3LYP functional.[205] The cartesian coordinate system was chosen in a way that

the *xz* plane coincides with the molecular plane and the $C_2(y)$ axis passes through the phenothiazinium central ring.

4.1.1. Electronic states of thionine (TH^+)

For the ground state of TH^+ as well as for the S_1, T_1 and T_2 electronically excited states, C_{2v} symmetry constraints were employed in the geometry optimization. For the S_2 and T_3 states the geometry optimization ended at saddle points of the PES when C_{2v} symmetry constraints were imposed. Minima could be found when C_S and C_1 symmetry restrictions were applied for the S_2 and T_3 optimizations, respectively. All the geometry optimization were performed at the at the (TD-)B3LYP/TZVP level of theory.

Three different basis sets were tested for optimizing and analyzing the electronic structure at the ground state geometry: the standard valence triple zeta TZVP and TZVPP basis sets [206] from the Turbomole library, and a TZVP basis set augmented by a set of 1s1p1d diffuse Gaussian Rydberg functions with exponents of 0.01125, 0.009988 and 0.014204 (see Ref [87] for details), which were located at a dummy center in the central ring of the phenothiazinium. The position of this dummy center was allowed to adjust in the geometry optimizations. A numerical grid, usually employed for the cesium atom, was chosen for the quadrature of the exchange correlation at the dummy center. This basis set has been denoted TZVP+R in **Chapter 5**. The main characterization of the excited states and the photophysics was performed using the geometries obtained with the TZVP basis set.

4.1.2. Electronic states of diprotonated thionine (TH_2^{2+})

For the ground state of diprotonated thionine (TH_2^{2+}) as well as for the S_1 and T_2 electronically excited states, C_{2v} symmetry constraints were employed in the geometry optimization. For the S_2 state the geometry optimization ended at saddle point of the PES when C_{2v} symmetry constraints were imposed. After elongations along the imaginary mode, a minimum of the S_2 state could

be found when C_2-symmetry constrains were imposed. All of these optimizations were performed at the at the (TD-)B3LYP/TZVP level of theory. Because of triplet instabilities, the minimum nuclear arrangement of the T_1 triplet state was determined by unrestricted density functional theory (UDFT) at the UB3LYP/TZVP level of theory. Because of the low adiabatic excitation energy of the T_1 triplet state of TH_2^{2+} at this theoretical level, geometry optimizations tests using the more polarized TZVPP basis set were also performed using the UB3LYP functional.

4.1.3. Electronic states of neutral thionine (T)

For the ground state of neutral thionine (T), the optimization performed using C_s symmetry constrains yielded a very flat first order saddle point. Geometry distortions along the imaginary mode followed by geometry optimization without symmetry constrains ended in a non-planar ground state minimum. Similar situations were found when optimizing the S_1, S_2, T_1 and T_2 excited states of T using C_s symmetry constrains. Therefore, all geometry optimizations were performed without symmetry constrains at the (TD-)B3LYP/TZVP level of theory. An exception is the T_1 state, which was optimized at the UB3LYP/TZVP level of theory because of triplet instabilities.

4.1.4. Electronic states of oxonine (OXH^+)

The characterization of the electronic ground and excited states minima of oxonine was performed using the split valence basis set with (d) polarization functions for non-hydrogen atoms (SV(P)) basis set, due to the difficulties when employing the TZVP basis set for optimizing structures of the excited states. For consistency, the performance of the SV(P), the TZVP and the TZVPP basis sets have been compared. For the low-lying singlet and triplet $\pi \rightarrow \pi^*$ states of interest, only minor energy shifts between 0.01 - 0.04 eV are found. The C_{2v} symmetry constrains were imposed on the ground state geometry and its S_1, S_2, T_1 and T_2 electronically excited states. A minimum of

the T_3 state could be found when the molecule had no symmetry restrictions. These computations were performed at the (TD-)B3LYP/SV(P) level of theory.

4.1.5. Electronic states of selenine (SEH^+)

For selenine, the geometry optimizations of the ground and the S_1, S_2, T_1 and T_2 electronically excited states were performed using at the (TD-)B3LYP/TZVP level of theory and setting C_{2v} symmetry constrains. The performance of the TZVPP basis set on the optimization of the electronic states has been also evaluated. This in order to check the validity of using the TZVP basis set for the accurate description of the heavy-atom (Se). It is found that the additional polarization functions have almost no effect in the computed vertical excitation energies.

4.2. Calculation of the electronic excitation energies

Vertical electronic excitation energies, transition dipole matrix elements and oscillator strengths were obtained from single point calculations performed at the optimized ground and excited state geometries of each dye using the DFT/MRCI method. In addition, the DFT/MRCI calculations were performed always using the same basis sets as for the geometry optimizations. This approach represents an effective means to obtain the electronic spectra for closed-shell organic systems with errors typically less than 0.2 eV.[207]

The main idea of this approach is to include major parts of the dynamic electron correlation by DFT, while static correlation effects are taken into account by short CI expansions. The configuration state functions (CSFs) in the MRCI expansion are built up from Kohn–Sham (KS) orbitals employing the BHLYP functional.[208-209] Diagonal elements of the effective DFT/MRCI Hamiltonian are constructed from the corresponding Hartree–Fock based expression and a DFT-specific correction term. All in all the effective DFT/MRCI Hamiltonian contains five empirical parameters which depend only

on the multiplicity of the excited state, the number of open shells of a configuration, and the density functional employed. For additional details of the DFT/MRCI method see Section **1.5.2**.

For calculating the vertical and adiabatic excitation spectra of the dyes, a total of 20 roots have been accounted. For C_{2v}-symmetric geometries, we calculated five roots for each of the four (A_1, A_2, B_1 and B_2) irreducible representations. For C_s (A' and A'') and C_1 (A) point groups, ten and twenty roots for each irreducible representation was accounted in the calculation. The adiabatic excitation energies in vacuum were computed relative to the energy of the ground state at each the ground state minima.

As is common practice in the DFT/MRCI approach, the CI space was kept moderate by only selecting CSFs whose estimated energy was 1.0 Hartree above the highest reference space energy (selection threshold δE_{sel}=1.0). The CI reference space was determined iteratively by first performing a DFT/MRCI calculation with a configuration selection threshold δE_{sel} = 0.8 and a reference space that included all configurations which can be generated by up to doubly exciting ten electrons within the ten frontier MOs. In the next iteration the selection threshold δE_{sel} was set to 1.0 and all configurations with a squared coefficient of at least 0.003 were included in the reference space. All valence electrons (identified by their MO energies) were correlated.

For comparison we also determined the vertical excitation energies using the coupled cluster method with approximate treatment of doubles (CC2, see Section **1.5.3**) and the TDDFT method (see Section **1.5.1**) using the B3LYP functional.

4.3. Linear interpolations between electronic states minima

In addition to these calculations, linearly interpolated pathways connecting minima of electronically excited states were constructed. Along these pathways the symmetry of the molecule was lowered, and single-point

DFT/MRCI calculations were performed at each interpolated geometry. The same numbers of roots for each irreducible representation was calculated as mentioned above in Section **4.2**.

4.4. Treatment of the solvent effects on the photophysics: Hydration models

Dye-water models were built in order to investigate the photophysical properties and the possible deactivation channels in aqueous solution of the dyes under investigation. For estimating the effects due to electrostatic interaction with water, we employed the conductor-like screening model (COSMO, see details of the model in Section **1.6**) which is implemented in the Turbomole package.[123-124] In addition, the effects of hydrogen bonding were mimicked by micro-hydration with up to five water molecules which were placed near to the hetero atoms of the phenothiazinium ring. All of the ground states of the clusters were optimized without symmetry constraints at the B3LYP/TZVP level of theory. In consistency with the procedure followed for calculating the minima in vacuum for oxonine (see Section **4.1.4**), the solvation models of this dye were optimized at the B3LYP/SV(P) theoretical level. Furthermore, all of the geometry optimizations of the dye-water complexes were carried out with and without embedding the models in a COSMO environment.

For calculating the DFT/MRCI excitation energies in aqueous solution, the MRCI expansion was built up from the one-particle basis of COSMO optimized Kohn–Sham orbitals and using the procedure as already described in Section **4.2**. For the simulation of a bulk water environment we used a dielectric constant of $\varepsilon = 78$.[210] These calculations were performed without symmetry restrictions and 20 roots for the *A* irreducible representation were computed.

The DFT/MRCI adiabatic excitation energies in aqueous solution (ΔE_w^{ad}) were calculated in two ways. In **Chapter 5** and **Chapter 7**, the solvation effects on the adiabatic excited states were computed by applying the corresponding hydration shifts experienced by each state at ground state of the dye-water models (δ_w), **Eq 92**, to the adiabatic energies of the respective states computed in vacuum (ΔE_{vac}^{ad}) using **Eq 93**.

$$\textbf{Eq 92. } \delta_w = \Delta E_w - \Delta E_{vac}$$

$$\textbf{Eq 93. } \Delta E_w^{ad} = \Delta E_{vac}^{ad} + \delta_w$$

where ΔE_{vac} and ΔE_w correspond to the DFT/MRCI vertical excitation energies of the desired state calculated at the S_0 geometry in vacuum and at the S_0 geometry of dye-water model, respectively. This methodology (**Eq 93**) have show to work well for throwing light on the photophysics of organic chromophores in different solvents.[43,44,97,100,144,217] By using **Eq 93** we have been able describe the photophysics of thionine and oxonine with reasonable agreement with the available experimental data.

In the ground state of organic molecules, it is found that continuum solvation methods could work quite well for the description of *e. g.* chemical reactions, diffusion processes and structural analysis. Nevertheless, at this point one should address on the several difficulties that could be found on the description of excited states in condensed media using small solvation models. While optimization of ground state structures could be considered as routine procedures, this is not the case for the geometry optimization of excited states and even more when embedded in a solvent environment.

When the electronic structure and the excitation energies of the electronic states are strongly perturbated by the environment, **Eq 93** is not longer appropiated. For example, when the geometry or the charge distribution of the excited state largely differs compared to that of the ground state it could give results that does not agree with the common behavior of the

spectroscopic solvation shifts to the excited states (e. g. hydration effects of TH_2^{2+} on Section **6.2.2.1**). For getting deeper understanding on how the solvation effects could affect the electronic structure and adiabatic energy distribution of the excited states in water of T, TH^+, TH_2^{2+} (**Chapter 6**), the DFT/MRCI ΔE_w^{ad} have been also calculated at optimized excited state geometries of the corresponding dye-water model. The optimization of the S_1, S_2 and T_2 states T, TH^+, TH_2^{2+} using dye-water models were performed without symmetry constrains and at the TD-B3LYP/TZVP level of theory. The T_1 states were computed at the UB3LYP/TZVP level of theory because of triplet instabilities when using the time dependent branch. Moreover, the computations were performed at the electronically excited clusters in vacuum and embedding them in a COSMO environment.

4.5. Rate constants for radiative decay processes

The fluorescence and phosphorescence rate constants were computed from the S_1 and T_1 adiabatic minima of the dyes according to **Eq 54** (details in Section **2.4**). For fluorescence, DFT/MRCI transition dipole moments were used. Spin-orbit mixed wavefunctions for the calculation of phosphorescence rates were computed at the multi-reference spin-orbit configuration interaction (MRSOCI) level [58], as already described in Section **4.6**.

4.6. Spin-orbit coupling matrix elements (SOMEs)

For the computation of the spin–orbit matrix elements $\langle i|\widehat{H}_{SO}|f\rangle$ (SOMEs) between the correlated DFT/MRCI wavefunctions, we used the spin-orbit coupling kit SPOCK [58,59,60] where the one-center mean-field approximation to the Breit-Pauli Hamiltonian [61] is used for the description of the spin-orbit coupling (See section **2.5.2.3**).

Two different procedures have been used for calculating the SOMEs: one for calculating the ISC rate constants and one for calculating the phosphorescence rate constants. The SPOCK program contains modules

that determine spin-orbit coupling interactions of MRCI wavefunctions either in a perturbational (SPOCK.PT) or variational (SPOCK.CI) manner. Key features of SPOCK.PT are a fast determination of coupling coefficients between eigenfunctions of the $\hat{S}^2$ operator [configuration state functions (CSFs)] for spin-dependent one-electron operators [60] and the use of a nonempirical effective one-electron spin-orbit mean-field Hamiltonian.[61-211] The application of these techniques and approximations in combination with the generation of correlated wave functions via the DFT/MRCI makes it possible to compute the SOMEs in organic molecules efficiently and with high confidence. In many cases, a perturbational treatment of spin–orbit coupling is computationally less demanding than a variational approach because spin and spatial symmetries of the zeroth-order wave functions can be exploited separately. Furthermore, perturbation theory is advantageous if ISC rates of light molecules are to be determined. This, because ISC probabilities depend directly on the SOMEs between two states of different multiplicities. Obtaining this information from a variational spin-orbit calculation would require a subsequent diabatization of the states under consideration. A disadvantage of Rayleigh-Schrödinger perturbation theory is the slow convergence of perturbation expansions for second-order properties, such as phosphorescence rates or electronic g factors.[212-213] The calculation of the SOMEs and its derivatives for calculating ISC rate constants was performed within the perturbational framework using the SPOCK.PT module.

For calculating second-order spin-dependent properties that would require an infinite summation over zero-order states like in phosphorescence rates, the spin-orbit mixed wavefunctions have been generated in an uncontracted MRSOCI treatment implemented in the SPOCK.CI module (spin-orbit coupling is treated variationally). Sum-over-states perturbation theory expansions of phosphorescence rates have been shown to converge very slowly with the number of intermediate electronic states. In this context “uncontracted” means that the coefficients of all CSFs are allowed to vary

freely. This full variational freedom has the advantage that spin-orbit interaction is treated on the same footing with electron correlation. Because of the large dimensions of the secular problem, the solutions are determined iteratively by a modified Davidson scheme that has been extended to complex-valued matrices which is accelerated by using spin-orbit coupled QDPT wavefunctions to start up the iteration. Due to the small spin-orbit splitting of the T_1 sublevels, the convergence threshold of the Davidson iterative procedure in the MRSOCI step was set to 5×10^{-9} E_h.

4.7. Derivatives of the spin-orbit coupling matrix elements (∂SOMEs)

The first-order derivatives of the SOMEs with respect to the normal mode coordinates ($\frac{\partial}{\partial q_k}\langle i|\hat{H}_{SO}|f\rangle$) (∂SOMEs) in **Eq 76** have been calculated numerically by finite difference techniques by means of the symmetrized two-point formula as in **Eq 94** at the corresponding initial state (S_1 or S_2 minimum) of the dyes.

$$\textbf{Eq 94.}\ \frac{\partial}{\partial q_k}\langle i|\hat{H}_{SO}|f\rangle \approx \frac{\langle i|\hat{H}_{SO}|f\rangle|_{\mathbf{q_0}+\varepsilon\mathbf{e}_k} - \langle i|\hat{H}_{SO}|f\rangle|_{\mathbf{q_0}-\varepsilon\mathbf{e}_k}}{2\varepsilon}$$

where $\mathbf{e}_k$ denotes the unit vector pointing into the direction of the normal mode v_k and ε represents the displacement increment referring to dimensionless harmonic oscillator coordinates $\mathbf{q}_k$ (set to ε = 0.1). Single-point DFT/MRCI and SOMEs calculations were carried out at the two distorted geometries $\mathbf{q}_0 \pm \varepsilon\mathbf{e}_k$ for each normal mode. Therefore, the single-point calculations are carried out without symmetry constraints regardless of the actual point group of the respective distorted structures. The CI space from a preceding DFT/MRCI run without symmetry constraints at the reference geometry $\mathbf{q}_0$ will be used while the molecular orbitals will be reoptimized in all calculations . Typically, the ∂SOMEs along *out-of-plane* vibrational modes become important and the totally symmetric *in-plane* modes act as possible

accepting modes. The vibronic spin-orbit coupling terms arising from the all *out-of-plane* promoting and *in-plane* accepting modes were evaluated. Furthermore, the influence of the asymmetric and *out-of-plane* accepting modes have been considered.

Since the ISC rate constants calculated taking vibronic coupling into account are sensitive to the signs of the ∂SOMEs, special care has been taken with respect to the phase of the wavefunctions. As even the SOMEs for π→π* / π→π* transitions are commonly very close to zero they may undergo true sign changes near the reference geometry $\mathbf{q}_0$ and, therefore, they cannot be considered as a reliable criterion for fixing the phases. All the unwanted phase leaps happening in the single-point calculations to the DFT/MRCI wavefunctions of the initial $|i\rangle$ (singlet) and final $|f\rangle$ (triplet) states were eliminated by relating their phases to the signs of two sizeable reference SOMEs $\langle r|\widehat{H}_{SO}|i\rangle$ and $\langle r|\widehat{H}_{SO}|f\rangle$ between a given third state $|r\rangle$ and the states under consideration (initial and final). For more details, see Ref. [54]. The target states that were taken under consideration for fixing the phases of the dyes under investigation is presented in the following.

For the monoprotonated dyes: thionine (TH^+), oxonine and selenine, the phases of the SOMEs of the $S_{1,2}/T_{1,2}$ couplings at each distorted geometry of the $S_{1,2}$ minima were obtained by relating their phases to the sign of the $S_{1,2}/T_3$ and $T_{1,2}/T_3$ SOMEs as reference for the calculation of the sign of the ∂SOMEs.

For the diprotonated and neutral dyes: The phases of the SOMEs of the $S_{1,2}/T_{1,2}$ couplings for TH_2^{2+} at each distorted geometry of the corresponding $S_{1,2}$ minima were obtained by relating their phases to the sign of the S_1/T_6, T_1/T_8 and T_2/T_3 SOMEs as reference at the S_1 minimum and S_2/T_8, T_1/T_6 and T_2/T_3 SOMEs as reference at the S_2 minimum. The phases of the SOMEs of the $S_1/T_{1,2}$ couplings for T at each distorted geometry of the corresponding S_1

minimum were obtained by relating their phases to the sign of the S_1/T_3, T_1/T_3 and T_2/T_5 SOMEs as reference.

4.8. Time-independent ISC rate constants calculations

The rate constants for ISC (k_{ISC}^{TI}) using the time-independent approach were calculated using the VIBES program [54,147] taking vibronic spin-orbit coupling into account. In this framework, the ISC rate constants were evaluated using the discretized form of the Fermi's Golden Rule expressions (see Section **2.5.2.4**). The effect of different choices for the interval width parameter η ranging from 0.001 to 100 cm^{-1} on the calculated ISC rates were evaluated as well as the effect on the energy gap between the singlet (initial) and triplet (final) states.

The ISC rate constants of oxonine, thionine and selenine have been evaluated using the time-independent approach. These dyes have a total of 72 vibrational modes. Taking into account the choice of the mirror plane as the *xz*-plane of the C_{2v} molecular point group in this work and symmetry arguments, we included the vibronic spin-orbit coupling terms arising from the eleven A_2 and twelve B_2 *out-of-plane* promoting modes in the calculation of the ISC rate constants. Our first calculations including only the 25 symmetric A_1 modes as accepting modes led to very low ISC rate constants (especially for those corresponding to the $S_1 \rightsquigarrow T_1$ channel). Therefore we tested the influence of the asymmetric modes using all 49 *in-plane* modes as accepting modes in the calculation. Moreover, test calculations including the 72 *out-of-plane* and *in-plane* modes as accepting modes were performed.

The analysis of the ISC rate constants of T and TH_2^{2+} has been performed only within the time-dependent method (Section **4.9**) because of technical reasons. *i*) When using the time-independent approach, the calculated rate constants arising from the S_1 state of TH_2^{2+} were very low when only the A_1-symmetric modes were accounted as accepting modes. As the experience

with TH^+ shown that these ISC rate constants have dependency on the number of accepting modes (see Section **5.2.4**), computations including a higher number of them had to be performed. *ii*) The minimum of S_1 state of T has no symmetry (C_1) where there is not a distinction of *in-plane* and *out-of-plane* modes and the ISC calculations had to be performed using all vibrational modes for the initial and final states. These facts (*i*) and (*ii*) significantly increased the time for the computations (sometimes to months) when utilizing the time-independent approach, which is mainly caused by the expenses of calculating a high number of FC integrals.

4.9. Time-dependent ISC rate constants calculations

The rate constants for ISC (k_{ISC}^{TD}) using the time-dependent branch were calculated using the recently updated version of the VIBES program using the time-correlation function method.[56-152,56] Here, the correlation function is expressed with the help of Mehler's formula for the sum of the Hermite polynomials which is exact within the framework of the harmonic oscillator and the Condon-Herzberg-Teller approximation (see Section **2.5.2.5**). The ISC rate constants where calculated taking direct, mixed and vibronic spin-orbit coupling terms into account. The mixed and vibronic spin-orbit coupling terms arising from the all of the promoting initial state and accepting final state vibrational modes of each of the dyes were evaluated.

As already mentioned in Section **2.5.2.5**, the technical parameters for a time-dependent ISC rate constant calculation are the value for the damping function, the time interval and the number of grid points for the integration of the time correlation function. These parameters have been found to vary for the situations when only the direct or vibronic spin-orbit coupling is taken into account. In the case of direct coupling, it has been found that small time intervals (between 3000 and 20000 fs) and damping (0.1 - 10 cm^{-1}) values accompanied by a small number of points (6000 - 40000, ~ twice the time interval) for the integration are enough for getting a converged time

correlation function for thymine, flavone, phenalenone, and free-base porphyrin.[151] By using these parameters, the ISC rate constant calculations are quite fast (some hours). When vibronic coupling is taken into account, it is found that larger time intervals (> 30000 fs) are needed for getting a converged time correlation function than for the case of direct coupling. Furthermore, the number of points that leads to a smooth plot of the time correlation function are also very large (30-times the time interval!).[††††] All of these makes the time for computing ISC rate constants taking into account vibronic coupling to be very long and a set optimal parameters should be evaluated. These will depend on the system, *e. g.* the number of normal modes and their frequencies. For the dyes under investigation, we tested the following values: damping parameters of 0.1, 1, 10, 100 and 1000 cm^{-1}; time intervals of (the interval always begin in t = 0) 30000, 50000, 100000, 300000, 500000, 900000 fs; and the number of points between 900000 to 2700000 depending on the time interval. When the calibration of these technical parameters is performed, the ISC rate constants calculation could became very efficient (less than one week).

[††††] When less points are included in the calculation, discontinuities on the time correlation function are obtained (a *zig-zag* like plot) which could lead to negative values of the ISC rate constants.

Chapter 5. Theoretical insights into the photophysics of thionine (TH^+)

5.1. Overview

Quantum chemical methods have been employed to study the photophysics of thionine in vacuum and in aqueous solution (see **Fig. 8**). In Sections **5.2.1** and **5.2.2**, we present a detailed study of the electronic and molecular structure of thionine in the electronic ground and low-lying singlet and triplet electronically excited states. Solvent (water) effects on the vertical excitation spectrum (see discussion on section **5.2.1.2**) were estimated using the COSMO model and micro-hydration with up to five explicit water molecules. The rate constants for fluorescence (Section **5.2.2.1.1**), ISC (sections **5.2.4** and **5.2.5**) and phosphorescence (section **5.2.6**) were computed and a qualitative interpretation of the photophysics is presented.

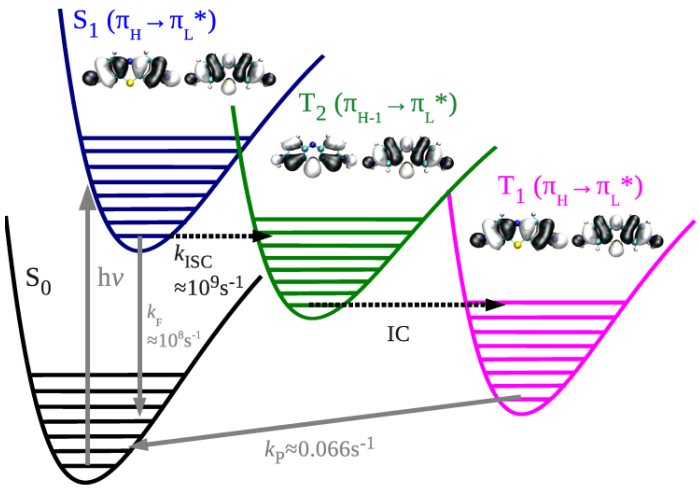

Fig. 8 Summary of the photophysical decay kinetics of thionine in aqueous solution.

In this chapter, a complete description of the electronic structure is provided emphasizing on the possible ISC mechanisms that could promote the efficient population of the triplet manifold of thionine in vacuum and aqueous solution. The lowest excited singlet and triplet states are of $\pi \rightarrow \pi^*$ (S_1, S_2, T_1, T_2) and

$n \rightarrow \pi^*$ (S_3, T_3) character. Since the direct ISC does not explain the high triplet quantum yield in this system, attention has been centered on the vibronic spin-orbit coupling between the low-lying singlet and triplet ($\pi \rightarrow \pi^*$) states of interest. The radiationless deactivation channels $\{S_1,S_2(\pi \rightarrow \pi^*) \nrightarrow T_1,T_2(\pi \rightarrow \pi^*)\}$ have been examined. An efficient population transfer from the $S_1(\pi_H \rightarrow \pi_L^*)$ state to the $T_2(\pi_{H-1} \rightarrow \pi_L^*)$ state via this channel is confirmed. The calculated ISC rate constant for this channel is $k_{ISC}^{TI} \approx 3.35 \times 10^8\ s^{-1}$, which can compete with the radiative depopulation of the $S_1(\pi_H \rightarrow \pi_L^*)$ state via fluorescence ($k_F \approx 1.66 \times 10^8\ s^{-1}$) in vacuum. The $S_1(\pi_H \rightarrow \pi_L^*) \nrightarrow T_1(\pi_H \rightarrow \pi_L^*)$ and $\{S_2(\pi_{H-1} \rightarrow \pi_L^*) \nrightarrow T_1,T_2(\pi \rightarrow \pi^*)\}$ ISC channels have been estimated to be less efficient ($k_{ISC}^{TI} \approx 10^5 - 10^6\ s^{-1}$). Based on the computed ISC rate constants and excited-state solvent shifts, it is suggested that the efficient triplet quantum yield of thionine in water (see **Fig. 8**) is primarily due to the $S_1(\pi_H \rightarrow \pi_L^*) \nrightarrow T_2(\pi_{H-1} \rightarrow \pi_L^*)$ channel with a computed rate constant of the order of $k_{ISC}^{TI} \approx 10^8 - 10^9\ s^{-1}$ which is in accord with the experimental finding ($k_{ISC} = 2.8 \times 10^9\ s^{-1}$).[171]

5.2. Results and discussion

5.2.1. Optimized ground state geometries and vertical electronic spectra of thionine (TH^+)

In this section we present a detailed characterization of the minima of the electronic ground state of thionine in vacuum (Section **5.2.1.1**) and in aqueous solution (Section **5.2.1.2**).

5.2.1.1. Vacuum

Selected geometrical parameters of the B3LYP/TZVP ground state equilibrium geometry of thionine are presented in **Fig. 9(a)**. The ground state minimum is found to be of C_{2v} symmetry. The two C - S bonds have a length of 175 pm and the <C - S - C angle is 103°. In order to test whether the TZVP

basis set is adequate for the description of the central ring C - S bond, we compared the TZVP geometrical parameters with those calculated with the other two AO basis sets at the ground state geometry, TZVPP and TZVP+R. We found that going beyond the TZVP basis set neither affects the C - S bond lengths nor the overall geometry. To our knowledge, there are no experimental geometrical parameters available for thionine which could be used for comparison. Only X-ray data for the amine-methylated derivative, methylene blue, is available in literature. For methylene blue pentahydrate, the C - S bond lengths are 174 and 172 pm and C - S - C bond angle is 104°, which is in good agreement with our calculated results for thionine obtained with the TZVP basis.[214]

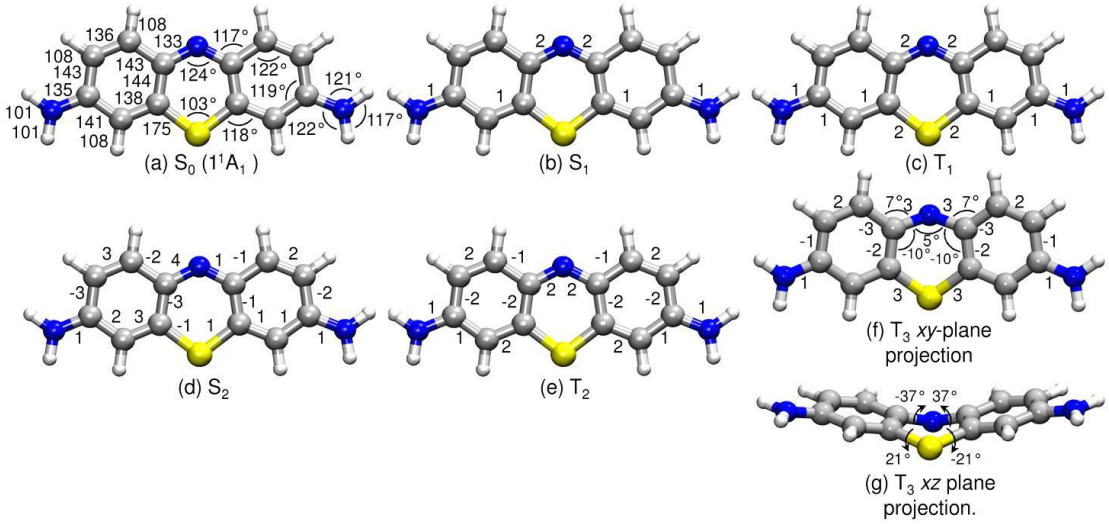

Fig. 9 TDDFT equilibrium structures of the lowest-lying triplet and singlet excited states of thionine in comparison with the ground state geometry. Numbers indicate bond lengths in pm (S_0 structure) and changes of bond lengths relative to the S_0 structure (all other structures). Bond angles and dihedrals are given in degrees. Changes larger than 1 pm and changes > 4° are given.

To test the performance of our approach for describing the excited electronic states, we calculated the vertical excitation energies of thionine using three different methods (DFT/MRCI, RI-CC2 and TD-B3LYP) and two different basis sets (TZVP and TZVP+R). The excited-state properties and their leading electronic configurations at the ground state geometry are shown in

Table 4, together with theoretical and experimental values from the literature. In addition, the valence molecular orbitals which dominate the corresponding excitations are depicted in **Fig. 10**. The orbital contributions to the excitations obtained with CC2, DFT/MRCI and TD-B3LYP are very similar. We therefore only show the molecular orbitals which are relevant for the DFT/MRCI results. Adding diffuse functions to the basis set (TZVP+R) has no significant effect on excitation energies and oscillator strengths. This justifies our choice of the computationally much less-demanding TZVP basis set.

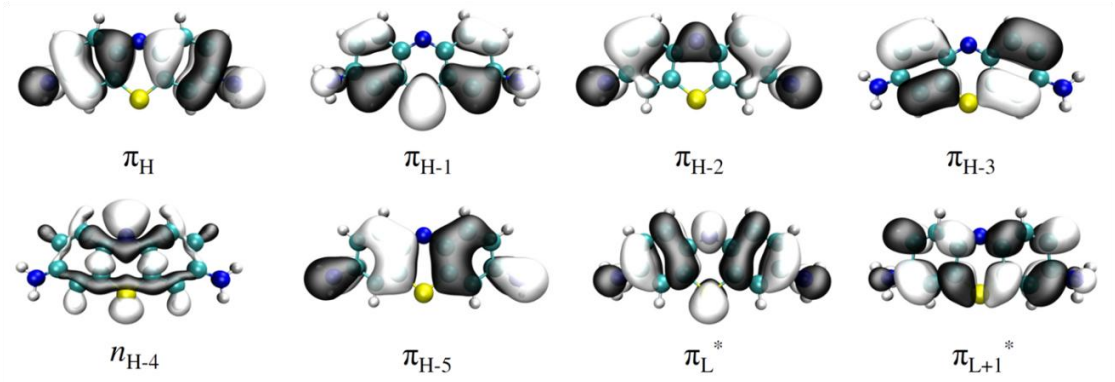

Fig. 10 Frontier BHLYP/TZVP Kohn-Sham molecular orbitals computed at the ground-state (S_0) minimum of thionine (isovalue 0.03).

At the C_{2v} ground state geometry the DFT/MRCI/TZVP//B3LYP/TZVP calculations predict the lowest singlet excited state S_1 to be a 1^1B_1 state with an excitation energy of 2.29 eV. With an oscillator strength of *f(L)* = 0.833 it can be assigned to the strong band maximum in the experimental spectrum. The dominant configuration for this state corresponds to a $\pi_H \rightarrow \pi_L^*$ transition. The occupied π_H and the virtual π_L orbitals are of a_2 and b_2 symmetry. Both contributing MOs are delocalized over the whole molecule. The second singlet excited state S_2 is a 2^1A_1 $\pi_{H-1} \rightarrow \pi_L^*$ state which is 0.20 eV higher in energy than S_1 vertically. Both π_{H-1} and the virtual π_L are of b_2 symmetry. The following excited state S_3 is 1^1B_2, dominated by a $n_{H-4} \rightarrow \pi_L^*$ transition. The lone-pair n_{H-4}-orbital is mostly localized at the phenothiazinium nitrogen in the central ring and has a_1 symmetry. The oscillator strength for the S_2 and S_3

transitions of *f(L)* = 0.012 and *f(L)* = 0.003 indicate negligible absorption intensities.

Table 4 Vertical singlet and triplet excitation energies ΔE_{vac} (eV) of thionine in vacuum.

E. State	Electronic Structure[a]	DFT/MRCI/TZVP// B3LYP/TZVP[b]	TD-B3LYP/TZVP// B3LYP/TZVP[b]	RI-CC2/TZVP// B3LYP/TZVP[b]	Other reported values.
$S_0(1^1A_1)$	(0.93) Ground State			.	
$S_1(1^1B_1)$	(0.80) $\pi_H \rightarrow \pi_L^*$	2.29(0.833)	2.74(0.613)	2.56(0.836)	2.26[d], 2.08[e], 2.06[f]
$S_2(2^1A_1)$	(0.82) $\pi_{H-1} \rightarrow \pi_L^*$	2.49(0.012)	2.73(0.010)	2.72(0.009)	
$S_3(1^1B_2)$	(0.79) $n_{H-4} \rightarrow \pi_L^*$	3.11(0.003)	3.21(0.001)	3.51(0.001)	
$S_4(3^1A_1)$	(0.52) $\pi_{H-2} \rightarrow \pi_L^*$ (0.21) $\pi_H \rightarrow \pi_L^* \pi_H \rightarrow \pi_L^*$	3.56(0.014)	4.03(0.002)[g]	4.33(0.000)[g]	
. :	. :	. :	. :	. :	
$S_8(4^1A_1)$	(0.64) $\pi_H \rightarrow \pi_{L+1}^*$	4.37(0.133)	4.53(0.089)	4.71(0.147)	
$S_9(3^1B_1)$	(0.50) $\pi_H \rightarrow \pi_{L+2}^*$ (0.23) $\pi_{H-1} \rightarrow \pi_{L+1}^*$	4.42(0.056)	4.62(0.027)	4.79(0.163)	
$S_{10}(4^1B_1)$	(0.34) $\pi_{H-1} \rightarrow \pi_L^* \pi_H \rightarrow \pi_L^*$ (0.20) $\pi_{H-1} \rightarrow \pi_{L+1}^*$	4.57(0.526)	5.02(1.058)[h]	5.19(1.073)[h]	4.42[e]
⋮	⋮	⋮	⋮	⋮	
$S_{12}(5^1B_1)$	(0.33) $\pi_{H-5} \rightarrow \pi_L^*$ (0.14) $\pi_H \rightarrow \pi_L^* \pi_H \rightarrow \pi_{L+1}^*$ (0.12) $\pi_H \rightarrow \pi_{L+2}^*$	4.90(0.201)	5.50(0.010)[i]	5.73(-0.002)[i]	
$T_1(1^3B_1)$	(0.92) $\pi_H \rightarrow \pi_L^*$	1.63	1.53	1.91	
$T_2(1^3A_1)$	(0.88) $\pi_{H-1} \rightarrow \pi_L^*$	2.11	2.03	2.33	
$T_3(1^3B_2)$	(0.81) $n_{H-4} \rightarrow \pi_L^*$	2.78	2.61	3.00	
$T_4(2^3A_1)$	(0.78) $\pi_{H-2} \rightarrow \pi_L^*$	3.12	3.01	3.68	

[a]Dominant contributions at the DFT/MRCI/TZVP level in parentheses. [b]Oscillator strengths (length form) in parentheses. [d]ZINDO//B3LYP/6-31+G(d) calculation taken from ref [163]. [e]Experimental absorption band taken from refs [39] and [37], solvent: water. [f]Experimental absorption band taken from ref [156], solvent: ethanol. [g]The dominant contribution of these states is a combination of two single excitations: $\pi_{H-2} \rightarrow \pi_L^*$ and $\pi_H \rightarrow \pi_{L+1}^*$. [h]The dominant contribution of these states is a combination of two single excitations: $\pi_{H-1} \rightarrow \pi_{L+1}^*$ and $\pi_H \rightarrow \pi_{L+2}^*$. [i]The dominant contribution of these states is a single excitation: $\pi_{H-5} \rightarrow \pi_L^*$, the negative value of the oscillator strength is due to numerical inaccuracies of the RI aproximation.

The RI-CC2 method predicts the same energetic ordering of the low-lying $\pi \rightarrow \pi^*$ and $n \rightarrow \pi^*$ excited states. Compared to DFT/MRCI, the CC2 excitation energies for the S_1 1^1B_1 ($\pi_H \rightarrow \pi_L^*$), S_2 2^1A_1 ($\pi_{H-1} \rightarrow \pi_L^*$) and S_3 1^1B_2 ($n_{H-4} \rightarrow \pi^*$) states are energetically higher by up to 0.27, 0.30 and 0.40 eV, respectively. These deviations are consistent with recent systematic benchmarks in which CASPT2 reference excitation energies were typically overestimated in CC2 by ≈ 0.3 eV, and underestimated in DFT/MRCI by ≈0.2 eV.[52,207] Despite the deviations in excitation energies, the relative energies of the excited

states are very similar at the DFT/MRCI and CC2 level. This shows that the different types of the states are well described by these methods. The TD-B3LYP/TZVP//B3LYP/TZVP vertical singlet excitation energies are always higher than those calculated with the DFT/MRCI method. In addition, on the TD-B3LYP/TZVP//B3LYP/TZVP PES the bright S_1 1^1B_1 ($\pi_H \rightarrow \pi_L^*$) state is below the S_2 2^1A_1 ($\pi_{H-1} \rightarrow \pi_L^*$) state by 0.01 eV while the energy difference between these two states is 0.16 eV using CC2 and 0.20 eV at the DFT/MRCI level.

No experimental gas phase spectrum is available for comparison. The comparison with aqueous experimental absorption maximum will be postponed to Section **5.2.1.2**, where we discuss the results obtained with our solvation models. Here, we only state that the DFT/MRCI gas-phase results are very similar to the previously published ZINDO//B3LYP/6-31+G(d) excitation energy [163] (2.26 eV) and are 0.2 eV larger than the experimental absorption maximum measured in aqueous solution, which is within the error of the DFT/MRCI method.

Regarding the higher-energy region of the singlet manifold, we found some bright transitions with oscillator strengths larger than *f(L)* = 0.1. At the DFT/MRCI/TZVP//B3LYP/TZVP level, transitions to the S_8 (4^1A_1, 4.37 eV), S_{10} (4^1B_1, 4.57 eV) and S_{12} (5^1B_1, 4.90 eV) $\pi \rightarrow \pi^*$ excited states with oscillator strengths of *f(L)* = 0.133, *f(L)* = 0.532 and *f(L)* = 0.201 were obtained. The TD-B3LYP/TZVP method predicts only one optically bright S_{10} (4^1B_1, 5.02 eV) $\pi \rightarrow \pi^*$ state with a strong oscillator strength of *f(L)* = 1.058. CC2 predicts three consecutive optically bright transitions to the S_8 4^1A_1 (4.71 eV), S_9 3^1B_1 (4.79 eV) and S_{10} 4^1B_1 (5.19 eV) excited states with oscillator strengths of *f(L)* = 0.147, *f(L)* = 0.163 and *f(L)* = 1.073. The three methods predict the strongest absorption in this energy region as the 4^1B_1 ($\pi \rightarrow \pi^*$) bright state. However, the state character is different at the DFT/MRCI and the TDDFT and CC2 levels, see **Table 4**. At the DFT/MRCI level the state has significant

contributions from doubly excited configurations, which cannot be described by TDDFT and CC2. As a consequence the DFT/MRCI oscillator strength (which is due to the $\pi_{H-1} \rightarrow \pi_{L+1}^*$ singly excited configuration) is lower, resulting in correct relative intensities of the two bright transitions. Furthermore, the calculated DFT/MRCI excitation energy of this state (4.57 eV) is only 0.15 eV higher than the experimental ultraviolet absorption (4.42 eV,[39]) measured in aqueous and alcoholic solutions, while the TD-B3LYP and CC2 methods place the absorption at higher energies.

Analogous to the singlet states, in the triplet manifold the lowest-lying excited state $T_1(1^3B_1)$ is dominated by a $\pi_H \rightarrow \pi_L^*$ transition and has an excitation energy of 1.63 eV computed at the DFT/MRCI/TZVP level. 0.48 eV above this state is the T_2 (1^3A_1) $\pi_{H-1} \rightarrow \pi_L^*$ state. At the ground state geometry T_1 and T_2 are located below S_1, T_2 being energetically close to S_1 (0.18 eV). Above T_2 and S_1 is the T_3 state (by 0.67 and 0.49 eV, respectively), characterized by the $n_{H-4} \rightarrow \pi_L^*$ transition. The DFT/MRCI vertical excitation energies of the T_1, T_2 and T_3 states are always higher than those obtained with TD-B3LYP/TZVP (0.10, 0.08 and 0.17 eV, respectively) and lower than the ones obtained with CC2 (0.28, 0.22 and 0.22 eV, respectively). Additionally, at the TD-B3LYP/TZVP level T_3 is 0.15 eV below S_1.

5.2.1.2. Hydration effects

Because there is no gas-phase spectroscopic data of thionine available, we have to refer to measurements in aqueous and alcoholic solution. These solvents are expected to have a significant effect on the electronic structure, so we calculated the vertical excitation energies of thionine using several solvation models. All models were fully optimized at the B3LYP/TZVP level of theory. Electrostatic effects of the solvent environment were estimated using the COSMO model with a dielectric constant $\varepsilon = 78$ corresponding to water. This model is labeled TH^+C. In a protic solvent, hydrogen bonds between the solute and the solvent are expected to be important, in particular for $n \rightarrow \pi^*$

states. Therefore we created additional models consisting of the solute and one (TH^+1W) to five (TH^+5W) water molecules, which were additionally embedded in a COSMO environment. The optimized ground state structures of these models are presented in **Fig. 11**. The DFT/MRCI vertical excitation energies and oscillator strengths are displayed in **Fig. 12**.

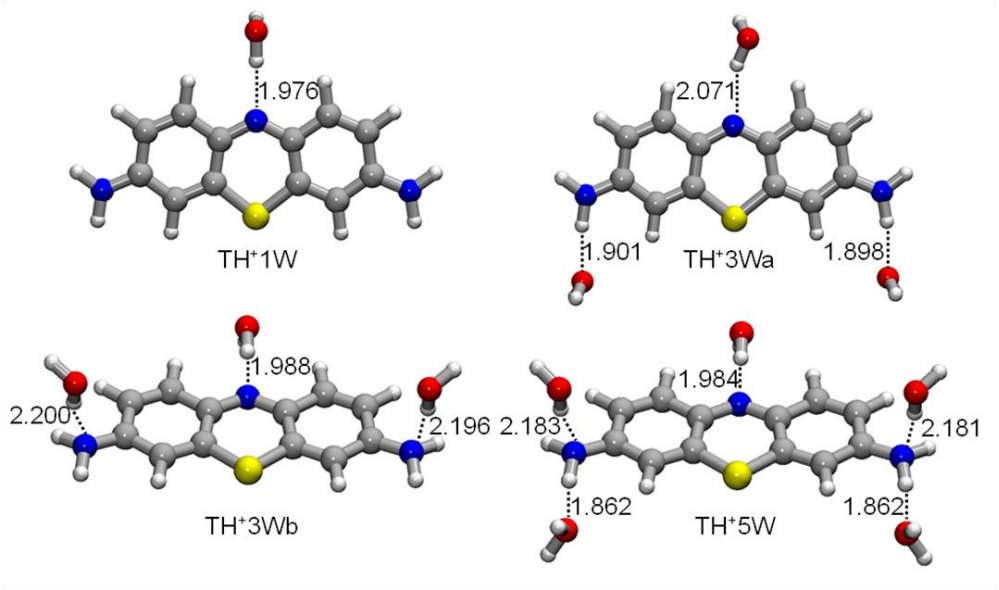

Fig. 11 Ground state minimum of thionine-water hydrogen bonded complexes optimized with COSMO at the B3LYP/TZVP level. Numbers indicate hydrogen bond lengths in Å.

Thionine can form hydrogen bonds with water molecules at several sites. The starting geometries were generated by placing water molecules around thionine molecule in positions where the formation of hydrogen bonds with nitrogen atoms were to be expected: (i) the nitrogen atom of the phenothiazinium central ring (N_{ring}) can form a hydrogen bond with its lone-pair orbital which is located in the ring plane (H-O-H ⋯ N_{ring}), (ii) the two amine groups (N_{amine}) can form hydrogen bonds with their lone-pair orbitals which are perpendicular to the ring and are involved in the conjugated π-system (H-O-H ⋯ N_{amine}) and (iii) the hydrogen atoms of these two amine groups (N_{amine}) can also form hydrogen bonds with water (N_{amine} - H ⋯ O).

The hydrogen bonds between water molecules and the lone pairs of the N_{amine} atoms are relatively weak, indicated by (H-O-H ⋯ N_{amine}) lengths in the range of 2.181 – 2.200 Å in TH^+3Wb – TH^+5W. The H-O-H ⋯ N_{amine} hydrogen bond formation is accompanied by a slight pyramidization of the amine groups. The hydrogen bonds to N_{ring} (H-O-H ⋯ N_{ring}) of the phenothiazinium central ring and to the hydrogen atoms of the amine groups (N_{amine} - H ⋯ O) are stronger.

In a simplified picture, the energetic stabilization or destabilization of the ground and excited states in polar solvents is related to their dipole moments and the extent of polarization they induce in the surrounding solvent. Because thionine is charged, its calculated dipole moment depends on the origin of the coordinate system, which is arbitrary. Therefore in **Table 5** the differences of the magnitudes of the dipole moments (Δμ) calculated relative to the ground state S_0 are listed. According to these results, the effect of a polar solvent on the excitation energies of the S_1 - S_2 and T_1 - T_2 $\pi\rightarrow\pi^*$ states should be small while the effect on the S_3 and T_3 $n\rightarrow\pi^*$ states is expected to be stronger.

Table 5 Differences of the magnitudes of the dipole moments (Δμ, Deybe) of the lowest singlet and triplet electronic states of thionine calculated at the DFT/MRCI/TZVP level at S_0. The Δμ magnitudes were calculated relative to the ground state dipole moment.

State	S_0	S_1	S_2	S_3	T_1	T_2	T_3
Δμ	0.0	0.1	0.4	-0.9	0.1	0.4	-1.1

We first discuss the solvent effect on the energy of the first two lowest excited singlet $\pi\rightarrow\pi^*$ states (see **Fig. 12**). The effect of the COSMO environment is a slight lowering of the two S_1 and S_2 $\pi\rightarrow\pi^*$ states (0.07 eV for TH^+C), bringing the excitation energy of the bright S_1 state closer to the experimental absorption maximum of 2.07 eV. These solvent shifts are somewhat smaller than the solvent shifts obtained by Homem-de-Mello *et al.* with a polarizable continuum model (-0.29 eV) using a combination of AM1 for optimization of

the molecular structure and ZINDO for calculating the electronic spectrum.[163-164]

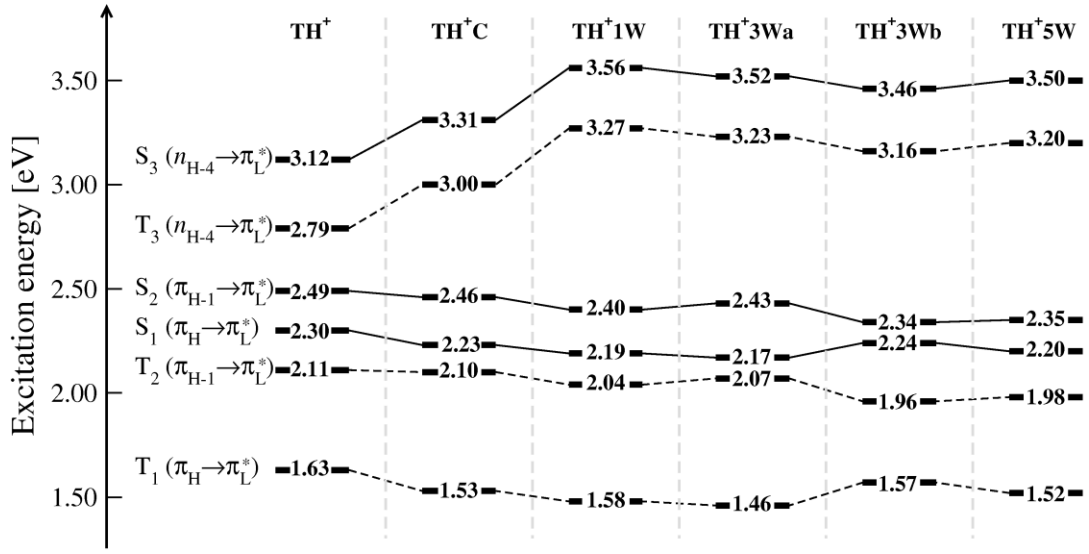

Fig. 12 Comparison of the singlet and triplet vertical excitation energies for the vacuum (TH^+), solvation with COSMO (TH^+C) and micro-hydration with one to five explicit water molecules (TH^+1W - TH^+5W).

The H-O-H ⋯ N_{ring} hydrogen bond (TH^+1W) causes a further redshift of the two $\pi\rightarrow\pi^*$ states which is more pronounced for S_2 than for S_1 due to the different spatial distributions (see **Fig. 12**) of the contributing orbitals at each state, (HOMO for S_1 and HOMO-1 for S_2). The addition of water molecules at the two amine groups of thionine (model TH^+3Wa, N_{amine}-H ⋯ O hydrogen bonds) has no effect on the energies of the two S_1 and S_2 $\pi\rightarrow\pi^*$ states. But if the two water molecules are hydrogen-bonded to the lone-pairs of the two amine groups (model TH^+3Wb, H-O-H ⋯ N_{amine} hydrogen bonds) instead of the amine H-atoms, the energy of S_2 in TH^+3Wb is 0.1 eV lower than with the water molecules in "equatorial" position (model TH^+3Wa), while the S_1 energy is higher by 0.07 eV. Compared to model TH^+1W, S_1 is slightly blue-shifted by 0.05 eV, while S_2 is red-shifted by 0.06 eV. Adding two more water molecules (model TH^+5W) partly compensates the effect of the water molecules at the lone-pairs of the two amine groups, see **Fig. 12**. Assuming that the water molecules preferably bind to the ring-nitrogen N_{ring} and to the H-atoms of the

amine-groups (an assumption which is supported by the different lengths of the hydrogen bonds), we regard complexes TH^+3Wa and TH^+5W as our best models for solvated thionine. The absorption energies of the optically bright $S_1(\pi_H \rightarrow \pi_L^*)$ state of 2.17 eV (TH^+3Wa) and 2.20 eV (TH^+5W) are in good agreement with the experimental value of 2.07 eV for thionine.

A significantly larger solvent effect is found for the $S_3(n_{H-4} \rightarrow \pi_L^*)$ state. This state is blueshifted by 0.19 eV by electrostatic effects mimicked by the COSMO environment. The H-O-H $\cdots$ N_{ring} hydrogen bond causes an additional 0.21 eV blueshift. Adding more water molecules partially compensates the blueshift. For our best models, the blueshift of S_3 amounts to 0.33 eV (TH^+3Wa) and 0.28 eV (TH^+5W). The blueshift of the $n \rightarrow \pi^*$ state caused by the H-O-H $\cdots$ N_{ring} hydrogen bond can qualitatively easily be understood: it causes a stabilization of the n_{H-4}-orbital, resulting in a higher excitation energy to the π_L^* orbital, whose energy is only less affected. The triplet states are affected by the solvent environment in a very similar way as their singlet counterparts. The $\pi \rightarrow \pi^*$ states are slightly redshifted, in agreement with previous INDO/CIS calculations in methylene blue-water hydrogen bond complexes, while the $n \rightarrow \pi^*$ states exhibit a strong blueshift.

The strong blueshift of the $n \rightarrow \pi^*$ states in polar and/or protic solvents has consequences for the photophysics of thionine. In the gas phase T_3 is nearly degenerate to S_1 and we expect large spin-orbit coupling elements between these states, so $S_1 \rightarrow T_3$ is a possible channel for efficient ISC. However, in water this channel is no longer accessible due to the strong blueshift of $T_3(n \rightarrow \pi_L^*)$ making these channels inaccessible from the ground vibrational levels of the S_1 and $S_2(\pi \rightarrow \pi^*)$ states. Thus, on the basis of these results, the T_1 and $T_2(\pi \rightarrow \pi^*)$ states have been considered as main target states for effective ISC channels via a vibronic spin-orbit coupling mechanism.

5.2.2. Excited state geometries and adiabatic excitation energies

In this section, we discuss the TD-B3LYP minimum energy nuclear arrangements of the two lowest singlet and the three lowest triplet excited states as well as the excitation energies calculated at these geometries. The most important geometrical parameters of the optimized excited states are depicted in **Fig. 9**. An overview of the energetic locations of the lowest singlet and triplet states at each minimum is given in **Fig. 13**. The adiabatic excitation energies and the zero point vibrational energy corrections (ZPVEC) are listed in **Table 6**. The results will be discussed in more detail in the following sections.

Table 6 Adiabatic singlet and triplet DFT/MRCI in vacumm (ΔE_{vac}^{ad}, eV) and taking into account the water solvation shifts (ΔE_{w}^{ad}, eV) and scaled zero point vibrational corrections (ZPVEC, eV) of the excited states of thionine computed using the TZVP basis set. Oscillator strengths for emission at the excited-state minima are listed in parentheses. The computed TD-B3LYP ($\Delta E_{TD\text{-}B3LYP}^{ad}$, eV) adiabatic energies in vacuum are also listed.

Geometry	Electronic structure[a]	ΔE_{vac}^{ad}	ΔE_{w}^{ad}	$\Delta E_{TD\text{-}B3LYP}^{ad}$	ZPVEC[c]
$S_1(1^1B_1)$	(0.80) $\pi_H \rightarrow \pi_L^{*}$[e]	2.27 (0.790)	2.14	2.71 (0.587)	0.02
$S_2(2^1A')$	(0.45) $\pi_{H-1} \rightarrow \pi_L^{*}$ (0.36) $\pi_H \rightarrow \pi_L^{*}$[e]	2.29 (0.269)	2.23	2.55 (0.025)	-0.16[d]
$T_1(1^3B_1)$	(0.92) $\pi_H \rightarrow \pi_L^{*}$[e]	1.63	1.46	1.47	-0.07
$T_2(1^3A_1)$	(0.88) $\pi_{H-1} \rightarrow \pi_L^{*}$[e]	1.97	1.93	1.86	-0.08
$T_3(2^3A)$	(0.50) $n_{H-2} \rightarrow \pi_L^{*}$[f] (0.26) $\pi_{H-4} \rightarrow \pi_L^{*}$[f]	2.31	2.75	2.17	0.03

[a]Dominant contributions at the DFT/MRCI/TZVP level. [b]ΔE^{ad} in aqueous solution calculated applying the vertical excitation energy shifts of TH^+3Wa model. [c]Difference between the zero point vibrational energy of the excited state and the zero point vibrational energy of S_0. [d]Does not include the mode with imaginary frequency. [e]MOs are shown in **Fig. 10**.[f]MOs are shown in **Fig. 17**.

5.2.2.1.1. S_1 and T_1 minima

We obtained a planar C_{2v} symmetric minimum for the $S_1(\pi_H \rightarrow \pi_L^{*})$ excited state. This minimum is very similar to the ground state geometry (see **Fig. 9(b)**) where the elongation of the bonds is not more than 2 pm relative to their values in the electronic ground state. From an energetic point of view the geometry relaxation has almost no effect on the energy of the $S_1(\pi_H \rightarrow \pi_L^{*})$ state. Its adiabatic DFT/MRCI excitation energy amounts to ΔE_{vac}^{ad} = 2.27 eV, corresponding to a stabilization of only 0.02 eV. At the same time the

electronic ground state is destabilized by 0.07 eV yielding a vertical emission energy of 2.20 eV, which is in good agreement with the maximum of the experimental fluorescence band at 2.04 eV. [165] Due to the small emission energy entering the equation for k_F at the third power, the rate of fluorescence calculated at the $S_1(\pi_H \rightarrow \pi_L^*)$ minimum is rather low ($k_F \sim 1.66 \times 10^8\ s^{-1}$). This value is in excellent agreement with the experimental one determined at pH 2.5 ($k_F = 1.31 \times 10^8\ s^{-1}$).[169] To shed light on other possible relaxation mechanisms, we constructed a linearly interpolated path from the Franck–Condon region to the $S_1(\pi_H \rightarrow \pi_L^*)$ minimum, **Fig. 14**. No crossing between electronic states is observed along this path and the dark $S_2(\pi_{H-1} \rightarrow \pi_L^*)$ excited state is always ≈ 0.2 eV above the S_1 state.

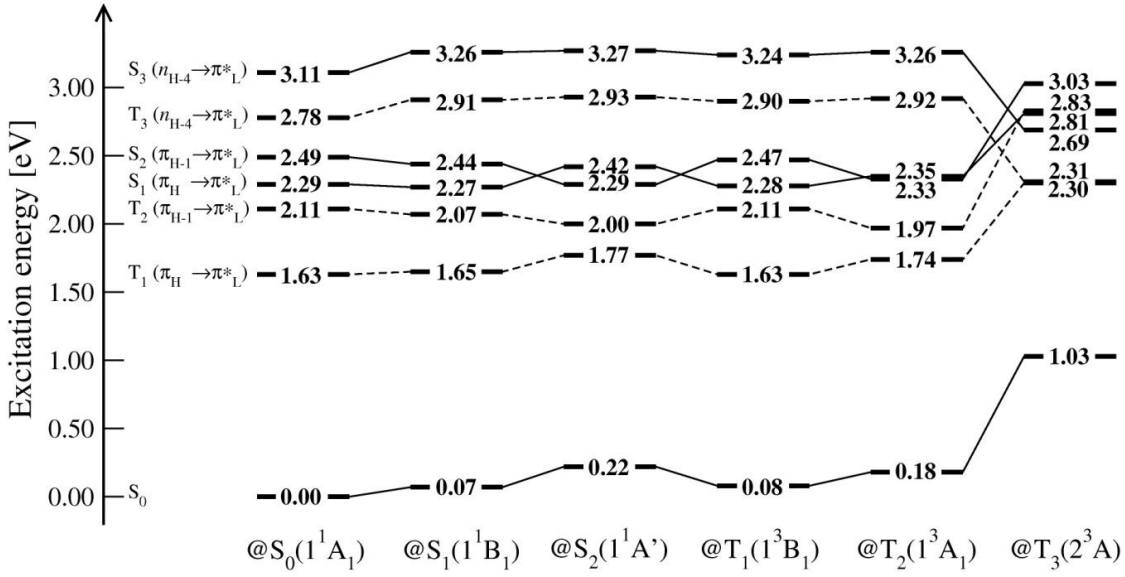

Fig. 13 DFT/MRCI electronic excitation energies [eV] at the various excited state geometries. The electronic ground state energy at the S_0 geometry has been chosen as the common origin.

As can be expected from the electronic character of these states ($\pi_H \rightarrow \pi_L^*$ transition), the geometry of the T_1 minimum is very similar to that of the S_1 state (see **Fig. 9(c)**). The main difference between both geometries is the additional widening of the C - S bond by 2 pm. The adiabatic excitation energy of the T_1 state is ΔE_{vac}^{ad} = 1.63 eV (1.65 eV including the ZPVEC),

which is in excellent agreement with the reported values of 1.68 eV [166] and of 1.69 ± 0.07 eV.[162,215-216] As for the $S_1(\pi_H \rightarrow \pi_L^*)$ state, there is almost no energetic relaxation effect on this state.

Furthermore, the excitation energies of the other low-lying singlet and triplet excited states are only slightly affected when proceeding from the FC region to the S_1 and $T_1(\pi_H \rightarrow \pi_L^*)$ minima, see **Fig. 13**. It is important to note that the third excited singlet and triplet (S_3 and $T_3(n_{H-4} \rightarrow \pi_L^*)$) states are blue-shifted between by 0.13 and 0.12 eV at each minimum (S_1 and T_1) moving them energetically away from the $S_1(\pi_H \rightarrow \pi_L^*)$ state.

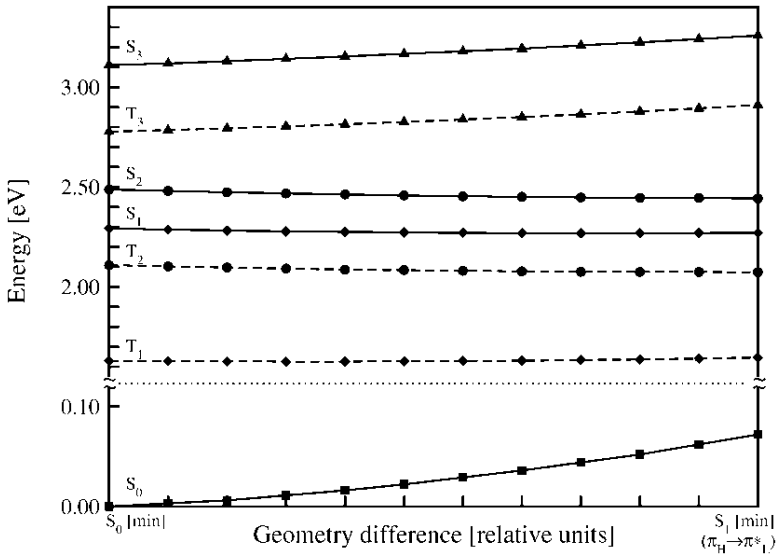

Fig. 14 DFT/MRCI energies of the low-lying states of thionine along a linearly interpolated path between the S_0 and S_1 geometries. The singlet profiles are represented by solid lines and the triplet profiles by dashed lines.

5.2.2.1.2. S_2 and T_2 minima

The computed geometry of the stationary point obtained in the optimization of $S_2(\pi_{H-1} \rightarrow \pi_L^*)$ state has C_S symmetry and is characterized by an asymmetric elongation of the bonds. For example, the N_{ring}-C bond (in the left of **Fig. 9(d)**) is elongated by 4 pm while the other N_{ring}-C bond (in the right of **Fig. 9(d)**) by only 1 pm. The same holds for the other bond lengths. However, at the level of TDDFT (TD-B3LYP/TZVP) this structure is found to constitute a saddle-

point on the PES. One vibrational mode with an imaginary frequency of $\nu_1 = i89.2\ cm^{-1}$ is obtained and corresponds to an *out-of-plane* movement of the carbon atoms of the central ring and a bending of the amine-groups. We calculated the TDDFT and DFT/MRCI energies along this imaginary normal mode. As has been found before in other systems like flavins,[217] psolaren,[130] cytosine[92] and thiophene,[218] the TDDFT PES exhibits an extremely shallow double minimum potential well along this imaginary mode, while the DFT/MRCI PES shows a minimum with C_S symmetry.

Furthermore, a distortion along the imaginary normal mode followed by optimization without symmetry constraints (C_1-symmetry) led to a minimum at the TD-B3LYP/TZVP PES, which differs only very slightly from the previously obtained C_S symmetric structure (the difference is a slightly non-planar ring-system). At the DFT/MRCI level, this point is energetically higher than the previously described C_S-symmetry geometry by 0.01 eV. Therefore we considered the imaginary frequency as an artefact of the TDDFT (B3LYP) method and chose the C_S symmetric structure as the minimum of the S_2 excited state.

Due to the relaxation effects and the loosening of the symmetry constraints, the irreducible representation of this state changed from A_1 (C_{2v} representation) to A' (C_S representation). The electronic structure of this S_2 state is now a linear combination of two single excitations $\pi_{H-1}\rightarrow\pi_L^*$ and $\pi_H\rightarrow\pi_L^*$ in *A*' symmetry, with a major contribution from the $\pi_{H-1}\rightarrow\pi_L^*$ transition. In addition, the oscillator strength of this state rises to *f(L)* = 0.269 due to mixing with the $\pi_H\rightarrow\pi_L^*$ optically bright transition, see **Table 6**. At the same time, the $S_1(\pi_H\rightarrow\pi_L^*)$ state corresponds to a linear combination of the $\pi_H\rightarrow\pi_L^*$ and $\pi_{H-1}\rightarrow\pi_L^*$ transitions with a larger contribution of the $\pi_H\rightarrow\pi_L^*$ and is blue-shifted by 0.13 eV above the $S_2(\pi_{H-1}\rightarrow\pi_L^*)$ state. This means that during the relaxation from the FC region, an intersection between the S_1 and S_2 PESs occurs.

With regard to the excitation energies, the relaxation effects on $S_2(\pi_{H-1}\rightarrow\pi_L^*)$ are larger than those obtained for the $S_1(\pi_H\rightarrow\pi_L^*)$ state and yield an adiabatic excitation energy of ΔE_{vac}^{ad} = 2.29 eV (a stabilization of 0.2 eV compared with the ground state vertical spectrum), see **Table 6** and **Fig. 14**. In order to investigate the crossing between S_1 and S_2 in more detail a linearly interpolated path between the S_1 and the S_2 minima has been constructed. The DFT/MRCI energies of the low-lying states along the path are depicted in **Fig. 15**. As expected, the two states mix strongly and a crossing of the S_2 and S_1 PESs can easily be reached from the $S_1(\pi_H\rightarrow\pi_L^*)$ minimum in the proximity of the $S_2(\pi_{H-1}\rightarrow\pi_L^*)$ minimum. The mixing of the two states is reflected in the oscillator strengths. At the $S_1(\pi_H\rightarrow\pi_L^*)$ minimum, the $S_1(\pi_H\rightarrow\pi_L^*)$ state has an oscillator strength of *f(L)* = 0.790 which is reduced at the crossing region. Even at the $S_2(\pi_{H-1}\rightarrow\pi_L^*)$ minimum, the $S_1(\pi_H\rightarrow\pi_L^*)$ state has significant oscillator strength of *f(L)* = 0.533. On the other hand, the oscillator strength of the $S_2(\pi_{H-1}\rightarrow\pi_L^*)$ state increases from *f(L)* = 0.010 to *f(L)* = 0.339 as the $S_1(\pi_H\rightarrow\pi_L^*)$ geometry gets closer to the crossing region and then drops to *f(L)* = 0.269 at the $S_2(\pi_{H-1}\rightarrow\pi_L^*)$ geometry. In the proximity of the $S_2(\pi_{H-1}\rightarrow\pi_L^*)$ minimum the contributions of the $\pi_H\rightarrow\pi_L^*$ and the $\pi_{H-1}\rightarrow\pi_L^*$ configurations, which account for ~80% of the total contributions, are very similar. We therefore expect strong vibronic coupling between these states.

The minimum of the $T_2(\pi_{H-1}\rightarrow\pi_L^*)$ state is C_{2v} symmetric (see **Fig. 9(e)**). The geometry of the $T_2(\pi_{H-1}\rightarrow\pi_L^*)$ state show substantial differences from that calculated for the $S_2(\pi_{H-1}\rightarrow\pi_L^*)$state. The changes in the bonding patterns are of maximum 2 pm. The adiabatic excitation energy of the T_2 $(\pi_{H-1}\rightarrow\pi_L^*)$ state amounts to ΔE_{vac}^{ad} = 1.97 eV, which is 0.30 eV below the $S_1(\pi_H\rightarrow\pi_L^*)$ state, see **Table 6**. The other singlet and triplet excitation energies calculated at this geometry are slightly higher and the ground state is destabilized by 0.18 eV. It is important to note that the energy gap between the $S_1(\pi_H\rightarrow\pi_L^*)$ and

$S_2(\pi_{H-1}\rightarrow\pi_L^*)$ states computed at this geometry is only 0.02 eV, compared with the energy differences between these states at the other minima (0.13 - 0.20 eV). Nevertheless, the same state ordering is preserved as in the FC region at this energy region.

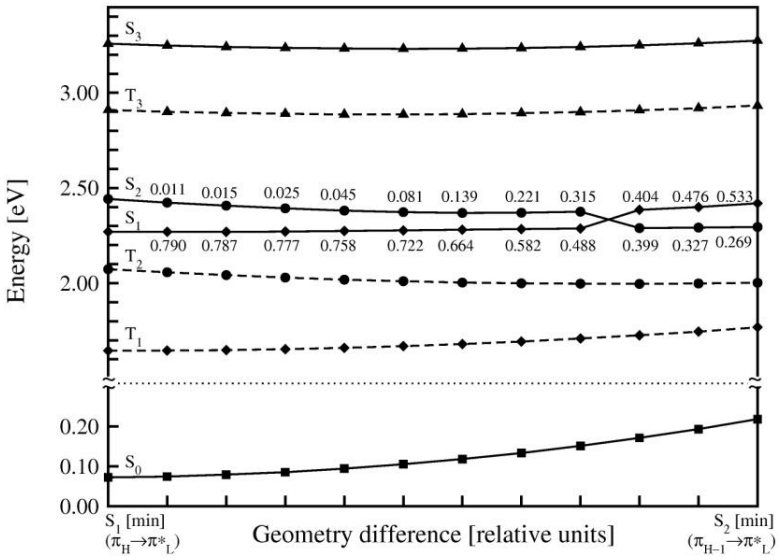

Fig. 15 DFT/MRCI energies of the low-lying states along a linearly interpolated path between the S_1 and S_2 minima of thionine. The singlet profiles are represented by solid lines and the triplet profiles by dashed lines.

5.2.2.1.3. S_3 and T_3 minima

The location of minima of the S_3 and $T_3(n\rightarrow\pi^*)$ states was very difficult. Due to mixing of the S_3 state with the lower lying states during optimization it was not possible to find the minimum of the S_3 state and we were only able to locate a minimum of the T_3 state.

In our initial attempts, we started the search for the T_3 minimum using the FC geometry (C_{2v} symmetry) as starting point, which resulted in a planar stationary point on the PES with C_{2v} symmetry. The vibrational analysis indicated that this geometry was a saddle point on the TDDFT PES with an imaginary frequency of $i45$ cm^{-1}. A scan along this imaginary mode showed that this planar structure was a very flat saddle point on the TDDFT PES.

Distorting this structure along the imaginary mode resulted in a non-planar geometry with C_1-symmetry. Geometry optimization using this structure as the starting point ended at a non-planar stationary point (see **Fig. 9(f,g)**),which turned out to be a minimum on the PES. Due to the very close proximity of the $T_1(\pi_H \rightarrow \pi_L^*)$ state at this geometry (see **Fig. 16**) it was necessary to change the default atom displacement from 0.02 a.u. to 0.01 a.u. in the numerical frequency calculation in order to avoid root flipping of the two triplet states.

As can be seen in **Fig. 9(g)**, the geometry of the T_3 excited state is characterized by changes of the <C - S - C - C and <C - N_{ring} - C - C dihedral angles of ±21° and ±37° from planarity (180°). Other geometrical changes compared with the ground state geometry include the increase in the <C- N_{ring}- C and <C -C - N_{ring} angles by 5° and 7°; and the elongations of the N_{ring} - C and S - C bonds by 3 pm. Geometry relaxation leads to an adiabatic excitation energy of ΔE_{vac}^{ad} = 2.31 eV (see **Table 6**) corresponding to a stabilization by more than 0.47 eV with respect to the vertical absorption energy (see **Table 4**). The energetic order of the molecular orbitals changes at this minimum. The energy of the n_{H-4} MO calculated at S_0 is lowered and the MO is now n_{H-2}. Furthermore, a new π_{H-4} MO appears (**Fig. 17**). Since the V shape of the molecular frame allows for a mixing between *n* and π character, the electronic wave function of the T_3 state is a linear combination of the $n_{H-2} \rightarrow \pi_L^*$ and $\pi_{H-4} \rightarrow \pi_L^*$ transitions with a larger contribution of the $n_{H-2} \rightarrow \pi_L^*$. Note also that the $S_1(\pi_H \rightarrow \pi_L^*)$ and $T_3(n \rightarrow \pi^*)$ DFT/MRCI adiabatic energies are nearly degenerate, T_3 still being 0.04 eV above the S_1 minimum (0.05 eV including ZPVEC). This energy difference is below the accuracy of our method, so we cannot give a definite answer whether T_3 is accessible from S_1.

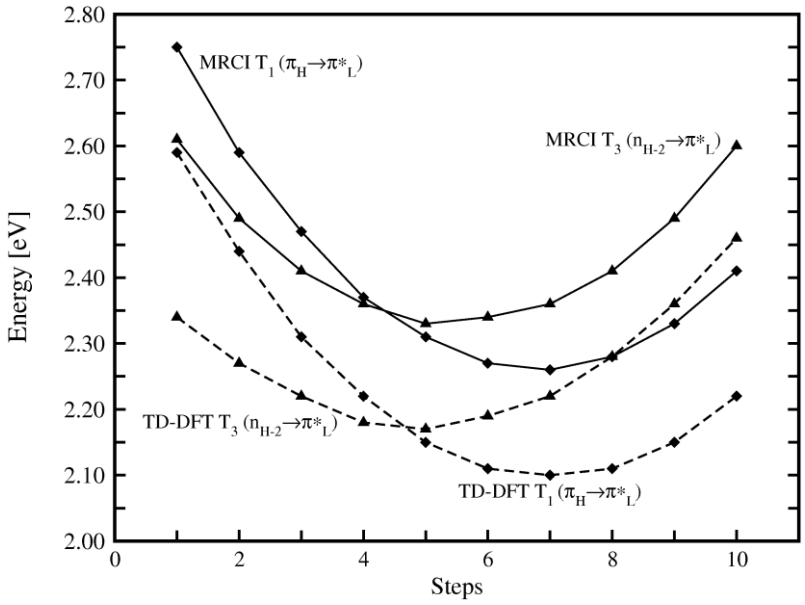

Fig. 16 DFT/MRCI and TDDFT excitation energies along coordinate elongations along the imaginary frequency (509*i* cm^{-1}) obtained from the default atom displacement from 0.02 a.u in the numerical frequency calculation of the T_3 non-planar minimum.

At the $T_3(n\rightarrow\pi^*)$ minimum, the electronic ground state is strongly destabilized by 1.03 eV (see **Fig. 13**). This non-planar nuclear arrangement is very favorable for the $n\rightarrow\pi^*$ electronic states indicated by a reversal of the energetic ordering of the $n\rightarrow\pi^*$ and the $\pi\rightarrow\pi^*$ states with respect to the FC region. At the T_3 minimum the $S_3(n\rightarrow\pi^*)$ excited state is below the S_1 $\pi_H\rightarrow\pi_L^*$ state by 0.12 eV and below the S_2 $\pi_{H-1}\rightarrow\pi_L^*$ state by 0.34 eV. The $T_3(n\rightarrow\pi^*)$ excited state is nearly degenerate to the $T_1(\pi_H\rightarrow\pi_L^*)$ state (0.01 eV above) and 0.52 eV below the $T_2(\pi_{H-1}\rightarrow\pi_L^*)$ state at the $T_3(n\rightarrow\pi^*)$ geometry. The change of the energetic order of the states is due to intersections between them, which lie very close to the $T_3(n\rightarrow\pi^*)$ minimum (see **Fig. 13** and **Fig. 18**). Moreover, at this region of the coordinate space the energy of the $T_3(n\rightarrow\pi^*)$ state is 0.50 eV lower than the energy of the S_1 $\pi_H\rightarrow\pi_L^*$ state. This suggests the existence of several conical intersections between the electronically excited singlet and triplet surfaces near to this point.

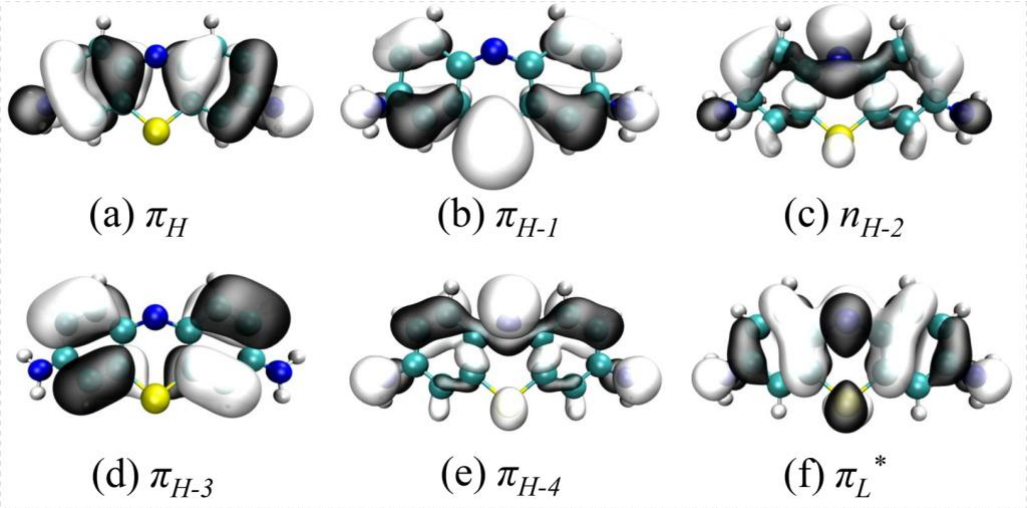

Fig. 17 Frontier BHLYP/TZVP Kohn-Sham molecular orbitals computed at the T_3 ($n\rightarrow\pi^*$) state minimum (isovalue 0.03) of thionine.

It is known experimentally that a part of the singlet population undergoes ISC to the triplet states. The ISC is expected to be efficient if the singlet and triplet states involved are close in energy, their spin–orbit coupling is reasonably strong and the density of vibrational levels is high in the accepting state. According to El-Sayed's rule, [63] sizeable spin-orbit coupling is expected between states with $\pi\rightarrow\pi^*$ and states with $n\rightarrow\pi^*$character, while the spin-orbit coupling between $\pi\rightarrow\pi^*$states is only weak. Thus, the FC approximation will yield non-efficient ISC between, *e. g.*, two $\pi\rightarrow\pi^*$ states. In thionine, the geometry at the T_3 minimum is non-planar, so there is no strict separation between $n\rightarrow\pi^*$ and $\pi\rightarrow\pi^*$ states, (**Fig. 9(c,e)**). However, even at the non-planar $T_3(n\rightarrow\pi^*)$ minimum, the T_3 state still has predominantly $n\rightarrow\pi^*$ character, so we expect sizeable spin-orbit coupling between T_3 and $\pi\rightarrow\pi^*$ singlet states. According to our results the lowest vibronic level of $T_3(n\rightarrow\pi^*)$ is located slightly above the lowest vibronic level of $S_1(\pi_H\rightarrow\pi_L^*)$. In order to further explore possible ISC channels from S_1 we performed a linearly interpolated scan of the PES between the $S_1(\pi_H\rightarrow\pi_L^*)$ and $T_3(n\rightarrow\pi^*)$ minima (**Fig. 18**). Along the interpolated path, $T_3(n\rightarrow\pi^*)$ is lowered in energy by about 0.60 eV while the $S_1(\pi_H\rightarrow\pi_L^*)$ energy rises by 0.54 eV. An intersection between the S_1 and T_3 PESs is found about 0.25 eV above the $S_1(\pi_H\rightarrow\pi_L^*)$

minimum, where ISC is expected to be efficient (due to the linear interpolation this value is an upper limit for the barrier height). Nevertheless, with such energy barrier zero-point motion alone should be insufficient to couple these states. In this framework, ISC to the $T_3(n\rightarrow\pi_L^*)$ without thermal activation might be plausible in the gas phase. From the present results, no $S_1(\pi_H\rightarrow\pi_L^*)$ and $T_3(n\rightarrow\pi^*)$ mechanism for ISC in thionine can be derived. Even if we assume that $T_3(n\rightarrow\pi^*)$ can be reached from $S_1(\pi_H\rightarrow\pi_L^*)$ in the gas phase, the situation changes when solvent effects are taken into account, which will be discussed in the following section.

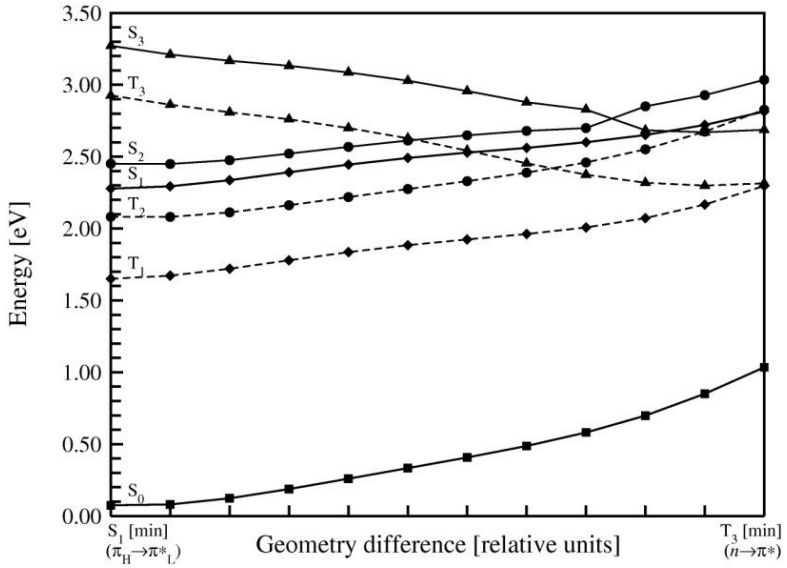

Fig. 18 DFT/MRCI energies of the low-lying states along a linearly interpolated path between the S_1 and T_3 minima of thionine. The singlet profiles are represented by solid lines and the triplet profiles by dashed lines.

5.2.3. Dependence of spin-orbit coupling on molecular structure

ISC rates do not only depend on the energy gap between the involved states but also on the strength of the spin-orbit coupling, which can be estimated quantitatively by the evaluation of the spin-orbit coupling matrix elements (SOMEs). The computed purely electronic SOMEs $\langle i|\hat{H}_{SO}|f\rangle$ at the S_1, S_2 and $T_1(\pi\rightarrow\pi^*)$ minima of thionine are compiled in **Table 7**. The results show that the magnitude of the SOMEs does not change when going from the S_1 to the

$T_1(\pi\rightarrow\pi^*)$ minimum. This is an indication that the SOMEs are relatively insensitive to *in-plane* motions at these minima. According to symmetry selection rules, the $\langle {}^1A_1|\hat{H}_{SO}|{}^3A_1\rangle$ and $\langle {}^1B_1|\hat{H}_{SO}|{}^3B_1\rangle$ ($\pi\rightarrow\pi^*$) transitions are forbidden and hence all the corresponding SOMEs vanish at these C_{2v}-symmetric minima.

Table 7 Spin-orbit matrix elements (SOMEs, cm^{-1}) between low-lying singlet and triplet states at the $S_1(\pi_H\rightarrow\pi_L^*)$, $S_2(\pi_{H-1}\rightarrow\pi_L^*)$ and $T_1(\pi_H\rightarrow\pi_L^*)$ equilibrium geometries. The direction of the coupling *x*, *y* or *z* is given in parenthesis

SOMEs $\langle i\|\hat{H}_{SO}\|f\rangle$	@$S_1(\pi_H\rightarrow\pi_L^*)$	@$S_2(\pi_{H-1}\rightarrow\pi_L^*)$	@$T_1(\pi_H\rightarrow\pi_L^*)$
$\langle S_0\|\hat{H}_{SO}\|T_1(\pi_H\rightarrow\pi_L^*)\rangle$	0.01(*y*)	0.02(*y*)	0.00(*y*)
$\langle S_1(\pi_H\rightarrow\pi_L^*)\|\hat{H}_{SO}\|T_1(\pi_H\rightarrow\pi_L^*)\rangle$	-	0.02(*z*)	-
$\langle S_1(\pi_H\rightarrow\pi_L^*)\|\hat{H}_{SO}\|T_2(\pi_{H-1}\rightarrow\pi_L^*)\rangle$	-0.08(*y*)	0.06(*z*)	-0.09(*y*)
$\langle S_1(\pi_H\rightarrow\pi_L^*)\|\hat{H}_{SO}\|T_3(n\rightarrow\pi_L^*)\rangle$	0.39(*z*)	5.92(*x*) / -1.09(*y*)	-0.42(*z*)
$\langle S_2(\pi_{H-1}\rightarrow\pi_L^*)\|\hat{H}_{SO}\|T_1(\pi_H\rightarrow\pi_L^*)\rangle$	-0.02(*y*)	-0.02(*z*)	-0.02(*y*)
$\langle S_2(\pi_{H-1}\rightarrow\pi_L^*)\|\hat{H}_{SO}\|T_2(\pi_{H-1}\rightarrow\pi_L^*)\rangle$	-	0.05(*z*)	-
$\langle S_2(\pi_{H-1}\rightarrow\pi_L^*)\|\hat{H}_{SO}\|T_3(n\rightarrow\pi_L^*)\rangle$	-9.90(*x*)	-6.88(*x*) / 0.89(*y*)	10.55(*x*)

[a]The $S_1(\pi_H\rightarrow\pi_L^*)$, $T_1(\pi_H\rightarrow\pi_L^*)$ and $T_2(\pi_{H-1}\rightarrow\pi_L^*)$ minima are C_{2v} symmetric and the $S_2(\pi_{H-1}\rightarrow\pi_L^*)$ minimum is C_s symmetric.

At the $S_1(\pi_H\rightarrow\pi_L^*)$ minimum, small coupling matrix elements (≈ 0.4 cm^{-1}) between the $S_1(\pi_H\rightarrow\pi_L^*)$ and $T_3(n\rightarrow\pi_L^*)$ states are found. Following the El-Sayed rules, these small values of the SOMEs are rather unexpected due to the character of the states involved in the transition. Instead, it is found that the coupling at the $S_2(\pi_{H-1}\rightarrow\pi_L^*)/T_3(n\rightarrow\pi_L^*)$ pair is two orders of magnitude larger, up to 9.90 cm^{-1}. These larger SOMEs could be explained due to a heavy-atom effect, in this case the higher probability for the electrons to be at the sulphur center in the molecular orbitals π_{H-1} and n_{H-4} involved in the coupling. In contrast, no electron density is found at the sulphur center in the π_H MO that is decisive for the $S_1(\pi_H\rightarrow\pi_L^*)/T_3(n\rightarrow\pi_L^*)$ interaction (see **Fig. 10**).

The coupling between the low-lying singlet and triplet states follows somewhat different trends at the $S_2(\pi_{H-1}\rightarrow\pi_L^*)$ minimum. The interactions of the $S_1(\pi_H\rightarrow\pi_L^*)$ and $S_2(\pi_{H-1}\rightarrow\pi_L^*)$ states with the $T_3(n\rightarrow\pi_L^*)$ state are nearly of the same magnitude in their *x* and *y* components at this geometry. At this

point, the $S_1(\pi_H \rightarrow \pi_L^*)$ state is composed by an additional contribution of the $\pi_{H-1} \rightarrow \pi_L^*$ transition (nearly 50%). Therefore, the S_1/T_3 coupling significantly increases as a consequence of the larger coupling between the $n \rightarrow \pi_L^*$ with the $\pi_{H-1} \rightarrow \pi_L^*$configurations. As expected, the opposite trend could be found for the coupling between the S_2 and T_3 states.

As noted before, the spin-orbit coupling between the S_1, S_2 and the T_1 and $T_2(\pi \rightarrow \pi^*)$ states is either small or symmetry forbidden. Nevertheless, the population of *out-of-plane* vibrational states can lead to an increase in these couplings. The dependence of the $\langle S_1 | \hat{H}_{SO} | \mathrm{T}_{\{1x,1z,2x,2z\}} \rangle$ SOMEs against displacements along selected A_2 and the B_2 *out-of-plane* vibrational coordinates at the $S_1(\pi_H \rightarrow \pi_L^*)$ minimum are depicted in **Fig. 19**. In addition, the vibrational normal modes and the numerical derivatives of these SOMEs (*∂*SOMEs) are presented in **Fig. 20** and **Table 8**, respectively.

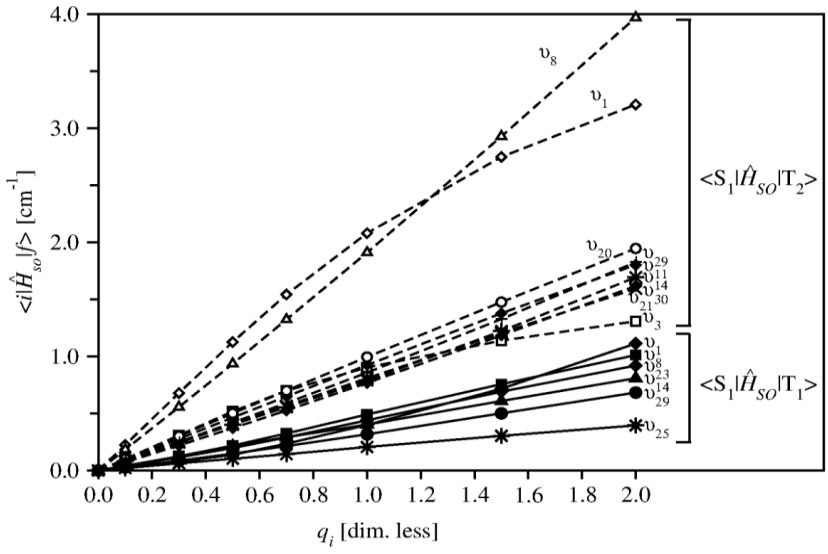

Fig. 19 Change of the SOMEs upon elongation of the *out-of-plane* vibrational normal modes. The SOMEs $\langle S_1 | \hat{H}_{SO} | \mathrm{T}_1 \rangle$ are represented by solid lines and the SOMEs $\langle S_1 | \hat{H}_{SO} | \mathrm{T}_2 \rangle$ by dashed lines

Once the system is distorted along these *out-of-plane* modes, the point group selection rules do not hold and the SOMEs of these $\pi \rightarrow \pi^*$ states could increase to an extent which depends on how the distorted geometry can allow

an efficient interaction with the $n \rightarrow \pi^*$ state. The most important increase in magnitude is obtained for the SOMEs $\langle S_1|\hat{H}_{SO}|T_{2(x,z)}\rangle$ upon the geometry distortions along the v_1 and v_8 normal mode coordinates. The lowest vibrational coupling mode v_1 is of A_2 symmetry, exhibits a frequency of 50.0 cm^{-1}which corresponds to an asymmetric deformation of the phenothiazinium ring and promotes an increase in the $\langle S_1|\hat{H}_{SO}|T_{2x}\rangle$ SOME up to ≈ 3.2 cm^{-1} for a displacement by two unit lengths. The symmetric (B_2) v_8 mode shows up at 263.7 $cm^{-1}$and leads to an increase in the $\langle S_1|\hat{H}_{SO}|T_{2z}\rangle$ matrix element (≈ 4.0 cm^{-1}, see **Fig. 19**). This mode corresponds to a symmetric deformation of the phenothiazinium which includes a pyramidalization of the nitrogen and sulphur atoms of the central ring. Noteworthy, v_1 and v_8 should be considered here as important promoting modes for the $S_1(\pi_H \rightarrow \pi_L^*) \rightsquigarrow T_2(\pi_{H-1} \rightarrow \pi_L^*)$ decay channel since they are able to induce an efficient mixing between *n* and π molecular orbitals. On the contrary, only modest increments of the $\langle S_1|\hat{H}_{SO}|T_{1(x,z)}\rangle$ SOMEs are found along these normal modes (≈ 1 cm^{-1}, see **Fig. 19**).This appears reasonable taking into account that these states possess the same $\pi_H \rightarrow \pi_L^*$ character which is not able to induce an efficient coupling with the $n \rightarrow \pi_L^*$ transition.

Table 8 Harmonic frequencies $\bar{\nu}_i$ (cm^{-1}) of the *out-of-plane* modes and ∂SOMEs with respect to the corresponding dimensionless normal coordinates at the $S_1(\pi_H \rightarrow \pi_L^*)$ minimum. The direction of the coupling *x* or *z* is given in parenthesis

Mode number	$\bar{\nu}_i$	$\frac{\partial\langle S_1\|\hat{H}_{SO}\|T_1\rangle}{\partial q_i}$	$\frac{\partial\langle S_1\|\hat{H}_{SO}\|T_2\rangle}{\partial q_i}$	Mode number	$\bar{\nu}_i$	$\frac{\partial\langle S_1\|\hat{H}_{SO}\|T_1\rangle}{\partial q_i}$	$\frac{\partial\langle S_1\|\hat{H}_{SO}\|T_2\rangle}{\partial q_i}$
$v_1(A_2)$	50.0	-0.27(*z*)	-2.23(*x*)	$v_2(B_2)$	56.2	0.06(*x*)	-0.11(*z*)
$v_3(A_2)$	127.2	-0.18(*z*)	-1.00(*x*)	$v_4(B_2)$	169.2	0.19(*x*)	-0.19(*z*)
$v_5(A_2)$	170.3	0.05(*z*)	0.12(*x*)	$v_7(B_2)$	178.5	0.00(*x*)	0.37(*z*)
$v_{11}(A_2)$	304.2	0.14(*z*)	-0.93(*x*)	$v_8(B_2)$	263.7	0.39(*x*)	-1.84(*z*)
$v_{14}(A_2)$	404.9	-0.41(*z*)	0.84(*x*)	$v_{13}(B_2)$	397.9	-0.06(*x*)	-0.33(*z*)
$v_{17}(A_2)$	477.2	0.01(*z*)	-0.14(*x*)	$v_{18}(B_2)$	477.9	-0.02(*x*)	-0.09(*z*)
$v_{21}(A_2)$	534.0	0.14(*z*)	-0.81(*x*)	$v_{20}(B_2)$	527.0	-0.08(*x*)	1.00(*z*)
$v_{25}(A_2)$	586.6	0.21(*z*)	-0.41(*x*)	$v_{23}(B_2)$	563.7	0.38(*x*)	-0.53(*z*)
$v_{29}(A_2)$	781.4	0.28(*z*)	-0.83(*x*)	$v_{24}(B_2)$	581.8	-0.06(*x*)	0.64(*z*)
$v_{32}(A_2)$	826.4	0.05(*z*)	-0.44(*x*)	$v_{30}(B_2)$	788.5	-0.19(*x*)	0.73(*z*)
$v_{37}(A_2)$	947.7	-0.03(*z*)	0.41(*x*)	$v_{33}(B_2)$	830.1	-0.09(*x*)	0.32(*z*)
				$v_{38}(B_2)$	950.1	-0.06(*x*)	0.12(*z*)

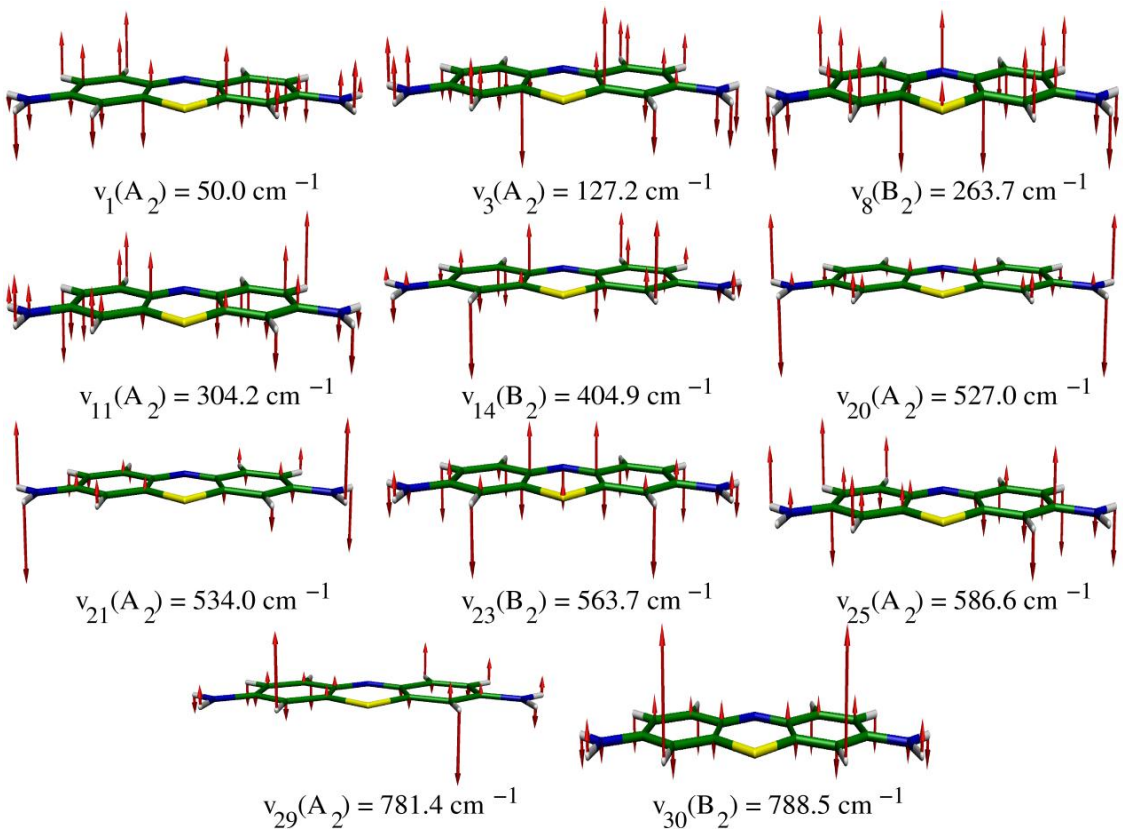

Fig. 20 Important coupling vibrational normal modes at the S_1 ($\pi_H \rightarrow \pi_L^*$) minimum of thionine

The increase in the SOMEs along the vibrational mode coordinates shown in **Fig. 19** is seen to be mostly linear. Only few deviations from the linearity are noticeable, in particular for the $\langle S_1|\hat{H}_{SO}|T_{2x}\rangle$ coupling along the ν_1 and ν_3 A_2 normal modes. This has consequences for the magnitude of the calculated ∂SOMEs for the coupling of the S_1 and $T_2(\pi \rightarrow \pi^*)$ states in the x and z components: the ∂SOMEs along the ν_1 A_2 mode (2.23 cm^{-1}) is larger than that obtained at the ν_8 mode (1.84 cm^{-1}) in opposition to the trend observed in **Fig. 19**. In addition, substantial contributions to the $S_1/T_2(\pi \rightarrow \pi^*)$ vibronic spin-orbit coupling originating from ν_3, ν_{11}, ν_{14}, ν_{20}, ν_{21}, and ν_{30} normal modes are obtained.

5.2.4. ISC channels: Rate constants calculated using the time-independent approach

5.2.4.1. Vacuum

The results of the {$S_1(\pi\rightarrow\pi^*) \rightsquigarrow T_1,T_2(\pi\rightarrow\pi^*)$} ISC rate constants obtained from time-independent formulation for the golden rule and taking vibronic spin-orbit coupling into account are presented in **Table 9**, together with the parameters employed for the calculation of these rates. Our results clearly show sizeable rate constants for the ISC from the zero vibrational level of the $S_1(\pi_H\rightarrow\pi_L^*)$ to the vibrational levels of the T_{2x} and $T_{2z}(\pi_{H-1}\rightarrow\pi_L^*)$ substates, being of the order of $k_{ISC}^{TI} \approx 10^8$ s^{-1}. These rate constants are of the same order of magnitude than the fluorescence decay ($k_F \approx 1.66 \times 10^8$ s^{-1}). In contrast, the ISC to the $T_1(\pi_H\rightarrow\pi_L^*)$ state is found to be much slower ($k_{ISC}^{TI} \approx 10^5$ - 10^6 s^{-1}). According to these results, the $S_1(\pi_H\rightarrow\pi_L^*) \rightsquigarrow T_2(\pi_{H-1}\rightarrow\pi_L^*)$ ISC is proposed as the main responsible channel for the efficient population of the triplet manifold. The participation of the v_1 and v_8 vibrational normal modes as important promoting modes can be quantitatively observed by accounting for the ∂SOMEs of these individual modes only in the calculation of the ISC rate (see **Table 9**). Their contribution to the rate constant are of the order of ≈ 10^8 and ≈ 10^7 s^{-1}, respectively. Moreover, this channel benefits from a crossing between the $S_1(\pi_H\rightarrow\pi_L^*)$ and $T_2(\pi_{H-1}\rightarrow\pi_L^*)$ PESs along a linearly interpolated path connecting the corresponding minima (see **Fig. 21**), increasing the overlap between the vibrational wavefunctions of the $S_1(\pi_H\rightarrow\pi_L^*) \rightsquigarrow T_2(\pi_{H-1}\rightarrow\pi_L^*)$ channel.

It is worth mentioning that the magnitude of the rate constants depends on the number of vibrational levels and *in-plane* accepting modes that is accounted for in the calculation. For example, including only the 25 A_1 accepting modes in the rate computation results in k_{ISC}^{TI} ($S_1 \rightsquigarrow T_1$) ≈ 10^3 s^{-1}, whereas an extension of the accepting modes to include the B_1 *in-plane* modes enhances the rate by two orders of magnitude, i.e., to $k_{ISC}^{TI} \approx 10^5$ s^{-1}.

For the $S_1(\pi\rightarrow\pi^*) \rightsquigarrow T_2(\pi\rightarrow\pi^*)$ channel, an increase by a factor of three is obtained in this case. A further enhancement by a factor of two is observed when all 72 vibrational modes are accounted for. This behavior could be explained due to combination of two asymmetric modes that could result in a totally symmetric A_1 mode. Furthermore, test calculations showed that the calculated ISC rate constants are quite sensitive to the S_1-T_2 energy gap. Therefore, the calculated k_{ISC}^{TI} ($S_1 \rightsquigarrow T_2$) values can be considered only are rough estimates.

Table 9 Calculated rate constants $k_{ISC}^{TI}(s^{-1})$ in vacuum for the $S_1 \rightsquigarrow T_{i(x,z)}$($i$ = 1,2) channels. Other columns: adiabatic energy difference (ΔE^{ad}, eV),number of derivatives with respect of *out-of-plane* modes ($\#_{derivs}$), number of accepting modes ($\#_{acc}$), width of the search interval η = 0.1 cm^{-1}) and number of final state vibrational levels within the search interval ($\#_{v'}$)

Channel	ΔE^{ad}	$\#_{derivs}$	$\#_{acc}$	$\#_{v'}$	k_{ISC}^{TI}
$S_1 \rightsquigarrow T_{1x}$	0.64	12	25	6×10^4	2.73×10^3
$S_1 \rightsquigarrow T_{1x}$	0.64	12	49	3×10^6	2.40×10^5
$S_1 \rightsquigarrow T_{1x}$	0.68[a]	12	49	7×10^6	3.06×10^5
$S_1 \rightsquigarrow T_{1z}$	0.64	11	25	4×10^4	3.62×10^3
$S_1 \rightsquigarrow T_{1z}$	0.64	11	49	2×10^6	2.14×10^5
$S_1 \rightsquigarrow T_{1z}$	0.68[a]	11	49	5×10^6	1.27×10^6
$S_1 \rightsquigarrow T_{2x}$	0.30	11	49	5×10^3	1.55×10^8
$S_1 \rightsquigarrow T_{2x}$	0.30	1[b]	49	5×10^3	1.28×10^8
$S_1 \rightsquigarrow T_{2x}$	0.21[a]	11	49	7×10^2	1.29×10^9
$S_1 \rightsquigarrow T_{2z}$	0.30	12	25	4×10^2	1.93×10^7
$S_1 \rightsquigarrow T_{2z}$	0.30	12	49	4×10^3	6.30×10^7
$S_1 \rightsquigarrow T_{2z}$	0.30	12	72	1×10^5	1.39×10^8
$S_1 \rightsquigarrow T_{2z}$	0.30	1[c]	49	4×10^3	1.48×10^7
$S_1 \rightsquigarrow T_{2z}$	0.21[a]	12	49	6×10^2	3.72×10^6

Rate constants calculated: applying spectroscopic solvation shifts from model [a]TH^+3Wa; including only the [b]mode v_1 and [c]mode v_8 cm^{-1}.

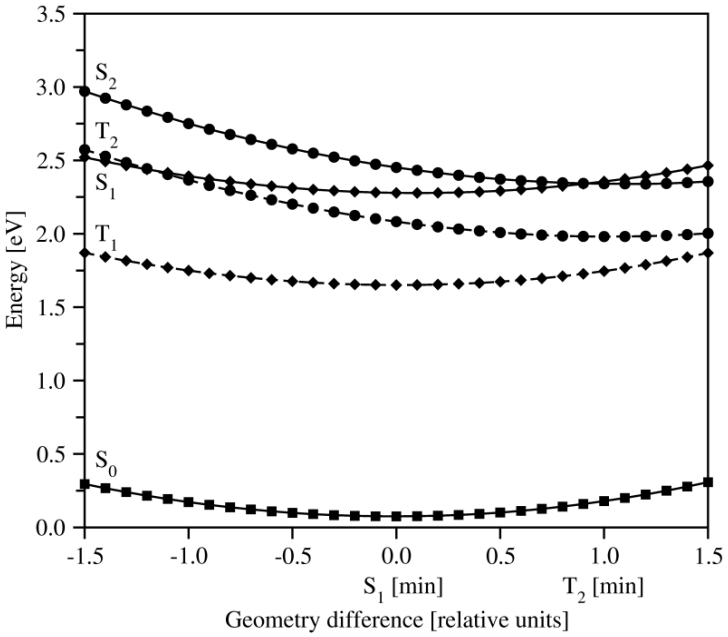

Fig. 21 Thionine DFT/MRCI energies of the low-lying states along a linearly interpolated path between the $S_1(\pi_H \rightarrow \pi_L^*)$ and $T_2(\pi_{H-1} \rightarrow \pi_L^*)$ minima. The singlet profiles are represented by solid lines and the triplet profiles by dashed lines.

To gain further insight, the $\{S_2(\pi_{H-1} \rightarrow \pi_L^*) \rightsquigarrow T_1(\pi_H \rightarrow \pi_L^*), T_2(\pi_{H-1} \rightarrow \pi_L^*)\}$ channels have also been analyzed. The rate constants characterizing these transitions are presented in **Table 10**. As aforementioned, the dark $S_2(\pi_{H-1} \rightarrow \pi_L^*)$ state may possibly be populated after vertical excitation to the $S_1(\pi_H \rightarrow \pi_L^*)$ state ($\Delta E = 0.20$ eV) via a conical intersection and $S_1(\pi_H \rightarrow \pi_L^*)$ - $S_2(\pi_{H-1} \rightarrow \pi_L^*)$ character mixing. However, with an ISC rate constant of the order of $k_{ISC}^{TI} \approx 10^6$ s^{-1}, these channels cannot compete with the relaxation channel involving the $S_1(\pi_H \rightarrow \pi_L^*)$ state.

The golden rule approach (see Section **2.5.2.4**) assumes that at sufficiently high adiabatic energy gaps between initial and final vibronic states, the final vibrational levels form a quasi-continuum. In this case, the (isoenergetic) transfer to the final state is irreversible on time scales accessible to experiment. Instead of treating a strictly isoenergetic transition, an interval of final states is considered in **Eq 75**, taking into account all final states within ±η of the vibronic energy of the initial level. Therefore, the results depend on the choice of η and there is no unique choice for this parameter. On the one

hand, η should be chosen as small as possible, because the transition $i \rightarrow f$ should be isoenergetic. On the other hand, η should be chosen large enough to cover a sufficient number of acceptor states. We therefore tested a number of different η values in order to find a value that is as small as possible, while still yielding numerically stable and therefore meaningful results. The results regarding these tests can be found as Supplementary Information (SI, Section **5.4**). The computed data show that as η increases, the ISC rate constants also substantially increase. the We found that η values of 0.1 and 1 cm^{-1} are adequate for the calculation of the ISC rate constants in this system.

Table 10 Calculated rate constants $k_{ISC}^{TI}(s^{-1})$ in vacuum for the $S_2 \rightsquigarrow T_{i(x,z)}$($i$ = 1,2) channels. Other columns: adiabatic energy difference (ΔE^{ad}, eV),number of derivatives with respect of *out-of-plane* modes ($\#_{derivs}$), number of accepting modes ($\#_{acc}$), width of the search interval η (cm^{-1}) and number of final state vibrational levels within the search interval ($\#_{v'}$)

Channel	ΔE^{ad}	$\#_{derivs}$	$\#_{acc}$	η	$\#_{v'}$	k_{ISC}^{TI}
$S_2 \rightsquigarrow T_{1x}$	0.66	23	49	0.1	2×10^4	5.71×10^6
$S_2 \rightsquigarrow T_{1y}$	0.66	23	49	0.1	2×10^4	4.02×10^6
$S_2 \rightsquigarrow T_{1y}$	0.66	23	49	1	2×10^5	8.63×10^6
$S_2 \rightsquigarrow T_{2x}$	0.32	23	49	0.1	41	5.14×10^5
$S_2 \rightsquigarrow T_{2x}$	0.32	23	49	1	4×10^2	7.40×10^6
$S_2 \rightsquigarrow T_{2y}$	0.32	23	49	0.1	41	9.43×10^4
$S_2 \rightsquigarrow T_{2y}$	0.32	23	49	1	4×10^2	2.68×10^5

5.2.4.2. Hydration effects on ISC

In the following we present a qualitative discussion of the various possible decay channels available to the chromophore in aqueous solution. For this purpose an estimate of the adiabatic excitation energies is obtained by applying solvent shifts to the individual electronic states using **Eq 92** and **Eq 93** (**Table 6**). The employed solvent shifts correspond to our best model TH^+3Wa. As is expected, the $T_3(n \rightarrow \pi_L^*)$ adiabatic excitation energy is strongly blueshifted to 2.75 eV, resulting in an adiabatic energy difference of 0.61 eV to the optically bright state in aqueous medium as compared to

0.04 eV in vacuum. As a consequence, the participation of any ISC channel involving the $T_3(n\rightarrow\pi_L^*)$ state in the photophysics of thionine in water can safely be ruled out.

The adiabatic excitation energies of the two low-lying triplet and singlet ($\pi\rightarrow\pi^*$) states experience very small redshifts. The adiabatic energy separation of the S_1 and $T_1(\pi\rightarrow\pi^*)$ states ($\Delta E^{ad}(S_1\rightarrow T_1)$ = 0.68 eV) is quite similar to the one calculated in the gas phase. As a consequence, the calculated $S_1(\pi_H\rightarrow\pi_L^*)$ ⇝ $T_1(\pi_H\rightarrow\pi_L^*)$ ISC rate constants in water are also very similar to those found in vacuum ($k_{ISC}^{TI}(S_1\rightarrow T_1) \approx 10^5$ - 10^6 s^{-1}, see **Table 9**. In contrast, the $\Delta E^{ad}(S_1\rightarrow T_2)$ gap is decreased from 0.30 eV in vacuum to 0.21 eV in our water model. This accelerates the $S_1(\pi_H\rightarrow\pi_L^*)$ ⇝ $T_{2x}(\pi_{H-1}\rightarrow\pi_L^*)$ transition while reducing the efficiency of the $S_1(\pi_H\rightarrow\pi_L^*)$ ⇝ $T_{2z}(\pi_{H-1}\rightarrow\pi_L^*)$ channel by one order of magnitude. As the total rate is the sum over the contributions of all channels, all-in-all the ISC rate is enhanced due to solvation. With a sufficient number of vibrational states within the search interval (η = 0.1) and 49 coupling accepting modes involved, a rate of $k_{ISC}^{TI} \approx 10^9$ s^{-1} is obtained which is in very good agreement with the experimental value of $k_{ISC} = 2.8 \times 10^9$ s^{-1} in aqueous solution.[171] Moreover, these results show that the $S_1(\pi_H\rightarrow\pi_L^*)$ ⇝ $T_2(\pi_{H-1}\rightarrow\pi_L^*)$ channel should be considered as the main efficient channel for population transfer into the triplet manifold (ϕ_T = 0.55). It thus may efficiently quench the fluorescence of the $S_1(\pi_H\rightarrow\pi_L^*)$ state ($k_F \approx 1.31 \times 10^8$ s^{-1}) in aqueous solution which is evidenced by its smaller experimental quantum yield ($\phi_F \approx$ 0.1 - 0.027). It should be kept in mind that many factors affect the rate constant, *e. g.* the thermodynamics of the water molecules including the geometrical relaxation of the excited states and their participation in the spin-orbit coupling. However, within the limitations of the computational models used, the qualitative picture obtained is in very good accord with the experimental data, validating the results thus obtained.

5.2.5. ISC rate constants calculated using the time-dependent approach

The calculated ISC rate constants for the {$S_1(\pi\rightarrow\pi^*) \rightsquigarrow T_1,T_2(\pi\rightarrow\pi^*)$} channels obtained from the time-dependent spin-vibronic formulation of the golden rule are listed in **Table 11**, together with the parameters employed for the calculation of these rates (see Section **2.5.2.5**). More data about the dependency of the ISC rate constants upon technical parameters can be found in the SI (Section **5.4**). It is found that when a small number for damping function (*e. g.* $\eta = 0.1\ cm^{-1}$) is used for the calculation of the ISC rate constants, the time correlation function need a very large time interval for convergence (> 30000 fs). When a larger value of η is accounted, the time interval needed for the convergence is also shorter which significantly speeds up the calculation. The ISC rate constants displayed in **Table 11** show the variation of the rate constants when increasing the η value for 1, 10, 100 and 1000 cm^{-1} within the time interval 0 - 30000 fs. For this system, we found that the damping does not significantly influence the ISC rates. Moreover, we observed that once the time correlation function have converged (which means that the time interval is large enough for the integration) within a fixed η value, the ISC rate constant is exactly the same upon increasing the time interval (see **Table 20** at Section **5.4**).

We found good agreement with the previously calculated rate constants using the time-independent approach (**Table 9**) in vacuum and taking into account the hydration effects to the adiabatic energy gap (**Table 11**). The k_{ISC}^{TD} obtained in vacuum are slightly higher than the k_{ISC}^{TI}. In this comparison, it has to be taken into account that in the time-independent approach restrictions had to be made with respect to the number of promoting and accepting modes and to the maximal number of quanta (*e. g.* when all modes were included as accepting modes). These restrictions are not necessary when using the time-dependent approach. With regard to the computation times, considerable advantages are observed using the time-dependent formalism

over the time-independent method particularly for those cases where the final density of states is large. These are the instances when the adiabatic energy gap *e. g.* the $S_1 \rightsquigarrow T_1$ channel. The k_{ISC}^{TI} listed in **Table 9** show a strong direct dependency on the number of accepting modes accounted for the calculation. As the k_{ISC}^{TD} rates shown in **Table 9** include all vibrational modes as accepting modes, it is understandable that these rates show slightly higher magnitudes. Moreover, the mixed direct-vibronic terms which are also accounted in the calculation of the k_{ISC}^{TD} which can also contribute to enhance the rate constants in some extent (see Section **2.5.2.5**).

Table 11 Calculated rate constants $k_{ISC}^{TD}(s^{-1})$ of thionine for the $S_1 \rightsquigarrow T_i$ (i = 1,2) channels within the time-dependent approach. Other columns: adiabatic energy difference (ΔE^{ad}, eV), time interval (30000 fs), number of points (900000) and damping factor (η, cm^{-1})

Channel	ΔE^{ad}	η	k_{ISC}^{TD},
$S_1 \rightsquigarrow T_1$	0.64	1	3.40×10^6
$S_1 \rightsquigarrow T_1$	0.64	10	3.57×10^6
$S_1 \rightsquigarrow T_1$	0.64	100	3.36×10^6
$S_1 \rightsquigarrow T_1$	0.64	1000	3.06×10^6
$S_1 \rightsquigarrow T_1$	0.68[a]	0.10	6.43×10^6
$S_1 \rightsquigarrow T_1$	0.68[a]	1	3.54×10^6
$S_1 \rightsquigarrow T_1$	0.68[a]	10	2.52×10^6
$S_1 \rightsquigarrow T_1$	0.68[a]	100	1.91×10^6
$S_1 \rightsquigarrow T_1$	0.68[a]	1000	2.27×10^6
$S_1 \rightsquigarrow T_2$	0.30	0.10	7.26×10^8
$S_1 \rightsquigarrow T_2$	0.30	1	6.45×10^8
$S_1 \rightsquigarrow T_2$	0.30	10	7.59×10^8
$S_1 \rightsquigarrow T_2$	0.30	100	7.83×10^8
$S_1 \rightsquigarrow T_2$	0.30	1000	9.42×10^8
$S_1 \rightsquigarrow T_2$	0.21[a]	0.10	1.07×10^9
$S_1 \rightsquigarrow T_2$	0.21[a]	1	1.07×10^9
$S_1 \rightsquigarrow T_2$	0.21[a]	10	1.07×10^9
$S_1 \rightsquigarrow T_2$	0.21[a]	100	1.09×10^9
$S_1 \rightsquigarrow T_2$	0.21[a]	1000	1.36×10^9

[a]Rate constants calculated: applying spectroscopic solvation shifts from models TH^+3Wa

5.2.6. Phosphorescence

In addition to energy transfer to $^3O_2$ and photo-redox reactions, the decay of the triplet excited state of thionine could include radiative or non-radiative

relaxation processes. The radiative depopulation of the $T_1(\pi_H \rightarrow \pi_L^*)$ state to the ground state could result in phosphorescence which, however, in the case of thionine has never been observed. In order to check the consistency of our calculations with these findings, we calculated the $T_1(\pi_H \rightarrow \pi_L^*) \rightarrow S_0$ phosphorescence rates ($\Gamma_{1,\zeta}$), which are presented in Table 5. Since, the $T_{1,a}$, $T_{1,b}$ and $T_{1,c}$ sublevels are degenerate, it can be assumed that each level is equally populated (high temperature average). The computed MRSOCI electronic transition dipole moments are all nearly zero, leading to very slow phosphorescence (from zero to 10^{-1} s^{-1}), which is common for a radiative decay originating from "pure" $\pi \rightarrow \pi^*$ states.[219] The phosphorescence lifetime ($\tau_{P,\zeta}$) calculated from the averaged transition rate constants is very large (≈ 4500 s) verifying the experimentally non-observed phosphorescence.

Table 12 Vertical excitation energies ($^{\Delta E_{S_0 \leftarrow T_{1,\zeta}}}$,cm-1), transition dipole moments ($\mu_{el}(S_0 \leftarrow T_{1,\zeta})$, a.u.), phosphorescence rates ($\Gamma_{1,\zeta}$, s^{-1}) and radiative lifetimes ($\tau_{P,\zeta}$, s) for the three fine-structure sublevels of the $T_1(\pi_H \rightarrow \pi_L^*)$ state. The polarization direction of $\mu_{el}(S_0 \leftarrow T_{1,\zeta})$ is given in parenthesis

Sublevel	$\Delta E_{S_0 \leftarrow T_{1,\zeta}}$	$\lvert\mu_{el}(S_0 \leftarrow T_{1,\zeta})\rvert$	$\Gamma_{1,\zeta}$	$\tau_{P,\zeta}$
$T_{1,a}$	12524.1	$4.30 \times 10^{-6}(z)$	7.36×10^{-5}	1.36×10^{4}
$T_{1,b}$	12524.1	-	-	-
$T_{1,c}$	12524.1	$2.24 \times 10^{-4}(y)$	2.00×10^{-1}	5.01
	High temperature average		6.66×10^{-2}	4.53×10^{3}

5.3. Conclusions

We have examined the molecular and electronic structures of the lowest excited electronic states of monocationic thionine (TH^+) using a combination of (time dependent) density functional theory and a density functional theory based multi reference CI method. We found the lowest two singlet and triplet states to be of $\pi\rightarrow\pi^*$ character, S_1 being the spectroscopically bright state. The third singlet and triplet states both have $n\rightarrow\pi^*$ character. Our estimated fluorescence rate from S_1 is low, in agreement with the experimental value.

Locating the minima of the S_3 and T_3 $n\rightarrow\pi^*$ states turned out to be difficult and we have only been able to locate the minimum of the T_3 state. This minimum has a non-planar structure with an energy which is only 0.04 eV above the adiabatic energy of S_1 $\pi_H\rightarrow\pi_L^*$ minimum. Furthermore, at the T_3 $n\rightarrow\pi^*$ minimum, T_3 is nearly degenerate with T_1 $\pi_H\rightarrow\pi_L^*$, so we expect a conical intersection between T_3 and T_1 very close to the T_3 minimum.

Effects of water solvent were taken into account using the COSMO solvation model and microsolvation with up to five water molecules. The vertical excitation energy calculated with these models is in excellent agreement with the experimental value. The effects of the water environment on the $\pi\rightarrow\pi^*$ states are moderate, but the $n\rightarrow\pi^*$ states are shifted up in energy by several tenths of eV.

Irradiation of thionine with visible light will populate primarily the first excited singlet state $S_1(\pi_H\rightarrow\pi_L^*)$. At the $S_1(\pi_H\rightarrow\pi_L^*)$ minimum only the first two triplet states T_1 and $T_2(\pi\rightarrow\pi^*)$ are energetically accessible. Their electronic spin-orbit coupling matrix elements with the $S_1(\pi_H\rightarrow\pi_L^*)$ state nearly vanish. Since the direct spin-orbit coupling does not explain the high triplet quantum yield in this system, we focused on the ISC driven by vibronic spin-orbit coupling.

In vacuum, the $S_1(\pi_H\rightarrow\pi_L^*) \rightsquigarrow T_2(\pi_{H-1}\rightarrow\pi_L^*)$ ISC channel was found to efficiently proceed with an ISC rate constant of $k_{ISC} \approx 3 \times 10^8\ s^{-1}$, well able to

compete with fluorescence from the $S_1(\pi_H \rightarrow \pi_L^*)$ state ($k_F \approx 2 \times 10^8\ s^{-1}$). The $S_1(\pi_H \rightarrow \pi_L^*) \rightsquigarrow T_1(\pi_H \rightarrow \pi_L^*)$ ISC channel was estimated to be less efficient ($k_{ISC} \approx 10^5$ - $10^6\ s^{-1}$). The higher efficiency of the $S_1(\pi_H \rightarrow \pi_L^*) \rightsquigarrow T_2(\pi_{H-1} \rightarrow \pi_L^*)$ ISC channel originates on the one hand due to a more pronounced vibronic spin-orbit coupling, arising from the presence of the high electron density at the sulphur center in the π_{H-1} molecular orbital. This in turn induces a more effective mixing with the *n* molecular orbital upon elongations along certain *out-of-plane* vibrational normal modes. On the other hand, the accessibility of this channel is promoted by more favorable FC factors, evidenced by the presence of a crossing between the S_1 and $T_2(\pi \rightarrow \pi^*)$ states. Due to the near degeneracy of the adiabatic $S_1(\pi_H \rightarrow \pi_L^*)$ and $S_2(\pi_{H-1} \rightarrow \pi_L^*)$ minima and the nearby barrierless conical intersection, a small population of the dark $S_2(\pi_{H-1} \rightarrow \pi_L^*)$ state might be thought to be plausible. However, transitions starting out from the $S_2(\pi_{H-1} \rightarrow \pi_L^*)$ to the T_1 and $T_2(\pi \rightarrow \pi^*)$ states are not realistic candidates for efficient ISC channels as the calculated rates are of the order of $k_{ISC} \approx 10^6\ s^{-1}$.

The effect of water as solvent on the ISC rates was also studied. Hydration effects were estimated by applying the calculated vertical spectroscopic shifts to the adiabatic energies of the excited states in vacuum. Based on our results, we propose that the efficient triplet quantum yield of thionine in water is primarily caused by the $S_1(\pi_H \rightarrow \pi_L^*) \rightsquigarrow T_2(\pi_{H-1} \rightarrow \pi_L^*)$ channel with a computed rate constant of the order of $k_{ISC} \approx 10^8$ - $10^9\ s^{-1}$ which agrees well with the experimental finding ($k_{ISC} = 2.8 \times 10^9\ s^{-1}$). The ratio of the calculated ISC rate constant $k_{ISC} \approx 10^9\ s^{-1}$ to the fluorescence rate constant which is of the order of $k_F \approx 10^8\ s^{-1}$ is also consistent with the measured lower fluorescence ($\phi_F \approx 0.1$ - 0.027) and sizeable triplet quantum yields ($\phi_T = 0.55$) in water. We can therefore conclude that the experimentally observed triplet quantum yield is mainly due to the $S_1(\pi_H \rightarrow \pi_L^*) \rightsquigarrow T_2(\pi_{H-1} \rightarrow \pi_L^*)$ ISC channel which is driven by vibronic spin-orbit coupling.

5.4. Supplementary information

Table 13 Thionine: calculated rate constants k_{ISC}^{TI} for the $S_1 \rightsquigarrow T_{1x}$ channel. Remaining columns: adiabatic energy difference ΔE^{ad}, number of derivatives with respect of *out-of-plane* modes ($\#_{derivs}$), width of the search interval η, number of accepting modes within the search interval ($\#_{acc}$) and number of final state vibrational levels within the search interval ($\#_{v'}$).

Channel	ΔE^{ad}/eV	$\#_{derivs}$	$\#_{acc}$	η/cm^{-1}	$\#_{v'}$	k_{ISC}^{TI} /s^{-1}
$S_1 \rightsquigarrow T_{1x}$	0.64	12	25	0.001	5×10^2	1.07×10^0
$S_1 \rightsquigarrow T_{1x}$	0.64	12	25	0.01	6×10^3	4.43×10^1
$S_1 \rightsquigarrow T_{1x}$	0.64	12	25	0.1	6×10^4	2.73×10^3
$S_1 \rightsquigarrow T_{1x}$	0.64	12	25	1	6×10^5	1.96×10^3
$S_1 \rightsquigarrow T_{1x}$	0.64	12	25	10	6×10^6	2.57×10^3
$S_1 \rightsquigarrow T_{1x}$	0.64	12	25	100	6×10^7	3.28×10^3
$S_1 \rightsquigarrow T_{1x}$	0.64	12	49	0.001	3×10^4	2.75×10^3
$S_1 \rightsquigarrow T_{1x}$	0.64	12	49	0.01	3×10^5	3.36×10^5
$S_1 \rightsquigarrow T_{1x}$	0.64	12	49	0.1	3×10^6	2.40×10^5
$S_1 \rightsquigarrow T_{1x}$	0.64	12	49	1	3×10^7	3.63×10^5
$S_1 \rightsquigarrow T_{1x}$	0.64	12	49	10	1×10^8	7.51×10^5

Table 14 Thionine: Calculated rate constants k_{ISC}^{TI} for the $S_1 \rightarrow T_{1z}$ channel. Remaining columns: adiabatic energy difference ΔE^{ad}, number of derivatives with respect of *out-of-plane* modes ($\#_{derivs}$), width of the search interval η, number of accepting modes within the search interval ($\#_{acc}$) and number of final state vibrational levels within the search interval ($\#_{v'}$).

Channel	ΔE^{ad}/eV	$\#_{derivs}$	$\#_{acc}$	η/cm^{-1}	$\#_{v'}$	k_{ISC}^{TI} /s^{-1}
$S_1 \rightsquigarrow T_{1z}$	0.64	11	25	0.001	4×10^2	1.66×10^1
$S_1 \rightsquigarrow T_{1z}$	0.64	11	25	0.01	4×10^3	1.27×10^2
$S_1 \rightsquigarrow T_{1z}$	0.64	11	25	0.1	4×10^4	3.62×10^3
$S_1 \rightsquigarrow T_{1z}$	0.64	11	25	1	4×10^5	5.10×10^3
$S_1 \rightsquigarrow T_{1z}$	0.64	11	25	10	4×10^6	3.96×10^3
$S_1 \rightsquigarrow T_{1z}$	0.64	11	25	100	4×10^7	4.31×10^3
$S_1 \rightsquigarrow T_{1z}$	0.64	11	49	0.001	2×10^4	4.51×10^4
$S_1 \rightsquigarrow T_{1z}$	0.64	11	49	0.01	2×10^5	1.98×10^5
$S_1 \rightsquigarrow T_{1z}$	0.64	11	49	0.1	2×10^6	2.14×10^5
$S_1 \rightsquigarrow T_{1z}$	0.64	11	49	1	2×10^7	4.15×10^6
$S_1 \rightsquigarrow T_{1z}$	0.64	11	49	10	1×10^7	1.56×10^5

Table 15 Thionine: Calculated rate constants k_{ISC}^{TI} for the $S_1 \rightarrow T_{2x}$ channel. Remaining columns: adiabatic energy difference ΔE^{ad}, number of derivatives with respect of *out-of-plane* modes ($\#_{derivs}$), width of the search interval η, number of accepting modes within the search interval ($\#_{acc}$) and number of final state vibrational levels within the search interval ($\#_{v'}$).

Channel	ΔE^{ad}/eV	$\#_{derivs}$	$\#_{acc}$	η/cm^{-1}	$\#_{v'}$	k_{ISC}^{TI} /s^{-1}
$S_1 \rightsquigarrow T_{2x}$	0.30	11	25	0.001	6	2.27×10^6
$S_1 \rightsquigarrow T_{2x}$	0.30	11	25	0.01	33	1.50×10^8
$S_1 \rightsquigarrow T_{2x}$	0.30	11	25	0.1	3×10^2	9.73×10^7
$S_1 \rightsquigarrow T_{2x}$	0.30	11	25	1	3×10^3	1.03×10^8
$S_1 \rightsquigarrow T_{2x}$	0.30	11	25	10	3×10^4	1.28×10^8
$S_1 \rightsquigarrow T_{2x}$	0.30	11	25	100	3×10^5	1.40×10^8
$S_1 \rightsquigarrow T_{2x}$	0.30	11	49	0.001	42	4.86×10^7
$S_1 \rightsquigarrow T_{2x}$	0.30	11	49	0.01	5×10^2	1.96×10^8
$S_1 \rightsquigarrow T_{2x}$	0.30	11	49	0.1	5×10^3	1.55×10^8
$S_1 \rightsquigarrow T_{2x}$	0.30	11	49	1	5×10^4	2.81×10^8
$S_1 \rightsquigarrow T_{2x}$	0.30	11	49	10	5×10^5	2.79×10^8
$S_1 \rightsquigarrow T_{2x}$	0.30	11	49	100	5×10^6	2.94×10^8
$S_1 \rightsquigarrow T_{2x}$	0.30	11	72	0.001	9×10^3	5.16×10^7
$S_1 \rightsquigarrow T_{2x}$	0.30	11	72	0.01	9×10^4	2.06×10^8
$S_1 \rightsquigarrow T_{2x}$	0.30	11	72	0.1	9×10^5	1.89×10^8
$S_1 \rightsquigarrow T_{2x}$	0.30	11	72	1	9×10^6	3.13×10^8
$S_1 \rightsquigarrow T_{2x}$	0.30	11	72	10	2×10^7	3.07×10^8
$S_1 \rightsquigarrow T_{2x}$	0.30	11	72	100	2×10^8	3.23×10^8
$S_1 \rightsquigarrow T_{2x}$	0.30	1 (ν_1)	25	0.001	6	4.69×10^5
$S_1 \rightsquigarrow T_{2x}$	0.30	1 (ν_1)	25	0.01	33	3.51×10^7
$S_1 \rightsquigarrow T_{2x}$	0.30	1 (ν_1)	25	0.1	3×10^2	9.52×10^7
$S_1 \rightsquigarrow T_{2x}$	0.30	1 (ν_1)	25	1	3×10^3	3.11×10^7
$S_1 \rightsquigarrow T_{2x}$	0.30	1 (ν_1)	25	10	3×10^4	4.00×10^7
$S_1 \rightsquigarrow T_{2x}$	0.30	1 (ν_1)	25	100	3×10^5	5.10×10^7
$S_1 \rightsquigarrow T_{2x}$	0.30	1 (ν_1)	49	0.001	42	1.46×10^7
$S_1 \rightsquigarrow T_{2x}$	0.30	1 (ν_1)	49	0.01	5×10^2	1.24×10^8
$S_1 \rightsquigarrow T_{2x}$	0.30	1 (ν_1)	49	0.1	5×10^3	1.28×10^8
$S_1 \rightsquigarrow T_{2x}$	0.30	1 (ν_1)	49	1	5×10^4	1.44×10^8
$S_1 \rightsquigarrow T_{2x}$	0.30	1 (ν_1)	49	10	5×10^5	1.04×10^8
$S_1 \rightsquigarrow T_{2x}$	0.30	1 (ν_1)	49	100	5×10^6	1.12×10^8
$S_1 \rightsquigarrow T_{2x}$	0.30	1 (ν_1)	72	0.001	9×10^3	1.59×10^7
$S_1 \rightsquigarrow T_{2x}$	0.30	1 (ν_1)	72	0.01	9×10^4	1.30×10^8
$S_1 \rightsquigarrow T_{2x}$	0.30	1 (ν_1)	72	0.1	9×10^5	1.43×10^8
$S_1 \rightsquigarrow T_{2x}$	0.30	6	25	0.001	6	2.30×10^6
$S_1 \rightsquigarrow T_{2x}$	0.30	6	25	0.01	33	1.53×10^8
$S_1 \rightsquigarrow T_{2x}$	0.30	6	25	0.1	3×10^2	1.07×10^8
$S_1 \rightsquigarrow T_{2x}$	0.30	6	25	1	3×10^3	9.81×10^7
$S_1 \rightsquigarrow T_{2x}$	0.30	6	25	10	3×10^4	1.26×10^8
$S_1 \rightsquigarrow T_{2x}$	0.30	6	25	100	3×10^5	1.26×10^8
$S_1 \rightsquigarrow T_{2x}$	0.30	6	49	0.001	42	4.72×10^7
$S_1 \rightsquigarrow T_{2x}$	0.30	6	49	0.01	5×10^2	1.88×10^8
$S_1 \rightsquigarrow T_{2x}$	0.30	6	49	0.1	5×10^3	1.62×10^8
$S_1 \rightsquigarrow T_{2x}$	0.30	6	49	1	5×10^4	2.76×10^8
$S_1 \rightsquigarrow T_{2x}$	0.30	6	49	10	5×10^5	2.72×10^8
$S_1 \rightsquigarrow T_{2x}$	0.30	6	49	100	5×10^6	2.73×10^8

Table 16 Thionine: Calculated rate constants k_{ISC}^{TI} for the $S_1 \rightarrow T_{2z}$ channel. Remaining columns: adiabatic energy difference ΔE^{ad}, number of derivatives with respect of *out-of-plane* modes ($\#_{derivs}$), width of the search interval η, number of accepting modes within the search interval ($\#_{acc}$) and number of final state vibrational levels within the search interval ($\#_{v'}$).

Channel	ΔE^{ad}/eV	$\#_{derivs}$	$\#_{acc}$	η/cm^{-1}	$\#_{v'}$	k_{ISC}^{TI} /s^{-1}
$S_1 \rightsquigarrow T_{2z}$	0.30	12	25	0.001	3	2.87×10^{2}
$S_1 \rightsquigarrow T_{2z}$	0.30	12	25	0.01	33	2.49×10^{7}
$S_1 \rightsquigarrow T_{2z}$	0.30	12	25	0.1	4×10^{2}	1.93×10^{7}
$S_1 \rightsquigarrow T_{2z}$	0.30	12	25	1	4×10^{3}	7.70×10^{7}
$S_1 \rightsquigarrow T_{2z}$	0.30	12	25	10	4×10^{4}	6.34×10^{7}
$S_1 \rightsquigarrow T_{2z}$	0.30	12	25	100	4×10^{5}	2.93×10^{7}
$S_1 \rightsquigarrow T_{2z}$	0.30	12	49	0.001	28	2.14×10^{3}
$S_1 \rightsquigarrow T_{2z}$	0.30	12	49	0.01	3×10^{2}	2.67×10^{7}
$S_1 \rightsquigarrow T_{2z}$	0.30	12	49	0.1	4×10^{3}	6.30×10^{7}
$S_1 \rightsquigarrow T_{2z}$	0.30	12	49	1	4×10^{4}	9.16×10^{7}
$S_1 \rightsquigarrow T_{2z}$	0.30	12	49	10	4×10^{5}	1.60×10^{8}
$S_1 \rightsquigarrow T_{2z}$	0.30	12	49	100	4×10^{6}	1.98×10^{8}
$S_1 \rightsquigarrow T_{2z}$	0.30	12	72	0.001	5×10^{3}	7.32×10^{6}
$S_1 \rightsquigarrow T_{2z}$	0.30	12	72	0.01	5×10^{4}	8.81×10^{7}
$S_1 \rightsquigarrow T_{2z}$	0.30	12	72	0.1	1×10^{5}	1.39×10^{8}
$S_1 \rightsquigarrow T_{2z}$	0.30	12	72	1	1×10^{6}	1.39×10^{8}
$S_1 \rightsquigarrow T_{2z}$	0.30	12	72	10	5×10^{7}	2.33×10^{8}
$S_1 \rightsquigarrow T_{2z}$	0.30	1 (ν_8)	25	0.001	3	1.39×10^{3}
$S_1 \rightsquigarrow T_{2z}$	0.30	1 (ν_8)	25	0.01	33	2.69×10^{7}
$S_1 \rightsquigarrow T_{2z}$	0.30	1 (ν_8)	25	0.1	4×10^{2}	3.65×10^{6}
$S_1 \rightsquigarrow T_{2z}$	0.30	1 (ν_8)	25	1	4×10^{3}	1.15×10^{7}
$S_1 \rightsquigarrow T_{2z}$	0.30	1 (ν_8)	25	10	4×10^{4}	2.97×10^{7}
$S_1 \rightsquigarrow T_{2z}$	0.30	1 (ν_8)	25	100	4×10^{5}	3.70×10^{7}
$S_1 \rightsquigarrow T_{2z}$	0.30	1 (ν_8)	49	0.001	28	1.54×10^{3}
$S_1 \rightsquigarrow T_{2z}$	0.30	1 (ν_8)	49	0.01	3×10^{2}	2.74×10^{7}
$S_1 \rightsquigarrow T_{2z}$	0.30	1 (ν_8)	49	0.1	4×10^{3}	1.48×10^{7}
$S_1 \rightsquigarrow T_{2z}$	0.30	1 (ν_8)	49	1	4×10^{4}	3.60×10^{7}
$S_1 \rightsquigarrow T_{2z}$	0.30	1 (ν_8)	49	10	4×10^{5}	8.66×10^{7}
$S_1 \rightsquigarrow T_{2z}$	0.30	1 (ν_8)	49	100	4×10^{6}	1.20×10^{8}
$S_1 \rightsquigarrow T_{2z}$	0.30	1 (ν_{20})	25	0.001	3	6.63×10^{1}
$S_1 \rightsquigarrow T_{2z}$	0.30	1 (ν_{20})	25	0.01	33	1.42×10^{3}
$S_1 \rightsquigarrow T_{2z}$	0.30	1 (ν_{20})	25	0.1	4×10^{2}	3.13×10^{5}
$S_1 \rightsquigarrow T_{2z}$	0.30	1 (ν_{20})	25	1	4×10^{3}	6.33×10^{6}
$S_1 \rightsquigarrow T_{2z}$	0.30	1 (ν_{20})	25	10	4×10^{4}	1.05×10^{7}
$S_1 \rightsquigarrow T_{2z}$	0.30	1 (ν_{20})	25	100	4×10^{5}	1.25×10^{7}
$S_1 \rightsquigarrow T_{2z}$	0.30	1 (ν_{20})	49	0.001	28	1.62×10^{2}
$S_1 \rightsquigarrow T_{2z}$	0.30	1 (ν_{20})	49	0.01	3×10^{2}	9.59×10^{4}
$S_1 \rightsquigarrow T_{2z}$	0.30	1 (ν_{20})	49	0.1	4×10^{3}	1.67×10^{6}
$S_1 \rightsquigarrow T_{2z}$	0.30	1 (ν_{20})	49	1	4×10^{4}	3.71×10^{7}
$S_1 \rightsquigarrow T_{2z}$	0.30	1 (ν_{20})	49	10	4×10^{5}	4.00×10^{7}
$S_1 \rightsquigarrow T_{2z}$	0.30	1 (ν_{20})	49	100	4×10^{6}	2.99×10^{7}

Table 17 Thionine: Harmonic frequencies v_i of the A" *out-of-plane* vibrational modes for the $S_2(\pi_{H-1}\rightarrow\pi_L^*)$ state. ∂SOMEs with respect to the corresponding (dimensionless) normal coordinates at the $S_2(\pi_{H-1}\rightarrow\pi_L^*)$ DFT/MRCI minimum.

Modes	$\bar{\nu}_i / cm^{-1}$	$\frac{\partial\langle S_2\lvert\hat{H}_{SO}\rvert T_{1x}\rangle}{\partial q_i}$	$\frac{\partial\langle S_2\lvert\hat{H}_{SO}\rvert T_{1y}\rangle}{\partial q_i}$	$\frac{\partial\langle S_2\lvert\hat{H}_{SO}\rvert T_{2x}\rangle}{\partial q_i}$	$\frac{\partial\langle S_2\lvert\hat{H}_{SO}\rvert T_{2y}\rangle}{\partial q_i}$
1	20.0	-0.18	1.31	1.97	-0.62
2	43.5	0.03	-0.21	-0.19	0.12
3	78.8	0.52	-0.02	-0.44	0.06
4	153.1	0.20	-0.18	-0.37	0.11
6	170.1	-0.08	0.31	0.05	0.05
7	181.9	-0.05	-0.03	-0.02	-0.08
9	250.5	-0.16	-0.05	0.10	0.04
10	269.5	0.31	0.09	-0.37	-0.15
11	291.5	0.09	1.10	-0.17	-0.82
13	317.6	0.39	0.27	-0.44	-0.33
15	386.5	0.41	0.64	-0.37	-0.36
17	398.5	0.48	-0.28	-0.60	0.20
18	429.1	-0.61	-0.60	0.63	0.67
20	433.8	-0.32	0.65	0.17	-0.56
23	534.6	-0.06	0.11	-0.18	-0.33
24	545.6	-0.20	0.01	0.08	-0.01
25	555.1	0.18	0.34	0.00	-0.40
29	747.7	-0.37	-0.72	0.48	0.32
30	788.9	0.43	-0.46	-0.28	0.26
32	831.5	0.41	0.06	-0.45	-0.10
33	836.3	0.12	0.47	-0.26	-0.39
37	924.4	-0.29	-0.10	0.39	0.10
38	928.1	-0.01	0.16	-0.22	-0.04

Table 18 Thionine: Calculated rate constants k_{ISC}^{TI} for the $S_2 \rightarrow T_{i(x/y)}$ (i = 1, 2) channels. Remaining columns: adiabatic energy difference ΔE^{ad}, number of derivatives with respect of *out-of-plane* modes ($\#_{derivs}$), width of the search interval η, number of accepting modes within the search interval ($\#_{acc}$) and number of final state vibrational levels within the search interval ($\#_{v'}$).

Channel	ΔE^{ad}/eV	$\#_{derivs}$	$\#_{acc}$	η/cm^{-1}	$\#_{v'}$	k_{ISC}^{TI} /s^{-1}
$S_2 \rightsquigarrow T_{1x}$	0.66	23	49	0.001	2×10^2	2.10×10^4
$S_2 \rightsquigarrow T_{1x}$	0.66	23	49	0.01	2×10^3	6.53×10^5
$S_2 \rightsquigarrow T_{1x}$	0.66	23	49	0.1	2×10^4	5.71×10^6
$S_2 \rightsquigarrow T_{1x}$	0.66	23	49	1	2×10^5	5.56×10^6
$S_2 \rightsquigarrow T_{1x}$	0.66	23	49	10	2×10^6	3.17×10^6
$S_2 \rightsquigarrow T_{1y}$	0.66	23	49	0.001	2×10^2	4.53×10^4
$S_2 \rightsquigarrow T_{1y}$	0.66	23	49	0.01	2×10^3	1.64×10^6
$S_2 \rightsquigarrow T_{1y}$	0.66	23	49	0.1	2×10^4	4.02×10^6
$S_2 \rightsquigarrow T_{1y}$	0.66	23	49	1	2×10^5	8.63×10^6
$S_2 \rightsquigarrow T_{1y}$	0.66	23	49	10	2×10^6	5.67×10^6
$S_2 \rightsquigarrow T_{2x}$	0.32	23	49	0.01	3	3.91×10^1
$S_2 \rightsquigarrow T_{2x}$	0.32	23	49	0.1	41	5.14×10^5
$S_2 \rightsquigarrow T_{2x}$	0.32	23	49	1	4×10^2	7.40×10^6
$S_2 \rightsquigarrow T_{2x}$	0.32	23	49	10	5×10^3	3.22×10^6
$S_2 \rightsquigarrow T_{2x}$	0.32	23	49	100	5×10^4	2.62×10^6
$S_2 \rightsquigarrow T_{2y}$	0.32	23	49	0.01	3	1.63×10^3
$S_2 \rightsquigarrow T_{2y}$	0.32	23	49	0.1	41	9.43×10^4
$S_2 \rightsquigarrow T_{2y}$	0.32	23	49	1	4×10^2	2.68×10^5
$S_2 \rightsquigarrow T_{2y}$	0.32	23	49	10	5×10^3	4.03×10^6
$S_2 \rightsquigarrow T_{2y}$	0.32	23	49	100	5×10^4	3.58×10^6

Table 19 Thionine: Calculated rate constants k_{ISC}^{TI} for the $S_1 \rightarrow T_{i(x/z)}$ (i = 1, 2) channel varying the adiabatic energy difference ΔE^{ad}. Remaining columns: number of derivatives with respect of *out-of-plane* modes ($\#_{derivs}$), width of the search interval η, number of accepting modes within the search interval ($\#_{acc}$) and number of final state vibrational levels within the search interval ($\#_{v'}$).

Channel	ΔE^{ad}/eV	$\#_{derivs}$	$\#_{acc}$	η/cm^{-1}	$\#_{v'}$	k_{ISC}^{TI} /s^{-1}
$S_1 \rightsquigarrow T_{1x}$	0.68	12	49	0.001	7×10^4	1.34×10^4
$S_1 \rightsquigarrow T_{1x}$	0.68	12	49	0.01	7×10^5	2.05×10^4
$S_1 \rightsquigarrow T_{1x}$	0.68	12	49	0.1	7×10^6	3.06×10^5
$S_1 \rightsquigarrow T_{1x}$	0.68	12	49	1	7×10^7	2.44×10^5
$S_1 \rightsquigarrow T_{1z}$	0.68	11	49	0.001	5×10^4	2.04×10^4
$S_1 \rightsquigarrow T_{1z}$	0.68	11	49	0.01	5×10^5	2.54×10^5
$S_1 \rightsquigarrow T_{1z}$	0.68	11	49	0.1	5×10^6	1.27×10^6
$S_1 \rightsquigarrow T_{1z}$	0.68	11	49	1	5×10^7	4.00×10^5
$S_1 \rightsquigarrow T_{2x}$	0.19	11	49	0.001	4	3.60×10^5
$S_1 \rightsquigarrow T_{2x}$	0.19	11	49	0.01	41	2.08×10^8
$S_1 \rightsquigarrow T_{2x}$	0.19	11	49	0.1	5×10^2	7.79×10^7
$S_1 \rightsquigarrow T_{2x}$	0.19	11	49	1	5×10^3	1.31×10^9
$S_1 \rightsquigarrow T_{2x}$	0.21	11	49	0.001	3	8.41×10^4
$S_1 \rightsquigarrow T_{2x}$	0.21	11	49	0.01	78	3.49×10^7
$S_1 \rightsquigarrow T_{2x}$	0.21	11	49	0.1	8×10^2	1.29×10^9
$S_1 \rightsquigarrow T_{2x}$	0.21	11	49	1	8×10^3	6.21×10^8
$S_1 \rightsquigarrow T_{2x}$	0.22	11	49	0.01	1×10^2	6.22×10^8
$S_1 \rightsquigarrow T_{2x}$	0.22	11	49	0.1	1×10^3	2.12×10^8
$S_1 \rightsquigarrow T_{2x}$	0.22	11	49	1	1×10^4	1.98×10^8
$S_1 \rightsquigarrow T_{2x}$	0.31	11	49	0.001	90	9.33×10^6
$S_1 \rightsquigarrow T_{2x}$	0.31	11	49	0.01	9×10^2	1.94×10^7
$S_1 \rightsquigarrow T_{2x}$	0.31	11	49	0.1	9×10^3	7.72×10^7
$S_1 \rightsquigarrow T_{2x}$	0.31	11	49	1	9×10^4	3.04×10^8
$S_1 \rightsquigarrow T_{2z}$	0.19	12	49	0.001	6	2.69×10^3
$S_1 \rightsquigarrow T_{2z}$	0.19	12	49	0.01	41	3.36×10^6
$S_1 \rightsquigarrow T_{2z}$	0.19	12	49	0.1	4×10^2	1.08×10^7
$S_1 \rightsquigarrow T_{2z}$	0.19	12	49	1	4×10^3	4.69×10^7
$S_1 \rightsquigarrow T_{2z}$	0.21	12	49	0.001	5	9.88×10^3
$S_1 \rightsquigarrow T_{2z}$	0.21	12	49	0.01	75	2.46×10^5
$S_1 \rightsquigarrow T_{2z}$	0.21	12	49	0.1	6×10^2	3.72×10^6
$S_1 \rightsquigarrow T_{2z}$	0.21	12	49	1	6×10^3	9.39×10^7
$S_1 \rightsquigarrow T_{2z}$	0.22	12	49	0.001	13	4.34×10^1
$S_1 \rightsquigarrow T_{2z}$	0.22	12	49	0.01	91	5.47×10^6
$S_1 \rightsquigarrow T_{2z}$	0.22	12	49	0.1	9×10^2	1.42×10^7
$S_1 \rightsquigarrow T_{2z}$	0.22	12	49	1	9×10^3	5.24×10^8
$S_1 \rightsquigarrow T_{2z}$	0.31	12	49	0.001	80	2.00×10^5
$S_1 \rightsquigarrow T_{2z}$	0.31	12	49	0.01	7×10^2	4.49×10^7
$S_1 \rightsquigarrow T_{2z}$	0.31	12	49	0.1	7×10^3	1.50×10^8
$S_1 \rightsquigarrow T_{2z}$	0.31	12	49	1	7×10^4	6.96×10^7

Table 20 Calculated rate constants $k_{ISC}^{TD}(s^{-1})$ of thionine for the $S_1 \rightsquigarrow T_i$ (i = 1,2) channels within the time-dependent approach. Other columns: adiabatic energy difference (ΔE^{ad}, eV), time interval (t, fs), number of points ($\#_{points}$) and damping factor (η, cm^{-1})

Channel	ΔE^{ad}	η	t	$\#_{points}$	k_{ISC}^{TD},
$S_1 \rightsquigarrow T_1$	0.64	0.10	30000	900000	3.72×10^{5}
		0.10	50000	1500000	1.83×10^{6}
		0.10	100000	3000000	8.79×10^{5}
		0.10	300000	9000000	1.08×10^{6}
		0.10	500000	15000000	1.08×10^{6}
		0.10	900000	27000000	3.72×10^{5}
		1	30000	900000	3.40×10^{6}
		1	50000	1500000	3.40×10^{6}
		1	100000	3000000	3.40×10^{6}
		1	300000	9000000	3.40×10^{6}
		1	500000	15000000	3.40×10^{6}
		1	900000	27000000	3.40×10^{6}
		10	30000	900000	3.57×10^{6}
		10	50000	1500000	3.57×10^{6}
		10	100000	3000000	3.57×10^{6}
		10	300000	9000000	3.57×10^{6}
		10	500000	15000000	3.57×10^{6}
		10	900000	27000000	3.57×10^{6}
		100	30000	900000	3.36×10^{6}
		100	50000	1500000	3.36×10^{6}
		100	100000	3000000	3.36×10^{6}
		100	300000	9000000	3.36×10^{6}
		1000	30000	900000	3.06×10^{6}
		1000	50000	1500000	3.06×10^{6}
		1000	100000	3000000	3.06×10^{6}
		1000	300000	9000000	3.06×10^{6}
	0.68[a]	0.10	30000	900000	6.43×10^{6}
		0.10	50000	1500000	4.44×10^{6}
		0.10	100000	3000000	3.48×10^{6}
		0.10	300000	9000000	3.15×10^{6}
		0.10	500000	15000000	3.15×10^{6}
		0.10	900000	27000000	6.43×10^{6}
		1	30000	900000	3.54×10^{6}
		1	50000	1500000	3.54×10^{6}
		1	100000	3000000	3.54×10^{6}
		1	300000	9000000	3.54×10^{6}
		1	500000	15000000	3.54×10^{6}
		1	900000	27000000	3.54×10^{6}
		10	30000	900000	2.52×10^{6}
		10	50000	1500000	2.52×10^{6}
		10	100000	3000000	2.52×10^{6}
		10	300000	9000000	2.52×10^{6}
		10	500000	15000000	2.52×10^{6}
		10	900000	27000000	2.52×10^{6}

		100	30000	900000	1.91×10^{6}
		100	50000	1500000	1.91×10^{6}
		100	100000	3000000	1.91×10^{6}
		100	300000	9000000	1.91×10^{6}
		1000	30000	900000	2.27×10^{6}
		1000	50000	1500000	2.27×10^{6}
		1000	100000	3000000	2.27×10^{6}
		1000	300000	9000000	2.27×10^{6}
$S_1 \rightsquigarrow T_2$	0.30	0.10	30000	900000	7.26×10^{8}
		0.10	50000	1500000	6.58×10^{8}
		0.10	100000	3000000	6.34×10^{8}
		0.10	300000	9000000	6.13×10^{8}
		0.10	500000	15000000	6.13×10^{8}
		1	30000	900000	6.45×10^{8}
		1	50000	1500000	6.45×10^{8}
		1	100000	3000000	6.45×10^{8}
		1	300000	9000000	6.45×10^{8}
		1	500000	15000000	6.45×10^{8}
		1	900000	27000000	6.45×10^{8}
		10	30000	900000	7.59×10^{8}
		10	50000	1500000	7.59×10^{8}
		10	100000	3000000	7.59×10^{8}
		10	300000	9000000	7.59×10^{8}
		10	500000	15000000	7.59×10^{8}
		10	900000	27000000	7.59×10^{8}
		100	30000	900000	7.83×10^{8}
		100	50000	1500000	7.83×10^{8}
		100	100000	3000000	7.83×10^{8}
		100	300000	9000000	7.83×10^{8}
		1000	30000	900000	9.42×10^{8}
		1000	50000	1500000	9.42×10^{8}
		1000	100000	3000000	9.42×10^{8}
		1000	300000	9000000	9.42×10^{8}
	0.21[a]	0.10	30000	900000	1.07×10^{9}
		0.10	50000	1500000	1.12×10^{9}
		0.10	100000	3000000	1.27×10^{9}
		0.10	300000	9000000	1.31×10^{9}
		0.10	500000	15000000	1.31×10^{9}
		1	30000	900000	1.07×10^{9}
		1	50000	1500000	1.07×10^{9}
		1	100000	3000000	1.07×10^{9}
		1	300000	9000000	1.07×10^{9}
		1	500000	15000000	1.07×10^{9}
		1	900000	27000000	1.07×10^{9}
		10	30000	900000	1.07×10^{9}
		10	50000	1500000	1.07×10^{9}
		10	100000	3000000	1.07×10^{9}
		10	300000	9000000	1.07×10^{9}
		10	500000	15000000	1.07×10^{9}
		10	900000	27000000	1.07×10^{9}

100	30000	900000	1.09×10^{9}
100	50000	1500000	1.09×10^{9}
100	100000	3000000	1.09×10^{9}
100	300000	9000000	1.09×10^{9}
1000	30000	900000	1.36×10^{9}
1000	50000	1500000	1.36×10^{9}
1000	100000	3000000	1.36×10^{9}
1000	300000	9000000	1.36×10^{9}

[a]Rate constants calculated: applying spectroscopic solvation shifts from models TH^{+}3Wa

Chapter 6. Effect of the protonation state on the electronic structure and photophysics of thionine

6.1. Overview

In this chapter, the photophysics and electronic structure of the diprotonated and neutral imine forms of thionine in vacuum and taking into account solvation effects are studied. An overview of the studied reactions and the obtained results can be found in **Fig. 22**. The nomenclature for naming the dyes in this chapter follows the number of protons and its charge: diprotonated thionine: TH_2^{+2}, thionine: TH^+ and neutral thionine: T.

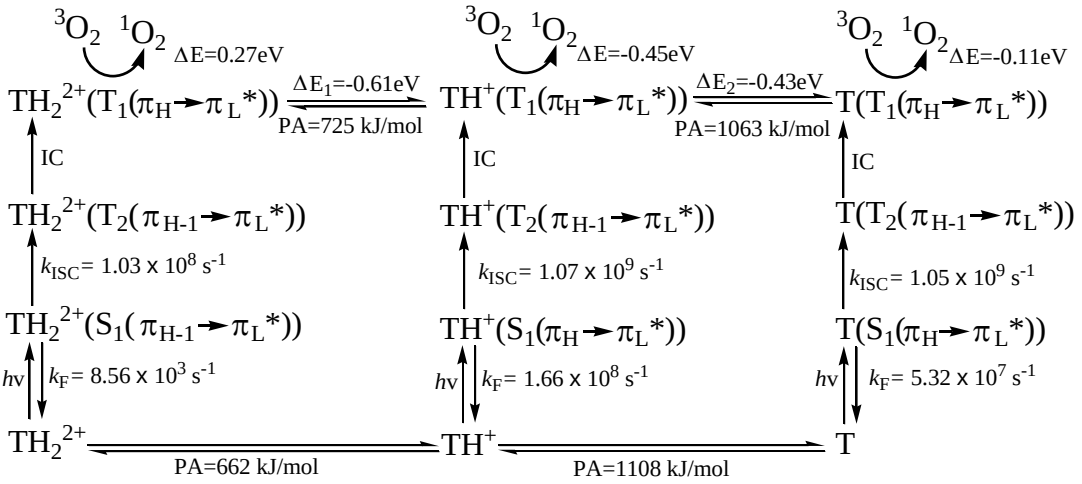

Fig. 22 Representative estimated rate constants of the decay kinetics in aqueous solution. The ΔE values refer to the global reaction energy for the energy transfer process from the triplet state of the dye to the ground state of oxygen ($^3O_2$) calculated at the DFT/MRCI/TZVP//UB3LYP/TZVP level of theory. The estimated energy gaps ΔE_1 and ΔE_2 are calculated between the T_1 state of TH^+, and the T_1 states of TH_2^{2+} and T, respectively. PA corresponds to the DFT/MRCI proton affinities of the ground and triplet state of TH^+ calculated in vacuum.

A detailed discussion of the electronic structure and the photophysics of TH^+ can be found in **Chapter 5**. The actual chapter is organized as follows: In Section **6.2.1**, the vertical and adiabatic excitation energies of TH_2^{+2} and T in

vacuum are presented. In Section **6.2.2** we present a detailed characterization of the electronic structure of TH_2^{+2} and T in aqueous solution using different solvation models. In Section **6.2.3**, the (de)protonation equilibrium at the first triplet state minima are discussed both in vacuum and in aqueous solution. In Section **6.2.4** we present the effects of (de)protonation and hydration on the ISC efficiencies.

After photoexcitation to the $S_1(\pi_H \rightarrow \pi_L^*)$ state of TH^+ and subsequent population of the $T_1(\pi_H \rightarrow \pi_L^*)$ state, this state may undergo protonation and deprotonation reactions in aqueous solution (see **Fig. 22**). The released energy is calculated to be higher for the protonation process (ΔE_1 = -0.61) than for the deprotonation process (ΔE_2 = -0.43). Moreover, the proton affinity of the $T_1(\pi_H \rightarrow \pi_L^*)$ state of TH^+ is 68 kJ/mol higher than for the ground state which is in agreement with the increased basicity of the triplet state observed experimentally.[33-175] In aerated aqueous solution at pH ~ 7 the $T_1(\pi_H \rightarrow \pi_L^*)$ states of TH_2^{2+}, TH^+ and T may coexist. Our results show that the reaction of the $T_1(\pi_H \rightarrow \pi_L^*)$ state of TH_2^{2+} with $^3O_2$ to produce $^1O_2$ is endergonic. These facts satisfactorily explain the experimental observation of a much lower $^1O_2$ production efficiency for TH_2^{2+} than for TH^+ and also the increased photoreduction of the dye in acidic media.[176,34] In contrast, the energy transfer from the $T_1(\pi_H \rightarrow \pi_L^*)$ states of TH^+ and T to $^3O_2$ releases energy (see **Fig. 22**).

In addition, we found that the protonation and deprotonation has remarkable effects on the electronic structure and ISC processes of TH^+. The electronic structure of the low-lying excited states of each protonation state are summarized in **Fig. 22**. In very acid aqueous solution (pH < 2), where TH_2^{2+} may be present in some extent, the ISC decay takes place from a dark $S_1(\pi_{H-1} \rightarrow \pi_L^*)$ state to the $T_2(\pi_{H-1} \rightarrow \pi_L^*)$ state with a rate constant ($k_{ISC}^{TD} \sim 10^8$ s^{-1}) which is four orders of magnitude larger than its fluorescence ($k_F \sim 10^4$ s^{-1}). In basic aqueous solution (pH > 10), where T is present, the

bright $S_1(\pi_H \rightarrow \pi_L^*)$ state is populated after photoexcitation and it may decay to the $T_2(\pi_{H-1} \rightarrow \pi_L^*)$ state via a thermally activated channel ($\Delta E_{T2\text{-}S1}$ = +0.05 eV). This channel has a ISC rate constant ($k_{ISC}^{TD} \sim 10^9$ s^{-1}) which is nearly two orders of magnitude faster than the fluorescence decay ($k_F \sim 10^7$ s^{-1}) from the $S_1(\pi_H \rightarrow \pi_L^*)$ state of T. According to these results, ISC is more efficient for TH_2^{2+} and T than for TH^+. We therefore expect increased ISC efficiency at very low and very high pH.

6.2. Results and discussion

6.2.1. Electronic structure in vacuum

A description of the low-lying singlet and triplet excited states of TH_2^{+2} and T in vacuum is provided in this section. This part is divided into four subsections. In Sections **6.2.1.1** and **0**, the vertical and adiabatic excitation energies of TH_2^{2+} are presented. In Sections **6.2.1.3** and **0** the vertical and adiabatic excitation energies of T are presented. The optimized geometries for the ground and excited states in vacuum are shown in **Fig. 23** and **Fig. 27**. The vertical excited state properties and their leading electronic configurations are shown in **Table 21** for TH_2^{+2} and **Table 23** for T, respectively. In addition, the valence molecular orbitals (MOs) which dominate the corresponding excitations are depicted in **Fig. 24** and **Fig. 28**. The calculated adiabatic energies of the low-lying energy singlet and triplet states are presented in **Table 22** for TH_2^{+2} and **Table 24** for T.

6.2.1.1. TH_2^{2+}: Vertical spectrum

As found for TH^+, the ground state of TH_2^{+2} in vacuum also has a C_{2v}-symmetric planar geometry (see **Fig. 23(a)**. The geometrical parameters are quite similar for both protonation states. The central ring C-N-C angle is just slightly enlarged (by 6°) because of the presence of the additional N-H bond (of 102 pm). Therefore, the π_H, π_{H-1}, π_L^* and π_{L+1}^* MOs of TH_2^{+2} (**Fig. 24**) have similar shapes as those already described for TH^+. Due to the

presence of the proton at the central ring on TH_2^{+2}, there are no low-lying *n* MOs. The electron density distributions of the MOs below the π_{H-1} and above the π_{L+1}* are different from those already shown for TH^+, see **Fig. 24** and **Fig. 10**. The π_{H-2} of TH^+ has similar shape to the π_{H-3} of TH_2^{+2}, where the latter is differentiated by an additional p-AO located at the sulfur center. The π_{H-3} of TH^+ resembles the π_{H-2} of TH_2^{+2} with no apparent differences.

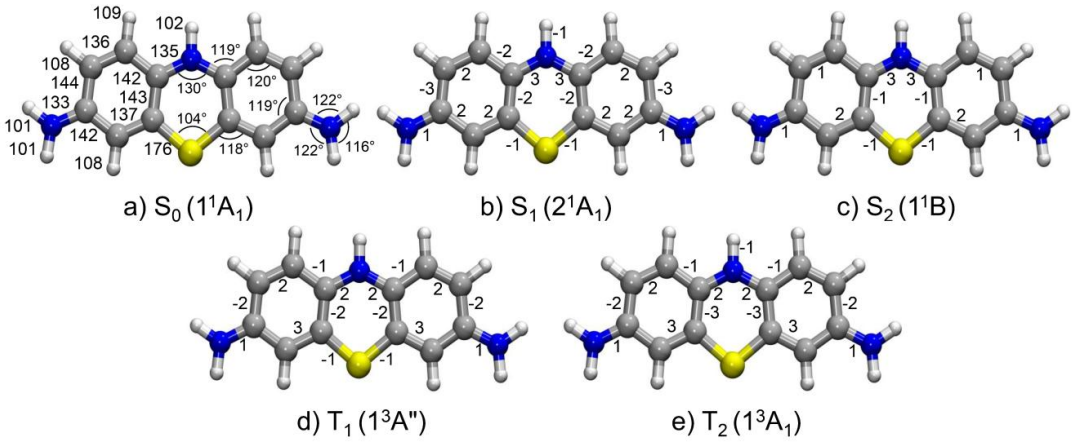

Fig. 23 Computed (TD-)DFT equilibrium structures of excited states of TH_2^{2+} in comparison with the ground state (S_0) geometry. Numbers indicate bond lengths in pm (S_0 structure) and changes of bond lengths relative to the S_0 structure (all other structures). Bond angles are given in degrees.

Due to the lack of energetically low-lying *n* MOs in TH_2^{+2}, there are no low-lying energy excited states arising from *n*→π* electronic transitions. Therefore, these states are all of π→π* character. The DFT/MRCI vertical spectrum of TH_2^{+2} may be described as follows, **Table 21**. In the singlet manifold, the first excited state (S_1) is located at ΔE_{vac} = 1.80 eV and is found to be dominated by the optically forbidden A_1-symmetric $\pi_{H-1}\rightarrow\pi_L$* transition. Only 0.10 eV above this state, we found the second excited state (S_2), where the B_1-symmetric single $\pi_H\rightarrow\pi_L$* excitation prevails. This state also presents minor contributions of a $\pi_{H-1}\rightarrow\pi_L$* $\pi_H\rightarrow\pi_L$* double excitation. Since the $S_2(\pi_H\rightarrow\pi_L^*)$ is connected to the ground state by a considerable transition dipole moment and oscillator strength ($f(L)$ = 0.684), we expect the $S_0\rightarrow S_2(\pi_H\rightarrow\pi_L^*)$ absorption calculated at 1.90 eV to be the bright transition of

lowest energy and the most intense absorption TH_2^{+2} in vacuum. The following singlet excited states are the S_3 and S_4 states and are vertically degenerated (ΔE_{vac} = 2.78 eV), but can be differentiated by their oscillator strengths. The dark S_3 state ($f(L)$ = 0.008) is A_1-symmetric and is characterized by a linear combination of two transitions: a $\pi_H \rightarrow \pi_L^*$ $\pi_H \rightarrow \pi_L^*$ double excitation and a single $\pi_{H-3} \rightarrow \pi_L^*$ excitation. The S_4 state (B_1-symmetric) is a bright state ($f(L)$ = 0.105) dominated by a $\pi_{H-2} \rightarrow \pi_L^*$ transition and to lesser extent by a contribution of a $\pi_{H-1} \rightarrow \pi_L^*$ $\pi_H \rightarrow \pi_L^*$ double excitation. In the triplet manifold, there are two triplet states located vertically below the dark $S_1(\pi_{H-1} \rightarrow \pi_L^*)$ state: the $T_1(\pi_H \rightarrow \pi_L^*)$ state (B_1-symmetric) at ΔE_{vac} = 0.91 eV and the $T_2(\pi_{H-1} \rightarrow \pi_L^*)$ state at ΔE_{vac} = 1.50 eV (A_1-symmetric). The T_3 and T_4 states are energetically quasidegenerate (ΔE_{vac} = 2.85 and ΔE_{vac} = 2.90 eV) and are located ~ 1.0 eV above the low-lying singlet state. The dominant contribution to the T_3 (B_1-symmetric) is of $\pi_{H-2} \rightarrow \pi_L^*$ character, but there are also minor contributions of a $\pi_{H-1} \rightarrow \pi_L^*$ $\pi_H \rightarrow \pi_L^*$ double excitation. The T_4 state is A_1-symmetric and is characterized by a $\pi_{H-3} \rightarrow \pi_L^*$ excitation.

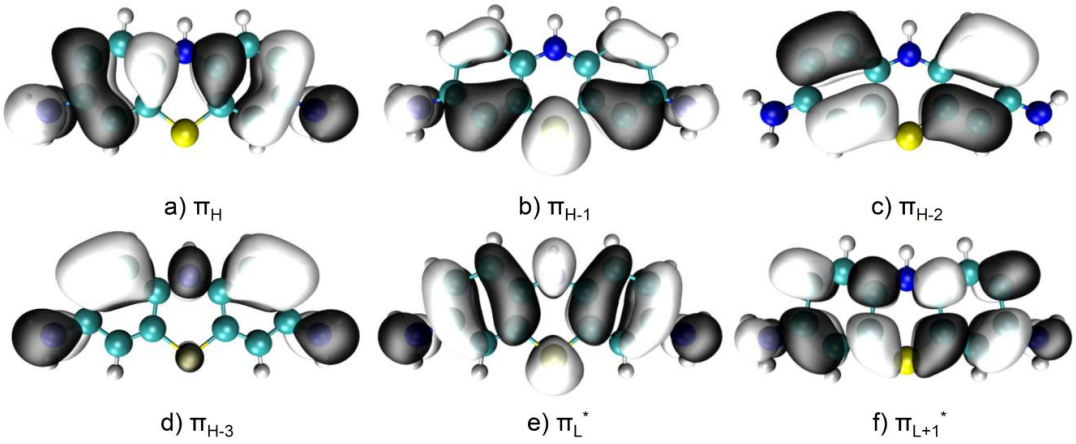

Fig. 24 Frontier BHLYP/TZVP Kohn-Sham molecular orbitals computed at the ground-state (S_0) minimum of TH_2^{+2} (isovalue 0.02).

At the TD-B3LYP/TZVP level the calculated vertical excitation energies of the $S_1(\pi_{H-1} \rightarrow \pi_L^*)$ and the $S_2(\pi_H \rightarrow \pi_L^*)$ states exhibit the same vertical ordering as

at the DFT/MRCI level. These states appear energetically more separated at the TDDFT level (by 0.34 eV). The $T_1(\pi_H \rightarrow \pi_L^*)$ and the $T_2(\pi_{H-1} \rightarrow \pi_L^*)$ states are located even more separated (by 0.68 eV). As known for TDDFT, states with double excitation character (as the S_3 and S_5 at the DFT/MRCI level) cannot be described with this method, **Table 21**.

Table 21 Vertical excitation energies ΔE_{vac} (eV) of the low-lying singlet and triplet states of TH_2^{2+}

Electronic State	Electronic structure[a]	DFT/MRCI/TZVP// B3LYP/TZVP[b]	TD-B3LYP/TZVP// B3LYP/TZVP[b]	Exp. values.
$S_0(1^1A_1)$	(0.87) Ground State			
$S_1(2^1A_1)$	(0.74) $\pi_{H-1} \rightarrow \pi_L^*$	1.80(0.001)	1.98(0.002)	1.85[e]
$S_2(1^1B_1)$	(0.68) $\pi_H \rightarrow \pi_L^*$	1.90(0.684)	2.32(0.562)	
	(0.12) $\pi_{H-1} \rightarrow \pi_L^* \pi_H \rightarrow \pi_L^*$			
$S_3(3^1A_1)$	(0.35) $\pi_H \rightarrow \pi_L^* \pi_H \rightarrow \pi_L^*$	2.78(0.008)	-	
	(0.33) $\pi_{H-3} \rightarrow \pi_L^*$			
$S_4(2^1B_1)$	(0.40) $\pi_{H-2} \rightarrow \pi_L^*$	2.78(0.105)	3.30(0.018)[c]	
	(0.26) $\pi_{H-1} \rightarrow \pi_L^* \pi_H \rightarrow \pi_L^*$			
$S_5(3^1B_1)$	(0.30) $\pi_{H-1} \rightarrow \pi_L^* \pi_H \rightarrow \pi_L^*$	3.69(0.053)	-	
	(0.24) $\pi_{H-2} \rightarrow \pi_L^*$			
$T_1(1^3B_1)$	(0.92) $\pi_H \rightarrow \pi_L^*$	0.91	0.56	
$T_2(1^3A_1)$	(0.88) $\pi_{H-1} \rightarrow \pi_L^*$	1.50	1.24	
$T_3(2^3B_1)$	(0.67) $\pi_{H-2} \rightarrow \pi_L^*$	2.85	2.83[d]	
	(0.19) $\pi_H \rightarrow \pi_L^* \pi_H \rightarrow \pi_L^*$			
$T_4(2^3A_1)$	(0.77) $\pi_{H-3} \rightarrow \pi_L^*$	2.90	2.70	

[a]Dominant contributions at the DFT/MRCI/TZVP level. [b]Oscillator strengths (length form) in parentheses. [c] The DC to this state is $(0.98)\pi_{H-2} \rightarrow \pi_L^*$. [d]The DC to this state is $(0.95)\pi_{H-2} \rightarrow \pi_L^*$. [e]From Ref. [37], aqueous solution.

Upon protonation of TH^+ to TH_2^{2+}, the experimental absorption band in aqueous solution is shifted to lower energies (longer wavelengths) from 2.08 eV to 1.85 eV.[37] The hydration effects on the vertical excitation energies will be described in a Section **6.2.2.1**. Here, it is just worth mentioning that this trend is well reproduced by the vertical excitation energies computed in vacuum, see **Table 4** and **Table 21**. The redshift is computed to be 0.39 eV at the DFT MRCI level taking into account the energies of the singlet states with the highest oscillator strengths. While in TH^+ the bright state corresponds to the first singlet state ($S_1(\pi_H \rightarrow \pi_L^*)$), in

TH_2^{2+} it is the second ($S_2(\pi_H \rightarrow \pi_L^*)$) singlet state. Moreover, the DFT/MRCI vertical energies for the two low-lying triplet states are also significantly redshifted in a way that their energetic ordering is preserved: *i*) the vertical energy of the $T_1(\pi_H \rightarrow \pi_L^*)$ state is appreciably lowered from 1.63 eV (TH^+) to 0.91 eV (TH_2^{2+}) and *ii*) the $T_2(\pi_{H-1} \rightarrow \pi_L^*)$ state is stabilized by 0.61 eV upon protonation. At the TDDFT level, these vertical redshifts upon protonation of TH^+ are calculated to be even larger: 0.42 eV being for the singlet $\pi_H \rightarrow \pi_L^*$ bright excitation, 0.97 eV for the $T_1(\pi_H \rightarrow \pi_L^*)$ state of and 0.79 eV for the $T_2(\pi_{H-1} \rightarrow \pi_L^*)$ state.

6.2.1.2. TH_2^{2+}: Adiabatic energies

The computed minima of the S_1,$T_2(\pi_{H-1} \rightarrow \pi_L^*)$ and S_2,$T_1(\pi_H \rightarrow \pi_L^*)$ states in vacuum do not show large geometry variations compared to the ground state of TH_2^{2+}, **Fig. 23**. The vertical S_1 and T_2 states arise from the same electronic transition ($\pi_{H-1} \rightarrow \pi_L^*$), hence the minima of these states have similar nuclear arrangements (**Fig. 23(b,e)**). The same applies to the S_2 and $T_1(\pi_H \rightarrow \pi_L^*)$ states (**Fig. 23(c,d)**). All of these minima have planar structures and the changes in bond lengths are not larger than 3 pm. The same energetic ordering of the states is preserved as in the FC region. The analysis of the corresponding adiabatic states in vacuum is presented in the following.

We obtained a C_{2v} symmetric minimum of the $S_1(\pi_{H-1} \rightarrow \pi_L^*)$ state of TH_2^{2+} which shows up at ΔE_{vac}^{ad} = 1.62 eV (**Table 22**). The effect of geometry relaxation on the adiabatic excitation energy is moderate (0.18 eV) with respect to the vertical energy (ΔE_{vac} = 1.80 eV, **Table 21**) at the DFT/MRCI level of theory. The destabilization of the electronic ground state at this minimum yields a vertical emission energy of 1.43 eV. Because the $S_0 \leftarrow S_1$ transition dipole moment for the dark $\pi_{H-1} \rightarrow \pi_L^*$ excitation is very small (0.05 a.u.), the fluorescence rate from the S_1 state is very low ($k_F = 8.56 \times 10^3$).

Table 22 Adiabatic excitation energies ΔE_{vac}^{ad} (eV) in vacuum and scaled zero point vibrational corrections (ZPVEC, eV) of the excited states of TH_2^{2+} computed using the TZVP basis set. Oscillator strengths for emission at the excited-state minimum are listed in parentheses.

Geometry	Electronic structure[a]	ΔE_{vac}^{ad}(DFT/MRCI)	ΔE_{vac}^{ad}(TD-B3LYP)	ZPVEC[b]
$S_1(2^1A_1)$	$(0.75)\pi_{H-1}\rightarrow\pi_L^*$	1.62(0.000)	1.77(0.001)	-0.09
$S_2(1^1B)$	$(0.66)\pi_H\rightarrow\pi_L^*$	1.85(0.621)	2.26(0.512)	-0.05
	$(0.13)\pi_{H-1}\rightarrow\pi_L^*\pi_H\rightarrow\pi_L^*$			
$T_1(1^3A'')$	$(0.91)\pi_H\rightarrow\pi_L^*$	0.98[c]	0.47[d]	-0.06
$T_2(1^3A_1)$	$(0.88)\pi_{H-1}\rightarrow\pi_L^*$	1.35	1.05	-0.04

[a]Dominant contributions at the DFT/MRCI/TZVP level. [b]Difference between the zero point vibrational energy of the excited state and the zero point vibrational energy of S_0. [d]Single point DFT/MRCI calculation at the optimized UB3LYP/TZVP geometry. [c]Single point TDDFT calculation at the optimized UB3LYP/TZVP geometry.

The geometry of the $S_2(\pi_H\rightarrow\pi_L^*)$ state is a C_2-symmetric structure for which the adiabatic excitation energy (ΔE_{vac}^{ad} = 1.85 eV) is rather unaffected by geometry relaxation. The electronic structure of this state is a linear combination of a single ($\pi_H\rightarrow\pi_L^*$) and a double excitation ($\pi_{H-1}\rightarrow\pi_L^*$ $\pi_H\rightarrow\pi_L^*$), with a major contribution from the former. The minimum of the $S_2(\pi_H\rightarrow\pi_L^*)$ state is only $\Delta E_{S2\text{-}S1}^{ad}$ = 0.23 eV above the $S_1(\pi_{H-1}\rightarrow\pi_L^*)$ minimum. As shown in Section **6.2.1.1**, the population of this bright $S_2(\pi_H\rightarrow\pi_L^*)$ state at the FC region (ΔE_{vac} = 1.90 eV, **Table 21**) is possible due to its high oscillator strength. Nevertheless, after photoexcitation and population of the singlet manifold the relaxation to the adiabatic $S_1(\pi_{H-1}\rightarrow\pi_L^*)$ state may occur at a very fast rate according to Kasha's rule [1] where a fast IC from the $S_2(\pi_H\rightarrow\pi_L^*)$ state to the $S_1(\pi_{H-1}\rightarrow\pi_L^*)$ state is expected. The linearly interpolated pathway between the S_0 and the $S_1(\pi_{H-1}\rightarrow\pi_L^*)$ states shows this trend (see **Fig. 25(a)**), where a S_1 / S_2 conical intersection is found near to the FC region. Also it is observed that the $\Delta E_{S2\text{-}S1}$ energy separation is increased when moving from the S_0 to the S_1 geometry. As the adiabatic S_2 state is also characterized by a $\pi_H\rightarrow\pi_L^*$ transition with a high *f*(L) of emission, the population of this state cannot completely be ruled out and the subsequent decay processes from this state should be taken into account in the photophysical kinetics in vacuum.

The optimization of higher-lying singlet states such as the S_3, S_4 and the S_5 states shown in the vertical spectrum with double excitation contributions (**Table 21**) is not possible using TDDFT for geometry optimization. As these states are placed vertically above 2.78 eV, it is not expected that their they are relevant for the photophysical kinetics. Therefore, we restrained the analysis to the two lowest-lying singlet states presented above for the singlet manifold.

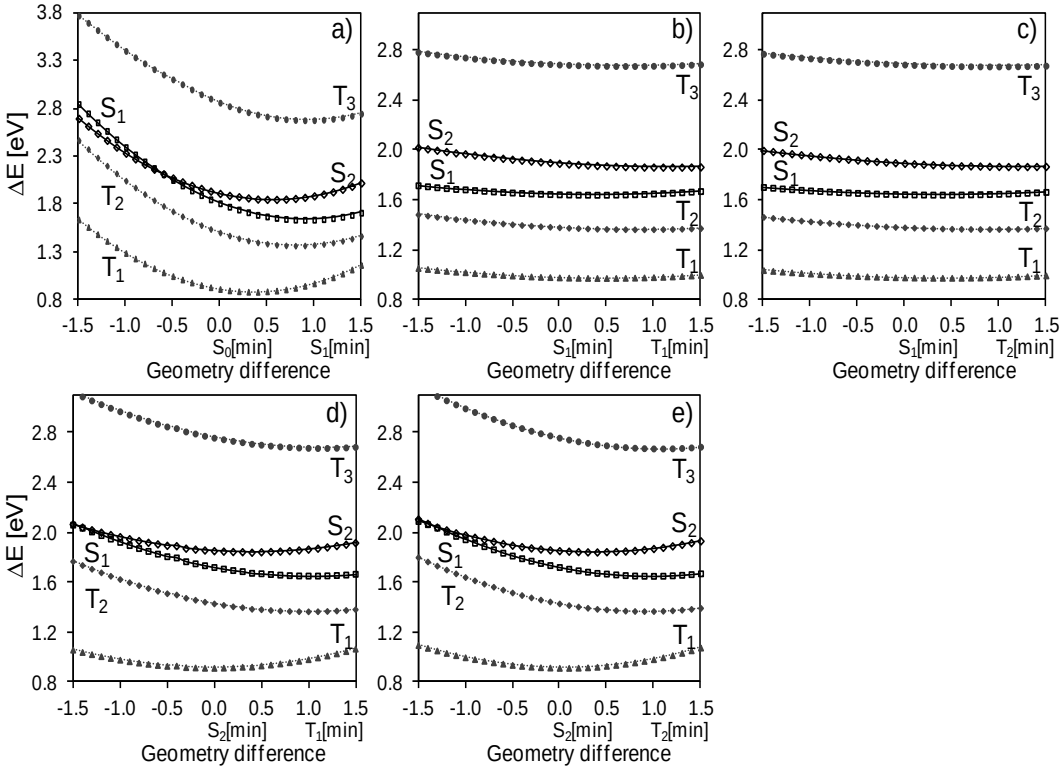

Fig. 25 DFT/MRCI excitation energy profiles along a linearly interpolated path between the ground state, the low-lying singlet and triplet states minima of TH_2^{2+}.

In the triplet manifold, we have located the minima for the $T_1(\pi_H \rightarrow \pi_L^*)$ and the $T_2(\pi_{H-1} \rightarrow \pi_L^*)$ states. The minimum nuclear structure of the $T_1(\pi_H \rightarrow \pi_L^*)$ state of TH_2^{2+} is similar to the $S_2(\pi_H \rightarrow \pi_L^*)$ state, but exhibits some additional changes in the bond length patterns, **Fig. 23(d,c)**. For minimizing the $T_1(\pi_H \rightarrow \pi_L^*)$ state, unrestricted DFT calculations at the UB3LYP/TZVP theoretical level were carried out because of triplet instabilities when using

TD-B3LYP/TZVP. Only when C_s symmetry constrains were imposed, the optimization procedure yielded a $T_1(\pi_H \rightarrow \pi_L^*)$ minimum at the UDFT level for which the DFT/MRCI adiabatic excitation energy (ΔE_{vac}^{ad} = 0.98 eV) approaches the DFT/MRCI vertical energy (ΔE_{vac} = 0.91 eV). For those structures optimized using C_{2v} and C_1 symmetry constraints and UDFT, the DFT/MRCI adiabatic excitation energies for the T_1 state are even higher ~ 1.35 eV. A geometry optimization of the $T_1(\pi_H \rightarrow \pi_L^*)$ state at the UB3LYP/TZVPP level of theory revealed a flat saddle point with a small imaginary frequency ($v = i29$ cm^{-1}). At this level of theory, the optimization of the $T_1(\pi_H \rightarrow \pi_L^*)$ state was possible only without symmetry constrains. Its calculated DFT/MRCI adiabatic excitation energy of ΔE_{vac}^{ad} = 0.93 eV is below the DFT/MRCI vertical energy (ΔE_{vac} = 0.95 eV) calculated with the same basis set as used in the optimization (TZVPP). This shows a basis set dependence of the calculations for describing the electronic structure of TH_2^{2+}. Exploring all the adiabatic electronic states using the TZVPP basis set is very difficult due to the extended computing time. Nevertheless, elongations along the imaginary mode were performed in order to find a minimum on the $T_1(\pi_H \rightarrow \pi_L^*)$ state PES at the UB3LYP/TZVPP level, but the efforts were not successful. The basis set dependency of the molecular structure and energetics of TH_2^{2+} is currently investigated.

The computed minimum of the $T_2(\pi_{H-1} \rightarrow \pi_L^*)$ state has C_{2v} symmetry (**Fig. 23(e)**) and has an adiabatic energy of ΔE_{vac}^{ad} = 1.35 eV. Geometry relaxation makes this state 0.15 eV more stable than at the FC region (ΔE_{vac} = 1.50 eV, **Table 21**). The adiabatic excitation energy of the $T_2(\pi_{H-1} \rightarrow \pi_L^*)$ state is below the two lowest-lying adiabatic singlet states ($S_1(\pi_{H-1} \rightarrow \pi_L^*)$ and $S_2(\pi_H \rightarrow \pi_L^*)$) by ΔE_{T2-S1} = -0.27 and ΔE_{T2-S2} = -0.50 eV, see **Table 22**. Thus, from the energetic point of view, this triplet state is more suitable for a fast radiationless decay (ISC) from the singlet manifold than the lowest-lying

$T_1(\pi_H \rightarrow \pi_L^*)$ state which is placed at a significantly lower energy ($\Delta E_{T1\text{-}S1}$ = -0.94 and $\Delta E_{T1\text{-}S2}$ = -0.87 eV).

Comparing the adiabatic excitation energies computed at the DFT/MRCI and TD-B3LYP/TZVP levels of theory, it is seen that at the TD-B3LYP/TZVP level the singlet states are located at higher energies while the triplet states are stabilized relative to DFT/MRCI. This trend also has been observed in the computed vertical excitation energies (**Table 21**). The $S_2(\pi_H \rightarrow \pi_L^*)$ state experiences a stronger blueshift (0.41 eV) than the $S_1(\pi_{H-1} \rightarrow \pi_L^*)$ state at the TDDFT level (0.15 eV) compared to DFT/MRCI. In contrast, the $T_1(\pi_H \rightarrow \pi_L^*)$ and the $T_2(\pi_{H-1} \rightarrow \pi_L^*)$ states are redshifted by 0.30 and 0.51 eV, respectively. In this case, we note the very low adiabatic energy (0.47 eV) of the $T_1(\pi_H \rightarrow \pi_L^*)$ state at the TD-B3LYP/TZVP level of theory (**Table 22**). The optimization of this $T_1(\pi_H \rightarrow \pi_L^*)$ state performed using UB3LYP/TZVP was possible because this state possess a significantly higher adiabatic energy of 1.22 eV at this theoretical level.

6.2.1.3. T: Vertical spectrum

The optimized planar (C_s) ground state of T turned out to be a first order saddle point at the TD-B3LYP/TZVP level of theory. This saddle point has an A_2-symmetric imaginary normal mode of $i49\ cm^{-1}$. We calculated the DFT/MRCI energies along this imaginary mode and found that both (TDDFT and DFT/MRCI) PES exhibit a shallow double minimum potential well (see **Fig. 26**), which confirms that this stationary point also corresponds to a flat saddle point at the DFT/MRCI theoretical level. A distortion along the imaginary mode followed by optimization without symmetry constraints led to a minimum on the PES. This ground state minimum exhibits a non-planar equilibrium geometry, which is due to the pyramidalization of the amine group ($-NH_2$), see **Fig. 27(a)**. The other geometrical features such as bond lengths and ring angles at this non-planar minimum are equal to the planar C_s-symmetric saddle point. The energy difference between the non-planar

minimum and the C_s-symmetric saddle point is of only $\Delta E = 0.01$ eV at the DFT/MRCI level. The vertical energetic order of the low-lying excited electronic states calculated at both stationary points (planar and non-planar) is nearly the same and will be described below. Therefore, due to the features described above, the non-planar geometry has been elected as the ground state minimum geometry for describing the electronic properties of T.

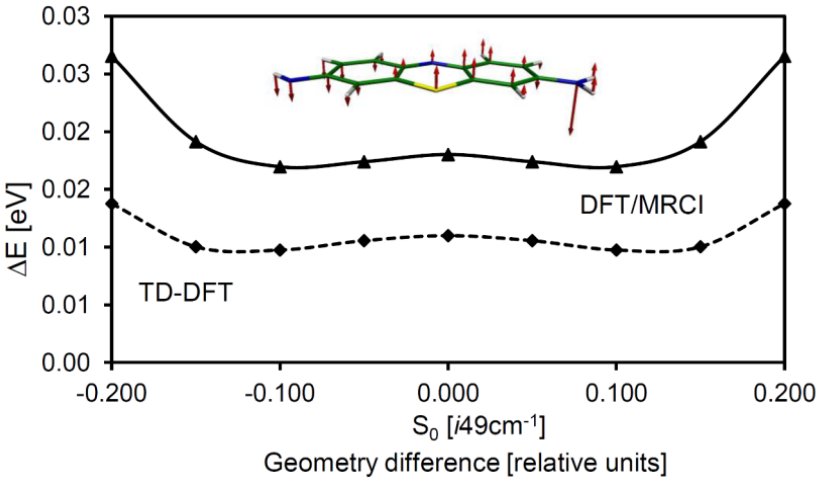

Fig. 26 TD-B3LYP and DFT/MRCI excitation energies calculated at displacements along the imaginary frequency (*i*49 cm^{-1}) found at a planar C_s-symmetric stationary point of T.

The influence of deprotonation on the excitation energies of TH^+ is due to appreciable changes in the electronic structure as a result of the redistribution of the charge in T. The different patterns of the MOs of TH^+ and T involved in the low-lying electronic transitions provide evidence of these effects. Both π_H and π_{H-1} MOs (**Fig. 28(a-b)**) of T could be compared with the π_H and π_{H-1} found for TH^+. For T, these MOs have electron density at the sulphur atom and also the bonding localization near to the imino group is different from the one found for of TH^+, **Fig. 10**. Also, all of these MOs present the π bonding pattern distributed over the whole heterocyclic system. For T, two low-lying *n* MOs have been obtained: the n_{H-4} and n_{H-5}. In the n_{H-4} (**Fig. 28(e)**), the lone pair of the *n* orbital is mostly located at the nitrogen atom of the imino group. While the n_{H-5} (**Fig. 28(f)**) MO is mostly localized at the phenothiazinium

nitrogen in the central ring with lower contributions of the *n* orbital of the imino group. The shapes of the electron density distributions of the low-lying π* MOs are similar to those found for TH^+ (**Fig. 10**), but present some differences in the patterns localized in the heterocyclic system at the side near to the amine group (in the case of the π_L*, **Fig. 28(f)**) and near to the imino group (in the case of the π_{L+1}*, **Fig. 28(g)**) are found.

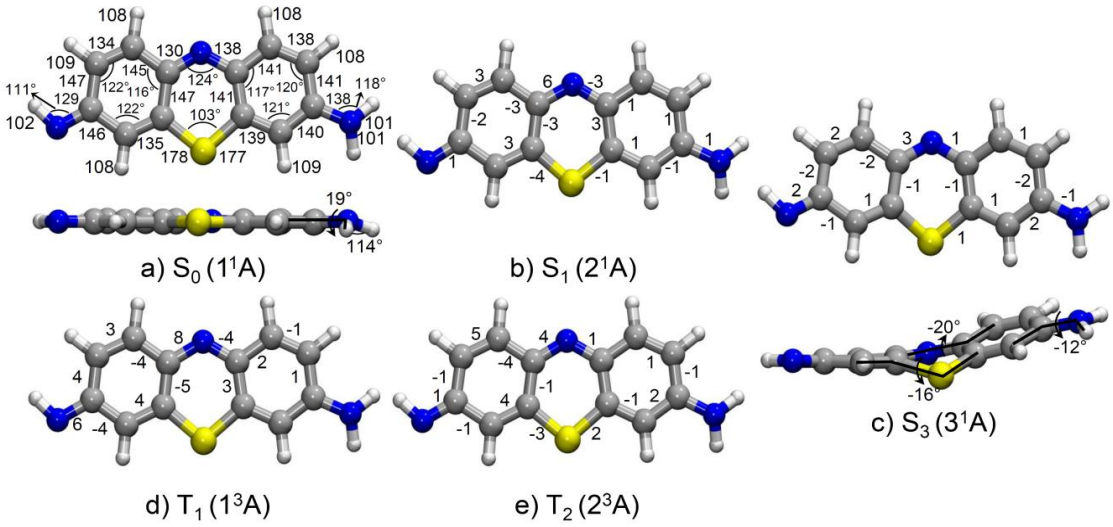

Fig. 27 Computed (TD-)DFT equilibrium structures of excited states of T in comparison with the ground state (S_0) geometry. Numbers indicate bond lengths in pm (S_0 structure) and changes of bond lengths relative to the S_0 structure (all other structures). Bond angles and dihedrals are given in degrees.

In vacuum the first singlet excited state S_1 of T is characterized by the $\pi_H \rightarrow \pi_L$* transition. It is an optically bright state located at ΔE_{vac} = 2.67 eV with the highest oscillator strength (*f*(L) = 0.441), see **Table 23**. Thus, the effect of the deprotonation of TH^+ to form T in the maximum absorption band is a blueshift of the vertical excitation energy of the $S_1(\pi_H \rightarrow \pi_L^*)$ bright state (by 0.38 eV) and also a decrease in the oscillator strength (*f*(L) = 0.833 of the $S_1(\pi_H \rightarrow \pi_L^*)$ state of TH^+), **Table 4**. In general, the other low-lying singlet excited states appear also at higher energy levels in T compared to TH^+. The charge transfer $S_2(n_{H-4} \rightarrow \pi_L^*)$ state is located 0.48 eV above the $S_1(\pi_H \rightarrow \pi_L^*)$ state. Energetically quasidegenerate to this state (ΔE_{S3-S2} = 0.05 eV), is a

bright $S_3(\pi_{H-1}\rightarrow\pi_L^*)$ state with an oscillator strength of $f(L) = 0.225$, which is smaller than the oscillator strength of the first optically bright transition. Other bright singlet excited states with similar oscillator strength ($f(L) \sim 0.2$) are found at high energies ($S_n > S_5$ and $\Delta E > 3.9$ eV, see Section **6.4**).

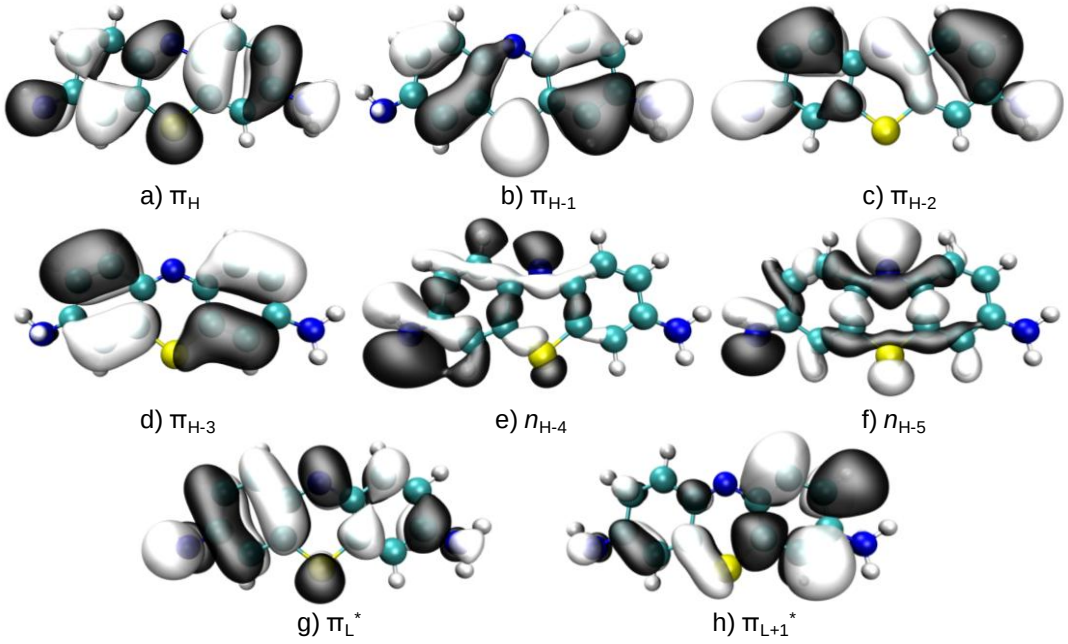

Fig. 28 Frontier BHLYP/TZVP Kohn-Sham molecular orbitals computed at the ground-state (S_0) minimum of T (isovalue 0.02).

With a vertical energy of 1.51 eV, the $T_1(\pi_H\rightarrow\pi_L^*)$ state is located $\Delta E_{S1\text{-}T1} = 1.16$ eV below the $S_1(\pi_H\rightarrow\pi_L^*)$ state. Only this triplet state is stabilized (by 0.12 eV) in T compared to its analog at TH^+, **Table 4**. Upon deprotonation of TH^+, the other higher lying triplet states are destabilized. The T_2 state is dominated by a $\pi_{H-1}\rightarrow\pi_L^*$ transition and is vertically quasidegenerate to the $S_1(\pi_H\rightarrow\pi_L^*)$ excited state (by $\Delta E_{S1\text{-}T2} = 0.03$ eV). Above the $T_2(\pi_{H-1}\rightarrow\pi_L^*)$ state the T_3 charge transfer state shows up and is characterized by a $n_{H-4}\rightarrow\pi_L^*$ transition. This state is 0.41 eV higher in energy than the $S_1(\pi_H\rightarrow\pi_L^*)$ state. The T_4 and T_5 states are also quasidegenerate ($\Delta E_{T5\text{-}T4} \sim 0.01$ eV). The T_4 state is characterized by a combination of the

$\pi_{H-2}\rightarrow\pi_L^*$, $\pi_H\rightarrow\pi_{L+1}^*$ and $\pi_H\rightarrow\pi_{L+3}^*$ excitations, while the T_5 state is dominated by a single $n_{H-5}\rightarrow\pi_L^*$ transition.

Table 23 Vertical excitation energies ΔE_{vac} (eV) of the low-lying singlet and triplet states of T.

Electronic State	Electronic structure[a]	DFT/MRCI/TZVP// B3LYP/TZVP[b]	TD-B3LYP/TZVP// B3LYP/TZVP[b]	Exp. values.
S_0	(0.91) Ground State			
S_1	(0.74) $\pi_H\rightarrow\pi_L^*$	2.67(0.441)	2.68(0.331)	2.44[c], 2.39[d]
S_2	(0.61) $n_{H-4}\rightarrow\pi_L^*$	3.15(0.002)	3.55(0.000)	
S_3	(0.64) $\pi_{H-1}\rightarrow\pi_L^*$	3.20(0.225)	3.21(0.212)	
S_4	(0.63) $n_{H-5}\rightarrow\pi_L^*$	3.38(0.004)	3.63(0.002)	
S_5	(0.28) $\pi_H\rightarrow\pi_L^*\pi_H\rightarrow\pi_L^*$	3.53(0.019)	-	
	(0.21) $\pi_{H-2}\rightarrow\pi_L^*$			
	(0.17) $\pi_H\rightarrow\pi_{L+1}^*$			
T_1	(0.82) $\pi_H\rightarrow\pi_L^*$	1.51	1.20	
T_2	(0.69) $\pi_{H-1}\rightarrow\pi_L^*$	2.70	2.51	
T_3	(0.70) $n_{H-4}\rightarrow\pi_L^*$	3.08	3.04	
T_4	(0.40) $\pi_{H-2}\rightarrow\pi_L^*$	3.21	3.12	
	(0.16) $\pi_H\rightarrow\pi_{L+1}^*$			
	(0.11) $\pi_H\rightarrow\pi_{L+3}^*$			
T_5	(0.73) $n_{H-5}\rightarrow\pi_L^*$	3.22	3.09	

[a] Dominant contributions (DC) at the DFT/MRCI/TZVP level. [b] Oscillator strengths (length form) in parentheses. [c] From Ref. [38], aqueous solution. [d] From Ref. [37], aqueous solution.

The calculated vertical excitation energies of the low-lying singlet and triplet excited states at the TD-B3LYP/TZVP geometries show a reasonable agreement with the DFT/MRCI energies (see, **Table 23**). Nevertheless, the vertical energetic ordering of the electronically excited states is not always the same. As already found for the other protonation states, TDDFT often places the excited states at higher energies with varying shifts. For example, the first absorption maximum ($S_1(\pi_H\rightarrow\pi_L^*)$ state) is only 0.01 eV higher than the one calculated with DFT/MRCI, while the $S_2(n_{H-4}\rightarrow\pi_L^*)$ state is appreciably energetically destabilized by 0.4 eV becoming the third singlet excited state at the TD-B3LYP/TZVP level. Similarly the $S_3(\pi_{H-1}\rightarrow\pi_L^*)$ state is located at approximately the same vertical excitation energy at both DFT/MRCI and TDDFT levels, while in the latter it appears to be the second singlet excited state. The S_5 state, characterized by a $\pi_H\rightarrow\pi_L^*$ $\pi_H\rightarrow\pi_L^*$ double excitation and

a $\pi_{H-2}\rightarrow\pi_L^*$ transition at the DFT/MRCI level, could not be located at the TDDFT level. The ordering of the three low-lying triplet excited states $T_1(\pi_H\rightarrow\pi_L^*)$, $T_2(\pi_{H-1}\rightarrow\pi_L^*)$ and $T_3(n_{H-4}\rightarrow\pi_L^*)$ is preserved. In the case of the triplet states, the TDDFT vertical excitation energies are predicted to have lower energies, with calculated redshifts (relative to the DFT/MRCI energies) which are larger for the $\pi\rightarrow\pi^*$ states (0.2 - 0.3 eV) than for the $n\rightarrow\pi^*$ states (<0.11 eV $\pi_H\rightarrow\pi_L^*$).

6.2.1.4. T: Adiabatic energies

Minima of the S_1, S_3, T_1 and T_2 ($\pi\rightarrow\pi^*$) states in vacuum could be found when the geometry optimizations were performed without symmetry constrains. Saddle points were found when C_s symmetry was imposed during the optimizations. The minima of these states show larger geometry variations respect to the ground state (**Fig. 27**) than those found for the protonated dyes (**Fig. 9** and **Fig. 23**). A characterization of each of the adiabatic states is presented in the following.

The computed geometry of the stationary point obtained after the optimization of the $S_1(\pi_H\rightarrow\pi_L^*)$ state using C_s symmetry constrains represents a very flat saddle point at the TD-B3LYP/TZVP ($v = i369\text{cm}^{-1}$ of A" symmetry) and DFT/MRCI PESs, see **Fig. 29**. A distortion along this imaginary mode and further optimization without symmetry constrains yielded a non-planar minimum, see **Fig. 27(b)**, and is characterized by an asymmetric pattern of the elongation of the bonds. The changes in the bond lengths on the left (on the side of the imino group) are larger than on the right (on the side of the amine group). For example, the changes in the C - N and C - S bond lengths are 6 and -4 pm in the left; and -3 and -1 pm in the right. The adiabatic excitation energy of this non-planar geometry is 2.38 eV (see **Table 24**) which is only 0.01 eV below than the planar geometry. The geometry relaxation effects make this state 0.29 eV more stable than at the FC region. At the same time, the ground state is destabilized by 0.08 eV, yielding a vertical

emission energy of 2.18 eV. Due to the smaller emission energy and transition dipole moment (2.20 Deybe/a.u.) for the $S_0 \leftarrow S_1$ radiative relaxation of this state to the ground state, the fluorescence rate ($k_F = 5.32 \times 10^7$ s^{-1}) calculated at the $S_1(\pi_H \rightarrow \pi_L^*)$ minimum of T is lower than that calculated for TH^+ ($k_F = 1.66 \times 10^8$ s^{-1}).

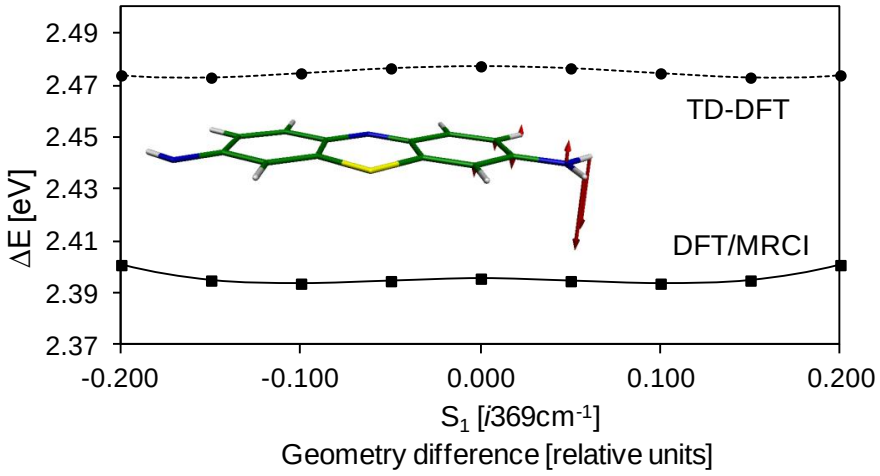

Fig. 29 DFT/MRCI excitation energies calculated upon geometry elongations along the imaginary mode ($v = i369$ cm^{-1}) obtained at the C_s-symmetric $S_1(\pi_H \rightarrow \pi_L^*)$ state saddle point of T.

It is known in the literature that TD-B3LYP fails to optimize charge transfer states and yields excitation energies with an average error > 1.0 eV.[203] This was the case for the $S_2(n_{H-4} \rightarrow \pi_L^*)$ charge transfer state which was not possible to optimize. In order to get an idea of the energetic accesibility of this state, a scan along a linearly interpolated pathway connecting the FC region with the $S_1(\pi_H \rightarrow \pi_L^*)$ state was performed (see **Fig. 30(left)**). As can be seen, the $S_2(n_{H-4} \rightarrow \pi_L^*)$ and $S_3(\pi_{H-1} \rightarrow \pi_L^*)$ state PESs appear energetically very close to each other at the DFT/MRCI level. Nevertheless, we were successful tp optimize two stationary points for the $S_3(\pi_{H-1} \rightarrow \pi_L^*)$ state. A C_s-symmetric planar geometry is a second order saddle point (v_1(A") = i41 and v_2(A") = i4 cm^{-1}) with an adiabatic DFT/MRCI energy of 3.03 eV. Distorting this structure along the first imaginary mode and after optimization without symmetry constrains yielded a $S_3(\pi_{H-1} \rightarrow \pi_L^*)$ state minimum on the TD-B3LYP/TZVP

PES, see **Fig. 27(c)**. This geometry is characterized by a particular V-shaped non-planar structure, where not only the hydrogen atoms at the amine group are placed *out-of-plane* but also the nitrogen and sulphur heteroatoms at the central ring (<C-S-C-C= 16° and <C-C-N-C= 20°). These appreciable changes upon relaxation of the geometry places this state at an adiabatic energy of 3.01 eV (see **Table 24**), 0.19 eV less than the vertical energy. Therefore we do not expect that relaxation effects on the geometry and energy would place the $S_2(n_{H-4}\rightarrow\pi_L^*)$ and $S_3(\pi_{H-1}\rightarrow\pi_L^*)$ states below the $S_1(\pi_H\rightarrow\pi_L^*)$ state.

Table 24 Adiabatic excitation energies ΔE^{ad} (eV) and scaled zero point vibrational corrections (ZPVEC, eV) of the excited states of T. Oscillator strengths for emission at the excited-state minimum are listed in parentheses.

Geometry	Electronic structure[a]	ΔE_{vac}^{ad}(DFT/MRCI)	ΔE_{vac}^{ad}(TD-B3LYP)	ZPVEC[b]
$S_1(2^1A)$	(0.66) $\pi_H\rightarrow\pi_L^*$	2.38(0.258)	2.45(0.215)	-0.08
	(0.10) $\pi_{H-1}\rightarrow\pi_L^*$			
$S_3(3^1A)$	(0.62) $\pi_{H-1}\rightarrow\pi_L^*$	3.01(0.093)	3.04(0.176)	-0.05
$T_1(1^3A)$	(0.85) $\pi_H\rightarrow\pi_L^*$	1.16[c]	-[d]	-0.05
$T_2(2^3A)$	(0.72) $\pi_{H-1}\rightarrow\pi_L^*$	2.51	2.29	-0.09

[a]Dominant contributions at the DFT/MRCI/TZVP level. [b]Difference between the zero point vibrational energy of the excited state and the zero point vibrational energy of S_0. [c]Single point DFT/MRCI calculation at a UB3LYP/TZVP optimized structure. [d]Not possible to calculate the TD-B3LYP/TZVP adiabatic energy due to triplet instabilities.

A look on **Fig. 30** reveals that only one triplet state, the $T_1(\pi_H\rightarrow\pi_L^*)$ state, is located energetically below the $S_1(\pi_H\rightarrow\pi_L^*)$ state. The optimized geometry of this state (see **Fig. 27(d)**) is also a non-planar minimum which was located at the UB3LYP/TZVP level of theory. Due to triplet instabilities, it is not possible to calculate the corresponding TDDFT energy. At the DFT/MRCI level of theory, the adiabatic energy of the $T_1(\pi_H\rightarrow\pi_L^*)$ state is 1.16 eV (see **Table 24**). The effect of geometry relaxation on the excitation energy of this state is 0.35 eV, relatively large for a state of this character and type of transition compared to those found for TH^+ (see Section **5.2.2.1.1**) and TH_2^{2+} (see Section **6.2.2.1**). This is reflected on the geometry of this state, which presents slightly elongated bond lenghts: *e. g.* the N_{ring} - C bond by 8 pm and

the N_{imino} - C bond by 6 pm, see **Fig. 27(d)**. As found for the geometry of its analogue transition at the singlet manifold ($S_1(\pi_H \rightarrow \pi_L^*)$ state), the changes on the bond lengths at the side of the imino group are larger than at the side of the amine group. On the other hand, a planar C_s-symmetric structure optimized for this state corresponds to a second order saddle point with $v_1 = i807$ and $v_2 = i92$ cm^{-1} (A"-symmetric modes) with an adiabatic excitation energy of 1.93 eV, significantly higher than that calculated for the non-planar structure.

Through the optimization of the $T_2(\pi_{H-1} \rightarrow \pi_L^*)$ state, we confirmed that this state is adiabatically above the $S_1(\pi_H \rightarrow \pi_L^*)$ state. The computed non-planar geometry shown in **Fig. 27(e)** is a minimum over the TD-B3LYP/TZVP PES of the $T_2(\pi_{H-1} \rightarrow \pi_L^*)$ state. Its DFT/MRCI adiabatic excitation energy is 2.51 eV (see **Table 24**), 0.13 eV above the adiabatic $S_1(\pi_H \rightarrow \pi_L^*)$ state. The geometry of this state preserves the planarity of the phenothiazinium ring (which is not observed for its the singlet counterpart, the $S_3(\pi_{H-1} \rightarrow \pi_L^*)$ state), and the hydrogen atoms of the amine group are shifted *out-of-plane* relative to it. When a C_s-symmetric structure was optimized for this state, we found a saddle point characterized by an imaginary A"-symmetric mode of $v = i315$ cm^{-1}, which is energetically above the non-planar minimum by only 0.02 eV.

At the TD-B3LYP/TZVP level of theory, the adiabatic energy of the $S_1(\pi_H \rightarrow \pi_L^*)$ and $S_3(\pi_{H-1} \rightarrow \pi_L^*)$ states of T in vacuum is nearly the same, with negligible blueshifts. The adiabatic energy of the $T_1(\pi_H \rightarrow \pi_L^*)$ state was not possible to calculate due to triplet instabilities at this theoretical level (perhaps because of a strong energetic stabilization) while the $T_2(\pi_{H-1} \rightarrow \pi_L^*)$ state presents a moderate redshift of 0.22 eV.

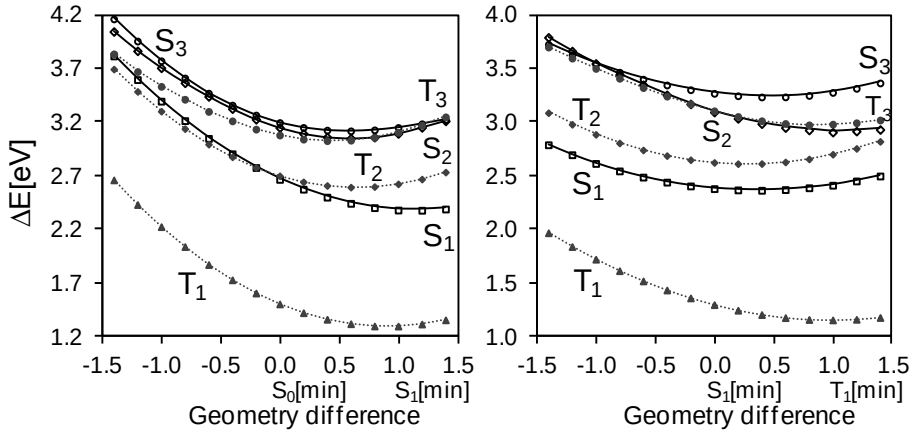

Fig. 30 DFT/MRCI excitation energy profiles along a linearly interpolated path between the ground state, the low-lying singlet and triplet states minima of T.

6.2.2. Hydration effects on the excitation energies

In the following, the effects of hydration on the excitation energies of TH_2^{+2} and T are presented. These effects are presented keeping in mind the limitations of the methods used for describing the electronic structure for these dyes in water. For simplicity, a summary of the most important aspects are described. This section is divided into four subsections: In Sections **6.2.2.1** and **6.2.2.2**, the hydration effects in the vertical and adiabatic energies of TH_2^{+2} are presented. In Sections **6.2.2.3** and **6.2.2.4**, the hydration effects in the vertical and adiabatic energies of T are discussed.

The geometries of the representative dye-water clusters employed for the description of the electronic structure in aqueous solution are presented in **Fig. 31** for TH_2^{+2} and **Fig. 32** for T. The vertical DFT/MRCI excitation energies computed at the ground state geometries of these clusters are reported in **Table 25** and **Table 28**. The adiabatic excitation enegies calculated at each optimized minima using different solvation models are displayed in **Table 27** and **Table 29**.

Due to the complex description of the electronic structure and energies in aqueous solution for TH_2^{2+} and T, a detailed discussion of the adiabatic excited states in this medium is presented. For TH^+ (Section **5.2.4.2**), the

calculation of the adiabatic energies in aqueous solution was performed by adding the spectroscopic hydration shifts calculated at the ground state of the TH^+3W complex embedded in a COSMO environment to the corresponding adiabatic energies computed in vacuum. Such description of the adiabatic excited states was sufficient case for the description of the ISC in water and yielded satisfactory results reproducing the experimental findings. However, for TH_2^{2+} the calculated vertical spectroscopic hydration shifts are not in agreement with the common behavior of chromophores in polar medium. Therefore, to deeply understand the excited state (de)protonation equilibrium processes in TH^+, the optimization of the electronically excited states in the micro-hydrated clusters has been performed. Different solvation models such as only explicit solvation and micro-hydration clusters embedded in a COSMO environment were tested for the description of the adiabatic electronically excited states for which the electronic properties and adiabatic energies are collected in **Table 27** and **Table 29**. Because of limitations of the current COSMO implementation in Turbomole we have to assume here that the electron distribution in the excited states is sufficiently similar to the one in the electronic ground state so that the solvent polarization in the excited state can be approximated by the solvent polarization in the ground state. Because in this case we were more interested in analyzing the effects on the energetics than on the geometries, the cartesian coordinates of each of the corresponding optimized geometries are included in the Supplementary Information (SI, Section **6.4)**. These results may also be useful for benchmarking purposes.

6.2.2.1. TH_2^{2+}: Vertical spectrum

It has been very difficult to describe the electronic structure of the diprotonated TH_2^{2+} dye in aqueous solution using water-dye clusters plus COSMO environment methodologies as used in Section **5.2.1.2** for describing the photophysics of the monoprotonated TH^+ state. First, the results obtained

with these clusters tests are described (**Table 25** and **Fig. 31**) where the vertical excitation energies were computed taking into account the following solvation models: *i)* only COSMO environment (TH_2^{2+}C), *ii)* COSMO plus one water molecule making N-H···O hydrogen bonds at the central ring (TH_2^{2+}1W) and *iii)* the latter plus additional hydrogen bonds N-H···O at the peripheral amine groups (TH_2^{2+}3W).

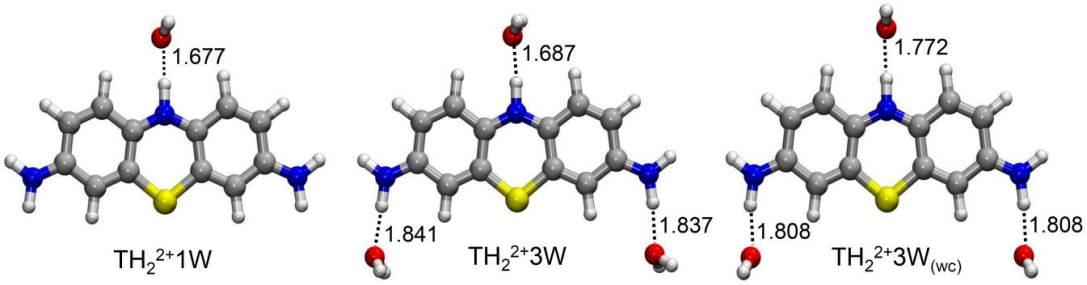

Fig. 31 Ground state minimum of TH_2^{2+}-water hydrogen bonded complexes optimized with COSMO at the B3LYP/TZVP level. Numbers indicate hydrogen bond lengths in Å.

Due to the π→π* character of the low-lying singlet and triplet states of TH_2^{2+}, these are expected to be vertically redshifted when embedded in the polar solvent environment. However, using these models it can be seen that most of these vertical excitation energies are blueshifted, which contradicts the common behavior of organic dyes in polar solvents (in this case, water). For example, the $S_2(\pi_H \rightarrow \pi_L^*)$ bright state ($\Delta E_w \sim 2.00$ eV for the models TH_2^{2+}1W and TH_2^{2+}3W, **Table 25**) is shifted away from the experimental value (1.85 eV [37]) and compared to the vertical energy obtained in vacuum ($\Delta E_{vac} = 1.90$ eV, from **Table 21**). This blueshift is smaller when calculating the vertical energies without using the COSMO environment ($TH_2^{2+}3W_{(wc)}$), as can also be seen in **Table 25**. Nevertheless, the strengths of these blueshifts obtained with the proposed hydration models are in accordance with the changes of the calculated dipole moments at the ground state geometry in vacuum reported in **Table 26** (the magnitude of dipole moments of the two lowest-lying singlet and triplet states are lower than in the ground state). On

the other hand, a small redshift of the $S_2(\pi_H \rightarrow \pi_L^*)$ bright state is observed when comparing the calculated DFT/MRCI vertical energy in vacuum ($\Delta E_{vac} = 1.90$ eV) with the experimental value of the maximum absorption band in aqueous solution (1.85 eV [37]). Local hydrogen bond interactions must be responsible for this redshift in the absorption band which would increase the dipole moment in the excited state like the electron density distribution in the atoms involved in the hydrogen bonds and the elongation of the hydrogen bond lengths.

Table 25 Vertical excitation energies ΔE_w (eV) of the low-lying singlet and triplet states of diprotonated thionine (TH_2^{2+}) in aqueous solution: solvation with COSMO (TH_2^{2+}C) and micro-hydration with one to three water molecules (TH_2^{2+}1W-TH_2^{2+}3W). Oscillator strengths (length form) in parentheses.

Electronic state	Electronic structure[a]	TH_2^{2+}C	TH_2^{2+}1W	TH_2^{2+}3W	$TH_2^{2+}3W_{(wc)}$[b]	Exp.
S_0	(0.89) Ground State					
S_1	(0.75) $\pi_{H-1} \rightarrow \pi_L^*$	1.93(0.001)	1.99(0.202)[b]	2.00(0.001)	1.89(0.000)	1.85[c]
S_2	(0.72) $\pi_H \rightarrow \pi_L^*$	1.97(0.756)	1.99(0.573)[c]	1.98(0.789)	1.94(0.749)	
S_3	(0.35)$\pi_H \rightarrow \pi_L^* \pi_H \rightarrow \pi_L^*$	2.89(0.009)	2.96(0.019)	2.93(0.015)	2.84(0.011)	
	(0.34) $\pi_{H-3} \rightarrow \pi_L^*$					
S_4	(0.45) $\pi_{H-2} \rightarrow \pi_L^*$	2.91(0.078)	2.97(0.058)	2.98(0.063)	2.91(0.089)	
	(0.26)$\pi_{H-1} \rightarrow \pi_L^* \pi_H \rightarrow \pi_L^*$					
S_5	(0.31)$\pi_{H-1} \rightarrow \pi_L^* \pi_H \rightarrow \pi_L^*$	3.83(0.059)	3.89(0.068)	3.86(0.062)	3.77(0.054)	
	(0.20) $\pi_{H-2} \rightarrow \pi_L^*$					
	(0.10) $\pi_{H-4} \rightarrow \pi_L^*$					
T_1	(0.92) $\pi_H \rightarrow \pi_L^*$	0.98	1.03	1.00	0.93	
T_2	(0.88) $\pi_{H-1} \rightarrow \pi_L^*$	1.63	1.67	1.69	1.59	
T_3	(0.78) $\pi_{H-3} \rightarrow \pi_L^*$	2.94	2.95	3.02	2.94	
T_4	(0.71) $\pi_{H-2} \rightarrow \pi_L^*$	2.96	2.99	2.95	2.98	
	(0.15)$\pi_{H-1} \rightarrow \pi_L^* \pi_H \rightarrow \pi_L^*$					

[a]Dominant contributions at the DFT/MRCI/TZVP level calculated at the TH_2^{2+}C model. [b]Vertical energies calculated using a micro-hydrated complex optimized without COSMO environment. [c]From Ref. [37], aqueous solution.

Table 26 Differences of the magnitudes of the dipole moments ($\Delta\mu$, Deybe) of the lowest singlet and triplet electronic states of TH_2^{2+} at the S_0 geometry in vacuum. The $\Delta\mu$ magnitudes were calculated relative to the ground state dipole moment.

State	S_1	S_2	S_3	T_1	T_2	T_3
$\Delta\mu$	-2.2	-0.7	0.7	-0.4	-2.5	0.2

6.2.2.2. TH_2^{2+}: Adiabatic energies

As mentioned in Section **6.2.2.1**, when computing the vertical energies of the low-lying electronic excited states of TH_2^{2+} using the solvation models TH_2^{2+}C, TH_2^{2+}1W and TH_2^{2+}3W the low-lying electronic excited states of TH_2^{2+} are blueshifted in energy (**Table 23**) compared to the vertical energies computed in vacuum (**Table 25**). Due to this unexpected energetic behavior of the low-lying singlet and triplet states in water since they are of $\pi\rightarrow\pi^*$ character, the calculation of the adiabatic energies employing the vertical spectroscopic solvation shifts to the excited states of TH_2^{2+} using **Eq 92** and **Eq 93** is not feasible. Therefore, the adiabatic excitation energies have been calculated at the optimized of the S_1,$T_2(\pi_{H-1}\rightarrow\pi_L^*)$ and S_2,$T_1(\pi_H\rightarrow\pi_L^*)$ states in aqueous solution within the TH_2^{2+}3W and $TH_2^{2+}3W_{(wc)}$ models (**Table 27**). For comparison, the same analysis has been carried out for the electronic states of the monoprotonated form TH^+. We can ensure that the optimized geometries of the electronic states in vacuum within the $TH^+3Wa_{(wc)}$ and $TH_2^{2+}3W_{(wc)}$ clusters are minima over their PESs. While, the optimization of the structures using the TH^+3Wa and TH_2^{2+}3W models which are embedded in a COSMO environment was more difficult. The optimization of the excited states was performed as follows. The S_1,$T_2(\pi_{H-1}\rightarrow\pi_L^*)$ and $S_2(\pi_H\rightarrow\pi_L^*)$ states of the TH^+3Wa and TH_2^{2+}3W models were optimized at the TD-B3LYP/TZVP(COSMO) level of theory. For optimizing the $T_1(\pi_H\rightarrow\pi_L^*)$ states, unrestricted DFT calculations at the UB3LYP/TZVP(COSMO) theoretical level were carried out due to triplet instabilities when using TD-B3LYP/TZVP(COSMO). For the $TH^+3Wa_{(wc)}$ and $TH_2^{2+}3W_{(wc)}$ models, the same procedures were followed but performing the computations in vacuum.

A close look to **Table 27** reveals that the calculated DFT/MRCI adiabatic excitation energies of TH^+ computed at the optimized states within the solvation model TH^+3W are similar to those computed applying the vertical spectroscopic hydration shifts (**Table 6**). Minor energy shifts between 0.02 to

0.04 eV are found when comparing both sets of results. When COSMO is not used in the calculations ($TH^+3Wa_{(wc)}$), most of the adiabatic energies of the states closely resembles to those calculated using the TH^+3Wa model except for the $S_2(\pi_{H-1}\rightarrow\pi_L^*)$ state where it is destabilized by ~0.2 eV.

Table 27 Adiabatic excitation energies ΔE_w^{ad} (eV) in water of the excited states of TH^+ and TH_2^{2+}. Oscillator strengths for emission at the excited-state minimum are listed in parentheses.

State	Electronic structure[a]	ΔE_w^{ad}(DFT/MRCI)	ΔE_w^{ad}(TD-B3LYP)
	TH^+3Wa		
S_1	$(0.79)\pi_H\rightarrow\pi_L^*$	2.11(0.822)	2.53(0.544)
S_2	$(0.59)\pi_{H-1}\rightarrow\pi_L^*$ $(0.21)\pi_H\rightarrow\pi_L^*$	2.25(0.270)	2.39(0.013)
T_1	$(0.92)\pi_H\rightarrow\pi_L^*$	1.42	1.18
T_2	$(0.88)\pi_{H-1}\rightarrow\pi_L^*$	1.89	1.71
	$TH^+3Wa_{(wc)}$		
S_1	$(0.79)\pi_H\rightarrow\pi_L^*$	2.17(0.808)	2.62(0.541)
S_2	$(0.52)\pi_{H-1}\rightarrow\pi_L^*$ $(0.29)\pi_H\rightarrow\pi_L^*$	2.43(0.463)	2.47(0.050)
T_1	$(0.92)\pi_H\rightarrow\pi_L^*$	1.51	1.33
T_2	$(0.88)\pi_{H-1}\rightarrow\pi_L^*$	1.94	1.80
	$TH_2^{2+}3W$		
S_1	$(0.76)\pi_{H-1}\rightarrow\pi_L^*$	1.55(0.002)	1.96(0.003)
S_2	$(0.71)\pi_H\rightarrow\pi_L^*$	1.67(0.722)	2.32(0.503)
T_1	$(0.92)\pi_H\rightarrow\pi_L^*$	0.70[c]	0.56[b]
T_2	$(0.88)\pi_{H-1}\rightarrow\pi_L^*$	1.26	1.26
	$TH_2^{2+}3W_{(wc)}$		
S_1	$(0.75)\pi_{H-1}\rightarrow\pi_L^*$	1.72(0.000)	1.85(0.002)
S_2	$(0.68)\pi_H\rightarrow\pi_L^*$ $(0.11)\pi_{H-1}\rightarrow\pi_L^*\pi_H\rightarrow\pi_L^*$	1.87(0.680)	2.28(0.482)
T_1	$(0.92)\pi_H\rightarrow\pi_L^*$	0.90[c]	0.40[b]
T_2	$(0.88)\pi_{H-1}\rightarrow\pi_L^*$	1.44	1.14

[a]Dominant contributions at the DFT/MRCI/TZVP level. [b]Single point TDDFT calculation at the optimized UB3LYP/TZVP geometry. [c]Single point DFT/MRCI calculation at the UB3LYP/TZVP optimized structure.

For TH_2^{2+} in aqueous solution, the excitation energies computed at the minima of the low-lying singlet and triplet states of the $TH_2^{2+}3W$ model reproduces the well known behavior of electronic states with $\pi\rightarrow\pi^*$ character. The adiabatic excitation energies of the S_1,$T_2(\pi_{H-1}\rightarrow\pi_L^*)$ and S_2,$T_1(\pi_H\rightarrow\pi_L^*)$ states is redshifted respect to those obtained in vacuum. The S_1 and $T_2(\pi_{H-1}\rightarrow\pi_L^*)$ states experience a weaker stabilization by the interaction with the solvent (0.07 and 0.09 eV) while the S_2,$T_1(\pi_H\rightarrow\pi_L^*)$ states experience redshifts of 0.20 and 0.28 eV. At this point it is important to note the very low excitation energy of the $T_1(\pi_H\rightarrow\pi_L^*)$ state in aqueous solution

(ΔE_w^{ad} = 0.70 eV). This makes the energy gap between the S_1 and $T_1(\pi_H \rightarrow \pi_L^*)$ states significantly larger than in vacuum (by 0.21 eV). Moreover, the energy separation of the S_1 and $T_2(\pi_{H-1} \rightarrow \pi_L^*)$ states is not appreciably affected. The adiabatic energy difference between the $S_2(\pi_H \rightarrow \pi_L^*)$ and $T_2(\pi_{H-1} \rightarrow \pi_L^*)$ states is reduced by 0.11 eV and for the $S_2(\pi_H \rightarrow \pi_L^*)$ and $T_1(\pi_H \rightarrow \pi_L^*)$ states by 0.08 eV.

Taking into account explicit solvation effects exclusively in the geometry optimization of the excited state of the dye-water complex and the adiabatic energy calculation lead to a different description of the excited state energy levels of TH_2^{2+}. When the micro-hydrated complex of TH_2^{2+} is not embedded in a COSMO environment ($TH_2^{2+}3Wa_{(wc)}$ model), the adiabatic energy of the $S_1(\pi_{H-1} \rightarrow \pi_L^*)$ state is blueshifted by 0.10 eV with respect to that of the isolated dye. Moreover, the adiabatic energy of the $T_1(\pi_H \rightarrow \pi_L^*)$ state (ΔE_w^{ad} = 0.90 eV, **Table 27**) is 0.20 eV higher in energy than that calculated at the $TH_2^{2+}3W$ complex. The adiabatic energy of the $S_2(\pi_H \rightarrow \pi_L^*)$ state is the same than that of the isolated dye while the $T_2(\pi_{H-1} \rightarrow \pi_L^*)$ state is destabilized by ~0.1 eV. Here, it is observed by comparison of the $S_2(\pi_H \rightarrow \pi_L^*)$ state calculated for the isolated dye (**Table 22**) and that calculated from the $TH_2^{2+}3W_{(wc)}$ model (**Table 27**) that both posses the similar electronic structure. While, the $S_2(\pi_H \rightarrow \pi_L^*)$ state calculated at the $TH_2^{2+}3W$ model is mostly dominated by the $\pi_H \rightarrow \pi_L^*$ transition.

In Section **5.2.4.2**, the calculated ISC rate constants for the $S_1(\pi_H \rightarrow \pi_L^*) \dashrightarrow T_2(\pi_{H-1} \rightarrow \pi_L^*)$ decay of TH^+ in aqueous solution reproduced well the trends observed experimentally. This was because of the adiabatic energies calculated applying the spectroscopic solvation shifts to the states optimized in vacuum was a reliable approximation for calculating the energy gaps between singlet and triplet states. The $S_1, T_1(\pi_H \rightarrow \pi_L^*)$ states in aqueous solution of TH^+ are the only states for which experimental values are available (2.04[165] and 1.69 eV[166]). The experimental estimate of 1.69 eV[166] for

the $T_1(\pi_H \rightarrow \pi_L^*)$ state of TH^+ was determined by triplet-triplet energy transfer, continuous illumination and flash photolysis methods. The calculated DFT/MRCI adiabatic energies of these states in **Table 6** and in **Table 27** account for a deviation of about ~ 0.2 eV which is within the error bars of the method, where they are calculated to be above and below the experimental values, respectively. The calculated adiabatic energy of the $T_1(\pi_H \rightarrow \pi_L^*)$ state of TH^+ in vacuum accounts to a very good estimate (1.63 eV, see **Table 6**). For TH_2^{2+}, the only data available for comparison in aqueous solution is the energy of the $T_1(\pi_H \rightarrow \pi_L^*)$ state. The energy of this state have been estimated to be ~ 1.28 eV calculated within the framework of a Föster cycle, where the pK_a of the ground and triplet state of TH^+ is taken into account.[30,34] Taking into account this result, it is reported that the protonation of the T_1 state of TH^+ lowers the energy of this state by ~ 0.4 eV. In an early study using semiempirical SCF MO(CI) calculations, Sommer and Kramer[162] studied the site of protonation of the triplet state of TH^+. In this study they calculated an energy of 0.75 eV in vacuum for the $T_1(\pi_H \rightarrow \pi_L^*)$ state of TH_2^{2+}. The calculated DFT/MRCI adiabatic energies of the $T_1(\pi_H \rightarrow \pi_L^*)$ state in this work are between 0.70 and 0.90 eV in aqueous solution while the TD-B3LYP/TZVP level of theory locate this state even a lower energies (0.40 - 0.56 eV). This means that that with the theoretical methods used, a very underestimated value of the $T_1(\pi_H \rightarrow \pi_L^*)$ state of TH_2^{2+} is obtained and should be used with caution. Therefore, we take into account both models (the $TH_2^{2+}3W$ and the $TH_2^{2+}3W_{(wc)}$) for describing the energetic behavior of the adiabatic electronic states in further discussions.

6.2.2.3. T: Vertical spectrum

As already stated in Section **3.5**, T is expected to be formed in basic aqueous solution. Eight models in total were built for studying the hydration effects on the electronic structure of T. Model TC includes exclusively implicit solvation effects using COSMO. For five of the models, micro-hydration with up to five

water molecules and embedding the complexes in a COSMO environment were used for optimizing their ground state minima (T1W-T5W), see **Fig. 32**. For benchmarking proposes, the $T4W_{(wc)}$ and $T5W_{(wc)}$ hydrogen bonded complexes optimized in vacuum (without COSMO) were included in the analysis for comparison and these geometries can be found in the SI Section **6.4** (**Fig. 34**).

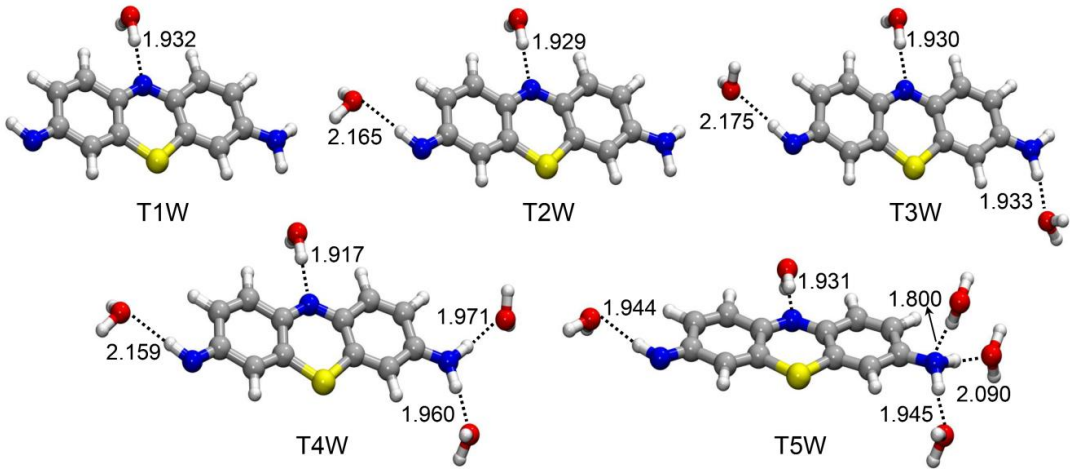

Fig. 32 Ground state minimum of the T-water hydrogen bonded complexes optimized with COSMO at the B3LYP/TZVP level. Numbers indicate hydrogen bond lengths in Å.

Let us first describe the solvation effects on the geometry of T analyzing the ground states minima of the models optimized in a COSMO environment. Interesting geometrical trends are found when successively adding water molecules. Starting with the model TC, the geometry of T is preserved non-planar with bond lengths and angles that resemble those of the ground state geometry found for the isolated molecule. This also holds for the complexes T1W and T2W. In T1W, a water molecule forms an $O\text{-}H^{\cdots}N_{ring}$ hydrogen bond. The complex T2W includes a second water molecule placed at the imino group and stabilized by an $N_{imino}\text{-}H \cdots O$ hydrogen bond. In contrast, the minimum of models T3W and T4W has an almost planar geometry of T (<C-C-N_{amine}-H less than 5°). These models contain one and two water molecules forming $N_{amine}\text{-}H \cdots O$ hydrogen bonds, respectively. As can be

seen in **Fig. 26**, the barrier for the pyramidalization of the amine group is very small. Therefore, the stabilizing interaction of the N_{amine}-H ⋯ O hydrogen bonds at the amine groups may easily cause these geometrical effects. However, if an additional water molecule is hydrogen bonded to the lone-pair of the nitrogen atom of the amine group (model T5W, O-H ⋯ N_{amine} hydrogen bond), it is again pyramidalized (<C-C-N_{amine}-H of 24°). The H ⋯ N_{amine} hydrogen bond length obtained at the T5W complex is significantly shorter (1.800 Á, see **Fig. 32**) than the same bond in the micro-hydrated model TH^+3Wb (for TH^+, **Fig. 11**), which has a length of 2.181 Á. This shows a more attractive H ⋯ N_{amine} interaction for model T5W. Regarding the pyramidalization of the amine group of T upon the interaction with water molecules, the same trends are found when the COSMO environment is not used during the geometry minimization ($T4W_{(wc)}$ and $T5W_{(wc)}$, see **Fig. 34**).

Some important differences in the vertical DFT/MRCI energies of the excited states calculated with the different solvation models were obtained. For simplicity here we summarize only the most relevant features found for T4W and T5W as representative hydration models (**Fig. 28** and **Table 28**) and compare these results to the vertical spectra calculated at $T4W_{(wc)}$ and $T5W_{(wc)}$ complexes. The information regarding the other models (T1W-T3W) can be found in the SI, Section **6.4**. The vertical ordering of the low-lying excited states in the water models is different with respect to the ones obtained in vacuum. At a glance, the calculated values for the $S_1(\pi_H \rightarrow \pi_L^*)$ optically bright transition are in reasonable agreement with the experimental absorption band in aqueous solution (2.39[37] and 2.44 eV[38]). In fact, the vertical energy of the $S_1(\pi_H \rightarrow \pi_L^*)$ state calculated at the T4W geometry nicely reproduces the second value. The corresponding excitation energy calculated at the T5W model is 0.11 eV higher. The oscillator strength for this transition computed with both models is increased, but is substantially higher for the T4W geometry ($f(L) = 0.759$). Similar trends are found for the vertical energies of this bright state calculated with the $T4W_{(wc)}$ and $T5W_{(wc)}$ models.

Nevertheless, these excitation energies are substantially higher than those obtained including the COSMO environment (**Table 28**).

The energetic (de)stabilization of the excited states in polar solvents is related to their dipole moments and the extent of polarization they induce in the surrounding solvent. As is to be expected, the π→π* states are red-shifted. The energy shifts for both low-lying π→π* excited states of the singlet manifold are in between 0.12 and 0.37 eV, for which those calculated with the T4W model are appreciably higher. Whereas the *n*→π* states are only slightly shifted to higher energies due to hydration. The destabilization caused by the environment to the $n_{H-4}\rightarrow\pi_L^*$ transition is low (0.09 and 0.07 eV). These energy shifts cause a reverse ordering of the S_2 and S_3 excited states: the corresponding $S_3(\pi_{H-1}\rightarrow\pi_L^*)$ state in vacuum to be the second singlet excited and the $S_2(n_{H-4}\rightarrow\pi_L^*)$ transition to be the third singlet excited state in aqueous solution. Moreover, the $S_2(n_{H-4}\rightarrow\pi_L^*)$ state in water presents an additional contribution of an $n_{H-5}\rightarrow\pi_L^*$ excitation. The energetic separation between these states (ΔE_{S2-S3}) is relatively larger in aqueous solution compared to vacuum, where it becomes 0.41 eV for model T4W and 0.24 eV for model T5W. As found in vacuum, the $\pi_{H-1}\rightarrow\pi_L^*$ transition (corresponding to the S_3 state) is a bright state with a $f(L) = 0.233$ in the T5W model. Interestingly, the oscillator strength of this transition vanishes in the case of model T4W (which either holds for model T3W, where also a planar T geometry is found). Here, It is important to note that the oscillator strength for this same transition in vacuum calculated at the planar saddle point of T is $f(L) = 0.194$. For the triplet states, the energetic stabilization induced by solvent effects is stronger for the $T_2(\pi_{H-1}\rightarrow\pi_L^*)$ state (0.24 and 0.16 eV) than for the $T_1(\pi_H\rightarrow\pi_L^*)$ state (0.16 and 0.08 eV). Due to the destabilization of the $T_3(n_{H-4}\rightarrow\pi_L^*)$ state by 0.14 eV and the small stabilization of the $T_4(\pi_{H-2}\rightarrow\pi_L^*)$ state (0.08 eV), their energetic ordering is reversed in the model T4W. Nevertheless, at model T5W these states are degenerate ($\Delta E_w = 3.17$ eV).

Table 28 Vertical excitation energies ΔE_w (eV) of the low-lying singlet and triplet states of neutral thionine (T) in aqueous solution: solvation with COSMO and micro-hydration with four and five water molecules (T4W-T5W). Oscillator strengths (length form) in parentheses.

Electronic State	Electronic structure[a]	T4W	T5W	T4W$_{(wc)}$	T5W$_{(wc)}$	Exp.
S_0	(0.91) Ground State					
S_1	(0.76) $\pi_H \rightarrow \pi_L^*$	2.44(0.759)	2.55(0.526)	2.57(0.647)	2.65(0.417)	2.44[g], 2.39[h]
S_2	(0.70) $\pi_{H-1} \rightarrow \pi_L^*$	2.83(0.053)	2.98(0.233)	2.98(0.087)	3.14(0.250)	
S_3	(0.45) $n_{H-4} \rightarrow \pi_L^*$	3.24(0.002)[b]	3.22(0.002)[b]	2.96(0.003)[b]	2.94(0.002)[b]	
	(0.23) $n_{H-5} \rightarrow \pi_L^*$					
S_4	(0.28)$\pi_H \rightarrow \pi_L^* \pi_H \rightarrow \pi_L^*$	3.39(0.004)	3.47(0.003)	3.42(0.003)	3.49(0.011)	
	(0.25) $\pi_{H-2} \rightarrow \pi_L^*$					
	(0.15) $\pi_H \rightarrow \pi_{L+1}^*$					
S_5	(0.45) $n_{H-5} \rightarrow \pi_L^*$	3.76(0.003)	3.71(0.003)	3.75(0.003)	3.70(0.003)	
	(0.21) $n_{H-4} \rightarrow \pi_L^*$					
T_1	(0.83) $\pi_H \rightarrow \pi_L^*$	1.35	1.43	1.41	1.46	
T_2	(0.74) $\pi_{H-1} \rightarrow \pi_L^*$	2.46	2.54	2.58	2.65	
T_3	(0.52) $\pi_{H-2} \rightarrow \pi_L^*$	3.13	3.17[c]	3.14	3.17	
	(0.12) $\pi_H \rightarrow \pi_{L+3}^*$					
T_4	(0.46) $n_{H-4} \rightarrow \pi_L^*$	3.22	3.17[d]	2.92[f]	2.87[f]	
	(0.30) $n_{H-5} \rightarrow \pi_L^*$					
T_5	(0.45) $n_{H-5} \rightarrow \pi_L^*$	3.61[e]	3.56[e]	3.60[e]	3.55[e]	
	(0.28) $n_{H-4} \rightarrow \pi_L^*$					
T_6	(0.55) $\pi_H \rightarrow \pi_{L+1}^*$	3.45	3.49	-	3.41	
	(0.15) $\pi_{H-3} \rightarrow \pi_L^*$					

[a]Dominant contributions (DC) at the DFT/MRCI/TZVP level of the TC model. [b]The DCs to these states are (0.6)$n_{H-4} \rightarrow \pi_L^*$ and (0.1)$n_{H-4} \rightarrow \pi_L^*$ $\pi_H \rightarrow \pi_L^*$. [c]The DCs to this state are (0.35)$\pi_{H-2} \rightarrow \pi_L^*$ and (0.19)$n_{H-4} \rightarrow \pi_L^*$. [d]The DCs to this state are (0.50)$n_{H-4} \rightarrow \pi_L^*$ and (0.13)$\pi_{H-2} \rightarrow \pi_L^*$. [e]The DCs to these states is (0.7)$n_{H-5} \rightarrow \pi_L^*$. [f]The DCs to this state is (0.7)$n_{H-4} \rightarrow \pi_L^*$.[g]From Ref. [38], aqueous solution. [h]From Ref. [37], aqueous solution.

The vertical energetic ordering of the low-lying singlet and triplet states calculated at the T4W$_{(wc)}$ and T5W$_{(wc)}$ micro-hydration models resembles more the vertical spectrum obtained in vacuum than to the other water models including COSMO. Nevertheless, the electronic structure of the excited states is somehow similar to the one obtained with the models with micro-hydration plus COSMO environment. The main contributions that characterize these energetically low-lying states are still dominant but some subtle changes are found. For example, the effects of the interaction of the dye with water are affecting the singlet excited state for which the $n_{H-4} \rightarrow \pi_L^*$ is the dominant transition. In vacuum, it is the only contributing transition (and the S_2 state) whereas in the TC model there is also a smaller contribution of a $n_{H-5} \rightarrow \pi_L^*$ excitation (and a mixing with the S_3 state). When only micro-hydration is accounted for the optimization, the T4W$_{(wc)}$ and T5W$_{(wc)}$ models,

a small contribution of an $n_{H-4}\rightarrow\pi_L^*$ $\pi_H\rightarrow\pi_L^*$ double excitation is found which is also appearing for this state in all micro-solvated models which were computed using COSMO. A similar situation could be found for the triplet state of the same character.

Assuming that the water molecules may form O-H$^{\cdots}$N$_{ring}$, N$_{amine}$-H $\cdots$ O, N$_{imino}$-H $\cdots$ O and O-H $\cdots$ N$_{amine}$ hydrogen bonds with T, and due to the better agreement with experimental measurements, we regard both complexes T4W and T5W as the best models for hydrated T. It is difficult to know in this case whether the geometry of T is more stable in the T4W or in the T5W model in order to study the photophysics in aqueous solution. The calculated DFT/MRCI binding energies of the models T5W and T5W$_{(wc)}$ are more negative than for the models T4W and T4W$_{(wc)}$. Nevertheless, the difference on the binding energies between the T5W and T4W models $\sim$ 5 kJ/mol. For the complexes in vacuum, the binding energies for the T5W$_{(wc)}$ model is $\sim$ 44 kJ/mol more negative than that of the T4W$_{(wc)}$ model. This shows that the non-planar dye is more stable than the planar geometry in this medium. Due to their rather similar binding energies calculated using the COSMO environment, the latter argument might not hold for the description of the dye in aqueous solution.

6.2.2.4. T: Adiabatic energies

The DFT/MRCI adiabatic energies of the S_1, S_3, T_1 and T_2 $\pi\rightarrow\pi^*$ excited states of T computed at their corresponding minima are presented in **Table 29**. The discussion in Section **6.2.2.3** opened the question which geometry of T (a planar or a non-planar arrangement of the hydrogen atoms of the amine group) is more stable in aqueous solution. Hence, we explored the PESs of this excited states at the T4W (where T posses a planar geometry) and the T5W (where T is non-planar) models. The optimization of the excited states was performed as follows. The $S_1(\pi_H\rightarrow\pi_L^*)$ and S_3,$T_2(\pi_{H-1}\rightarrow\pi_L^*)$ states of the T4W and T5W models were optimized at the TD-B3LYP/TZVP(COSMO) level

of theory. For minimizing the $T_1(\pi_H \rightarrow \pi_L^*)$ states, unrestricted DFT calculations at the UB3LYP/TZVP(COSMO) theoretical level were carried out. For the T4W and $T5W_{(wc)}$ models, the same procedures were followed, but the computations were performed without COSMO. For all the $\pi \rightarrow \pi^*$ states examined here, all the adiabatic energies calculated at the each of the solvation models are lower than in vacuum (redshifted, see **Table 29**).

Table 29 Adiabatic excitation energies ΔE_w^{ad} (eV) in water of the excited states of T. Oscillator strengths for emission at the excited-state minimum are listed in parentheses.

State	Electronic structure[a]	ΔE_w^{ad}(DFT/MRCI)	ΔE_w^{ad}(TD-B3LYP)
	T4W		
S_1	$(0.67)\pi_H \rightarrow \pi_L^*$	2.02(0.457)	2.22(0.275)
S_3	$(0.78)\pi_{H-1} \rightarrow \pi_L^*$	2.56(0.014)	2.51(0.151)
T_1	$(0.87)\pi_H \rightarrow \pi_L^*$	0.94[c]	0.42[b]
T_2	$(0.78)\pi_{H-1} \rightarrow \pi_L^*$	2.12	1.84
	$T4W_{(wc)}$		
S_1	$(0.67)\pi_H \rightarrow \pi_L^*$	1.96(0.457)	2.10(0.275)
S_3	$(0.78)\pi_{H-1} \rightarrow \pi_L^*$	2.49(0.014)	2.46(0.151)
T_1	$(0.87)\pi_H \rightarrow \pi_L^*$	1.08[c]	-[d]
T_2	$(0.78)\pi_{H-1} \rightarrow \pi_L^*$	2.04	1.79
	T5W		
S_1	$(0.65)\pi_H \rightarrow \pi_L^*$ $(0.13)\pi_{H-1} \rightarrow \pi_L^*$	2.08(0.291)	2.15(0.208)
S_3	$(0.73)\pi_{H-1} \rightarrow \pi_L^*$	2.64(0.085)	2.56(0.172)
T_1	$(0.86)\pi_H \rightarrow \pi_L^*$	0.92[c]	0.26[b]
T_2	$(0.77)\pi_{H-1} \rightarrow \pi_L^*$	2.13	1.86
	$T5W_{(wc)}$		
S_1	$(0.65)\pi_H \rightarrow \pi_L^*$ $(0.13)\pi_{H-1} \rightarrow \pi_L^*$	2.38(0.291)	2.39(0.208)
S_3	$(0.73)\pi_{H-1} \rightarrow \pi_L^*$	2.59(0.085)	2.53(0.172)[b]
T_1	$(0.86)\pi_H \rightarrow \pi_L^*$	1.05[c]	-[d]
T_2	$(0.77)\pi_{H-1} \rightarrow \pi_L^*$	2.07	1.82
	Applying hydration shifts[e]		
S_1	$(0.66)\ \pi_H \rightarrow \pi_L^*$ $(0.10)\ \pi_{H-1} \rightarrow \pi_L^*$[f]	2.26[e]	-
S_3	$(0.62)\ \pi_{H-1} \rightarrow \pi_L^*$[f]	2.79[e]	-
T_1	$(0.85)\ \pi_H \rightarrow \pi_L^*$[f]	1.08[e]	-
T_2	$(0.72)\ \pi_{H-1} \rightarrow \pi_L^*$[f]	2.35[e]	-

[a]Dominant contributions at the DFT/MRCI/TZVP level. [b]Single point TDDFT calculation at the optimized UB3LYP/TZVP geometry. [c]Single point DFT/MRCI calculation at the UB3LYP/TZVP optimized structure. [d]Not possible to calculate the TD-B3LYP/TZVP energy due to triplet instabilities. [e]Adiabatic excitation energies calculated applying the vertical hydration shifts (from the T5W model) to the adiabatic states in vacuum. [f]Dominant contributions of the adiabatic excited states in vacuum from **Table 24**.

Within the T4W and T5W models which are embedded in a COSMO environment, both models reproduce nearly the same DFT/MRCI adiabatic energy for the $S_1(\pi_H \rightarrow \pi_L^*)$ and $S_3(\pi_{H-1} \rightarrow \pi_L^*)$ states. The excited states

calculated at the T4W model are energetically more stable than those calculated at the non-planar T geometry of the T5W model by only 0.06 and 0.08 eV. For the $T_1(\pi_H \rightarrow \pi_L^*)$ and $T_2(\pi_{H-1} \rightarrow \pi_L^*)$ states the DFT/MRCI adiabatic energies are even more similar than for the singlet states, where differences between 0.01 and 0.02 eV are observed. Nevertheless, these small shifts lead to a rather different distribution of the states at both hydration models: while the $T_2(\pi_{H-1} \rightarrow \pi_L^*)$ state is energetically separated from the $S_1(\pi_H \rightarrow \pi_L^*)$ state by 0.10 eV in T4W, this energy difference is half as large in the T5W model, placing these states nearly at the same energy. As observed in vacuum, the $T_1(\pi_H \rightarrow \pi_L^*)$ state is located energetically below the $S_1(\pi_H \rightarrow \pi_L^*)$ state with a large energy gap (see **Table 29**). The DFT/MRCI adiabatic energy of the $T_1(\pi_H \rightarrow \pi_L^*)$ state in these models has been computed to be in the range 0.92 - 0.94 eV. At the level of TD-B3LYP/TZVP these states have even lower energies (0.26 - 0.42 eV).

The calculated DFT/MRCI adiabatic excitation energies of the excited states are similar for when comparing the models optimized with and without COSMO which may be due to the insufficient description of the excited state solvent polarization. Examining the energetic behavior of the $T4W_{(wc)}$ cluster, where a planar structure of T is present, the DFT/MRCI adiabatic energies of the two singlet states have the lowest value (compared to the other clusters studied). While the triplet states of the $T5W_{(wc)}$ model show up at similar excitation energy relative to those calculated at $T4W_{(wc)}$, the singlet states of the $T5W_{(wc)}$ complex are appreciably destabilized (by 0.42 eV for the $S_1(\pi_H \rightarrow \pi_L^*)$ state and by 0.10 eV for the $S_3(\pi_{H-1} \rightarrow \pi_L^*)$ state). At the $T4W_{(wc)}$-$T5W_{(wc)}$ models, the DFT/MRCI adiabatic energies of the $T_1(\pi_H \rightarrow \pi_L^*)$ state show that it is destabilized (~0.14 eV) compared to the adiabatic energy calculated at the T4W-T5W models. The contrary occurs for the $T_2(\pi_{H-1} \rightarrow \pi_L^*)$ states, which the $T4W_{(wc)}$-$T5W_{(wc)}$ models predict it to be located at lower energies compared to the T4W-T5W models including COSMO. While almost all models predicts the $T_2(\pi_{H-1} \rightarrow \pi_L^*)$ state to be above the $S_1(\pi_H \rightarrow \pi_L^*)$ state,

the $T5W_{(wc)}$ model predicts a different pattern. At the $T5W_{(wc)}$ model the $T_2(\pi_{H-1}\rightarrow\pi_L^*)$ state is located energetically below the $S_1(\pi_H\rightarrow\pi_L^*)$ state by ~0.10 eV due to the high adiabatic energy that the latter adopts at this geometrical configuration and without the inclusion of electrostatic interaction effects due to the COSMO environment. Here, this difference accounts to 0.30 eV of the adiabatic energy of the $S_1(\pi_H\rightarrow\pi_L^*)$ state comparing the T5W and the $T5W_{(wc)}$ models.

The DFT/MRCI adiabatic energies of T in aqueous solution have also been calculated applying the vertical adiabatic hydration shifts (employing **Eq 93**) and are also listed at the bottom of **Table 29** for comparison. As the geometry of T in the T5W cluster resembles the non-planar geometry of the ground state minimum obtained in vacuum, we chose this model for applying the spectroscopic solvation shifts to the adiabatic energies of the excited states in vacuum. These results show that for hydrated T, applying the solvent shifts, the DFT/MRCI adiabatic energies of the S_1, S_3, T_1 and T_2 $\pi\rightarrow\pi^*$ states are overestimated compared to most of the other solvation models. However, when solvation shifts are applied, the interest is in the energy gaps between singlet and triplet states than in the adiabatic energies per se. Because there is no experimental data avaliable for comparison with the adiabatic energies calculated here, it is important to take into account the different solvation interactions for comparison. The T4W and T5W models can both be expected in aqueous solution (taking into account the more complete theoretical description of system) and their stability will depend on lifetime of the $C\text{-}N_{amine}\cdots H$ hydrogen bond.

6.2.3. (De)Protonation equilibrium and effects on the singlet oxygen production

In this subsection, we aim to understand in more detail the ground and $T_1(\pi_H\rightarrow\pi_L^*)$ state protonation and deprotonation equilibrium of TH^+. Our results are compared with the experimental trends. The calculated DFT/MRCI

proton affinities at the ground and $T_1(\pi_H \rightarrow \pi_L^*)$ states of TH^+ and T are listed in **Table 30**.

Table 30 Calculated DFT/MRCI proton affinities in kJ/mol of TH^+ and T in vacuum.

Proton affinities	PA
@Ground states	
$TH^+ + H^+ \rightarrow TH_2^{2+}$	662.1[a]
$T + H^+ \rightarrow TH^+$	1108.2[a]
@Triplet states	
$^3TH^+ + H^+ \rightarrow {}^3TH_2^{2+}$	724.6[a]
$^3T + H^+ \rightarrow {}^3TH^+$	1062.6[a]

In aqueous solution, it is well known that the deprotonation of the ground state of TH^+ to T occurs easily (pK_a = 9.0)[37-38] than its protonation to TH_2^{2+} (pK_a = -0.3).[20-30] Here, we briefly describe this behavior comparing the proton affinities of the corresponding processes, see **Table 30**. For the isolated TH^+ and T, the calculated proton affinity of T is nearly twofold (1108.2 kJ/mol) than for TH^+ (662.1 kJ/mol). These results reflect the greater stability of the monoprotonated TH^+ specie than for TH_2^{2+}. This explains why the protonation of TH^+ is more difficult than its deprotonation in the ground state. Because of these proton affinities are not available from experimental measurements, it is pertinent to state that our DFT/MRCI calculations reproduce the experimental reported trends in aqueous solution (see Section **3.5**).

Regarding to the (de)protonation of the $S_1(\pi_H \rightarrow \pi_L^*)$ state of TH^+, it have not been detected experimentally perhaps because the ISC ($k_{ISC} \sim 10^9\ s^{-1}$) and fluorescence ($k_F \sim 10^8\ s^{-1}$) from this state are faster than a protonation reaction (if it takes place). Starting from the point that the protonation of the $T_1(\pi_H \rightarrow \pi_L^*)$ state of TH^+ is a very fast process at a pH close to neutral with a determined rate constant of the bimolecular decay of $k_{Pr} = 8.3 \times 10^9\ M^{-1}\ s^{-1}$ (21°C) [35], then it is reasonable that the protonation at the $S_1(\pi_H \rightarrow \pi_L^*)$ state of TH^+ cannot compete with ISC. Therefore, in the following we focus in the

triplet state equilibrium and we analyze the subsequent consequences in the singlet oxygen production. An overview of the calculated DFT/MRCI adiabatic energy gaps between the $T_1(\pi_H \rightarrow \pi_L^*)$ states of TH_2^{2+}, TH^+ and T in vacuum, and taking into account solvent effects is given in **Fig. 33**.

In aqueous solution and at pH close to neutral, the quantity of the $^3TH_2^{2+}$ form should be larger than that of ^3T.‡‡‡‡ As the pH become more and more basic, the concentration of ^3T is expected to be raised.[36] Comparing the adiabatic energies of the $T_1(\pi_H \rightarrow \pi_L^*)$ states of TH_2^{2+}, TH^+ and T, it is seen that the protonation of $^3TH^+$ releases more energy (ΔE_1) than the deprotonation (ΔE_2) as schematically seen in **Fig. 33**. The DFT/MRCI proton affinity of the adiabatic $^3TH^+$ state is 724.6 kJ/mol, which is 62.5 kJ/mol higher than that calculated in the ground state (see **Table 30**). The higher proton affinity of $^3TH^+$ reflects its increased basicity compared to the ground state of TH^+ experimentally observed in aqueous solution. The proton affinity of ^3T becomes lower (by 45.6 kJ/mol) in vacuum, which reflect the slightly lower pK_a of $^3TH^+$ for the corresponding equilibrium ($pK_a \sim 9.0$) compared to its gound state ($pK_a \sim 10$).[36]

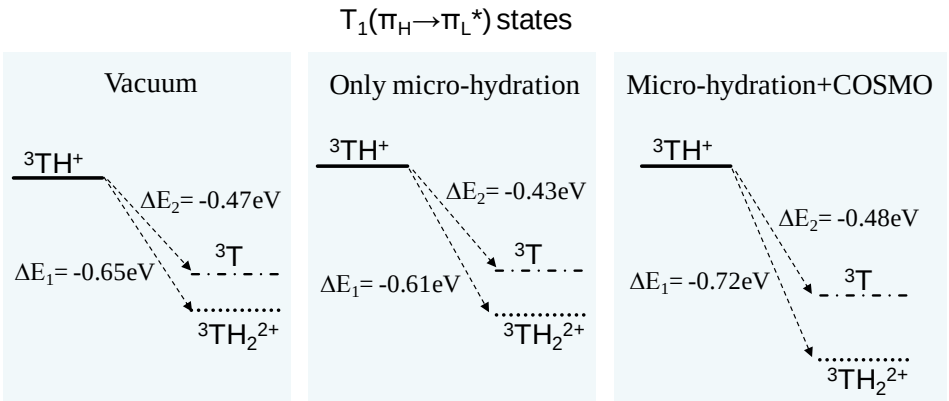

Fig. 33 Illustration of the DFT/MRCI adiabatic energy gaps between the $T_1(\pi_H \rightarrow \pi_L^*)$ states of TH_2^{2+}, TH^+ and T in vacuum, and taking into account solvent effects through micro-hydration ($TH^+3W_{(wc)}$, $TH_2^{2+}3W_{(wc)}$ and $T4W_{(wc)}$ models) and COSMO environment (TH^+3W, $TH_2^{2+}3W$ and T4W models).

‡‡‡‡ Here ^3T, $^3TH^+$ and $^3TH_2^{2+}$ refer to the $T_1(\pi_H \rightarrow \pi_L^*)$ state of the dyes for simplicity.

In the context of the singlet oxygen ($^1O_2(^1\Delta_g)$) production of these protonation states (as mentioned in Section **3.5**), a significantly smaller rate constant of oxygen quenching has been determined for $^3TH_2^{2+}$ ($k_{ox} = 1.5 \times 10^9\ M^{-1}\ s^{-1}$) than by $^3TH^+$ ($k_{ox} = 2.7 \times 10^9\ M^{-1}\ s^{-1}$). These rate constants show also that the energy transfer of the $^3O_2(^3\Sigma_g^-)$ with $^3TH^+$ might compete with the very fast protonation process of $^3TH^+$ ($k_{Pr} = 8.3 \times 10^9\ M^{-1}\ s^{-1}$ [35]) at pH close to neutral. When $^3TH_2^{2+}$ is formed, its interaction with $^3O_2$ to form $^1O_2$ is, according to our calculations, an endergonic process. Let us explain this in more detail in the following. The interaction of $^3O_2$ and organic dyes is believed to happen through the so-called excitation energy transfer mechanism between the photosensitizer in its lowest triplet (long-lived) excited state and $^3O_2$.[220-222] This energy transfer is triggered by electronic coupling between the dye in an excited state that acts as a donor and $^3O_2$ that acts as an acceptor. The interaction of the dye and $^3O_2$ form a collision complex, for which has been proposed that this mechanism strongly depends on their inter-fragment distance.[222-223] Nevertheless, the study of such excited state collision complex is very difficult within the framework of the actual quantum chemical methods (*e. g.* dispersion corrected PESs of the excited states of the complex are needed). The triplet-triplet energy transfer mechanism is a process that exchanges both spin and energy between the molecules. In this case, the electronic coupling is not the only factor that determines the efficiency of the energy transfer process but also a resonance condition. This means that the energy available in the donor must be at least equal or higher than that required to populate the excited state of the acceptor ($^1O_2$). This process is usually diffusion controlled and releases energy. When the energy of the donor is lower than that of the acceptor, the process becomes thermally activated and could lie in the endothermic region. This means that there is an energy barrier whose height will depend also on the nature of the acceptor with a larger or smaller decay in the process rate constant.[224] Lets us analyze these energy barriers in the actual context,

which helps to understand the protonation effects on the $^1O_2$ production of $^3TH^+$.

It has been argued by R. Bonneau et al. that the lower rate constant of oxygen quenching for $^3TH_2^{2+}$ reflects the lower energy of this state compared to $^3TH^+$ (1.28 *vs* 1.69 eV).[34] It was suggested that a reversible energy transfer between the $^1O_2$ and the sensitizer is possible, because of the energy of $^3TH_2^{2+}$ was found to be near to the $^1O_2$ energy level (0.97 eV[221]), therefore:

$$^3O_2(S_0) + {}^3TH_2^{2+} \rightleftharpoons {}^1O_2 + {}^1TH_2^{2+}(S_0)$$

Using the energy of the two molecules in the ground state as reference (0.00 eV), the ΔE of the reaction can be calculated as $\Delta E(^1O_2$-$^3TH_2^{2+}) = -0.31$ eV, considering the experimentally determined values. The same energy gap, but taking into account the calculated DFT/MRCI adiabatic energies for the $^3TH_2^{2+}$ state, is in the range of $-0.01_{(in\ vacuum)} < \Delta E(^1O_2$-$^3TH_2^{2+}) < 0.27_{(with\ solvent\ effects)}$ eV may be considered appropriated for this reversible process (**Table 22** and **Table 27**).

Since the energy of the ^3T state has not been determined experimentally in aqueous solution, there is no data for comparing our results in this case. Nevertheless, for the interaction of $^3O_2$ with ^3T there should be a similar situation than for $^3TH_2^{2+}$ solely comparing the energy gaps. As the calculated DFT/MRCI adiabatic energies of ^3T in vacuum and within the solvation models are slightly higher than that of $^1O_2$, this process is rather more exotermic: $-0.19_{(in\ vacuum)} < \Delta E(^1O_2$-$^3T) < -0.11_{(with\ solvent\ effects)}$ eV (**Table 24** and **Table 29**). On the other hand, for $^3TH^+$ this gap is calculated within an interval of $-0.66_{(in\ vacuum)} < \Delta E(^1O_2$-$^3TH^+) < -0.45_{(with\ solvent\ effects)}$ eV. These DFT/MRCI energy gaps correlate well with the trend of the reported rate constants of quenching of oxygen (k_{ox}) shown in **Table 3**: $^3TH^+ > {}^3T > {}^3TH_2^{2+}$.

6.2.4. Effects of the protonation state on the ISC efficiencies

In this section, the protonation effects on ISC rate constants ($k_{\mathrm{ISC}}^{\mathrm{TD}}$) of TH^+ are analyzed. These effects will reflect the rates and the available ISC channels in the pH medium where the corresponding species are present: in very acid aqueous solution in the case of TH_2^{2+} and basic aqueous solution in the case of T. The calculated ISC rate constants for T, TH_2^{2+} and TH^+ within the time-dependent approach and taking vibronic spin-orbit coupling into account are shown in **Table 31**. For the adiabatic energy gaps in water displayed in this table, the following solvation models were taken into account: *i*) for TH_2^{2+} the TH_2^{2+}3W model, *ii*) for TH^+ applying the vertical hydration shifts to the adiabatic energies in vacuum, *iii*) for T the T5W model. The solvation effects to the ISC rate constants were calculated applying the energy gaps obtained within the models explained above and using the vibrational frequencies and ∂SOMEs obtained in vacuum. Furthermore, the linearly interpolated pathways between the adiabatic electronic states in vacuum of TH_2^{2+} and T displayed in **Fig. 25** and **Fig. 30** are also analyzed. The calculated SOMEs and ∂SOMEs are listed in **Table 38** to **Table 39** at the SI (Section **6.4**) since their calculated values between the states of interest are low, therefore, we focusing our analysis to the ISC process.

In vacuum, the $T_1(\pi_H \rightarrow \pi_L^*)$ and $T_2(\pi_{H-1} \rightarrow \pi_L^*)$ states of TH_2^{2+} are energetically available for ISC from the $S_1(\pi_{H-1} \rightarrow \pi_L^*)$ state. The calculated ISC rate constants for the corresponding $S_1(\pi_{H-1} \rightarrow \pi_L^*)$ ⇝ $T_1(\pi_H \rightarrow \pi_L^*)$ and $S_1(\pi_{H-1} \rightarrow \pi_L^*)$ ⇝ $T_2(\pi_{H-1} \rightarrow \pi_L^*)$ channels are $k_{\mathrm{ISC}}^{\mathrm{TD}} = 3.86 \times 10^7\ s^{-1}$ and $k_{\mathrm{ISC}}^{\mathrm{TD}} = 9.46 \times 10^7\ s^{-1}$ (**Table 31**), where in this case we expect the latter to dominate the photophysical kinetics. These ISC rate constants are at least three orders of magnitude faster than the fluorescence rate ($k_F = 8.56 \times 10^3\ s^{-1}$) from the $S_1(\pi_{H-1} \rightarrow \pi_L^*)$ state. When solvation effects are taken into account, the DFT/MRCI adiabatic energy gaps between these states is higher where the effect is more prominent for the

$S_1(\pi_{H-1}\rightarrow\pi_L^*)$ ⇝ $T_1(\pi_H\rightarrow\pi_L^*)$ channel (by 0.29 eV) and negligible for the $S_1(\pi_{H-1}\rightarrow\pi_L^*)$ ⇝ $T_2(\pi_{H-1}\rightarrow\pi_L^*)$ transition (by 0.02 eV). The calculated ISC rate constants within these energy gaps are $k_{\mathrm{ISC}}^{\mathrm{TD}} = 1.68 \times 10^7$ s^{-1} and $k_{\mathrm{ISC}}^{\mathrm{TD}} = 1.03 \times 10^8$ s^{-1}, respectively. Comparing these results to the rate constants obtained for TH^+, ISC in vacuum competes with fluorescence and both are of the same order of magnitude ($\sim 10^8$ s^{-1}). The dominant ISC channel corresponds to an $S_1(\pi_H\rightarrow\pi_L^*)$ ⇝ $T_2(\pi_{H-1}\rightarrow\pi_L^*)$ transition, while transitions from the $S_2(\pi_{H-1}\rightarrow\pi_L^*)$ state have been calculated to be slower ($k_{\mathrm{ISC}}^{\mathrm{TI}} \sim 10^6$ s^{-1}). Solvation effects on TH^+ make the ISC process to succeed fluorescence, with an ISC rate constant which is enhanced by just one order of magnitude. We therefore can conclude that in very acid aqueous solution, where TH_2^{2+} protonation state is present (i.e. from photoexcited TH_2^{2+}), the population of the triplet manifold is expected to be very efficient.

Table 31 Calculated (time-dependent) rate constants $k_{\mathrm{ISC}}^{\mathrm{TD}}$(s^{-1}) for the S_i⇝T_i (i = 1, 2) ISC channels and the adiabatic excitation energy differences ΔE^{ad} (eV) between the corresponding electronic states for TH_2^{2+}, TH^+ and T species.

Channel	TH_2^{2+}		TH^+		T	
	ΔE^{ad}	$k_{\mathrm{ISC}}^{\mathrm{TD}}$	ΔE^{ad}	$k_{\mathrm{ISC}}^{\mathrm{TD}}$	ΔE^{ad}	$k_{\mathrm{ISC}}^{\mathrm{TD}}$
			Vacuum			
$^1(\pi_H\rightarrow\pi_L^*)$⇝$^3(\pi_H\rightarrow\pi_L^*)$	-0.87	6.50×10^7	-0.64	$3.57 \times 10^{6\,a}$	-1.22	1.31×10^6
$^1(\pi_H\rightarrow\pi_L^*)$⇝$^3(\pi_{H-1}\rightarrow\pi_L^*)$	-0.50	6.04×10^8	-0.30	$7.59 \times 10^{8\,a}$	+0.13	$8.17 \times 10^{7\,c}$
$^1(\pi_{H-1}\rightarrow\pi_L^*)$⇝$^3(\pi_H\rightarrow\pi_L^*)$	-0.64	3.86×10^7	-0.66	$\sim 10^{6\,b}$	-	-
$^1(\pi_{H-1}\rightarrow\pi_L^*)$⇝$^3(\pi_{H-1}\rightarrow\pi_L^*)$	-0.27	9.46×10^7	-0.32	$\sim 10^{6\,b}$	-	-
			Water			
$^1(\pi_H\rightarrow\pi_L^*)$⇝$^3(\pi_H\rightarrow\pi_L^*)$	-0.97^d	-	-0.68^e	$2.52 \times 10^{6\,a}$	-1.16^f	1.81×10^6
$^1(\pi_H\rightarrow\pi_L^*)$⇝$^3(\pi_{H-1}\rightarrow\pi_L^*)$	-0.41^d	7.91×10^8	-0.21^e	$1.07 \times 10^{9\,a}$	+0.05^f	1.05×10^{9c}
$^1(\pi_{H-1}\rightarrow\pi_L^*)$⇝$^3(\pi_H\rightarrow\pi_L^*)$	-0.85^d	1.68×10^7	-0.77^e	-	-	-
$^1(\pi_{H-1}\rightarrow\pi_L^*)$⇝$^3(\pi_{H-1}\rightarrow\pi_L^*)$	-0.29^d	1.03×10^8	-0.30^e	-	-	-

[a] $k_{\mathrm{ISC}}^{\mathrm{TD}}$ from Section **5.2.5**. [b] $k_{\mathrm{ISC}}^{\mathrm{TI}}$ from Section **5.2.4.1**. [c]Rate computed at T = 298 K. [d]DFT/MRCI adiabatic energy gap calculated at the minima computed for the TH_2^{2+}3W model. [e]DFT/MRCI energy gaps calculated applying the spectroscopic hydration shifts to the adiabatic energies in vacuum using the TH^+3W model. [f]DFT/MRCI adiabatic energy gap calculated at the minima computed for the T5W models.

The ISC channels arising from the bright $S_2(\pi_H\rightarrow\pi_L^*)$ state of TH_2^{2+}, as already stated before, are not accessible from the FC region (see, **Fig. 25(a)**). The parallel tracks between the $S_1(\pi_{H-1}\rightarrow\pi_L^*)$ and $S_2(\pi_H\rightarrow\pi_L^*)$ states PESs at the interpolated pathways between the S_1 - T_1 and S_1 - T_2 geometries **Fig.**

25(b-c) show that the population of the $S_2(\pi_H \rightarrow \pi_L^*)$ state is also not possible from the $S_1(\pi_{H-1} \rightarrow \pi_L^*)$ minimum. Because the adiabatic energy separation between the $S_1(\pi_{H-1} \rightarrow \pi_L^*)$ and $S_2(\pi_H \rightarrow \pi_L^*)$ state is appreciable ($\Delta E_{S1\text{-}S2}$ = -0.23 eV), IC from the former is not expected in vacuum. In fact, the interpolated pathways starting from the $S_2(\pi_H \rightarrow \pi_L^*)$ state show a conical intersection between these states but at high energies and at large geometry displacements. Nevertheless, the large oscillator strength of the $S_2(\pi_H \rightarrow \pi_L^*)$ state could allow its population to some extent and ISC rates arising from this state were also computed. The ISC rate constants for the $S_2(\pi_H \rightarrow \pi_L^*) \dashrightarrow T_1(\pi_H \rightarrow \pi_L^*)$ and $S_2(\pi_H \rightarrow \pi_L^*) \dashrightarrow T_2(\pi_{H-1} \rightarrow \pi_L^*)$ channels in **Table 31** show to be also efficient ($k_{\mathrm{ISC}}^{\mathrm{TD}} \sim 10^7$-$10^8$ s^{-1}). Being the S_2 - T_2 energy gap higher than that for S_1 - T_2 pair in both vacuum and aqueous medium, the ISC rate constant of the former is higher than for the latter. This finding is reasonable due to the higher vibronic spin-orbit coupling induced by the different electronic transitions that characterizes the initial and final states. If the $S_2(\pi_H \rightarrow \pi_L^*)$ state of TH_2^{2+} is populated, a faster ISC is possible than from the $S_1(\pi_{H-1} \rightarrow \pi_L^*)$ state.

In aqueous solution at basic pH the situation is rather different. For T, the only energetically available ISC pathway is the $S_1(\pi_H \rightarrow \pi_L^*) \dashrightarrow T_1(\pi_H \rightarrow \pi_L^*)$ channel. The energy gap between these states is very high in vacuum and in aqueous solution ($\Delta E_{T1\text{-}S1}$ = -1.22 and -1.16 eV). The calculated ISC rate constant are in the order of $k_{\mathrm{ISC}}^{\mathrm{TD}} \sim 10^6$ s^{-1} (see **Table 31**) both in vacuum and aqueous solution which are approximately one order of magnitude lower than the calculated fluorescence rate ($k_F = 5.32 \times 10^7$ s^{-1}). The low rate of this ISC process is also visible from the parallel tracks of the $S_1(\pi_H \rightarrow \pi_L^*)$ and $T_1(\pi_H \rightarrow \pi_L^*)$ state PESs in **Fig. 30(right)**. Moreover, the $T_2(\pi_{H-1} \rightarrow \pi_L^*)$ state of T is located 0.13 eV above the $S_1(\pi_H \rightarrow \pi_L^*)$ state in vacuum. At the FC region (see **Fig. 30(left)**), these two states are energetically close, but as the system relaxes to the $S_1(\pi_H \rightarrow \pi_L^*)$ state, the S_1 - T_2 energy gap becomes higher.

Taking into account the S_1 / T_2 conical intersection located energetically nearby the ground state geometry, a ISC $S_1(\pi_H \rightarrow \pi_L^*) \rightsquigarrow T_2(\pi_{H-1} \rightarrow \pi_L^*)$ channel could be thermally activated. Nevertheless, the computed ISC rate constant at 298 K in vacuum accounts to $k_{ISC}^{TD} = 8.17 \times 10^7\ s^{-1}$, which is able to compete with fluorescence. In aqueous solution, the $S_1(\pi_H \rightarrow \pi_L^*)$ and $T_2(\pi_{H-1} \rightarrow \pi_L^*)$ states became energetically degenerate (ΔE_{T2-S1} = +0.05 eV). As a consequence, the ISC rate constant is increased to $k_{ISC}^{TD} = 1.05 \times 10^9\ s^{-1}$ (298 K) being at least two orders of magnitude faster than fluorescence. Therefore, according to our calculations, the population of the triplet state of T is expected to be faster in aqueous solution than in vacuum. A similar conclusion was also found for TH^+, where the solvation effects also activate a fast ISC channel. Nevertheless, the probability that the $S_1(\pi_H \rightarrow \pi_L^*) \rightsquigarrow T_2(\pi_{H-1} \rightarrow \pi_L^*)$ ISC channel in T becomes accessible depends in fact that the solvation effects shift them energetically close. If the latter holds, then the ISC process in T is expected to proceed faster than in TH^+.

6.3. Conclusions

We have for the first time characterized the electronic structure of the ground and excited states of the diprotonated (TH_2^{2+}) and neutral forms (T) of thionine (TH^+). Energy descriptors were calculated for shedding light on the (de)protonation equilibrium experimentally observed for the $T_1(\pi_H \rightarrow \pi_L^*)$ state of TH^+ in aqueous solution at pH close to neutral. A number of properties like fluorescence and phosphorescence rates and the rate of intersystem crossing (ISC) were computed in order to analyze the protonation effects on the photophysics of TH^+.

A detailed analysis of the hydration effects on the electronic structure and energetics of of TH_2^{2+}, TH^+ and T was performed using several solvation models at their optimized ground and excited states. These models were built in order to take into account the different types of interaction with water: *i*) embedding the dye in a COSMO environment to take into account solely electrostatic interaction effects, *ii*) the explicit water molecules forming hydrogen bonds with the dye and *iii*) a mixture of those explicit and implicit solvent effects. Within this work, the DFT/MRCI adiabatic energy gaps between the low-lying singlet and triplet states of interest were calculated at the optimized states and were compared (were possible) to those calculated taking into account vertical solvation shifts. This analysis was performed due to its importance for describing the solvation effects on the adiabatic energy gaps between singlet and triplet states undergoing on ISC processes. We found that for TH^+, the adiabatic energies calculated at the optimized states of the solvation models resemble those calculated by adding the spectroscopic solvation shifts to the adiabatic energies calculated in vacuum. In contrast, this is not applicable for TH_2^{2+} and T in aqueous solution were these adiabatic energies significantly differ. Moreover, the vertical spectroscopic solvation shifts calculated at the solvation models of TH_2^{2+} predict blueshifts on the low-lying $\pi \rightarrow \pi^*$ excited states which does not follow the expected behavior of

these type of states in polar medium. Therefore, in this study we emphasize the importance of the exploration of the different solvent effects on the energetics of dyes for analyzing the photophysics in aqueous solution.

The DFT/MRCI adiabatic energy differences between the $T_1(\pi_H \rightarrow \pi_L^*)$ state of TH^+ and the $T_1(\pi_H \rightarrow \pi_L^*)$ state of TH_2^{2+} and T in aqueous solution show that the protonation of TH^+ (ΔE_1 = -0.43) is more exergonic than its deprotonation (ΔE_2 = -0.43). We found that the calculated DFT/MRCI proton affinity of the $T_1(\pi_H \rightarrow \pi_L^*)$ state of TH^+ is 68 kJ/mol higher than for the ground state while proton affinity of the $T_1(\pi_H \rightarrow \pi_L^*)$ state of T is lower by 45 kJ/mol than for the ground state in vacuum. This refletcts the increased basicity of the $T_1(\pi_H \rightarrow \pi_L^*)$ state of TH^+ compared to the ground state. Our calculations are in agreement with the experimentally observed behavior for these dyes.[33-175] Moreover, the calculated DFT/MRCI adiabatic energies of these triplet states give insights of the experimental observation of a much lower $^1O_2$ efficiency for TH_2^{2+} and T than for TH^+.[176,34] Our results show that the reaction of the $T_1(\pi_H \rightarrow \pi_L^*)$ state of TH_2^{2+} with $^3O_2$ to produce $^1O_2$ is endergonic (ΔE = 0.27 eV). Meanwhile, the energy transfer from the $T_1(\pi_H \rightarrow \pi_L^*)$ states of TH^+ and T to $^3O_2$ releases energy (ΔE = -0.43 and -0.11 eV), where the reaction is 4 times more exergonic for TH^+.

The pH also is found to affect the excitation energy of the states of TH^+ which have consequences in the photophysical decay of TH^+. According to our results, the protonation and deprotonation of TH^+ lead to a higher population of the triplet manifold in aqueous solution for TH_2^{2+} and T than for TH^+ ($k_F \sim 10^8$ s^{-1} and $k_{ISC} \sim 10^9$ s^{-1}):

i) In highly acidic aqueous solution: The lowest singlet excited state of TH_2^{2+} is a dark $S_1(\pi_{H-1} \rightarrow \pi_L^*)$ state. Energetically accessible from the these states are the $T_1(\pi_H \rightarrow \pi_L^*)$ and $T_2(\pi_{H-1} \rightarrow \pi_L^*)$ states. The fluorescence decay from the $S_1(\pi_{H-1} \rightarrow \pi_L^*)$ state is calculated to proceed with a very small rate constant ($k_F = 8.56 \times 10^3$ s^{-1}). The $S_1(\pi_H \rightarrow \pi_L^*) \rightsquigarrow T_2(\pi_{H-1} \rightarrow \pi_L^*)$ ISC is the

fastest energetically feasible channel, whose rate constant ($k_{ISC} \sim 10^8$ s^{-1}) is four orders of magnitude higher than the fluorescence rate constant either in vacuum and in aqueous solution.

ii) In basic aqueous solution (pH > 10): The bright $S_1(\pi_H \rightarrow \pi_L^*)$ state of T is populated after photoexcitation. The calculated fluorescence rate constant from this state amounts to $k_F = 5.32 \times 10^7$ s^{-1}. Adiabatically, only the $T_1(\pi_H \rightarrow \pi_L^*)$ state is energetically available for ISC. The calculated rate constant for this $S_1(\pi_H \rightarrow \pi_L^*) \rightsquigarrow T_1(\pi_H \rightarrow \pi_L^*)$ channel ($k_{ISC} \sim 10^6$ s^{-1}) is one order of magnitude lower than fluorescence of T. Nevertheless, the adiabatic energy of the $T_2(\pi_{H-1} \rightarrow \pi_L^*)$ state is close to that of the $S_1(\pi_H \rightarrow \pi_L^*)$ state and an ISC channel arising from these states could be thermally activated. In vacuum, the $T_2(\pi_{H-1} \rightarrow \pi_L^*)$ state is located $\Delta E_{T2\text{-}S1} = 0.13$ eV above the $S_1(\pi_H \rightarrow \pi_L^*)$ state where the ISC decay ($k_{ISC} = 8.17 \times 10^7$ s^{-1}) is predicted to compete with fluorescence. In aqueous medium, these states are energetically degenerated ($\Delta E_{T2\text{-}S1} = +0.05$ eV), and the corresponding $S_1(\pi_H \rightarrow \pi_L^*) \rightsquigarrow T_2(\pi_{H-1} \rightarrow \pi_L^*)$ process becomes activated. The calculated ISC rate constant of $k_{ISC} = 1.05 \times 10^9$ s^{-1} for this channel is found to dominate the photophysical decay kinetics of T in basic aqueous solution.

6.4. Supplementary information

Table 32 Vertical spectrum ΔE_{vac} (eV) of the low-lying singlet and triplet states of T.

Electronic State	Electronic structure[a]	DFT/MRCI/TZVP// B3LYP/TZVP[b]	TD-B3LYP/TZVP// B3LYP/TZVP[b]	Exp. values.
S_0	(0.91) Ground State			
S_1	(0.74) $\pi_H \rightarrow \pi_L^*$	2.67(0.441)	2.68(0.331)	2.44[g], 2.39[h]
S_2	(0.61) $n_{H-4} \rightarrow \pi_L^*$	3.15(0.002)	3.55(0.000)	
S_3	(0.64) $\pi_{H-1} \rightarrow \pi_L^*$	3.20(0.225)	3.21(0.212)	
S_4	(0.63) $n_{H-5} \rightarrow \pi_L^*$	3.38(0.004)	3.63(0.002)	
S_5	(0.28) $\pi_H \rightarrow \pi_L^* \pi_H \rightarrow \pi_L^*$	3.53(0.019)	-	
	(0.21) $\pi_{H-2} \rightarrow \pi_L^*$			
	(0.17) $\pi_H \rightarrow \pi_{L+1}^*$			
S_6	(0.26) $\pi_H \rightarrow \pi_{L+1}^*$	3.92(0.245)	4.03(0.109)	
	(0.18) $\pi_{H-3} \rightarrow \pi_L^*$			
S_7	(0.40) $\pi_H \rightarrow \pi_{L+2}^*$	4.29(0.007)	4.23(0.035)	
	(0.19) $\pi_{H-3} \rightarrow \pi_L^*$			
S_8	(0.25) $\pi_{H-3} \rightarrow \pi_L^*$	4.47(0.268)	4.37(0.001)[c]	
	(0.18) $\pi_H \rightarrow \pi_{L+2}^*$			
	(0.17) $\pi_H \rightarrow \pi_{L+1}^*$			
S_9	(0.49) $\pi_H \rightarrow \pi_{L+5}^*$	4.57(0.001)	4.78(0.000)	
	(0.13) $\pi_H \rightarrow \pi_{L+4}^*$			
	(0.11) $\pi_{H-1} \rightarrow \pi_{L+5}^*$			
S_{10}	(0.25) $\pi_{H-2} \rightarrow \pi_L^*$	4.66(0.172)	4.49(0.142)[d]	
S_{11}	(0.14) $\pi_H \rightarrow \pi_{L+3}^*$	4.76(0.019)	5.10(0.127)[e]	
	(0.10) $\pi_{H-1} \rightarrow \pi_{L+1}^*$			
S_{12}	(0.27) $\pi_{H-1} \rightarrow \pi_{L+1}^*$	4.97(0.199)	4.82(0.242)[f]	
T_1	(0.82) $\pi_H \rightarrow \pi_L^*$	1.51	1.20	
T_2	(0.69) $\pi_{H-1} \rightarrow \pi_L^*$	2.70	2.51	
T_3	(0.70) $n_{H-4} \rightarrow \pi_L^*$	3.08	3.04	
T_4	(0.40) $\pi_{H-2} \rightarrow \pi_L^*$	3.21	3.12	
	(0.16) $\pi_H \rightarrow \pi_{L+1}^*$			
	(0.11) $\pi_H \rightarrow \pi_{L+3}^*$			
T_5	(0.73) $n_{H-5} \rightarrow \pi_L^*$	3.22	3.09	

[a] Dominant contributions (DC) at the DFT/MRCI/TZVP level. [b] Oscillator strengths (length form) in parentheses. [c] The DCs to this state are $(0.45)\pi_{H-3} \rightarrow \pi_L^*$, $(0.30)\pi_H \rightarrow \pi_{L+2}^*$ and $(0.15)\pi_H \rightarrow \pi_{L+3}^*$. [d] The DCs to this are $(0.30)\pi_{H-3} \rightarrow \pi_L^*$, $(0.25)\pi_{H-2} \rightarrow \pi_L^*$, $(0.18)\pi_H \rightarrow \pi_{L+3}^*$ and $(0.13)\pi_H \rightarrow \pi_{L+1}^*$. [e] The DCs to this state are$(0.48)\pi_{H-1} \rightarrow \pi_{L+1}^*$ and $(0.21)\pi_H \rightarrow \pi_{L+3}^*$. [f] The DCs to this state are $(0.38)\pi_{H-1} \rightarrow \pi_{L+1}^*$ and $(0.36)\pi_H \rightarrow \pi_{L+3}^*$. [g] From Ref. [38], aqueous solution. [h] From Ref. [37], aqueous solution.

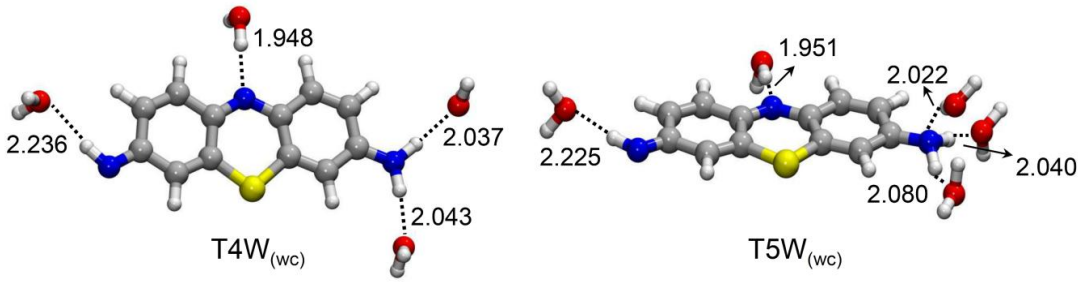

Fig. 34 Ground state minimum of the T-water hydrogen bonded complexes optimized at the B3LYP/TZVP level (wc: without applying COSMO). Numbers indicate hydrogen bond lengths in Å.

Table 33 Vertical excitation energies ΔE_w (eV) of the low-lying singlet and triplet states of neutral thionine (T) in aqueous solution: solvation with COSMO and micro-hydration with four and five water molecules (T4W-T5W). Oscillator strengths (length form) in parentheses.

Electronic State	Electronic structure[a]	T4W	T5W	T4W$_{(wc)}$	T5W$_{(wc)}$	Exp.
S_0	(0.91) Ground State					
S_1	(0.76) $\pi_H \rightarrow \pi_L^*$	2.44(0.759)	2.55(0.526)	2.57(0.647)	2.65(0.417)	2.44[k], 2.39[l]
S_2	(0.70) $\pi_{H-1} \rightarrow \pi_L^*$	2.83(0.053)	2.98(0.233)	2.98(0.087)	3.14(0.250)	
S_3	(0.45) $n_{H-4} \rightarrow \pi_L^*$	3.24(0.002)[b]	3.22(0.002)[b]	2.96(0.003)[b]	2.94(0.002)[b]	
	(0.23) $n_{H-5} \rightarrow \pi_L^*$					
S_4	(0.28) $\pi_H \rightarrow \pi_L^* \pi_H \rightarrow \pi_L^*$	3.39(0.004)	3.47(0.003)	3.42(0.003)	3.49(0.011)	
	(0.25) $\pi_{H-2} \rightarrow \pi_L^*$					
	(0.15) $\pi_H \rightarrow \pi_{L+1}^*$					
S_5	(0.45) $n_{H-5} \rightarrow \pi_L^*$	3.76(0.003)	3.71(0.003)	3.75(0.003)	3.70(0.003)	
	(0.21) $n_{H-4} \rightarrow \pi_L^*$					
S_6	(0.29) $\pi_{H-3} \rightarrow \pi_L^*$	3.85(0.162)	3.92(0.118)	4.36(0.147)[g]	3.91(0.214)	
	(0.20) $\pi_H \rightarrow \pi_{L+1}^*$					
S_7	(0.40) $\pi_H \rightarrow \pi_{L+2}^*$	4.08(0.032)	4.20(0.045)	3.82(0.235)[h]	4.24(0.016)	
	(0.21) $\pi_{H-3} \rightarrow \pi_L^*$					
S_8	(0.32) $\pi_H \rightarrow \pi_{L+1}^*$	4.30(0.088)	4.40(0.231)	4.82(0.039)[i]	4.41(0.299)	
	(0.19) $\pi_H \rightarrow \pi_{L+2}^*$					
	(0.16) $\pi_{H-3} \rightarrow \pi_L^*$					
S_9	(0.26) $\pi_{H-2} \rightarrow \pi_L^*$	4.45(0.104)	4.53(0.102)	4.52(0.140)	-	
	(0.14) $\pi_{H-6} \rightarrow \pi_L^*$					
S_{10}	(0.15) $\pi_{H-1} \rightarrow \pi_{L+1}^*$	4.63(0.186)	4.72(0.088)[c]	-	-	
	(0.15) $\pi_H \rightarrow \pi_L^* \pi_H \rightarrow \pi_{L+1}^*$					
	(0.12) $\pi_H \rightarrow \pi_{L+3}^*$					
S_{11}	(0.59) $\pi_H \rightarrow \pi_{L+4}^*$	4.55(0.000)	4.62(0.000)	-	-	
	(0.15) $\pi_{H-1} \rightarrow \pi_{L+4}^*$					
S_{12}	(0.33) $\pi_{H-1} \rightarrow \pi_{L+1}^*$	4.82(0.264)	4.92(0.360)	-	4.92(0.283)	
T_1	(0.83) $\pi_H \rightarrow \pi_L^*$	1.35	1.43	1.41	1.46	
T_2	(0.74) $\pi_{H-1} \rightarrow \pi_L^*$	2.46	2.54	2.58	2.65	
T_3	(0.52) $\pi_{H-2} \rightarrow \pi_L^*$	3.13	3.17[d]	3.14	3.17	
	(0.12) $\pi_H \rightarrow \pi_{L+3}^*$					
T_4	(0.46) $n_{H-4} \rightarrow \pi_L^*$	3.22	3.17[e]	2.92[j]	2.87[j]	
	(0.30) $n_{H-5} \rightarrow \pi_L^*$					
T_5	(0.45) $n_{H-5} \rightarrow \pi_L^*$	3.61[f]	3.56[f]	3.60[f]	3.55[f]	
	(0.28) $n_{H-4} \rightarrow \pi_L^*$					
T_6	(0.55) $\pi_H \rightarrow \pi_{L+1}^*$	3.45	3.49	-	3.41	
	(0.15) $\pi_{H-3} \rightarrow \pi_L^*$					

[a]Dominant contributions (DC) at the DFT/MRCI/TZVP level of the TC model. [b]The DCs to these states are (0.6)$n_{H-4} \rightarrow \pi_L^*$ and (0.1)$n_{H-4} \rightarrow \pi_L^*$ $\pi_H \rightarrow \pi_L^*$. [c]The DCs to this state are (0.35)$\pi_H \rightarrow \pi_{L+4}^*$, (0.13)$\pi_H \rightarrow \pi_{L+5}^*$ and (0.11)$\pi_{H-1} \rightarrow \pi_{L+4}^*$. [d]The DCs to this state are (0.35)$\pi_{H-2} \rightarrow \pi_L^*$ and (0.19)$n_{H-4} \rightarrow \pi_L^*$. [e]The DCs to this state are (0.50)$n_{H-4} \rightarrow \pi_L^*$ and (0.13)$\pi_{H-2} \rightarrow \pi_L^*$. [f]The DCs to these states is (0.7)$n_{H-5} \rightarrow \pi_L^*$. [g]The DCs to this state are (0.26) $\pi_{H-3} \rightarrow \pi_L^*$ and (0.23)$\pi_H \rightarrow \pi_{L+4}^*$. [h]The DCs to this state are (0.21)$\pi_H \rightarrow \pi_{L+2}^*$ and (0.11)$\pi_{H-3} \rightarrow \pi_L^*$. [i]The DCs to this state is (0.50)$\pi_H \rightarrow \pi_{L+1}^*$. [j]The DCs to this state is (0.7)$n_{H-4} \rightarrow \pi_L^*$. [k]From Ref. [38], aqueous solution. [l]From Ref. [37], aqueous solution.

Table 34 Vertical excitation energies ΔE (eV) of the low-lying singlet and triplet states of neutral thionine (T) in aqueous solution: solvation with COSMO (TC) and micro-hydration with one to three water molecules (T1W-T3W). Oscillator strengths (length form) in parentheses.

Electronic State	Electronic structure[a]	TC	T1W	T2W	T3Wa	T3Wb
S_0	(0.91) Ground State					
S_1	(0.76) $\pi_H \rightarrow \pi_L^*$	2.55(0.613)	2.51(0.613)	2.54(0.591)	2.47(0.721)	2.59(0.423)
S_2	(0.70) $\pi_{H-1} \rightarrow \pi_L^*$	2.97(0.166)	2.90(0.155)	2.94(0.169)	2.85(0.075)	3.08(0.304)
S_3	(0.45) $n_{H-4} \rightarrow \pi_L^*$	3.43(0.002)	3.35(0.002)[b]	3.22(0.002)[b]	3.23(0.002)[b]	3.21(0.002)
	(0.23) $n_{H-5} \rightarrow \pi_L^*$					
S_4	(0.28) $\pi_H \rightarrow \pi_L^* \pi_H \rightarrow \pi_L^*$	3.47(0.002)	3.43(0.004)	3.45(0.003)	3.40(0.004)	3.51(0.003)
	(0.25) $\pi_{H-2} \rightarrow \pi_L^*$					
	(0.15) $\pi_H \rightarrow \pi_{L+1}^*$					
S_5	(0.45) $n_{H-5} \rightarrow \pi_L^*$	3.47(0.003)	3.72(0.003)	3.74(0.003)	3.76(0.003)	3.71(0.003)
	(0.21) $n_{H-4} \rightarrow \pi_L^*$					
S_6	(0.29) $\pi_{H-3} \rightarrow \pi_L^*$	3.91(0.141)	3.90(0.125)	3.90(0.143)	3.87(0.153)	3.94(0.118)
	(0.20) $\pi_H \rightarrow \pi_{L+1}^*$					
S_7	(0.40) $\pi_H \rightarrow \pi_{L+2}^*$	4.20(0.034)	4.16(0.054)	4.17(0.044)	4.10(0.036)	4.25(0.040)
	(0.21) $\pi_{H-3} \rightarrow \pi_L^*$					
S_8	(0.32) $\pi_H \rightarrow \pi_{L+1}^*$	4.36(0.163)	4.36(0.158)	4.37(0.173)	4.32(0.104)	4.44(0.312)
	(0.19) $\pi_H \rightarrow \pi_{L+2}^*$					
	(0.16) $\pi_{H-3} \rightarrow \pi_L^*$					
S_9	(0.26) $\pi_{H-2} \rightarrow \pi_L^*$	4.57(0.158)	4.51(0.119)	4.53(0.124)	4.47(0.111)	4.59(0.102)
	(0.14) $\pi_{H-6} \rightarrow \pi_L^*$					
S_{10}	(0.15) $\pi_{H-1} \rightarrow \pi_{L+1}^*$	4.71(0.115)	4.69(0.127)	4.70(0.120)	4.65(0.170)	4.78(0.058)
	(0.15) $\pi_H \rightarrow \pi_L^* \pi_H \rightarrow \pi_{L+1}^*$					
	(0.12) $\pi_H \rightarrow \pi_{L+3}^*$					
S_{11}	(0.59) $\pi_H \rightarrow \pi_{L+4}^*$	4.75(0.000)	4.76(0.000)	4.72(0.000)	4.63(0.001)	4.77(0.003)
	(0.15) $\pi_{H-1} \rightarrow \pi_{L+4}^*$					
S_{12}	(0.33) $\pi_{H-1} \rightarrow \pi_{L+1}^*$	4.91(0.289)	4.89(0.306)	4.90(0.288)	4.84(0.278)	4.98(0.341)
T_1	(0.83) $\pi_H \rightarrow \pi_L^*$	1.44	1.40	1.41	1.37	1.46
T_2	(0.74) $\pi_{H-1} \rightarrow \pi_L^*$	2.55	2.50	2.52	2.47	2.58
T_3	(0.52) $\pi_{H-2} \rightarrow \pi_L^*$	3.18	3.15	3.16	3.13	3.20
	(0.12) $\pi_H \rightarrow \pi_{L+3}^*$					
T_4	(0.46) $n_{H-4} \rightarrow \pi_L^*$	3.26	3.32	3.19	3.21	3.15
	(0.30) $n_{H-5} \rightarrow \pi_L^*$					
T_5	(0.45) $n_{H-5} \rightarrow \pi_L^*$	3.43	3.56[f]	3.58[f]	3.60[f]	3.55[f]
	(0.28) $n_{H-4} \rightarrow \pi_L^*$					
T_6	(0.55) $\pi_H \rightarrow \pi_{L+1}^*$	3.49	3.48	3.48	3.46	3.50
	(0.15) $\pi_{H-3} \rightarrow \pi_L^*$					

[a]Dominant contributions (DC) at the DFT/MRCI/TZVP level in parentheses of the TC model. [b]The DCs to these states are (0.6) $n_{H-4} \rightarrow \pi_L^*$ and (0.1) $n_{H-4} \rightarrow \pi_L^*$ $\pi_H \rightarrow \pi_L^*$. [c]The DCs to these states are (0.35)$\pi_H \rightarrow \pi_{L+4}^*$, (0.13)$\pi_H \rightarrow \pi_{L+5}^*$ and (0.11)$\pi_{H-1} \rightarrow \pi_{L+4}^*$. [d]The DCs to these states are (0.35)$\pi_{H-2} \rightarrow \pi_L^*$ and (0.19)$\pi_{H-4} \rightarrow \pi_L^*$. [e]The DCs to these states are of (0.50)$\pi_{H-4} \rightarrow \pi_L^*$ and (0.13)$\pi_{H-2} \rightarrow \pi_L^*$. [f]The DCs to these states is (0.7)$\pi_{H-5} \rightarrow \pi_L^*$.

Optimized geometries of the electronically excited states of the micro-hydrated models.

TH^+3W, $S_1(\pi_H \rightarrow \pi_L^*)$

C	-0.8690262	0.0057473	-2.6291473
C	-0.2984346	0.0014481	-1.3623261
C	1.1227301	-0.0071546	-1.1858758
C	1.9198307	-0.0167622	-2.3742043
C	1.3693850	-0.0134001	-3.6200857
C	-0.0549932	-0.0040995	-3.7814840
N	1.7829700	-0.0104610	-0.0012702
C	1.1230571	-0.0090089	1.1835317
C	-0.2980458	0.0004620	1.3605589
S	-1.4023073	0.0146645	-0.0007001
C	-0.8681178	0.0024245	2.6276264
C	-0.0536765	-0.0081719	3.7796770
C	1.3706371	-0.0185246	3.6177154
C	1.9205423	-0.0202693	2.3716177
N	-0.5960600	-0.0081260	5.0064029
N	-0.5979301	-0.0037508	-5.0080289
O	-3.4630213	0.0104386	5.2610666
O	4.6799553	-0.0119922	0.0005233
H	2.9954573	-0.0251293	-2.2510334
H	2.0004495	-0.0265927	4.4987876
H	2.9961006	-0.0290702	2.2480647
H	-1.9454939	0.0096460	2.7432237
H	1.9988744	-0.0204754	-4.5014033
H	-1.9464284	0.0130536	-2.7443934
H	-0.0052415	-0.0130433	-5.8250203
H	-1.6127201	-0.0015278	-5.1486325
H	-0.0028927	-0.0147878	5.8230752
H	-1.6107785	-0.0001079	5.1480593
H	4.9511250	0.9137243	0.0113377
H	3.6984743	0.0086939	-0.0008051
H	-3.8590819	0.8010401	5.6503475
H	-3.8615333	-0.7293193	5.7379577
H	-3.8767881	-0.8003246	-5.5886984
O	-3.4664916	0.0063689	-5.2505238
H	-3.8604636	0.7221017	-5.7662876

TH^+3W, $S_2(\pi_{H-1} \rightarrow \pi_L^*)$

C	-0.8333264	-0.0009843	-2.6155546
C	-0.2407874	-0.0065508	-1.3586586
C	1.1744456	-0.0197607	-1.1777197
C	1.9331846	-0.0311012	-2.3716653
C	1.3658895	-0.0260606	-3.6325692
C	-0.0330268	-0.0107820	-3.7964664
N	1.8253973	-0.0236742	0.0077628
C	1.1605538	-0.0157748	1.2023330
C	-0.2437818	-0.0055805	1.3623939
S	-1.3418784	0.0044470	0.0051144
C	-0.8514784	0.0026783	2.6232824
C	-0.0592987	-0.0052040	3.8152906
C	1.3350953	-0.0159528	3.6633060
C	1.9072005	-0.0234827	2.3995257
N	-0.6771366	0.0000959	5.0096031
N	-0.6249850	-0.0044974	-5.0029840
O	-3.5828012	0.0154014	4.8060911
O	4.6910272	0.0253820	0.0337841
H	3.0117053	-0.0431171	-2.2743784
H	1.9683057	-0.0216926	4.5413549
H	2.9867809	-0.0324231	2.3099911
H	-1.9319799	0.0117360	2.7112361
H	2.0023620	-0.0346739	-4.5086914
H	-1.9128564	0.0100769	-2.7136389
H	-0.0680647	-0.0124066	-5.8432694
H	-1.6404893	0.0064978	-5.0943668
H	-0.1378805	-0.0054392	5.8615355
H	-1.6945993	0.0066023	5.0775000
H	4.9348182	0.9579906	-0.0016826
H	3.7064017	0.0177496	0.0210011
H	-4.0310424	0.7887125	5.1730204
H	-4.0396668	-0.7423831	5.1942252
H	-3.9739889	-0.7349124	-5.3298354
O	-3.5421720	0.0329256	-4.9330290
H	-3.9532541	0.7957629	-5.3603851

Optimized geometries of the electronically excited states of the micro-hydrated models.

TH^+3W, $T_1(\pi_H \rightarrow \pi_L^*)$

C	-0.8619303	0.0026563	-2.6320735
C	-0.3055681	0.0019691	-1.3740918
C	1.1156696	-0.0245069	-1.1885582
C	1.9180629	-0.0527745	-2.3670874
C	1.3757742	-0.0515417	-3.6202116
C	-0.0388431	-0.0252968	-3.7841762
N	1.7739926	-0.0309482	0.0001523
C	1.1151517	-0.0288398	1.1885305
C	-0.3059687	0.0014330	1.3737571
S	-1.4248760	0.0519961	-0.0003115
C	-0.8625944	0.0006808	2.6317968
C	-0.0397069	-0.0304774	3.7839508
C	1.3749179	-0.0615380	3.6201309
C	1.9173679	-0.0625186	2.3670556
N	-0.5851668	-0.0304399	5.0117270
N	-0.5841875	-0.0269118	-5.0119949
O	-3.4291659	0.0379382	5.2779204
O	4.6291309	0.1019257	0.0010601
H	2.9920879	-0.0732647	-2.2370923
H	2.0101825	-0.0863806	4.4972204
H	2.9912953	-0.0868715	2.2369303
H	-1.9387895	0.0237984	2.7575414
H	2.0113192	-0.0731921	-4.4971491
H	-1.9381834	0.0235559	-2.7579349
H	0.0090335	-0.0468818	-5.8292612
H	-1.6004806	-0.0079980	-5.1539855
H	0.0077931	-0.0523188	5.8291265
H	-1.6014664	-0.0075609	5.1531562
H	4.8457436	1.0416365	0.0238620
H	3.6437719	0.0654897	0.0003112
H	-3.8359164	0.8303867	5.6518692
H	-3.8769540	-0.7020813	5.7083046
H	-3.8719193	-0.7615398	-5.6159689
O	-3.4284783	0.0277684	-5.2789673
H	-3.8419463	0.7667349	-5.7439824

TH^+3W, $T_2(\pi_{H-1} \rightarrow \pi_L^*)$

C	-0.8416169	0.0015991	-2.6223152
C	-0.2368800	-0.0086679	-1.3593942
C	1.1704830	-0.0268827	-1.1829907
C	1.9257226	-0.0410943	-2.3843393
C	1.3526425	-0.0319593	-3.6365163
C	-0.0508980	-0.0121352	-3.7974621
N	1.8274607	-0.0371001	0.0000501
C	1.1683270	-0.0259311	1.1822201
C	-0.2393367	-0.0066609	1.3559694
S	-1.3419870	0.0121932	-0.0027776
C	-0.8464905	0.0034213	2.6178037
C	-0.0580778	-0.0096698	3.7943470
C	1.3456685	-0.0306332	3.6360832
C	1.9211998	-0.0400252	2.3850076
N	-0.6551772	-0.0003963	5.0036969
N	-0.6457029	-0.0037473	-5.0079683
O	-3.5674301	0.0258597	4.9061525
O	4.6906894	0.0606213	0.0206256
H	3.0046291	-0.0562911	-2.2921637
H	1.9752099	-0.0416792	4.5174188
H	3.0002190	-0.0572177	2.2947832
H	-1.9270136	0.0195833	2.7048973
H	1.9839898	-0.0425734	-4.5165952
H	-1.9219222	0.0169293	-2.7122001
H	-0.0891891	-0.0154908	-5.8483197
H	-1.6614402	0.0095938	-5.0971253
H	-0.1003984	-0.0125244	5.8452008
H	-1.6711813	0.0100367	5.0904905
H	4.9132493	0.9974555	0.0777852
H	3.7061809	0.0323438	0.0093919
H	-3.9885072	0.8007598	5.3009087
H	-4.0021340	-0.7307774	5.3209964
H	-3.9960463	-0.7349596	-5.3000965
O	-3.5582034	0.0343779	-4.9127769
H	-3.9789345	0.7961885	-5.3325280

Optimized geometries of the electronically excited states of the micro-hydrated models.

$TH_2^{2+}3W$, $S_1(\pi_{H-1}\rightarrow\pi_L^*)$

C	2.6337505	-0.0088862	-0.8651263
C	1.3802071	-0.0044689	-0.2606890
C	1.2472313	-0.0011433	1.1458236
C	2.4260877	-0.0031251	1.9092110
C	3.6812746	-0.0073479	1.3314458
C	3.8268305	-0.0083874	-0.0694662
N	0.0243775	0.0040072	1.7638118
C	-1.2023501	0.0079816	1.1561143
C	-1.3472447	0.0023886	-0.2501063
S	0.0132094	-0.0059728	-1.3468766
C	-2.6046027	0.0038747	-0.8434724
C	-3.7906642	0.0121097	-0.0394572
C	-3.6334880	0.0187958	1.3609099
C	-2.3749299	0.0160919	1.9303562
N	-4.9833527	0.0130889	-0.6394764
N	5.0138459	-0.0121840	-0.6806715
H	2.3407291	-0.0012079	2.9890091
H	-4.5096823	0.0254488	1.9959320
H	-2.2786955	0.0206457	3.0095409
H	-2.7004346	-0.0016599	-1.9228338
H	4.5617988	-0.0080441	1.9603214
H	2.7244238	-0.0128809	-1.9451751
H	5.8668552	-0.0074521	-0.1409517
H	5.0811813	-0.0004281	-1.7010313
H	-5.8312962	0.0188602	-0.0917672
H	-5.0630447	0.0038773	-1.6578244
H	0.0268087	0.0039947	2.8005197
O	-0.0827382	-0.0118539	4.5437273
H	0.1809626	-0.7987269	5.0385339
H	0.2144844	0.7413099	5.0709817
H	5.0282728	0.8320855	-3.9997042
O	4.7428656	0.0261326	-3.5493607
H	5.1618414	-0.6936830	-4.0394463
H	-4.7888648	-0.8174357	-4.0375960
O	-4.9973865	-0.0289652	-3.5206177
H	-4.7296721	0.7178875	-4.0711625

$TH_2^{2+}3W$, $S_2(\pi_H\rightarrow\pi_L^*)$

C	2.6482094	-0.0117752	-0.8814374
C	1.3844695	-0.0093432	-0.3077640
C	1.2385392	-0.0046453	1.1069804
C	2.4051082	-0.0045049	1.9186278
C	3.6467123	-0.0068457	1.3616743
C	3.8030899	-0.0081445	-0.0667723
N	0.0195465	0.0019777	1.7237904
C	-1.2028610	0.0072715	1.1108702
C	-1.3523474	-0.0010310	-0.3027036
S	0.0139547	-0.0155806	-1.3961262
C	-2.6184214	0.0031483	-0.8723726
C	-3.7708753	0.0156528	-0.0546540
C	-3.6098232	0.0253169	1.3728877
C	-2.3664781	0.0208754	1.9267368
N	-4.9907389	0.0192491	-0.5945497
N	5.0211654	-0.0059752	-0.6100277
H	2.2870713	-0.0021011	2.9949280
H	-4.4904119	0.0359015	2.0022899
H	-2.2425096	0.0278451	3.0024973
H	-2.7320110	-0.0033526	-1.9492310
H	4.5291101	-0.0058759	1.9886243
H	2.7603539	-0.0166552	-1.9585479
H	5.8419363	0.0001731	-0.0208678
H	5.1554775	0.0047931	-1.6289441
H	-5.8095670	0.0282863	-0.0026622
H	-5.1316099	0.0083312	-1.6117887
H	0.0197724	0.0025870	2.7647264
O	-0.0918345	-0.0116683	4.4827258
H	0.1601101	-0.7963193	4.9872206
H	0.1921866	0.7455130	5.0115788
H	5.3490426	0.8790650	-3.8681820
O	5.1710733	0.0237569	-3.4552427
H	5.7914707	-0.5893044	-3.8712665
H	-5.1551258	-0.8222842	-3.9128693
O	-5.3956684	-0.0267504	-3.4204339
H	-5.0876276	0.7102914	-3.9637700

Optimized geometries of the electronically excited states of the micro-hydrated models.

TH_2^{2+}3W, $T_1(\pi_H \rightarrow \pi_L^*)$

C	2.6529388	-0.0140623	-0.8797934
C	1.3977570	-0.0223652	-0.3228900
C	1.2458048	-0.0110376	1.0902330
C	2.3975184	0.0040884	1.9103298
C	3.6495399	0.0107089	1.3657182
C	3.8083295	0.0047543	-0.0532839
N	0.0180539	-0.0121772	1.7037603
C	-1.2117854	-0.0006797	1.0941115
C	-1.3675090	-0.0143309	-0.3190770
S	0.0135194	-0.0594608	-1.4313917
C	-2.6242014	-0.0005320	-0.8723132
C	-3.7772091	0.0254192	-0.0435951
C	-3.6140388	0.0387980	1.3750229
C	-2.3610422	0.0259733	1.9177781
N	-4.9943132	0.0377833	-0.5846796
N	5.0236135	0.0183408	-0.5984205
H	2.2699785	0.0113283	2.9851976
H	-4.4899539	0.0593797	2.0105026
H	-2.2285041	0.0367998	2.9921681
H	-2.7515898	-0.0103993	-1.9477186
H	4.5269051	0.0231126	1.9993853
H	2.7797519	-0.0233432	-1.9553953
H	5.8464788	0.0341883	-0.0101498
H	5.1582376	0.0260841	-1.6208700
H	-5.8151757	0.0563436	0.0061384
H	-5.1354662	0.0256026	-1.6049624
H	0.0185724	-0.0070801	2.7373205
O	-0.0933595	-0.0129235	4.5054606
H	0.1664185	-0.7941822	5.0110496
H	0.1937112	0.7449227	5.0315303
H	5.3121835	0.8927918	-3.8410830
O	5.1846133	0.0347188	-3.4155475
H	5.8222950	-0.5544329	-3.8398772
H	-5.1637696	-0.8017432	-3.8807626
O	-5.3969142	-0.0045862	-3.3873710
H	-5.0832451	0.7313639	-3.9289735

TH_2^{2+}3W, $T_2(\pi_{H-1} \rightarrow \pi_L^*)$

C	2.6331028	0.0018049	-0.8446989
C	1.3694516	0.0040970	-0.2440557
C	1.2178315	0.0031923	1.1552175
C	2.3954214	-0.0004190	1.9327960
C	3.6445310	-0.0028185	1.3626473
C	3.8045771	-0.0014659	-0.0443095
N	-0.0032902	0.0056642	1.7654392
C	-1.2182476	0.0072994	1.1429621
C	-1.3553844	0.0078111	-0.2578859
S	0.0124404	0.0077521	-1.3473873
C	-2.6130501	0.0085823	-0.8714194
C	-3.7924932	0.0078236	-0.0829497
C	-3.6464487	0.0087234	1.3256997
C	-2.4034675	0.0079076	1.9094372
N	-4.9909950	0.0060625	-0.6846973
N	5.0092080	-0.0028278	-0.6338734
H	2.3005043	-0.0014718	3.0115605
H	-4.5320436	0.0092970	1.9480189
H	-2.3168524	0.0082287	2.9890349
H	-2.6976437	0.0089069	-1.9517912
H	4.5235447	-0.0056298	1.9941682
H	2.7287358	0.0023592	-1.9241384
H	5.8505074	-0.0063099	-0.0764032
H	5.0984016	-0.0033259	-1.6525250
H	-5.8379659	0.0047664	-0.1358897
H	-5.0694225	0.0066133	-1.7042038
H	-0.0106483	0.0017783	2.8014727
O	-0.1465138	-0.0236148	4.5499737
H	0.1346486	-0.8087943	5.0377626
H	0.1641964	0.7304427	5.0681521
H	5.1973339	0.7635188	-3.9661557
O	4.8225754	-0.0025958	-3.5118761
H	5.1944653	-0.7687925	-3.9683706
H	-5.1109824	-0.8154765	-4.0018621
O	-4.7694399	-0.0265792	-3.5605306
H	-5.1645834	0.7155034	-4.0369899

Optimized geometries of the electronically excited states of the micro-hydrated models.

T4W, $S_1(\pi_H \rightarrow \pi_L^*)$

C	-0.5766338	-0.0589408	-4.0732537
C	-1.2644992	-0.0630181	-2.8874569
C	-0.6398625	-0.0433155	-1.6093313
C	0.7852444	-0.0149816	-1.6136481
C	1.5154266	-0.0130674	-2.7949319
C	0.8664697	-0.0243266	-4.0981783
N	-1.4142847	-0.0436049	-0.4799091
S	1.7315358	0.0047353	-0.1514866
C	0.5078914	-0.0175076	1.1071628
C	-0.8912623	-0.0301603	0.7599758
C	-1.7852962	-0.0357067	1.8672538
H	-2.8465251	-0.0437831	1.6513137
C	-1.3495330	-0.0252810	3.1669598
C	0.0419911	-0.0138319	3.4902717
C	0.9524356	-0.0056755	2.4238595
H	-1.1117706	-0.0764198	-5.0142344
H	-2.3484162	-0.0864654	-2.8986539
H	2.5993447	0.0075062	-2.7739655
H	-2.0716366	-0.0282414	3.9753618
H	2.0158624	0.0054373	2.6351973
N	0.4460079	-0.0109200	4.7830943
H	-0.2351505	-0.0002198	5.5366955
H	1.4344079	0.0135586	5.0161043
N	1.6419060	-0.0032514	-5.1531482
H	1.0776676	-0.0091149	-6.0090005
O	-4.2513313	0.0318376	-0.7963622
H	-4.4690678	0.9602456	-0.9416920
H	-3.2696674	0.0121371	-0.6940731
H	0.6808846	0.4654815	-8.5904411
O	0.1005949	0.0445448	-7.9432526
H	-0.6879249	0.6017116	-7.9300521
O	-1.5315632	0.0292584	7.0166555
H	-2.0105507	0.8589748	7.1392546
H	-2.2138052	-0.6542016	7.0261147
O	3.3616568	0.0579064	5.4389295
H	3.8940243	-0.6899331	5.1388796
H	3.8534580	0.8403523	5.1585081

T4W, $S_2(\pi_{H-1} \rightarrow \pi_L^*)$

C	-0.5350661	-0.1855504	-4.0531412
C	-1.2518777	-0.2314926	-2.8934453
C	-0.6419513	-0.1909010	-1.5952550
C	0.8103642	-0.1487502	-1.6145530
C	1.5366342	-0.1029205	-2.7759148
C	0.9110990	-0.1053412	-4.0735845
N	-1.4361395	-0.1908604	-0.5307502
S	1.7289315	-0.2432251	-0.0973694
C	0.4420593	-0.1218857	1.0964621
C	-0.9071195	-0.0888160	0.7725834
C	-1.8057158	0.0449597	1.8515508
H	-2.8627812	0.0752347	1.6140325
C	-1.4095070	0.1371911	3.1784718
C	-0.0479908	0.0982270	3.5064899
C	0.8853130	-0.0270282	2.4350806
H	-1.0566296	-0.2112790	-5.0041890
H	-2.3332700	-0.2875828	-2.9233654
H	2.6203936	-0.0718456	-2.7454620
H	-2.1508079	0.2351464	3.9615140
H	1.9462210	-0.0549905	2.6565393
N	0.4214538	0.1678422	4.7777626
H	-0.2224807	0.2313244	5.5667566
H	1.4235992	0.1437490	4.9604349
N	1.6490238	-0.0440942	-5.1607132
H	1.0517969	-0.0492458	-5.9894624
O	-4.2490519	-0.2226918	-0.8064231
H	-4.4845907	0.6623540	-1.1093812
H	-3.2622635	-0.2108484	-0.7254440
H	0.9315001	1.0168282	-8.3349280
O	0.0477347	0.7602443	-8.0428642
H	-0.3062510	1.5536033	-7.6219478
O	-1.3157119	0.3468350	7.1287987
H	-1.8372873	1.1509560	7.2490999
H	-1.9352295	-0.3765397	7.2899571
O	3.3084361	0.1059945	5.2758428
H	3.8298272	-0.6962707	5.1447790
H	3.8884619	0.8292608	5.0053396

Optimized geometries of the electronically excited states of the micro-hydrated models.

T4W, $T_1(\pi_H \rightarrow \pi_L^*)$

C	-0.5416518	-0.0317253	-4.0661974
C	-1.2324070	-0.0273050	-2.8795229
C	-0.5788570	-0.0196794	-1.6216284
C	0.8341169	-0.0163706	-1.6304534
C	1.5465078	-0.0224692	-2.8207471
C	0.8871260	-0.0289209	-4.0797544
N	-1.3818033	-0.0167299	-0.4939214
S	1.7886253	-0.0056457	-0.1328031
C	0.5235523	-0.0059113	1.1070834
C	-0.8692195	-0.0113298	0.7491387
C	-1.7903559	-0.0114350	1.8428738
H	-2.8458624	-0.0163873	1.6013453
C	-1.3857656	-0.0055872	3.1474556
C	-0.0001652	0.0001760	3.4814142
C	0.9344930	0.0001725	2.4249544
H	-1.0762368	-0.0401761	-5.0086589
H	-2.3155604	-0.0300137	-2.8787591
H	2.6305033	-0.0206676	-2.8146814
H	-2.1190469	-0.0032966	3.9453131
H	1.9924966	0.0047991	2.6618175
N	0.3958518	0.0047208	4.7712318
H	-0.2893744	0.0034607	5.5231083
H	1.3850838	0.0134269	5.0114835
N	1.6349366	-0.0331805	-5.1981039
H	1.0237375	-0.0308834	-6.0221411
O	-4.2047127	-0.0341800	-0.8277752
H	-4.4782278	0.8906051	-0.8127395
H	-3.2222204	-0.0141062	-0.7137213
H	0.6041793	0.2348605	-8.5856921
O	-0.0436789	0.0459593	-7.8947754
H	-0.6746069	0.7747105	-7.9517334
O	-1.5383584	-0.0002791	7.0152206
H	-1.9480358	0.8469820	7.2325672
H	-2.2691421	-0.6314328	6.9983069
O	3.2693405	0.0407649	5.4980957
H	3.8143819	-0.6913464	5.1821548
H	3.7625366	0.8369135	5.2618014

T4W, $T_2(\pi_{H-1} \rightarrow \pi_L^*)$

C	-0.5531692	-0.1939667	-4.0359692
C	-1.2663892	-0.1764971	-2.8641635
C	-0.6592590	-0.1276570	-1.5786620
C	0.7857306	-0.1058794	-1.6049500
C	1.5253649	-0.1237354	-2.7846541
C	0.8978335	-0.1658212	-4.0755401
N	-1.4455724	-0.1075830	-0.4897984
S	1.7173013	-0.0530582	-0.1232331
C	0.4414473	-0.0328546	1.1053923
C	-0.9233644	-0.0600090	0.7777834
C	-1.8145835	-0.0370180	1.8828564
H	-2.8751303	-0.0559139	1.6619312
C	-1.3973739	0.0119755	3.1963015
C	-0.0247861	0.0398311	3.5093425
C	0.8947926	0.0164532	2.4265535
H	-1.0859533	-0.2320981	-4.9800165
H	-2.3493342	-0.1991914	-2.8952748
H	2.6090342	-0.1045493	-2.7481730
H	-2.1275738	0.0283805	3.9961534
H	1.9583776	0.0365445	2.6378756
N	0.4445799	0.0871967	4.7824862
H	-0.1986014	0.1065766	5.5736497
H	1.4467081	0.1065809	4.9620685
N	1.6375550	-0.1756517	-5.1622500
H	1.0419514	-0.1994990	-5.9913775
O	-4.2568593	-0.0115295	-0.7885184
H	-4.4560595	0.9071140	-1.0048640
H	-3.2716146	-0.0443955	-0.6938729
H	0.9709010	0.8137446	-8.3667872
O	0.0792627	0.5380363	-8.1195802
H	-0.3205624	1.3301507	-7.7396081
O	-1.3055221	0.1438408	7.1383707
H	-1.8837996	0.9093900	7.2505120
H	-1.8756046	-0.6210581	7.2900761
O	3.3477613	0.1349100	5.2473621
H	3.8878985	-0.6489342	5.0849700
H	3.8994334	0.8794074	4.9755100

Optimized geometries of the electronically excited states of the micro-hydrated models.

T5W, $S_1(\pi_H \rightarrow \pi_L^*)$

C	-0.5520023	-0.0979655	-4.3830702
C	-1.2610559	-0.1012779	-3.2089754
C	-0.6645158	-0.0425633	-1.9192827
C	0.7664136	0.0170444	-1.8987621
C	1.5159188	0.0217619	-3.0647716
C	0.8891113	-0.0313247	-4.3828375
N	-1.4524085	-0.0447829	-0.8084464
S	1.6823753	0.0861065	-0.4237481
C	0.4373074	0.0603024	0.8125914
C	-0.9500486	0.0030436	0.4469230
C	-1.8566705	-0.0034186	1.5359877
H	-2.9144122	-0.0428872	1.3081895
C	-1.4357195	0.0405757	2.8469464
C	-0.0605342	0.0992559	3.1833170
C	0.8640358	0.1086119	2.1377512
H	-1.0689871	-0.1462747	-5.3328941
H	-2.3434919	-0.1503446	-3.2395616
H	2.5985962	0.0678876	-3.0266455
H	-2.1708402	0.0353543	3.6433857
H	1.9237166	0.1562718	2.3627919
N	0.3442500	0.0855808	4.5101710
H	-0.3473320	0.4266000	5.1785972
H	1.2781643	0.4590455	4.6827693
N	1.6882672	-0.0119500	-5.4155250
H	1.1476567	-0.0465241	-6.2861704
O	-4.2881601	0.0133713	-1.1425254
H	-4.5074102	0.9419994	-1.2839319
H	-3.3070665	-0.0044929	-1.0366685
H	0.8490464	0.3445742	-8.8889866
O	0.2294682	-0.0120584	-8.2396382
H	-0.5170652	0.6001514	-8.2583409
O	-1.6597111	1.0967993	6.5037047
H	-1.9796187	1.9931839	6.3393914
H	-2.4551523	0.5806919	6.6868696
O	3.1130549	1.1473605	4.9725618
H	3.8786957	0.5859161	4.7962733
H	3.3365536	2.0009498	4.5800886
H	-0.0228500	-3.0733595	5.5792131
O	0.8351547	-2.6856972	5.3688950
H	0.6412576	-1.7634088	5.0992596

T5W, $S_2(\pi_{H-1} \rightarrow \pi_L^*)$

C	-0.4994224	-0.3238537	-4.3267504
C	-1.2627496	-0.1691760	-3.2069739
C	-0.6955442	0.0146153	-1.9028494
C	0.7523863	0.1268816	-1.8786747
C	1.5254050	-0.0331575	-2.9967019
C	0.9494662	-0.2938584	-4.2922814
N	-1.5168831	0.0607417	-0.8575597
S	1.5595025	0.7001429	-0.3999621
C	0.3071584	0.3652789	0.7996302
C	-1.0011212	0.0545264	0.4520959
C	-1.8750286	-0.2793432	1.5099597
H	-2.8960727	-0.5313584	1.2494661
C	-1.4971149	-0.2770650	2.8451848
C	-0.1861223	0.0565974	3.1937892
C	0.7271814	0.3666852	2.1448955
H	-0.9823958	-0.4830260	-5.2851055
H	-2.3432316	-0.2167924	-3.2701574
H	2.6039307	0.0620251	-2.9396864
H	-2.2165084	-0.5267619	3.6148510
H	1.7543447	0.6092959	2.3917522
N	0.2654186	0.0756949	4.4884482
H	-0.4263557	0.0998653	5.2429050
H	1.1563611	0.5397594	4.6812254
N	1.7293805	-0.4631435	-5.3366744
H	1.1657342	-0.6185822	-6.1744766
O	-4.2898114	0.4835606	-1.1770413
H	-4.3733821	1.3014205	-1.6814541
H	-3.3153847	0.3347573	-1.0850111
H	1.2291596	-0.2132131	-8.7441358
O	0.3247712	-0.2044120	-8.4061154
H	0.1653356	0.7177169	-8.1693029
O	-1.5942309	0.1819453	6.7335412
H	-2.1617864	0.9608112	6.8010937
H	-2.1765548	-0.5659150	6.9196326
O	2.8048914	1.3996200	5.0489574
H	3.6648125	0.9964332	4.8735269
H	2.9238296	2.3380624	4.8537908
H	0.8659707	-3.3424633	5.0191350
O	1.5493808	-2.6608603	5.0151563
H	1.0745035	-1.8237951	4.8756369

Optimized geometries of the electronically excited states of the micro-hydrated models.

T5W, $T_1(\pi_H \rightarrow \pi_L^*)$

C	-0.4978128	-0.0752420	-4.3775217
C	-1.2120798	-0.0663876	-3.2056645
C	-0.5823798	-0.0170743	-1.9361018
C	0.8278786	0.0204623	-1.9158952
C	1.5659612	0.0113417	-3.0943139
C	0.9303709	-0.0353596	-4.3623043
N	-1.4059215	-0.0105773	-0.8226492
S	1.7520544	0.0815612	-0.4051728
C	0.4694183	0.0834977	0.8066391
C	-0.9160725	0.0362725	0.4274615
C	-1.8560924	0.0440155	1.5042265
H	-2.9071214	0.0107556	1.2464856
C	-1.4698589	0.0910330	2.8145361
C	-0.0941279	0.1399947	3.1660239
C	0.8565407	0.1329084	2.1361664
H	-1.0119304	-0.1158477	-5.3304954
H	-2.2946007	-0.0967785	-3.2253091
H	2.6490935	0.0409449	-3.0668347
H	-2.2158749	0.0976966	3.6004410
H	1.9098654	0.1708959	2.3901353
N	0.2860601	0.1400926	4.4869218
H	-0.4159837	0.4358165	5.1662722
H	1.2332377	0.4604195	4.6935234
N	1.7023146	-0.0383249	-5.4669204
H	1.1068254	-0.0633849	-6.3028544
O	-4.2324487	-0.0742278	-1.2100456
H	-4.5174043	0.8467158	-1.2423211
H	-3.2543722	-0.0367518	-1.0777216
H	0.6608604	0.0258012	-8.8610855
O	0.0195124	-0.0097881	-8.1397244
H	-0.4890919	0.8060933	-8.2298775
O	-1.7123319	1.0255298	6.5080954
H	-2.0255006	1.9321448	6.3939809
H	-2.5119773	0.5064965	6.6627262
O	3.0371915	1.0744736	5.1183657
H	3.7913162	0.4978838	4.9405963
H	3.2907433	1.9313240	4.7517008
H	-0.0982269	-3.0979893	5.4880325
O	0.7634174	-2.6959869	5.3240503
H	0.5704475	-1.7752681	5.0624098

T5W, $T_2(\pi_{H-1} \rightarrow \pi_L^*)$

C	-0.4652814	-0.1861219	-4.3549965
C	-1.2120985	-0.1699890	-3.1925806
C	-0.6398714	-0.0841418	-1.9010130
C	0.8068332	-0.0207688	-1.8915399
C	1.5746645	-0.0362547	-3.0492946
C	0.9835984	-0.1217057	-4.3597117
N	-1.4561382	-0.0746017	-0.8296992
S	1.6921585	0.0992013	-0.3869780
C	0.3837068	0.0836816	0.8143439
C	-0.9727701	-0.0000223	0.4478511
C	-1.8935084	-0.0030006	1.5257021
H	-2.9465375	-0.0608575	1.2780006
C	-1.5095225	0.0690352	2.8543681
C	-0.1560250	0.1543514	3.1988683
C	0.7938971	0.1570869	2.1405632
H	-0.9742249	-0.2543745	-5.3100935
H	-2.2928474	-0.2217746	-3.2519199
H	2.6559751	0.0151591	-2.9855196
H	-2.2623395	0.0658005	3.6332637
H	1.8490823	0.2231813	2.3825528
N	0.2863781	0.1845332	4.5022938
H	-0.3961107	0.4423504	5.2179668
H	1.2282418	0.5455213	4.6596298
N	1.7466253	-0.1333413	-5.4252351
H	1.1713147	-0.1877847	-6.2675960
O	-4.2649840	-0.0089650	-1.2161748
H	-4.4708798	0.9144833	-1.4040691
H	-3.2843262	-0.0317343	-1.0885031
H	0.8360740	0.2566198	-8.8190000
O	0.0319721	0.2352771	-8.2847082
H	-0.1420626	1.1614301	-8.0755458
O	-1.6073310	0.9658054	6.6299110
H	-2.0443019	1.8192483	6.5125270
H	-2.3147765	0.3596721	6.8849354
O	3.0348611	1.1983295	4.8872188
H	3.8250287	0.6554690	4.7717124
H	3.2876306	2.0769687	4.5762551
H	0.1650912	-3.1457630	5.3445400
O	0.9813685	-2.6332722	5.2981247
H	0.7026763	-1.7286512	5.0633764

Optimized geometries of the electronically excited states of the micro-hydrated models.

$TH^+3W_{(wc)}$, $S_1(\pi_H \rightarrow \pi_L^*)$

C	-0.9279348	0.0162617	-2.5736392
C	-0.3301249	0.0265670	-1.3195771
C	1.0959136	0.0135318	-1.1767270
C	1.8716060	-0.0466384	-2.3799924
C	1.2887285	-0.0641530	-3.6104859
C	-0.1367776	-0.0399802	-3.7404383
N	1.7815127	0.0270982	-0.0089946
C	1.1508178	-0.0015771	1.1886035
C	-0.2641601	0.0340563	1.4044956
S	-1.3990195	0.1232590	0.0695487
C	-0.7974090	0.0161403	2.6882723
C	0.0495550	-0.0515583	3.8135483
C	1.4661645	-0.1027298	3.6114751
C	1.9810002	-0.0834342	2.3507792
N	-0.4633782	-0.0718469	5.0577046
N	-0.7113495	-0.0669799	-4.9561907
O	-3.3500069	0.0169851	5.2615405
O	4.6497356	0.0654898	-0.6386321
H	2.9499990	-0.0713300	-2.2693920
H	2.1223476	-0.1646389	4.4712723
H	3.0498078	-0.1344501	2.1857703
H	-1.8699390	0.0439692	2.8415864
H	1.9005408	-0.1098844	-4.5034904
H	-2.0070866	0.0343667	-2.6724322
H	-0.1401431	-0.1062940	-5.7857324
H	-1.7257507	-0.0563554	-5.0691895
H	0.1474554	-0.1243798	5.8575720
H	-1.4706490	-0.0426169	5.2206413
H	5.1836650	0.8186821	-0.3663926
H	3.7712764	0.1849224	-0.2379423
H	-3.8504480	0.7939538	5.5373632
H	-3.8994990	-0.7436445	5.4845109
H	-4.1489222	-0.8068847	-5.2461209
O	-3.6077833	-0.0343771	-5.0447443
H	-4.1336530	0.7311836	-5.3045716

$TH^+3W_{(wc)}$, $S_2(\pi_{H-1} \rightarrow \pi_L^*)$

C	-0.9348825	0.0245872	-2.5654752
C	-0.2855414	0.0175191	-1.3096090
C	1.1111415	0.0080345	-1.2035484
C	1.8267462	-0.0579494	-2.4200751
C	1.2157196	-0.0625484	-3.6675212
C	-0.1775545	-0.0336791	-3.7783124
N	1.8197103	0.0172883	-0.0203045
C	1.2121854	0.0034938	1.1703174
C	-0.2062602	0.0215236	1.4120411
S	-1.3454020	0.0625034	0.0699037
C	-0.7434559	0.0055751	2.6866558
C	0.1016726	-0.0255080	3.8245575
C	1.5001896	-0.0458682	3.6080596
C	2.0233488	-0.0291659	2.3368721
N	-0.4263770	-0.0374018	5.0665111
N	-0.8401870	-0.0452747	-4.9538527
O	-3.3577559	-0.0055234	5.1507183
O	4.6212598	0.0296840	-0.8354376
H	2.9097292	-0.0882094	-2.3514063
H	2.1676166	-0.0755389	4.4613502
H	3.0952155	-0.0569208	2.1879789
H	-1.8173668	0.0204400	2.8353936
H	1.8271598	-0.1088554	-4.5598053
H	-2.0175616	0.0479429	-2.6225056
H	-0.3311858	-0.0814606	-5.8219640
H	-1.8565327	-0.0287890	-4.9865384
H	0.1739218	-0.0640807	5.8735083
H	-1.4322455	-0.0269821	5.2129831
H	5.1867224	0.7620337	-0.5705984
H	3.7846941	0.1276108	-0.3456219
H	-3.8692623	0.7620731	5.4323183
H	-3.8839313	-0.7748661	5.3985269
H	-4.3036473	-0.7556700	-4.8154913
O	-3.7459352	0.0107651	-4.6360826
H	-4.2814385	0.7805114	-4.8627550

Optimized geometries of the electronically excited states of the micro-hydrated models.

$TH^+3W_{(wc)}$, $T_1(\pi_H \rightarrow \pi_L^*)$

C	-0.9155580	0.0129062	-2.5820757
C	-0.3332673	0.0825412	-1.3375003
C	1.0914286	0.0433857	-1.1826617
C	1.8761664	-0.0700067	-2.3699859
C	1.3041729	-0.1309490	-3.6069575
C	-0.1131205	-0.0927131	-3.7446224
N	1.7717534	0.0872180	-0.0077496
C	1.1413992	0.0400723	1.1869836
C	-0.2762841	0.0822201	1.4066909
S	-1.4098948	0.2879440	0.0578927
C	-0.8034500	0.0124439	2.6751097
C	0.0461360	-0.0932148	3.8033748
C	1.4559495	-0.1354397	3.6041745
C	1.9713993	-0.0731380	2.3431471
N	-0.4749801	-0.1557153	5.0437200
N	-0.6864794	-0.1572670	-4.9608697
O	-3.3486259	-0.0667212	5.3023034
O	4.6251284	0.0414157	-0.5369344
H	2.9522348	-0.1077271	-2.2474077
H	2.1122026	-0.2233415	4.4619471
H	3.0392922	-0.1225349	2.1750422
H	-1.8755968	0.0427476	2.8317704
H	1.9232996	-0.2150215	-4.4923414
H	-1.9934691	0.0405681	-2.6927320
H	-0.1132022	-0.2354178	-5.7871851
H	-1.7018673	-0.1334854	-5.0792944
H	0.1318598	-0.2336854	5.8452562
H	-1.4837824	-0.1287092	5.2043816
H	5.1287067	0.8238273	-0.2907725
H	3.7177930	0.1767939	-0.2048254
H	-3.8511209	0.7034540	5.5926928
H	-3.9062474	-0.8318661	5.4856622
H	-4.1278569	-0.8412320	-5.2622772
O	-3.5637254	-0.0751724	-5.1043188
H	-4.0780282	0.6938033	-5.3767131

$TH^+3W_{(wc)}$, $T_2(\pi_{H-1} \rightarrow \pi_L^*)$

C	-0.9213227	0.0105052	-2.5624911
C	-0.2814099	0.0121912	-1.3143769
C	1.1316074	-0.0047883	-1.1786107
C	1.8570497	-0.0435907	-2.3976544
C	1.2419810	-0.0505833	-3.6330806
C	-0.1626153	-0.0259875	-3.7567726
N	1.8228167	-0.0055530	-0.0166509
C	1.2021886	-0.0082023	1.1831535
C	-0.1991953	0.0146886	1.4065107
S	-1.3424930	0.0520967	0.0762129
C	-0.7597792	0.0109942	2.6875607
C	0.0714416	-0.0252262	3.8341249
C	1.4661265	-0.0568574	3.6268668
C	1.9982326	-0.0494689	2.3554729
N	-0.4841684	-0.0289572	5.0680672
N	-0.7911372	-0.0334273	-4.9548539
O	-3.4175434	0.0186325	5.0122519
O	4.6555123	0.0533413	-0.7303614
H	2.9391554	-0.0648779	-2.3262407
H	2.1292709	-0.0914451	4.4830541
H	3.0716705	-0.0854673	2.2178017
H	-1.8360290	0.0329437	2.8204877
H	1.8526772	-0.0807362	-4.5276711
H	-2.0038780	0.0293083	-2.6275186
H	-0.2574436	-0.0610171	-5.8074749
H	-1.8051931	-0.0198745	-5.0166990
H	0.0988842	-0.0577952	5.8876451
H	-1.4928807	-0.0126423	5.1903697
H	5.1752677	0.8154440	-0.4559539
H	3.7879641	0.1342179	-0.2943129
H	-3.9324822	0.7889088	5.2805818
H	-3.9525270	-0.7475956	5.2513949
H	-4.2616327	-0.7598634	-4.9286759
O	-3.7166048	0.0079493	-4.7191134
H	-4.2472788	0.7764853	-4.9604132

Optimized geometries of the electronically excited states of the micro-hydrated models.

$TH_2^{2+}3W_{(wc)}$, $S_1(\pi_{H-1}\rightarrow\pi_L^*)$

C	2.6263123	-0.0004135	-0.8627176
C	1.3693916	-0.0000012	-0.2652653
C	1.2312385	-0.0000915	1.1431187
C	2.4060029	0.0004886	1.9135571
C	3.6635847	0.0004300	1.3423456
C	3.8180354	0.0003651	-0.0594865
N	0.0004203	0.0000720	1.7564220
C	-1.2302676	0.0000080	1.1425624
C	-1.3674474	-0.0005517	-0.2659252
S	0.0010376	-0.0006753	-1.3582307
C	-2.6242750	-0.0004494	-0.8638353
C	-3.8166035	-0.0003303	-0.0613652
C	-3.6629453	0.0001372	1.3406013
C	-2.4055188	0.0001093	1.9122665
N	-5.0048866	-0.0005313	-0.6680355
N	5.0068629	0.0005543	-0.6651633
H	2.3140100	0.0005793	2.9935620
H	-4.5390191	0.0002660	1.9763950
H	-2.3137336	0.0003763	2.9922578
H	-2.7259234	-0.0006530	-1.9439991
H	4.5393786	0.0009020	1.9785069
H	2.7286429	-0.0006361	-1.9427967
H	5.8584911	0.0015131	-0.1226344
H	5.0843568	0.0010024	-1.6875671
H	-5.8568570	-0.0005718	-0.1260339
H	-5.0817408	-0.0006693	-1.6907189
H	-0.0000584	0.0002046	2.7871740
O	-0.0074664	0.0000581	4.5968323
H	-0.0063152	-0.7709694	5.1785708
H	-0.0063934	0.7706412	5.1791566
H	5.0656134	0.7673968	-4.0427848
O	4.8167612	-0.0002954	-3.5118358
H	5.0645137	-0.7690896	-4.0417126
H	-5.0671341	-0.7664371	-4.0432275
O	-4.8184324	0.0014680	-3.5124483
H	-5.0685643	0.7703380	-4.0410848

$TH_2^{2+}3W_{(wc)}$, $S_2(\pi_H\rightarrow\pi_L^*)$

C	2.6386708	-0.0002053	-0.8820988
C	1.3721994	-0.0002506	-0.3094183
C	1.2265682	0.0001210	1.1059605
C	2.3924673	0.0005926	1.9184015
C	3.6355952	0.0006959	1.3628449
C	3.7958674	0.0003284	-0.0667688
N	0.0000018	-0.0000032	1.7218299
C	-1.2265573	-0.0001074	1.1058715
C	-1.3723049	-0.0004720	-0.3094627
S	0.0000095	-0.0009888	-1.3994241
C	-2.6387068	-0.0004175	-0.8821852
C	-3.7957799	-0.0002002	-0.0668635
C	-3.6354321	-0.0000049	1.3627379
C	-2.3923711	0.0000268	1.9184177
N	-5.0120438	-0.0001399	-0.6137026
N	5.0120833	0.0005025	-0.6137402
H	2.2728708	0.0008962	2.9952342
H	-4.5142995	0.0001254	1.9955812
H	-2.2728076	0.0002614	2.9952408
H	-2.7577217	-0.0005374	-1.9594842
H	4.5144404	0.0010925	1.9957119
H	2.7576614	-0.0004730	-1.9594161
H	5.8372093	0.0009358	-0.0300481
H	5.1446578	0.0003266	-1.6357371
H	-5.8371019	-0.0000084	-0.0299235
H	-5.1446568	-0.0000540	-1.6356591
H	-0.0000641	0.0000736	2.7557829
O	-0.0001630	-0.0000232	4.5475351
H	-0.0000161	-0.7714802	5.1291009
H	-0.0002909	0.7712357	5.1293625
H	5.3824131	0.7692739	-3.9525641
O	5.1126921	-0.0001101	-3.4347491
H	5.3834879	-0.7696007	-3.9518469
H	-5.3829091	-0.7675295	-3.9530155
O	-5.1127071	0.0013502	-3.4347079
H	-5.3835017	0.7713321	-3.9510702

Optimized geometries of the electronically excited states of the micro-hydrated models.

$TH_2^{2+}3W_{(wc)}$, $T_1(\pi_H \rightarrow \pi_L^*)$

C	2.6436366	-0.0000836	-0.8788428
C	1.3849364	-0.0024695	-0.3238998
C	1.2335795	-0.0015145	1.0910112
C	2.3841371	0.0010344	1.9129037
C	3.6374015	0.0026494	1.3686601
C	3.7993964	0.0023652	-0.0515353
N	0.0002548	-0.0028248	1.7030113
C	-1.2326520	-0.0002948	1.0905192
C	-1.3819481	-0.0025177	-0.3245612
S	0.0026259	-0.0102534	-1.4328772
C	-2.6398669	-0.0001611	-0.8809941
C	-3.7969709	0.0041115	-0.0545721
C	-3.6365962	0.0062003	1.3656358
C	-2.3840875	0.0040112	1.9114127
N	-5.0129114	0.0067935	-0.6047977
N	5.0169080	0.0044436	-0.5983644
H	2.2542429	0.0017246	2.9881142
H	-4.5114687	0.0097682	2.0041327
H	-2.2549340	0.0056113	2.9867599
H	-2.7704343	-0.0015077	-1.9569770
H	4.5113740	0.0044808	2.0082737
H	2.7755970	-0.0001138	-1.9546876
H	5.8414044	0.0054716	-0.0120821
H	5.1544029	0.0046628	-1.6224472
H	-5.8387559	0.0102768	-0.0202797
H	-5.1480698	0.0047036	-1.6295468
H	0.0025938	-0.0025007	2.7319721
O	-0.0168612	-0.0037427	4.5580117
H	-0.0119411	-0.7758952	5.1383492
H	-0.0098702	0.7655427	5.1420918
H	5.4458454	0.7756067	-3.9180690
O	5.1808437	0.0050737	-3.3995572
H	5.4445960	-0.7648539	-3.9195685
H	-5.4483038	-0.7717232	-3.9219874
O	-5.1806192	-0.0006464	-3.4056714
H	-5.4454884	0.7682947	-3.9265940

$TH_2^{2+}3W_{(wc)}$, $T_2(\pi_{H-1} \rightarrow \pi_L^*)$

C	2.6297726	0.0000306	-0.8658087
C	1.3666450	0.0001429	-0.2589637
C	1.2238126	0.0000292	1.1425474
C	2.4052656	-0.0003698	1.9148182
C	3.6516675	-0.0003805	1.3391552
C	3.8071727	-0.0002801	-0.0699874
N	0.0003735	0.0001024	1.7602862
C	-1.2232063	0.0001564	1.1428378
C	-1.3664213	0.0000812	-0.2586434
S	-0.0000050	0.0002942	-1.3565277
C	-2.6296805	0.0001718	-0.8651652
C	-3.8068781	0.0001156	-0.0690516
C	-3.6510309	0.0001597	1.3400537
C	-2.4044615	0.0001062	1.9153915
N	-5.0074762	0.0001637	-0.6656658
N	5.0076451	-0.0004876	-0.6668740
H	2.3145408	-0.0005736	2.9946397
H	-4.5302313	0.0001555	1.9721939
H	-2.3135036	0.0001010	2.9951951
H	-2.7265363	-0.0003110	-1.9457030
H	4.5310330	-0.0006074	1.9710706
H	2.7263293	0.0000270	-1.9463630
H	5.8540226	-0.0006940	-0.1163335
H	5.0937935	0.0000597	-1.6886440
H	-5.8537535	0.0000746	-0.1149868
H	-5.0939463	-0.0002093	-1.6874295
H	0.0004880	0.0000242	2.7906577
O	0.0009985	0.0000248	4.6016254
H	0.0003214	-0.7707781	5.1835980
H	0.0005712	0.7708522	5.1835659
H	5.1053888	0.7687566	-4.0430659
O	4.8497663	0.0005328	-3.5161294
H	5.1056839	-0.7677384	-4.0428590
H	-5.1065537	-0.7688631	-4.0431306
O	-4.8532376	-0.0007972	-3.5148963
H	-5.1074376	0.7676866	-4.0420979

Optimized geometries of the electronically excited states of the micro-hydrated models.

$T4W_{(wc)}$, $S_1(\pi_H \rightarrow \pi_L^*)$

C	-1.5106361	-0.1581595	-4.0666366
C	-1.9970697	-0.1200909	-2.7828613
C	-1.1758808	-0.0370200	-1.6277609
C	0.2334170	0.0089147	-1.8675492
C	0.7647776	-0.0284779	-3.1501292
C	-0.0962420	-0.1067478	-4.3256462
N	-1.7516875	0.0038162	-0.3920796
S	1.3985103	0.0977207	-0.5833704
C	0.3969624	0.0859984	0.8604107
C	-1.0349148	0.0540854	0.7471905
C	-1.7370784	0.0621481	1.9827918
H	-2.8191517	0.0361250	1.9344824
C	-1.0925021	0.1061083	3.1940025
C	0.3261353	0.1339665	3.2844663
C	1.0512409	0.1307060	2.0867957
H	-2.1899379	-0.2264929	-4.9076016
H	-3.0662810	-0.1642721	-2.6073125
H	1.8363825	0.0096784	-3.3204854
H	-1.6699113	0.1119582	4.1112579
H	2.1347014	0.1516593	2.1271343
N	0.9446832	0.1959172	4.5005405
H	0.4056036	0.0218851	5.3383756
H	1.9472223	0.0742384	4.5481136
N	0.5097628	-0.1276192	-5.4844845
H	-0.1615366	-0.1892034	-6.2498661
O	-4.6209553	0.1030613	-0.0912636
H	-4.8346410	1.0209417	-0.2864844
H	-3.6507829	0.0371789	-0.2318842
H	2.3863274	-0.0732249	-5.4672852
O	3.3233070	-0.0093377	-5.1698289
H	3.6956852	0.7318104	-5.6571961
O	-0.8253796	-0.3666130	6.9174976
H	-1.3143760	0.2867803	7.4293546
H	-1.2725887	-1.2067950	7.0663315
O	3.9576255	-0.1038813	4.1933262
H	4.4659894	-0.9222067	4.1854745
H	4.5994109	0.6035856	4.3181389

$T4W_{(wc)}$, $S_2(\pi_{H-1} \rightarrow \pi_L^*)$

C	-1.5076615	-0.1633287	-4.0189464
C	-2.0221569	0.0021649	-2.7683826
C	-1.1949535	0.0961613	-1.5976980
C	0.2369147	0.0923336	-1.8618689
C	0.7583226	-0.0736770	-3.1147623
C	-0.0834924	-0.2261873	-4.2735416
N	-1.7910030	0.1713864	-0.4174363
S	1.3684878	0.4938651	-0.5502637
C	0.3380811	0.2514942	0.8589307
C	-1.0369272	0.0892379	0.7721286
C	-1.7255182	-0.1685854	1.9765582
H	-2.7998485	-0.2975409	1.9083649
C	-1.0995898	-0.2401803	3.2112681
C	0.2861397	-0.0656296	3.3019650
C	1.0083948	0.1766409	2.0974498
H	-2.1795082	-0.2517573	-4.8669647
H	-3.0929872	0.0242939	-2.6048513
H	1.8298659	-0.0730537	-3.2830034
H	-1.6765655	-0.4326465	4.1064391
H	2.0841454	0.2996145	2.1450966
N	0.9690438	-0.1004943	4.4772474
H	0.4779121	-0.2384405	5.3544459
H	1.9783765	-0.0124205	4.4816458
N	0.4665483	-0.3963146	-5.4553921
H	-0.2412502	-0.4942642	-6.1811649
O	-4.6106020	0.2520331	0.0328448
H	-4.8854838	1.1605228	-0.1251183
H	-3.6511345	0.2349080	-0.1869544
H	2.3290743	-0.4409220	-5.5580223
O	3.3042251	-0.3577111	-5.4358506
H	3.5250578	0.4848531	-5.8446165
O	-0.5480455	-0.5319975	7.0092469
H	-1.0903474	0.1339648	7.4458902
H	-0.9011716	-1.3847346	7.2857591
O	3.9153222	0.1634216	4.0212853
H	4.5191631	-0.5760455	3.8896838
H	4.4716618	0.9388481	4.1540510

Optimized geometries of the electronically excited states of the micro-hydrated models.

T4W$_{(wc)}$, T$_1$($\pi_H \rightarrow \pi_L$*)

C	-0.5788718	-0.1719896	-4.0336698
C	-1.2586052	-0.1485139	-2.8400100
C	-0.5904067	-0.0532426	-1.5956390
C	0.8189843	0.0067400	-1.6206936
C	1.5185699	-0.0143105	-2.8204875
C	0.8464054	-0.0970026	-4.0663711
N	-1.3804497	-0.0274018	-0.4579588
S	1.7855084	0.1195846	-0.1350690
C	0.5396929	0.0501236	1.1177037
C	-0.8549179	0.0066003	0.7745684
C	-1.7651128	-0.0102716	1.8781434
H	-2.8209255	-0.0426414	1.6385853
C	-1.3440406	0.0093180	3.1773310
C	0.0419032	0.0433848	3.4967864
C	0.9626035	0.0672576	2.4352791
H	-1.1170113	-0.2543597	-4.9709073
H	-2.3402173	-0.2063040	-2.8148085
H	2.6010363	0.0330616	-2.8372118
H	-2.0652511	-0.0064611	3.9861189
H	2.0222767	0.0978684	2.6626027
N	0.4518711	0.0598183	4.7908718
H	-0.2229398	-0.0083689	5.5409442
H	1.4374876	0.0369996	5.0160476
N	1.5907925	-0.0965604	-5.1904723
H	0.9707659	-0.1485045	-6.0046433
O	-4.2461934	0.1255466	-0.6724981
H	-4.4002337	1.0618961	-0.8330436
H	-3.2673599	0.0386433	-0.6260587
H	0.5956774	-0.1273536	-8.5655042
O	-0.1093058	0.0486106	-7.9321073
H	-0.4016925	0.9467898	-8.1210427
O	-1.6737285	-0.1594997	6.9457616
H	-2.1884783	0.5770064	7.2926008
H	-2.1974806	-0.9505595	7.1115623
O	3.4570677	-0.0248469	5.2108307
H	3.9948989	-0.8088053	5.0540345
H	4.0532019	0.7268582	5.1249110

T4W$_{(wc)}$, T$_2$($\pi_{H-1} \rightarrow \pi_L$*)

C	-1.4988238	-0.0955504	-4.0321760
C	-2.0049278	-0.0812577	-2.7499608
C	-1.1887828	-0.0321436	-1.5935300
C	0.2347714	-0.0020692	-1.8679866
C	0.7632900	-0.0139448	-3.1515271
C	-0.0796143	-0.0551410	-4.3165963
N	-1.7787136	-0.0183479	-0.3862173
S	1.3998717	0.0426784	-0.5625993
C	0.3494671	0.0253195	0.8681965
C	-1.0532076	0.0031041	0.7723444
C	-1.7493059	-0.0090024	2.0088219
H	-2.8318148	-0.0291861	1.9581516
C	-1.1153186	0.0048809	3.2350594
C	0.2864556	0.0258241	3.3138914
C	1.0131511	0.0400805	2.0916286
H	-2.1846735	-0.1379747	-4.8718914
H	-3.0760673	-0.1161248	-2.5881515
H	1.8359160	0.0102665	-3.3140844
H	-1.6984172	-0.0067603	4.1475975
H	2.0969998	0.0574646	2.1296767
N	0.9635097	0.0380042	4.4947200
H	0.4622658	0.0032122	5.3747865
H	1.9753260	0.0268921	4.5006912
N	0.4714543	-0.0589879	-5.5070960
H	-0.2319983	-0.1030907	-6.2416528
O	-4.6232211	0.1027954	-0.0619357
H	-4.8298162	1.0254284	-0.2414782
H	-3.6536483	0.0292183	-0.2157010
H	2.3197963	-0.0454151	-5.5617960
O	3.2857815	0.0251987	-5.3663275
H	3.5516404	0.8643180	-5.7546770
O	-0.6062220	-0.1010940	7.0497014
H	-1.0823589	0.6361547	7.4470969
H	-1.0605781	-0.8983296	7.3434300
O	3.9363594	-0.0136601	4.0296855
H	4.4859660	-0.8051390	4.0387202
H	4.5453542	0.7307220	4.0884742

Optimized geometries of the electronically excited states of the micro-hydrated models.

$T5W_{(wc)}$, $S_1(\pi_H \rightarrow \pi_L^*)$

C	-0.4328232	-0.1015291	-4.4153985
C	-1.1744294	-0.1873669	-3.2653157
C	-0.6320891	-0.0568002	-1.9575465
C	0.7891095	0.1626976	-1.8888046
C	1.5676560	0.2568054	-3.0273429
C	0.9961117	0.1248053	-4.3658773
N	-1.4469814	-0.1487515	-0.8753622
S	1.6341588	0.3377484	-0.3815949
C	0.3584910	0.1637454	0.8116952
C	-0.9971732	-0.0549328	0.3964228
C	-1.9359442	-0.1826604	1.4514361
H	-2.9700561	-0.3493449	1.1753457
C	-1.5694478	-0.0974239	2.7757528
C	-0.2264611	0.1274088	3.1588742
C	0.7269778	0.2559656	2.1539561
H	-0.8989016	-0.2092908	-5.3865148
H	-2.2427591	-0.3641668	-3.3203938
H	2.6370549	0.4246870	-2.9689699
H	-2.3220044	-0.1993296	3.5494629
H	1.7652586	0.4194088	2.4224025
N	0.1306829	0.1510087	4.5114071
H	-0.6278670	0.4045770	5.1383203
H	0.9868824	0.6615902	4.7165229
N	1.8320626	0.2245943	-5.3554437
H	1.3371852	0.1158994	-6.2457460
O	-4.3086044	-0.3722300	-1.1600262
H	-4.5728483	0.5125416	-1.4314557
H	-3.3278676	-0.3339769	-1.1081339
H	0.4503283	-1.0476129	-8.5354234
O	0.2052548	-0.2296524	-8.0892243
H	0.2702535	0.4584431	-8.7604154
O	-2.3255750	0.8748458	6.1881119
H	-2.7180659	1.7545132	6.1751041
H	-2.7434426	0.4110527	6.9215565
O	3.0038464	0.5816679	5.3201634
H	2.9179789	-0.3863251	5.4192209
H	3.9108811	0.7511578	5.0492179
H	1.6904140	-2.6332754	5.9298194
O	1.9345050	-1.9697269	5.2773416
H	1.1150822	-1.4811564	5.0483109

$T5W_{(wc)}$, $S_2(\pi_{H-1} \rightarrow \pi_L^*)$

C	-1.3041497	-0.3809806	-4.3350245
C	-1.9477017	-0.1861528	-3.1507247
C	-1.2407276	0.0729721	-1.9275963
C	0.1974073	0.2426358	-2.0713521
C	0.8481154	0.0445348	-3.2560245
C	0.1373908	-0.3032140	-4.4605514
N	-1.9345874	0.1293828	-0.7991050
S	1.1141389	0.9597504	-0.7243571
C	0.0572866	0.5315076	0.6266189
C	-1.2614832	0.1371746	0.4383567
C	-1.9788081	-0.2795363	1.5823224
H	-3.0084170	-0.5841733	1.4321446
C	-1.4343716	-0.2826159	2.8563094
C	-0.1110436	0.1262204	3.0459130
C	0.6446917	0.5248660	1.9052741
H	-1.8797572	-0.6054985	-5.2275146
H	-3.0246547	-0.2793607	-3.0779995
H	1.9220351	0.1721506	-3.3373352
H	-2.0284670	-0.5959368	3.7053799
H	1.6800258	0.8185658	2.0380178
N	0.4961605	0.1379862	4.2743315
H	-0.0849511	0.0902889	5.1075166
H	1.4079811	0.5838213	4.3591297
N	0.8080506	-0.5069162	-5.5721236
H	0.1848154	-0.7453968	-6.3416587
O	-4.7517965	-0.2221215	-0.5237700
H	-5.1750125	0.6220450	-0.7086733
H	-3.7935758	-0.0715921	-0.6916395
H	2.6734669	-0.3881174	-5.5040572
O	3.6231505	-0.2226094	-5.2984167
H	3.8449419	0.5692835	-5.7978189
O	-1.3111292	0.0189276	6.6355977
H	-1.8987947	0.7357333	6.8982624
H	-1.5111011	-0.7188745	7.2216858
O	3.3235116	0.7469016	3.9388584
H	3.5099871	-0.2108294	3.9636505
H	4.1075182	1.2008401	4.2619717
H	2.9340856	-2.6693855	3.4299270
O	2.8729549	-1.9774743	4.0976997
H	1.9297028	-1.7816630	4.1995162

Optimized geometries of the electronically excited states of the micro-hydrated models.

T5W$_{(wc)}$, T$_1$($\pi_H \rightarrow \pi_L$*)

C	-0.3860627	-0.1607525	-4.3663711
C	-1.1309593	-0.2180405	-3.2145556
C	-0.5522149	-0.0447920	-1.9331764
C	0.8376000	0.1848691	-1.8754832
C	1.6058201	0.2457524	-3.0347253
C	1.0213536	0.0768644	-4.3133184
N	-1.4040450	-0.1167106	-0.8438027
S	1.6941101	0.4126390	-0.3416525
C	0.3922811	0.2296641	0.8339780
C	-0.9622806	0.0009349	0.4159626
C	-1.9292621	-0.1140908	1.4632549
H	-2.9556870	-0.2878966	1.1645030
C	-1.5903080	-0.0130205	2.7840702
C	-0.2464174	0.2175397	3.1709614
C	0.7285559	0.3354458	2.1772298
H	-0.8521071	-0.2976275	-5.3351703
H	-2.1977836	-0.4029508	-3.2515616
H	2.6738127	0.4228161	-2.9895975
H	-2.3492698	-0.1050946	3.5524393
H	1.7582053	0.5085582	2.4713040
N	0.0958995	0.2581368	4.5146560
H	-0.6562986	0.4822433	5.1597119
H	0.9806557	0.7086276	4.7311398
N	1.8306150	0.1500229	-5.3921365
H	1.2688342	0.0123130	-6.2383613
O	-4.2540035	-0.3919183	-1.2261356
H	-4.5359995	0.5042471	-1.4353070
H	-3.2787636	-0.3293766	-1.1247552
H	0.0686804	-0.9918949	-8.5266330
O	-0.1068706	-0.2477007	-7.9405274
H	-0.2060880	0.5168082	-8.5183993
O	-2.2563599	0.7706482	6.3513895
H	-2.6721196	1.6181850	6.5428897
H	-2.4981586	0.1864497	7.0781765
O	3.0321586	0.3941755	4.9013444
H	2.9168231	-0.5618558	5.0619913
H	3.9568433	0.6032037	5.0602238
H	1.7302512	-2.7819491	4.5789487
O	1.7618720	-2.0571946	5.2121603
H	0.9943611	-1.4863257	5.0059462

T5W$_{(wc)}$, T$_2$($\pi_{H-1} \rightarrow \pi_L$*)

C	-1.3100667	-0.2504461	-4.3901902
C	-1.9048148	-0.2740462	-3.1346233
C	-1.1819270	-0.1062707	-1.9366070
C	0.2474086	0.0729104	-2.1143892
C	0.8584308	0.1034836	-3.3562219
C	0.1110608	-0.0705933	-4.5782756
N	-1.8549339	-0.1387009	-0.7690845
S	1.2979118	0.3009296	-0.7334443
C	0.1594099	0.1774963	0.6284964
C	-1.2238493	-0.0169091	0.4345802
C	-2.0031109	-0.0903524	1.6148170
H	-3.0693305	-0.2388085	1.4898538
C	-1.4599929	0.0174581	2.8867050
C	-0.0886507	0.2100863	3.0562824
C	0.7232158	0.2873208	1.8898918
H	-1.9303297	-0.3827826	-5.2703238
H	-2.9749037	-0.4210025	-3.0456205
H	1.9302927	0.2476000	-3.4480237
H	-2.1022927	-0.0459213	3.7567306
H	1.7920851	0.4338598	2.0104349
N	0.5105126	0.2703085	4.3035442
H	-0.0949206	0.5101343	5.0841034
H	1.4349654	0.6927929	4.3308160
N	0.7405571	-0.0465555	-5.7263446
H	0.0980646	-0.1683437	-6.5064985
O	-4.7156487	-0.3623602	-0.6826922
H	-5.0215929	0.5324731	-0.8613897
H	-3.7357084	-0.3105015	-0.7455742
H	3.9807235	-0.3725678	-5.6993544
O	3.5039226	0.3849386	-5.3467033
H	2.5708672	0.2582298	-5.6421155
O	-1.4054253	0.9395567	6.5264822
H	-1.8812846	1.7710636	6.6271346
H	-1.6059058	0.4209670	7.3130735
O	3.4319762	0.3919153	3.8459173
H	3.3878853	-0.5365212	4.1460029
H	4.3057182	0.7212846	4.0765740
H	2.2260437	-2.8446854	4.3179939
O	2.3696169	-1.9986105	4.7545966
H	1.5291803	-1.5074412	4.6905262

Table 35. Spin-orbit matrix elements (SOMEs, cm^{-1}) between low-lying singlet and triplet states at the $S_1(\pi_{H-1}\rightarrow\pi_L^*)$, $S_2(\pi_H\rightarrow\pi_L^*)$ and $T_1(\pi_H\rightarrow\pi_L^*)$ minima of TH_2^{2+}. The direction of the coupling *x*, *y* or *z* is given in parenthesis.

SOMEs $\langle i\|\hat{H}_{SO}\|f\rangle$	@$S_1(\pi_{H-1}\rightarrow\pi_L^*)^a$	@$S_2(\pi_H\rightarrow\pi_L^*)^b$	@$T_1(\pi_H\rightarrow\pi_L^*)^c$
$\langle S_0\|\hat{H}_{SO}\|T_1(\pi_H\rightarrow\pi_L*)\rangle$	0.02(*y*)	0.16(*x*)/-0.02(*y*)	-0.03(*x*)/0.01(*y*)
$\langle S_1(\pi_{H-1}\rightarrow\pi_L*)\|\hat{H}_{SO}\|T_1(\pi_H\rightarrow\pi_L*)\rangle$	0.03(*y*)	-0.14(*x*)/0.03(*y*)	0.03(*x*)/-0.01(*y*)
$\langle S_1(\pi_{H-1}\rightarrow\pi_L*)\|\hat{H}_{SO}\|T_2(\pi_{H-1}\rightarrow\pi_L*)\rangle$	-	-0.05 (*z*)	0.01 (*z*)
$\langle S_2(\pi_H\rightarrow\pi_L*)\|\hat{H}_{SO}\|T_1(\pi_H\rightarrow\pi_L*)\rangle$	-	-0.16 (*z*)	0.00 (*z*)
$\langle S_2(\pi_H\rightarrow\pi_L*)\|\hat{H}_{SO}\|T_2(\pi_{H-1}\rightarrow\pi_L*)\rangle$	-0.01(*y*)	-0.06(*x*)/0.02(*y*)	0.01(*x*)/0.00(*y*)

[a] C_{2v} symmetric. [b] C_2 symmetric. [c] C_s symmetric.

Table 36. Spin-orbit matrix elements (SOMEs, cm^{-1}) between low-lying singlet and triplet states at the $S_1(\pi_H\rightarrow\pi_L^*)$ and $T_1(\pi_H\rightarrow\pi_L^*)$ minima of T. The direction of the coupling *x*, *y* or *z* is given in parenthesis.

SOMEs $\langle i\|\hat{H}_{SO}\|f\rangle$	@$S_1(\pi_{H-1}\rightarrow\pi_L^*)$	@$T_1(\pi_H\rightarrow\pi_L^*)$
$\langle S_0\|\hat{H}_{SO}\|T_1(\pi_H\rightarrow\pi_L*)\rangle$	0.02(*x*)/0.01(*y*)/0.02(*z*)	-0.03(*x*)/0.00(*y*)/-0.03(*z*)
$\langle S_1(\pi_H\rightarrow\pi_L*)\|\hat{H}_{SO}\|T_1(\pi_H\rightarrow\pi_L*)\rangle$	-0.01(*x*)/0.02(*y*)/-0.05(*z*)	0.02(*x*)/0.00(*y*)/0.06(*z*)
$\langle S_1(\pi_H\rightarrow\pi_L*)\|\hat{H}_{SO}\|T_2(\pi_{H-1}\rightarrow\pi_L*)\rangle$	0.01(*x*)/-0.02(*y*)/0.05(*z*)	-0.04(*x*)/0.01(*y*)/-0.06(*z*)
$\langle S_1(\pi_H\rightarrow\pi_L*)\|\hat{H}_{SO}\|T_3(n_{H-4}\rightarrow\pi_L*)\rangle$	-4.21(*x*)/11.78(*y*)/-0.02(*z*)	-1.87(*x*)/10.57(*y*)/-0.01(*z*)

Table 37. Harmonic frequencies (ν_i, cm^{-1}) and ∂SOMEs, (cm^{-1}) with respect to the corresponding (dimensionless) normal coordinates at the $S_1(\pi_{H-1}\rightarrow\pi_L^*)$ minima of TH_2^{2+}.

	$S_1(\pi_{H-1}\rightarrow\pi_L^*)\rightsquigarrow T_1(\pi_H\rightarrow\pi_L^*)$			$S_1(\pi_{H-1}\rightarrow\pi_L^*)\rightsquigarrow T_2(\pi_{H-1}\rightarrow\pi_L^*)$		
ν_i	x	y	z	x	y	z
43.7(B_2)	0.00	0.00	-0.21	0.00	0.00	0.00
80.6(A_2)	-0.87	0.00	0.00	0.00	0.00	0.27
134.1(A_2)	0.00	-0.23	0.00	0.00	0.00	-0.15
156.5(B_2)	0.00	0.00	-0.39	-0.38	0.00	0.00
172.4(A_2)	0.00	-0.23	0.00	0.00	0.00	-0.40
182.1(B_2)	0.00	0.00	0.45	0.00	0.00	0.00
284.8(B_1)	0.00	0.00	0.00	0.00	0.00	0.00
285.8(B_2)	0.00	-0.16	0.00	0.00	0.00	0.00
305.0(A_1)	0.00	0.24	0.00	0.00	0.00	0.00
334.3(A_2)	1.20	0.00	0.00	0.00	0.00	0.00
387.1(B_2)	0.00	-0.20	0.00	0.00	0.00	0.00
394.7(A_2)	0.30	0.00	0.00	0.00	0.00	-0.17
397.8(B_1)	0.00	0.24	0.00	0.00	0.00	0.00
398.3(A_1)	0.00	0.00	0.00	0.00	0.00	0.00
457.3(B_2)	0.00	0.00	-0.67	0.00	0.00	0.00
457.5(B_1)	0.00	0.00	0.00	0.00	0.00	0.00
485.1(A_1)	0.00	0.24	0.00	0.00	0.00	0.00
486.3(A_2)	1.00	0.00	0.00	0.00	0.00	-0.14
494.9(B_2)	0.00	-0.23	0.00	0.00	0.00	0.00
517.1(B_1)	0.00	0.24	0.00	0.00	0.00	0.00
538.8(A_2)	-0.48	0.00	0.00	0.00	0.00	0.00
544.0(B_2)	0.00	-0.23	0.00	0.39	0.00	0.00
558.6(A_2)	-0.08	0.00	0.00	0.00	0.00	0.12
563.5(B_2)	0.00	0.00	0.25	0.68	0.00	0.00
595.8(B_2)	0.00	0.00	0.63	-0.65	0.00	0.00
610.8(A_1)	0.00	-0.24	0.01	0.01	0.00	0.00
648.8(B_1)	0.00	0.24	0.00	0.00	0.00	0.00
700.6(A_1)	0.00	0.00	0.00	0.00	0.00	0.00
787.6(A_2)	0.82	0.00	0.00	0.00	0.00	-0.04
792.3(B_2)	0.00	0.16	0.00	-0.49	0.00	0.00
818.8(A_1)	0.00	0.00	0.00	0.00	0.00	0.00
832.0(A_2)	-0.37	0.00	0.00	0.00	0.00	0.00
834.3(B_2)	0.00	0.24	0.00	0.27	0.00	0.00
859.6(B_1)	0.00	0.00	0.00	0.00	0.00	0.00
892.0(B_1)	0.00	-0.24	0.00	0.00	0.00	0.00
919.7(A_1)	0.00	0.00	0.00	0.00	0.00	0.00
929.5(B_2)	0.00	0.00	-0.11	-0.55	0.00	0.00
929.6(A_2)	-0.26	0.00	0.00	0.00	0.00	0.07
1030.6(B_1)	0.00	0.24	0.00	0.00	0.00	0.00
1051.3(A_1)	0.00	0.00	0.00	0.00	0.00	0.00
1054.8(B_1)	0.00	0.00	0.00	0.00	0.00	0.00
1076.3(A_1)	0.00	0.24	0.00	0.00	0.00	0.00
1171.3(B_1)	0.00	0.00	0.00	0.00	0.00	0.00
1194.8(B_1)	0.00	0.00	0.00	0.00	0.00	0.00
1200.6(A_1)	0.00	0.00	0.00	0.00	0.00	0.00
1287.7(A_1)	0.00	0.00	0.00	0.00	0.00	0.00
1297.3(B_1)	0.00	0.00	0.00	0.00	0.00	0.00

1319.2(B_1)	0.00	-0.24	0.00	0.00	0.00	0.00
1319.7(A_1)	0.00	0.24	0.00	0.00	0.00	0.00
1361.2(A_1)	0.00	0.00	0.00	0.00	0.00	0.00
1366.0(B_1)	0.00	-0.24	0.00	0.00	0.00	0.00
1390.6(B_1)	0.00	0.24	0.00	0.00	0.00	0.00
1399.4(A_1)	0.00	0.24	0.00	0.00	0.00	0.00
1462.3(A_1)	0.00	0.24	0.00	0.00	0.00	0.00
1475.7(B_1)	0.00	0.24	0.00	0.00	0.01	0.00
1546.5(B_1)	0.00	-0.24	0.00	0.00	0.00	0.00
1553.1(A_1)	0.00	-0.24	0.00	0.00	0.00	0.00
1568.6(B_1)	0.00	-0.24	0.00	0.00	-0.01	0.00
1576.3(A_1)	0.00	0.00	0.00	0.00	0.00	0.00
1610.0(B_1)	0.00	0.00	0.00	0.00	0.00	0.00
1636.2(A_1)	0.00	-0.24	0.00	0.00	0.00	0.00
1682.1(B_1)	0.00	-0.24	0.00	0.00	0.00	0.00
1685.8(A_1)	0.00	0.00	0.00	0.00	0.00	0.00
3179.5(B_1)	0.00	0.24	0.00	0.00	0.00	0.00
3180.1(A_1)	0.00	-0.24	0.00	0.00	0.00	0.00
3184.5(B_1)	0.00	0.00	0.00	0.00	0.00	0.00
3184.6(A_1)	0.00	-0.24	0.00	0.00	0.00	0.00
3204.5(B_1)	0.00	0.24	0.00	0.00	0.00	0.00
3205.6(A_1)	0.00	0.00	0.00	0.00	0.00	0.00
3549.0(B_1)	0.00	0.00	0.00	0.00	0.00	0.00
3554.3(A_1)	0.00	0.24	0.00	0.00	0.00	0.00
3561.6(A_1)	0.00	0.00	0.00	0.00	0.00	0.00
3664.1(B_1)	0.00	0.00	0.00	0.00	0.00	0.00
3664.2(A_1)	0.00	0.24	0.00	0.00	0.00	0.00

Table 38. Harmonic frequencies (ν_i, cm^{-1}) and ∂SOMEs, (cm^{-1}) with respect to the corresponding (dimensionless) normal coordinates at the $S_2(\pi_H \rightarrow \pi_L^*)$ minima of TH_2^{2+}.

	$S_2(\pi_H \rightarrow \pi_L^*) \rightsquigarrow T_1(\pi_H \rightarrow \pi_L^*)$			$S_2(\pi_H \rightarrow \pi_L^*) \rightsquigarrow T_2(\pi_{H-1} \rightarrow \pi_L^*)$		
ν_i	x	y	z	x	y	Z
34.6(B)	0.00	0.00	1.49	0.00	0.00	0.21
74.8(A)	0.00	0.00	0.16	0.43	0.00	0.00
147.9(B)	0.00	0.00	-1.49	0.69	-0.15	0.00
155.7(A)	0.00	0.00	0.22	0.13	0.00	0.00
158.4(B)	0.00	0.00	-1.49	0.00	0.00	0.50
166.3(A)	0.00	0.00	0.03	0.02	0.00	0.00
261.3(A)	0.00	0.00	0.78	0.23	0.00	0.00
276.4(B)	0.00	0.00	-1.49	0.69	-0.14	0.00
294.5(B)	-0.01	0.00	0.00	0.69	-0.15	0.00
300.1(A)	0.00	0.00	0.00	-0.03	0.00	0.00
327.5(A)	0.00	0.00	0.28	-0.69	0.15	0.00
389.0(B)	0.00	0.00	-1.49	0.69	-0.12	0.00
395.0(A)	0.00	0.00	0.02	-0.69	0.15	0.00
429.0(B)	0.00	0.00	-1.49	0.00	0.00	0.03
436.2(A)	0.00	0.00	-0.51	0.12	0.01	0.00
464.5(B)	-0.01	-0.01	0.00	0.69	-0.15	0.00
481.6(B)	0.21	0.01	0.00	0.69	-0.09	0.00
484.8(A)	0.00	0.00	-0.03	0.69	-0.15	0.00
504.7(B)	-0.57	0.00	0.00	0.69	-0.15	0.00
514.2(A)	0.00	0.00	-1.49	0.72	-0.01	0.00
530.4(B)	0.03	0.00	0.00	0.00	0.00	0.02
568.6(B)	0.32	-0.01	0.00	0.00	0.00	0.35
570.2(A)	0.00	0.00	0.00	0.07	0.00	0.00
573.2(B)	0.00	0.00	-1.49	0.00	0.00	0.30
585.1(A)	0.00	0.00	0.44	-0.39	0.00	0.00
607.5(A)	0.00	0.00	0.00	-0.03	0.00	0.00
611.0(B)	0.02	0.01	0.00	0.70	-0.14	0.00
690.4(A)	0.00	0.00	0.03	-0.69	0.15	0.00
707.1(B)	0.01	-0.01	0.00	0.00	0.00	-0.01
791.0(B)	0.00	0.00	-1.49	0.00	0.00	-0.64
793.8(A)	0.00	0.00	-0.51	0.36	0.00	0.00
815.2(A)	0.00	0.00	1.49	0.70	-0.15	0.00
819.4(B)	0.09	0.00	0.00	-0.69	0.15	0.00
821.4(A)	0.00	0.00	-0.17	-0.69	0.15	0.00
862.6(B)	0.00	0.00	-1.49	0.69	-0.15	0.00
914.8(A)	0.00	0.00	-1.48	-0.69	0.15	0.00
917.3(B)	0.00	-0.01	0.00	0.69	-0.15	0.00
943.7(A)	0.00	0.00	0.16	-0.11	-0.01	0.00
944.2(B)	0.00	0.00	-1.49	0.00	0.00	0.04
1042.7(B)	0.00	0.00	-1.49	0.69	-0.15	0.00
1054.7(A)	0.00	0.00	-0.01	-0.01	0.00	0.00
1062.7(B)	0.00	0.00	-1.49	0.00	0.00	0.00
1086.2(A)	0.00	0.00	0.02	0.01	0.00	0.00
1154.6(B)	-0.01	0.01	0.00	0.69	-0.15	0.00
1208.7(A)	0.00	0.00	-0.01	0.69	-0.15	0.00
1228.1(B)	0.05	-0.01	0.00	-0.69	0.15	0.00
1273.4(A)	0.00	0.00	0.00	-0.01	0.00	0.00

1278.9(B)	0.00	0.00	0.00	-0.69	0.15	0.00
1302.2(A)	0.00	0.00	0.00	0.69	-0.15	0.00
1344.8(B)	0.05	-0.01	0.00	-0.69	0.15	0.00
1374.4(B)	0.02	-0.01	0.00	0.69	-0.15	0.00
1377.4(A)	0.00	0.00	0.01	0.01	0.00	0.00
1415.0(A)	0.00	0.00	-1.49	0.69	-0.15	0.00
1440.7(A)	0.00	0.00	0.00	0.69	-0.15	0.00
1461.2(B)	0.03	0.00	0.00	0.69	-0.15	0.00
1507.5(B)	0.00	0.00	-1.49	0.00	0.00	0.00
1514.7(A)	0.00	0.00	0.01	-0.69	0.15	0.00
1538.3(A)	0.00	0.00	0.00	-0.69	0.15	0.00
1564.8(B)	0.00	0.00	-1.49	0.00	0.00	0.02
1622.4(B)	0.00	0.00	-1.49	0.69	-0.15	0.00
1644.5(A)	0.00	0.00	0.01	0.69	-0.15	0.00
1661.8(B)	0.00	0.00	-1.48	-0.69	0.15	0.00
1680.9(A)	0.00	0.00	1.49	0.69	-0.15	0.00
1693.8(B)	0.00	0.00	1.49	0.00	0.00	0.04
3181.0(A)	0.00	0.00	-0.01	0.00	0.00	0.00
3181.3(B)	0.00	0.00	1.49	0.69	-0.15	0.00
3186.3(A)	0.00	0.00	0.01	-0.69	0.15	0.00
3186.8(B)	0.00	0.01	0.00	0.00	0.00	0.01
3201.2(B)	0.00	0.00	-1.49	0.69	-0.15	0.00
3201.7(A)	0.00	0.00	0.01	0.00	0.00	0.00
3538.8(B)	0.00	0.00	1.49	0.69	-0.15	0.00
3539.5(A)	0.00	0.00	0.00	0.69	-0.15	0.00
3543.5(A)	0.00	0.00	0.00	-0.69	0.15	0.00
3649.1(A)	0.00	0.00	-1.49	-0.69	0.15	0.00
3649.2(B)	0.00	0.00	0.00	0.00	0.00	0.00

Table 39. Harmonic frequencies (ν_i, cm^{-1}) and ∂SOMEs (cm^{-1}) with respect to the corresponding (dimensionless) normal coordinates at the $S_1(\pi_H \rightarrow \pi_L^*)$ minima of T.

ν_i	$S_1(\pi_H \rightarrow \pi_L^*) \rightsquigarrow T_1(\pi_H \rightarrow \pi_L^*)$		
	x	y	z
41.5	0.41	0.43	0.00
62.8	-0.11	1.12	0.00
132.5	0.44	0.59	0.00
149.8	0.88	0.63	0.00
167.0	0.14	-0.11	0.00
167.9	0.69	-0.45	0.00
227.4	-0.29	0.57	0.00
280.9	0.00	0.03	0.00
295.3	0.00	0.02	0.00
307.5	-0.02	0.01	0.00
322.3	0.23	-0.53	0.00
324.0	-0.30	0.16	-0.01
388.3	-0.92	0.83	0.00
401.1	-0.02	-0.01	0.00
419.6	-0.26	-0.06	0.00
425.9	0.00	0.00	0.00
469.1	-0.01	-0.01	0.00
479.9	0.01	0.01	0.01
512.4	-0.10	-0.03	0.00
538.7	-0.16	-0.04	0.00
553.5	-0.39	-0.07	0.00
569.5	-0.10	0.06	0.00
599.0	0.07	-0.10	-0.01
604.3	0.01	-0.04	0.00
688.2	0.00	-0.01	0.00
696.0	0.00	0.00	0.00
720.8	-0.39	-0.29	0.00
789.9	0.22	-0.23	0.00
795.7	-0.08	-0.04	0.00
804.0	-0.38	-0.19	0.00
821.0	0.09	-0.20	0.00
846.8	-0.46	-0.85	0.00
865.3	-0.01	0.00	0.00
888.5	0.01	0.01	0.00
912.7	0.00	0.00	-0.01
918.9	-0.11	-0.35	0.00
933.5	0.21	0.25	0.01
1033.7	0.01	0.00	-0.01
1052.1	0.00	0.01	0.01
1092.8	-0.01	0.00	0.00
1101.2	0.01	0.00	0.00
1153.3	0.01	0.00	0.00
1173.2	0.01	0.00	0.00
1227.7	0.00	0.00	0.00
1255.6	0.00	0.00	0.00
1276.7	0.00	0.01	0.00
1298.0	-0.01	-0.01	-0.01
1313.9	-0.01	0.00	-0.01

1332.5	0.00	0.00	-0.01
1372.4	-0.01	-0.01	0.00
1405.7	0.01	0.01	0.00
1435.4	0.00	0.00	0.00
1448.2	0.00	0.01	0.00
1473.7	0.00	0.00	-0.01
1495.8	0.00	0.00	-0.01
1527.1	-0.01	-0.02	0.00
1553.5	0.00	0.00	0.00
1592.1	0.01	0.00	0.01
1627.4	-0.01	0.00	0.00
1662.3	0.00	0.01	0.00
3154.9	0.02	0.00	0.00
3164.3	-0.02	0.00	0.00
3173.7	0.01	0.00	0.00
3186.3	0.00	0.00	0.00
3189.1	0.01	0.00	0.00
3201.0	-0.01	0.01	0.00
3427.1	0.02	-0.01	0.00
3562.7	0.02	0.00	0.00
3664.9	0.00	0.03	0.00

Table 40. Calculated rate constants $k_{ISC}^{TD}(s^{-1})$ of diprotonated thionine (TH_2^{2+}) for the $S_i \rightsquigarrow T_i$ (i = 1,2) channels. Other columns: adiabatic energy difference (ΔE^{ad}, eV), time interval (t, fs), number of points ($\#_{points}$) and damping factor (η, cm^{-1})

Channel	ΔE^{ad}	η	t	$\#_{points}$	k_{ISC}^{TD}
$S_1 \rightsquigarrow T_1$	0.64	0.10	100000	3000000	1.05×10^{7}
		0.10	300000	9000000	9.21×10^{6}
		0.10	500000	15000000	9.21×10^{6}
		1	30000	900000	2.77×10^{7}
		1	50000	1500000	2.77×10^{7}
		1	100000	3000000	2.77×10^{7}
		1	300000	9000000	2.77×10^{7}
		1	500000	15000000	2.77×10^{7}
		1	900000	27000000	2.77×10^{7}
		10	30000	900000	3.86×10^{7}
		10	50000	1500000	3.86×10^{7}
		10	100000	3000000	3.86×10^{7}
		10	300000	9000000	3.86×10^{7}
		10	500000	15000000	3.86×10^{7}
		10	900000	27000000	3.86×10^{7}
		100	30000	900000	2.98×10^{7}
		100	50000	1500000	2.98×10^{7}
		100	100000	3000000	2.98×10^{7}
		100	300000	9000000	2.98×10^{7}
		1000	30000	900000	5.50×10^{7}
		1000	50000	1500000	5.50×10^{7}
		1000	100000	3000000	5.50×10^{7}
		1000	300000	9000000	5.50×10^{7}
$S_1 \rightsquigarrow T_2$	0.27	1	30000	900000	3.23×10^{7}
		1	50000	1500000	3.23×10^{7}
		1	100000	3000000	3.23×10^{7}
		1	300000	9000000	3.23×10^{7}
		1	500000	15000000	3.23×10^{7}
		1	900000	27000000	3.23×10^{7}
		10	30000	900000	9.46×10^{7}
		10	50000	1500000	9.46×10^{7}
		10	100000	3000000	9.46×10^{7}
		10	300000	9000000	9.46×10^{7}
		10	500000	15000000	9.46×10^{7}
		10	900000	27000000	9.46×10^{7}
		100	30000	900000	1.41×10^{8}
		100	50000	1500000	1.41×10^{8}
		100	100000	3000000	1.41×10^{8}
		100	300000	9000000	1.41×10^{8}
		1000	30000	900000	2.90×10^{8}
		1000	50000	1500000	2.90×10^{8}
		1000	100000	3000000	2.90×10^{8}
		1000	300000	9000000	2.90×10^{8}
$S_2 \rightsquigarrow T_1$	0.87	1	30000	900000	5.08×10^{7}
		1	50000	1500000	5.08×10^{7}

		1	100000	3000000	5.08×10^{7}
		1	300000	9000000	5.08×10^{7}
		1	500000	15000000	5.08×10^{7}
		1	900000	27000000	5.08×10^{7}
		10	30000	900000	6.50×10^{7}
		10	50000	1500000	6.50×10^{7}
		10	100000	3000000	6.50×10^{7}
		10	300000	9000000	6.50×10^{7}
		10	500000	15000000	6.50×10^{7}
		10	900000	27000000	6.50×10^{7}
		100	30000	900000	7.17×10^{7}
		100	50000	1500000	7.17×10^{7}
		100	100000	3000000	7.17×10^{7}
		100	300000	9000000	7.17×10^{7}
		1000	30000	900000	1.60×10^{8}
		1000	50000	1500000	1.60×10^{8}
		1000	100000	3000000	1.60×10^{8}
		1000	300000	9000000	1.60×10^{8}
$S_2 \rightsquigarrow T_2$	0.50	1	30000	900000	5.68×10^{8}
		1	50000	1500000	5.68×10^{8}
		1	100000	3000000	5.68×10^{8}
		1	300000	9000000	5.68×10^{8}
		1	500000	15000000	5.68×10^{8}
		1	900000	27000000	5.68×10^{8}
		10	30000	900000	6.04×10^{8}
		10	50000	1500000	6.04×10^{8}
		10	100000	3000000	6.04×10^{8}
		10	300000	9000000	6.04×10^{8}
		10	500000	15000000	6.04×10^{8}
		10	900000	27000000	6.04×10^{8}
		100	30000	900000	1.23×10^{9}
		100	50000	1500000	1.23×10^{9}
		100	100000	3000000	1.23×10^{9}
		100	300000	9000000	1.23×10^{9}
		1000	30000	900000	1.37×10^{9}
		1000	50000	1500000	1.37×10^{9}
		1000	100000	3000000	1.37×10^{9}
		1000	300000	9000000	1.37×10^{9}

Table 41. Calculated rate constants k_{ISC}^{TD} (s^{-1}) of neutral thionine (T) for the $S_1 \rightsquigarrow T_1$ channel. Other columns: adiabatic energy difference (ΔE^{ad}, eV), time interval (t, ps), number of points ($\#_{points}$) and damping factor (η, cm^{-1})

Channel	ΔE^{ad}	η	t fs	$\#_{points}$	k_{ISC}^{TD},
$S_1 \rightsquigarrow T_1$	1.22	0.10	100000	3000000	1.08×10^{6}
		0.10	300000	9000000	1.42×10^{6}
		0.10	500000	15000000	1.42×10^{6}
		1	30000	900000	1.37×10^{6}
		1	50000	1500000	1.37×10^{6}
		1	100000	3000000	1.37×10^{6}
		1	300000	9000000	1.37×10^{6}
		1	500000	15000000	1.37×10^{6}
		1	900000	27000000	1.37×10^{6}
		10	30000	900000	1.31×10^{6}
		10	50000	1500000	1.31×10^{6}
		10	100000	3000000	1.31×10^{6}
		10	300000	9000000	1.31×10^{6}
		10	500000	15000000	1.31×10^{6}
		10	900000	27000000	1.31×10^{6}
		100	30000	900000	1.33×10^{6}
		100	50000	1500000	1.33×10^{6}
		100	100000	3000000	1.33×10^{6}
		100	300000	9000000	1.33×10^{6}
		1000	30000	900000	2.24×10^{6}
		1000	50000	1500000	2.24×10^{6}
		1000	100000	3000000	2.24×10^{6}
		1000	300000	9000000	2.24×10^{6}
	1.16[a]	1	30000	900000	1.80×10^{6}
		1	50000	1500000	1.80×10^{6}
		1	100000	3000000	1.80×10^{6}
		1	300000	9000000	1.80×10^{6}
		10	30000	900000	1.81×10^{6}
		10	50000	1500000	1.81×10^{6}
		10	100000	3000000	1.81×10^{6}
		10	300000	9000000	1.81×10^{6}
		100	30000	900000	1.82×10^{6}
		100	50000	1500000	1.82×10^{6}
		100	100000	3000000	1.82×10^{6}
		100	300000	9000000	1.82×10^{6}

Rate constants calculated using the adiabatic energy gap calculated at the T5W model.

Chapter 7. Effects of substitution of the intracyclic sulfur by oxygen or selenium on the photophysics of thionine

7.1. Overview

In this chapter, an analysis of the effect of substituting the intra-cyclic sulphur of thionine (X = S) by oxygen (X = O, oxonine) and selenium (X = Se, selenine) on spin-orbit coupling as well as on the ISC efficiencies is presented in vacuum and in aqueous solution, see **Fig. 35**.

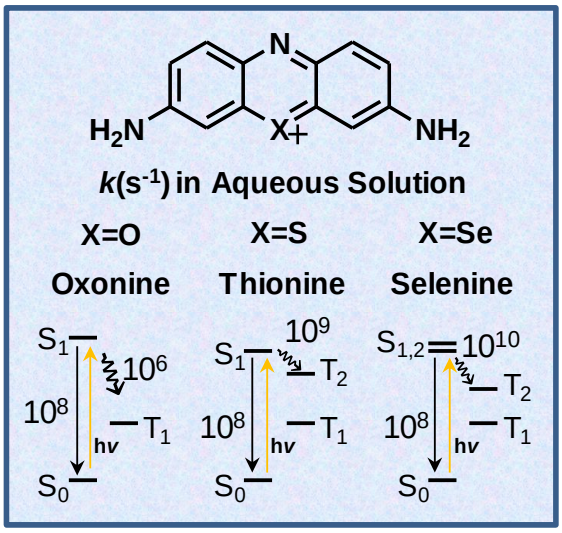

Fig. 35 Up: Heteroanalogues of thionine: oxonine and selenine. Down: Representative rate constants of the decay kinetics calculated in aqueous solution inserted in a Jablonsky diagram of the low-lying energy adiabatic electronic states.

This chapter is organized as follows: In Sections **7.2.1** and **7.2.2**, a brief characterization of the ground and low-lying excited states of oxonine and selenine is presented. To our knowledge there are no experimental gas phase spectra on oxonine and selenine, hence, the computed data is compared with measurements in aqueous solution by characterizing the electronic structure and excitation energies using the solvation models OXH^+3Wa and SEH^+3Wa (see Section **7.2.1.2**). A detailed discussion of

electronic structure and photophysics of cationic thionine was already given in **Chapter 5**. These results for thionine in vacuum and aqueous solution were included again in some of the tables and compared to those obtained for oxonine and selenine. Finally, the consequences of replacing the sulphur atom by oxygen and selenium on spin-orbit coupling (Section **7.2.3**) and the ISC efficiencies are discussed (Section **7.2.4**).

The interesting interplay of the ground and low-lying excited states has been investigated to qualitatively suggest the dominant relaxation pathways for the series of dyes under investigation. The ISC rate constants are considerably increased when going from O towards Se while the fluorescence rate constants remain unchanged. For the three dyes, all accessible ISC channels are El-Sayed forbidden and are driven by vibronic spin-orbit coupling between π→π* states. The interplay of the ground and low-lying excited states has been investigated in order to determine the dominant relaxation pathways. In oxonine the relaxation to the ground state after photoexcitation in water proceeds essentially via fluorescence from the $S_1(\pi_H \rightarrow \pi_L^*)$ bright state ($k_F = 2.10 \times 10^8$ s^{-1}), in agreement with the high experimental fluorescence quantum yield. In aqueous solution of thionine, the ISC rate constant ($k_{ISC}^{TD} = 1.07 \times 10^9$ s^{-1}) is one order of magnitude higher than fluorescence ($k_F = 1.66 \times 10^8$ s^{-1}) which is consistent with its high triplet quantum yield observed in water ($\phi_T = 0.53$). Due to a stronger vibronic spin-orbit coupling in selenine, which results from intensity borrowing from the direct spin-orbit coupling between low-lying singlet and triplet *n*→π* and π→π* states, the ISC rate is very high ($k_{ISC}^{TD} \sim 10^{10}$ s^{-1}) and much faster than fluorescence ($k_F = 1.59 \times 10^8$ s^{-1}) in vacuum and in aqueous solution. This suggests selenine-based dyes as efficient triplet state photosensitizers.

7.2. Results and discussion

7.2.1. Ground state geometries and vertical spectra

The computed DFT/MRCI vertical excitation energies of the low-lying singlet and triplet states of oxonine and selenine together with their leading electronic configurations at the ground state geometry are presented in **Table 42**. Selected geometrical parameters of the ground state minima are shown in **Fig. 36** and **Fig. 37**. In addition the valence molecular orbitals which dominate the corresponding excitations are depicted in **Fig. 38**. The best solvent model for thionine TH^+3Wa (which includes three explicit water molecules and the chromophore embedded in a COSMO environment, Section **5.2.1.2**) has also been applied to oxonine and selenine, see **Fig. 39**. The corresponding DFT/MRCI calculated vertical spectra of these dye-water models are listed in **Table 44**.

7.2.1.1. Vacuum

The theoretically determined electronic ground state minima of oxonine and selenine are C_{2v} symmetric, in analogy to thionine. The main geometrical variation between the three dyes is found to be the central ring angle <C-X-C (where X = O, S, Se) and the C-X bond lengths (see **Fig. 36** and **Fig. 37**). The presence of the selenium atom causes the C-Se bond (189 pm) to be longer than the corresponding bond lengths in thionine (C-S = 175 pm) and oxonine (C-O = 135 pm). Consequently a narrowing of the C-X-C angle from O (121°) to Se (99°) is observed. In the FC region, the vertical ordering of the lowest singlet and triplet states of oxonine and selenine remains the same as in thionine, see **Table 42** and **Fig. 38**. The characters of the states of interest are also the same in the three dyes: the S_1 and T_1 states have $\pi_H \rightarrow \pi_L^*$ character, the S_2 and T_2 states are dominated by a $\pi_{H-1} \rightarrow \pi_L^*$ configuration and the S_3 and T_3 states are characterized by a $n_{H-4} \rightarrow \pi_L^*$ transition.

The energetic position of the $T_1(\pi_H \rightarrow \pi_L^*)$ biradical state is remarkably constant in all cases. The $S_1(\pi_H \rightarrow \pi_L^*)$ state is found to be the optically bright state in the three dyes with oscillator strengths > 0.8. Despite the somewhat different structures of the center ring which are due to the size of the heteroatom of this series (X=O, S, Se), the absorption spectra in all the cases are quite similar and the S_1 state absorption is in the energy range of 2.39 - 2.26 eV (**Table 42**). This is in agreement with the experimentally observed behavior of these dyes.[174,225] The excitation energy of the $S_1(\pi_H \rightarrow \pi_L^*)$ state of oxonine is 0.1 eV higher than in thionine, whereas, the $T_1(\pi_H \rightarrow \pi_L^*)$ state is nearly unaffected by hetero-substitution (≈ 0.02 eV).

Due to the compact electron density of the oxygen p-orbitals, as compared to selenium, the exchange interaction is much larger in oxonine. This is reflected in the larger singlet-triplet energy gap in the vertical excitation spectrum of oxonine. In oxonine only one triplet state ($T_1(\pi_H \rightarrow \pi_L^*)$) is below the S_1 state in the vertical spectrum at the ground state geometry, whereas two triplet states ($T_1(\pi_H \rightarrow \pi_L^*)$ and $T_2(\pi_{H-1} \rightarrow \pi_L^*)$) are found below this state in thionine and selenine. For the case of the S_3/T_3 ($n_{H-4} \rightarrow \pi_L^*$) states, the n_{H-4} molecular orbitals of oxonine and thionine are more localized at the N ring atom than in the oxygen and sulphur atoms for which the hetero-atom substitution shows a negligible effect. For selenine the energetic stabilization of these $n_{H-4} \rightarrow \pi_L^*$ states which appear stabilized by ~0.1 eV which could be attributed to the fact that the electron density of the n_{H-4} molecular orbital has a increased localization at the selenium atom compared to the other two dyes. Furthermore, it could be observed that the $S_1(\pi_H \rightarrow \pi_L^*)$-$S_2(\pi_{H-1} \rightarrow \pi_L^*)$ excitation energy gap to be reduced in selenine (≈ 0.1 eV) compared to oxonine (0.44 eV) and thionine (0.20 eV).

One additional remark is how comparable are the calculated vertical energies obtained with the SV(P) basis set of oxonine with those calculated with the TZVP basis set for selenine and thionine. Due to difficulties during the

optimization search of a $S_1(\pi_H \rightarrow \pi_L^*)$ state minima of oxonine using the TZVP basis set, the performance of the SV(P) and TZVPP basis sets were tested. This electronic state is of main importance on the description of the photophysics of oxonine. The excitation energies computed with the three AO basis sets at the respective ground state geometries of oxonine are depicted in **Table 43**. The prominent vertical excitation energy shifts upon increasing the basis set polarization is seen on the S_3 and T_3 $n_{H-4} \rightarrow \pi_L^*$ states around 0.11 eV on going from the SV(P) to the TZVPP basis set. For the case of the $\pi \rightarrow \pi^*$ states, only minor energy shifts between 0.01 and 0.04 eV are observed. Since a ISC channel form $S_1(\pi_H \rightarrow \pi_L^*)$ to a $T_3(n_{H-4} \rightarrow \pi_L^*)$ for oxonine is not expected to be efficient, we considered the SV(P) basis set to be a good choice for studying the electronic structure. Hence, a comparison of the calculated DFT/MRCI/SV(P) vertical excitation energies of oxonine with those calculated for selenine and thionine using the DFT/MRCI/TZVP level of theory is considered reasonable.

Table 42 DFT/MRCI vertical excitation energies (ΔE_{vac}, eV) of the low-lying singlet and triplet states. The absorption oscillator strengths *f*(r) are shown in parenthesis.

Electronic state	Character	Oxonine[b]		Thionine[c]		Selenine[c]	
		DC[a]	ΔE_{vac}	DC[a]	ΔE_{vac}	DC[a]	ΔE_{vac}
$S_0(1^1A_1)$	Ground state	93		93		93	
$S_1(1^1B_1)$	$\pi_H \rightarrow \pi_L^*$	82	2.39(0.998)	80	2.29(0.833)	80	2.26(0.818)
$S_2(2^1A_1)$	$\pi_{H-1} \rightarrow \pi_L^*$	80	2.83(0.000)	82	2.49(0.012)	82	2.35(0.023)
$S_3(1^1B_2)$	$n_{H-4} \rightarrow \pi_L^*$	80	3.16(0.003)	79	3.11(0.003)	77	3.01(0.003)
$S_4(3^1A_1)$	$\pi_{H-2} \rightarrow \pi_L^*$	48	3.64(0.028)	52	3.56(0.014)	52	3.51(0.012)
	$\pi_H \rightarrow \pi_L^*$ $\pi_H \rightarrow \pi_L^*$	25		21		21	
$S_5(2^1B_1)$	$\pi_{H-3} \rightarrow \pi_L^*$	73	3.64(0.015)	70	3.58(0.011)	68	3.50(0.009)
$T_1(1^3B_1)$	$\pi_H \rightarrow \pi_L^*$	92	1.61	92	1.63	92	1.61
$T_2(1^3A_1)$	$\pi_{H-1} \rightarrow \pi_L^*$	86	2.49	88	2.11	88	1.97
$T_3(1^3B_2)$	$n_{H-4} \rightarrow \pi_L^*$	82	2.80	81	2.78	79	2.69
$T_4(2^3A_1)$	$\pi_{H-2} \rightarrow \pi_L^*$	79	3.13	78	3.12	77	3.10

[a]Percentage of the dominant contributions (DC) calculated at the [b]DFT/MRCI/SV(P) level of theory, [c]DFT/MRCI/TZVP level of theory.

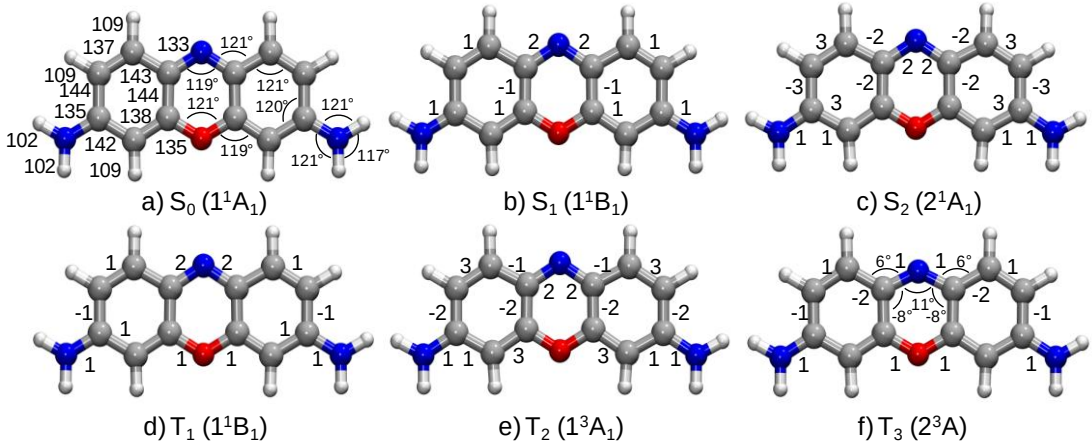

Fig. 36 Computed (TD-)DFT equilibrium structures of the excited states of oxonine in comparison with the ground state (S_0) geometry. Numbers indicate bond lengths in pm (S_0 structure) and changes of bond lengths relative to the S_0 structure (all other structures). Bond angles are given in degrees.

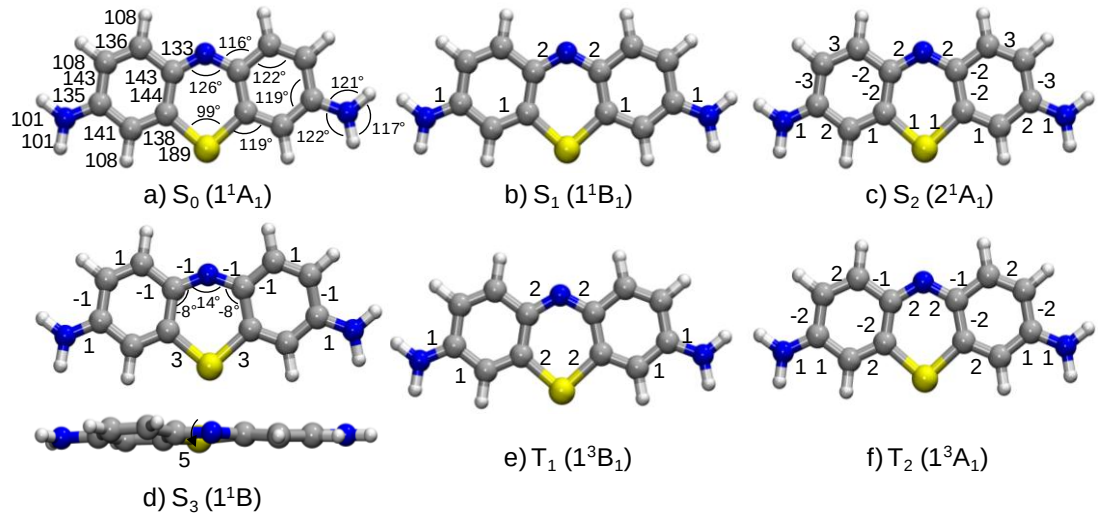

Fig. 37 Computed (TD-)DFT equilibrium structures of the excited states of selenine in comparison with the ground state (S_0) geometry. Numbers indicate bond lengths in pm (S_0 structure) and changes of bond lengths relative to the S_0 structure (all other structures). Bond angles and dihedrals are given in degrees.

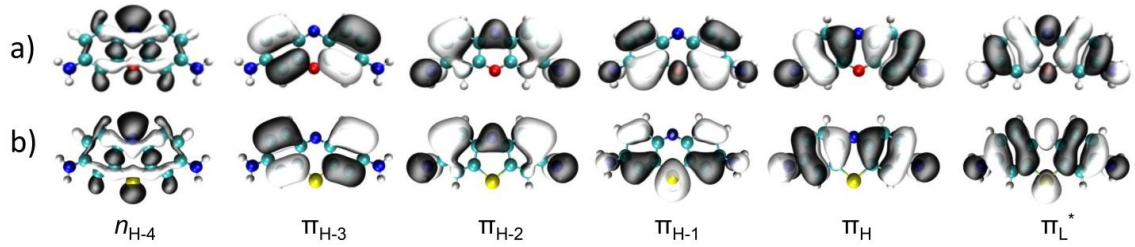

Fig. 38 Frontier Kohn-Sham molecular orbitals computed at the ground state minimum of a) oxonine and b) selenine (isovalue 0.02).

Table 43 Vertical excitation energies (ΔE_{vac}, eV) of the low-lying singlet and triplet states of oxonine calculated at the DFT/MRCI level and the SV(P), TZVP and TZVPP basis sets.

Electronic state	Electronic structure[a]	OXONINE		
		DFT/MRCI/SV(P)// B3LYP/SV(P)[b]	DFT/MRCI/TZVP// B3LYP/TZVP[b]	DFT/MRCI/TZVPP// B3LYP/TZVPP[b]
$S_0(1^1A_1)$	(93) Ground state			
$S_1(1^1B_1)$	(82) $\pi_H \rightarrow \pi_L^*$	2.39(0.998)	2.37(0.997)	2.41(0.996)
$S_2(2^1A_1)$	(80) $\pi_{H-1} \rightarrow \pi_L^*$	2.83(0.000)	2.82(0.000)	2.84(0.000)
$S_3(1^1B_2)$	(80) $n_{H-4} \rightarrow \pi_L^*$	3.16(0.003)	3.27(0.003)	3.27(0.002)
	(48) $\pi_{H-2} \rightarrow \pi_L^*$	3.64(0.028)	3.61(0.031)	3.63(0.028)
$S_4(3^1A_1)$	(25) $\pi_H \rightarrow \pi_L^*$ $\pi_H \rightarrow \pi_L^*$			
$S_5(2^1B_1)$	(73) $\pi_{H-3} \rightarrow \pi_L^*$	3.64(0.015)	3.61(0.015)	3.62(0.016)
$T_1(1^3B_1)$	(92) $\pi_H \rightarrow \pi_L^*$	1.61	1.59	1.59
$T_2(1^3A_1)$	(86) $\pi_{H-1} \rightarrow \pi_L^*$	2.49	2.49	2.53
$T_3(1^3B_2)$	(82) $n_{H-4} \rightarrow \pi_L^*$	2.80	2.90	2.92
$T_4(2^3A_1)$	(79) $\pi_{H-2} \rightarrow \pi_L^*$	3.13	3.13	3.18

[a]Dominant contributions at the DFT/MRCI/SV(P) level (percentage in parentheses). [b]The absorption oscillator strengths *f*(*L*) are shown in parenthesis.

7.2.1.2. Water

In this section we present our calculated DFT/MRCI vertical excitation energies of oxonine and selenine obtained using our best dye-water models OXH^+3Wa and SeH^+3Wa (see **Fig. 39**) and the experimental absorption spectra in aqueous solution (see **Table 44**). These dye-cluster models are similar to those studied in Chapter 3 for modeling the photophysics of thionine in water. A complete compilation of the results regarding to the other dye-water clusters tested and their calculated vertical excitation spectra are presented in the Supplementary Information (SI, Section **7.4**).

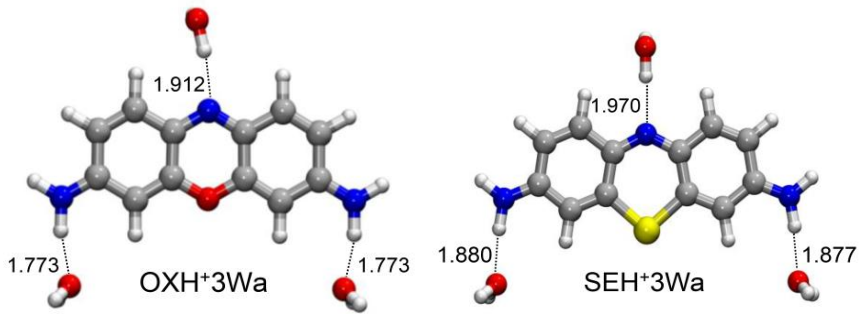

Fig. 39 Ground state water models for oxonine and selenine computed using solvation with COSMO and micro-hydration with three explicit water molecules.

In the OXH^+3Wa and SeH^+3Wa models, two types of hydrogen bonds formed by the specific water molecules are considered: (*i*) with the nitrogen atom of the central ring forms a hydrogen bond, which involves its lone-pair orbital located in the ring plane (H-O-H ⋯ N_{ring}) and (*ii*) with one hydrogen atom each of the two amine groups per water molecule (N-H ⋯ O). The H-O-H ⋯ N_{ring} hydrogen bonds are found to be somewhat weaker than the N-H ⋯ O bonds reflected by their larger hydrogen bond lengths (H ⋯ N_{ring} ~ 1.9 Å and H ⋯ O lies between 1.7 - 1.8 Å). The ground state geometries of the dyes are quite similar to those computed for the bare molecules in vacuum.

Electrostatic interaction and hydrogen bonding with water have a direct effect on the energies of the excited states, see **Table 44**. As expected, the π→π* states are red-shifted, whereas the *n*→π* states are blue-shifted due to hydration. The redshifts experienced by the various $\pi_H \rightarrow \pi_L^*$ states are larger (around δ_w = -0.12 – -0.21 eV) than the solvent shifts obtained for the $\pi_{H-1} \rightarrow \pi_L^*$ states (δ_w = -0.03 – -0.07 eV). The blueshifts experienced by the $n_{H-4} \rightarrow \pi_L^*$ states are significantly larger (δ_w ~ 0.5 eV) calculated using the SEH^+3Wa and OXH^+3Wa models. The calculated DFT/MRCI electronic excitation energy of ΔE_w = 2.25 eV for the bright $S_1(\pi_H \rightarrow \pi_L^*)$ state of oxonine agrees well with the reported experimental absorption maximum of 2.14 eV in aqueous solution.[198] For selenine the only available value of ΔE_w = 2.02 eV determined in benzene/acetyldimethylbenzylammonium chloride /H_2O reverse

microemulsions is in good accordance with our calculated value of 2.14 eV in aqueous solution.[225]

Table 44 DFT/MRCI vertical excitation energies (ΔE_w, eV) in aqueous solution using solvation with COSMO and micro-hydration with three explicit water molecules (OXH^+3Wa and SEH^+3Wa Models). The absorption oscillator strengths *f*(*L*) are shown in parenthesis.

Electronic state	Electronic structure	OXH^+3Wa^a		SEH^+3Wa^b	
		ΔE_w	Exp.	ΔE_w	Exp.
S_0	Ground state				
S_1	$\pi_H \rightarrow \pi_L^*$	2.25(1.026)	2.14[c]	2.14(0.858)	2.02[d]
S_2	$\pi_{H-1} \rightarrow \pi_L^*$	2.78(0.002)		2.28(0.013)	
S_3	$n_{H-4} \rightarrow \pi_L^*$	3.60(0.002)		3.50(0.003)	
S_4	$\pi_{H-2} \rightarrow \pi_L^*$ $\pi_H \rightarrow \pi_L^*$ $\pi_H \rightarrow \pi_L^*$	3.44(0.027)		3.37(0.017)	
S_5	$\pi_{H-3} \rightarrow \pi_L^*$	3.65(0.019)		3.46(0.020)	
T_1	$\pi_H \rightarrow \pi_L^*$	1.40		1.43	
T_2	$\pi_{H-1} \rightarrow \pi_L^*$	2.46		1.92	
T_3	$n_{H-4} \rightarrow \pi_L^*$	3.30		3.22	
T_4	$\pi_{H-2} \rightarrow \pi_L^*$	3.08		3.05	

[a]DFT/MRCI/SV(P) level. [b]DFT/MRCI/TZVP. Experimental absorption band in [c]aqueous solution Ref. [198], [d]benzene/cetyldimethylbenzylammonium chloride/H_2O reverse microemulsions Ref. [225].

7.2.2. Excited state minima and adiabatic excitation energies

The relative adiabatic energies of the low-lying singlet and triplet states reveal the accessible photophysical pathways for the dissipation of the excess energy of the dyes. In the following, we present the optimized geometries of the lowest-lying singlet and triplet states of oxonine and selenine. The adiabatic excitation energies calculated at these excited state minima in vacuum and those obtained after adding the corresponding spectral hydration shifts are listed in **Table 45**, along with the zero point vibrational energy corrections (ZPVEC). The dominant structural variations after electronic excitation relative to the ground state geometry are presented in **Fig. 36** and **Fig. 37**.

7.2.2.1. Vacuum: π→π states.*

The computed minima of the S_1,T_1($\pi_H \rightarrow \pi_L^*$) and S_2,T_2($\pi_{H-1} \rightarrow \pi_L^*$) states do not show significant geometrical variations in comparison to the ground state of each corresponding dye. The minima of these states are also planar and

C_{2v}-symmetric, see **Fig. 36** and **Fig. 37**. The structural changes at the adiabatic minima of the excited states geometries are consistent with the orbital contributions to the excitation. The S_1 and T_1 states arise from the same electronic transition ($\pi_H \rightarrow \pi_L^*$), hence it is not surprising that the minima of these states have nearly the same nuclear arrangement. The corresponding S_2 and $T_2(\pi_{H-1} \rightarrow \pi_L^*)$ minima display slightly more distorted geometries with changes in bond lengths within 3 pm.

Table 45 Adiabatic DFT/MRCI excitation energies (eV) in vacuum (ΔE_{vac}^{ad}) and in aqueous solution (ΔE_w^{ad}). oscillator strengths for emission at the excited-state minima are listed in parentheses and scaled zero point vibrational corrections (ZPVEC, eV) in squared brackets

State	Character	Oxonine[b]			Thionine[c]			Selenine[c]		
		DC[a]	ΔE_{vac}^{ad}	ΔE_w^{ad}	DC[a]	ΔE_{vac}^{ad}	ΔE_w^{ad}	DC[a]	ΔE_{vac}^{ad}	ΔE_w^{ad}
$S_1(1^1B_1)$	$\pi_H \rightarrow \pi_L^*$	81	2.35 (0.942) [-0.24]	2.21	80	2.27 (0.790) [0.02]	2.14	80	2.24 (0.776) [-0.05]	2.12
$S_2(2^1A_1)$	$\pi_{H-1} \rightarrow \pi_L^*$ $\pi_H \rightarrow \pi_L^*$	81	2.62 (0.000) [-0.24]	2.57	45 36	2.29 (0.269) [-0.16]	2.23	82	2.20 (0.018) [-0.14]	2.13
$S_3(1^1B)$	$n_{H-2} \rightarrow \pi_L^*$ $\pi_H \rightarrow \pi_L^*$	-	-	-	-	-	-	44 36	2.49 (0.274) [-0.10]	2.98
$T_1(1^3B_1)$	$\pi_H \rightarrow \pi_L^*$	92	1.61 [-0.14]	1.40	92	1.63 [-0.07]	1.46	92	1.62 [-0.08]	1.44
$T_2(1^3A_1)$	$\pi_{H-1} \rightarrow \pi_L^*$	87	2.33 [-0.20]	2.30	88	1.97 [-0.08]	1.93	88	1.85 [-0.08]	1.80
$T_3(2^3B_2)$	$n_{H-2} \rightarrow \pi_L^*$ $\pi_{H-4} \rightarrow \pi_L^*$	82	2.44 [-0.16]	2.94	50[d] 26	2.31[d] [0.03]	2.75	83	2.27[e] [-0.06][e]	2.80[e]

[a]Percentage of the dominant contributions. Adiabatic energies computed relative to the ground state energy at the ground state geometry at the [b]DFT/MRCI/SV(P) and [c]DFT/MRCI/TZVP theoretical levels. [d]This state has an irreducible representation of 2^3A. A planar C_{2v}-symmetric saddle point ($36.81i$ cm^{-1}) for this state has an energy of 2.36 eV. [e]Adiabatic energy calculated at a TD-B3LYP/TZVP planar C_{2v}-symmetric saddle point ($28.35i$ cm^{-1}).

The computed $S_1/T_1(\pi_H \rightarrow \pi_L^*)$ and $S_2/T_2(\pi_{H-1} \rightarrow \pi_L^*)$ excited state geometries of selenine were found to be minima at the TD-B3LYP/TZVP level. In the case of oxonine, however, only the $T_1(\pi_H \rightarrow \pi_L^*)$ and $T_2(\pi_{H-1} \rightarrow \pi_L^*)$ nuclear arrangements are minima on the TD-B3LYP/SV(P) PES. The optimized C_{2v} structures of the $S_1(\pi_H \rightarrow \pi_L^*)$ and $S_2(\pi_{H-1} \rightarrow \pi_L^*)$ states of oxonine turn out to be first order saddle points at the TD-B3LYP/SV(P) level, with imaginary

frequencies of *i*2475 cm^{-1} and *i*1342 cm^{-1} (B_1-symmetric modes), respectively. A distortion along the imaginary mode in the case of S_1, followed by optimization without symmetry constraints (C_1-symmetry, TD-B3LYP/SV(P)) led to a minimum for which the calculated DFT/MRCI adiabatic energy (ΔE_{vac}^{ad} = 2.45 eV) lies above the computed vertical DFT/MRCI energy (ΔE_{vac} = 2.39 eV) and the C_{2v} adiabatic DFT/MRCI energy of S_1 (ΔE_{vac}^{ad} = 2.35 eV). We calculated the TDDFT and DFT/MRCI energies along the imaginary mode and found that the TDDFT PES exhibits a shallow double minimum potential well caused by a S_1-S_2 conical intersection located extremely close to this geometry, see **Fig. 40(a)**. We verified that there is neither root flipping nor considerable state mixing in the numerical frequency calculation due to this nearby crossing. The C_{2v}-symmetric $S_1(\pi_H \rightarrow \pi_L^*)$ minimum was found to correspond to a point on the DFT/MRCI PES where the S_1 and the S_2 states are located energetically close to each other but do not intersect. The same behavior was found for the computed geometry of the $S_2(\pi_{H-1} \rightarrow \pi_L^*)$ state (see **Fig. 40(b)**).

Let us discuss more deep the situation found for the optimization of the $S_1(\pi_H \rightarrow \pi_L^*)$ state of oxonine. When the TZVP basis set was employed for the optimization, the C_{2v} structure is found to be a second order saddle point (v_1 = *i*2041 and v_2 = *i*145 cm^{-1}, $\Delta E_{DFT/MRCI}$ = 2.33 eV) and optimization procedures using lower symmetry constrains yielded structures whose DFT/MRCI adiabatic energies were also larger than the vertical DFT/MRCI energies. A one-dimension cut in the direction of both imaginary modes indicate that again the C_{2v} geometry is favored at the DFT/MRCI level, **Fig. 40(c-d)**. This show a poorer resemblance between the corresponding TD-B3LYP/TZVP and DFT/MRCI//TZVP compared to the TD-B3LYP/SV(P) and DFT/MRCI//SV(P) theoretical levels explained above. For further confirming our choice of the SV(P) basis set for describing the photophysics of oxonine, we optimized a C_{2v} geometry of the $S_1(\pi_H \rightarrow \pi_L^*)$ state using the more polarized TZVPP basis set. As found using the SV(P) basis set, at the TD-

B3LYP/TZVPP PES this is a first order saddle point (*i*1894 cm^{-1}) while at the corresponding DFT/MRCI level is a minimum (2.37 eV). A very similar behavior was found for the computed geometry of $S_2(\pi_{H-1}\rightarrow\pi_L^*)$ structure. Hence, we decided to use both minima with C_{2v} symmetry computed at the TD-B3LYP/SV(P) theoretical level for these two singlet states in oxonine for further discussion.

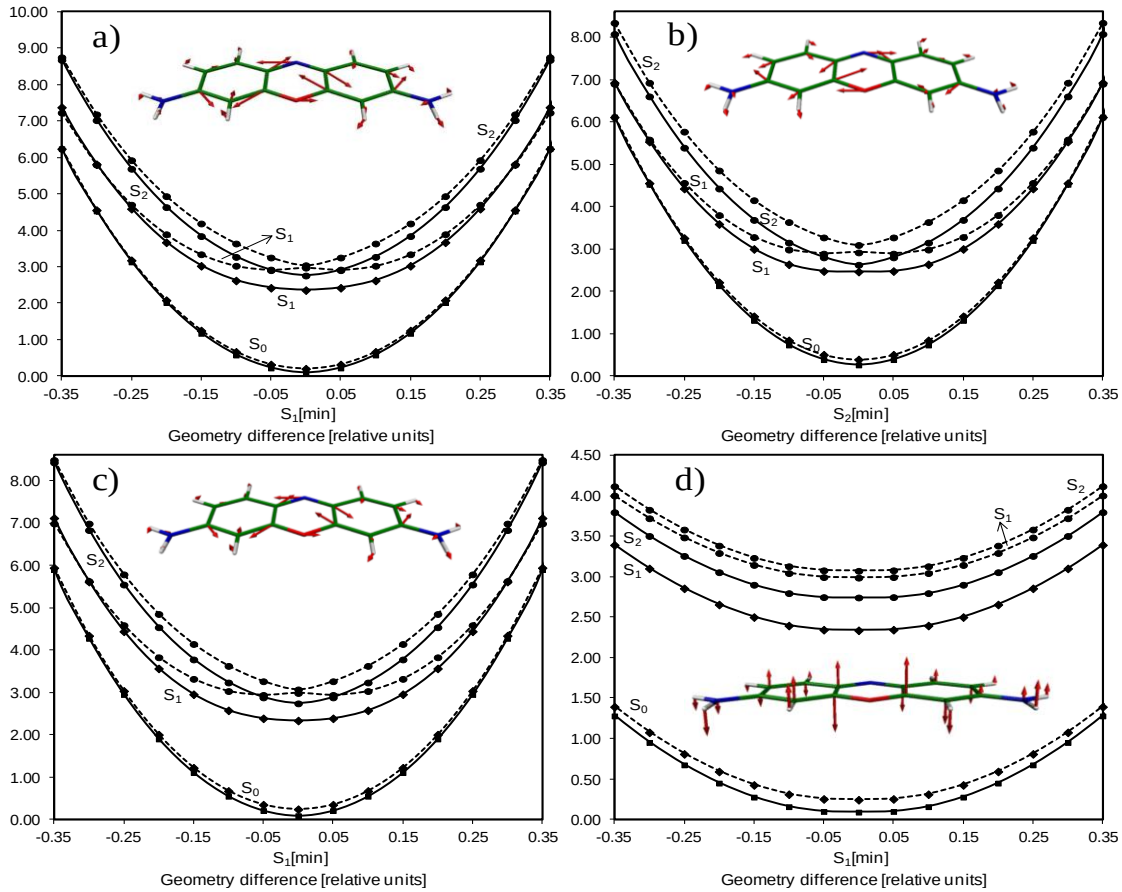

Fig. 40 DFT/MRCI excitation energies calculated upon geometry elongations along the imaginary modes obtained at the calculated the S_1 and S_2 structures of oxonine. Bold lines refer to DFT/MRCI energies and dashed lines to those calculated with the B3LYP functional. a) $S_1(\pi_H\rightarrow\pi_L^*)$ geometry (ν = *i*2475 cm^{-1}), SV(P) basis set, b) $S_2(\pi_{H-1}\rightarrow\pi_L^*)$ geometry (ν = *i*1342 cm^{-1}), SV(P) basis set, c) $S_1(\pi_H\rightarrow\pi_L^*)$ geometry (ν = *i*2041 cm^{-1}), TZVP basis set and d) $S_1(\pi_H\rightarrow\pi_L^*)$ state (ν = *i*145 cm^{-1}), TZVP basis set.

Structural relaxation has minor impact on the adiabatic energy of the $S_1(\pi_H\rightarrow\pi_L^*)$ electronic state of oxonine (0.04 eV) and selenine (0.02 eV) as

compared to the vertical absorption. The destabilization of the ground state at these minima yields vertical emission energies of 2.27 and 2.17 eV for oxonine and selenine, respectively. There is almost no energetic relaxation of the $T_1(\pi_H \rightarrow \pi_L^*)$ state of the dyes (see **Table 45**). The energy of the $T_2(\pi_{H-1} \rightarrow \pi_L^*)$ state shows significant stabilization upon geometry relaxation (X =O > S > Se, 0.16 - 0.12 eV). This variation in stabilization energies of the various states causes the S_1 - $T_1(\pi_H \rightarrow \pi_L^*)$ energetic gap to decrease slightly (X = O > S > Se, ΔE_{S1-T1} = 0.74 - 0.62 eV), while the $S_1(\pi_H \rightarrow \pi_L^*)$ - $T_2(\pi_{H-1} \rightarrow \pi_L^*)$ states become energetically more separated (X = O < S < Se, ΔE_{S1-T2} = 0.02 - 0.39 eV) than in the FC region.

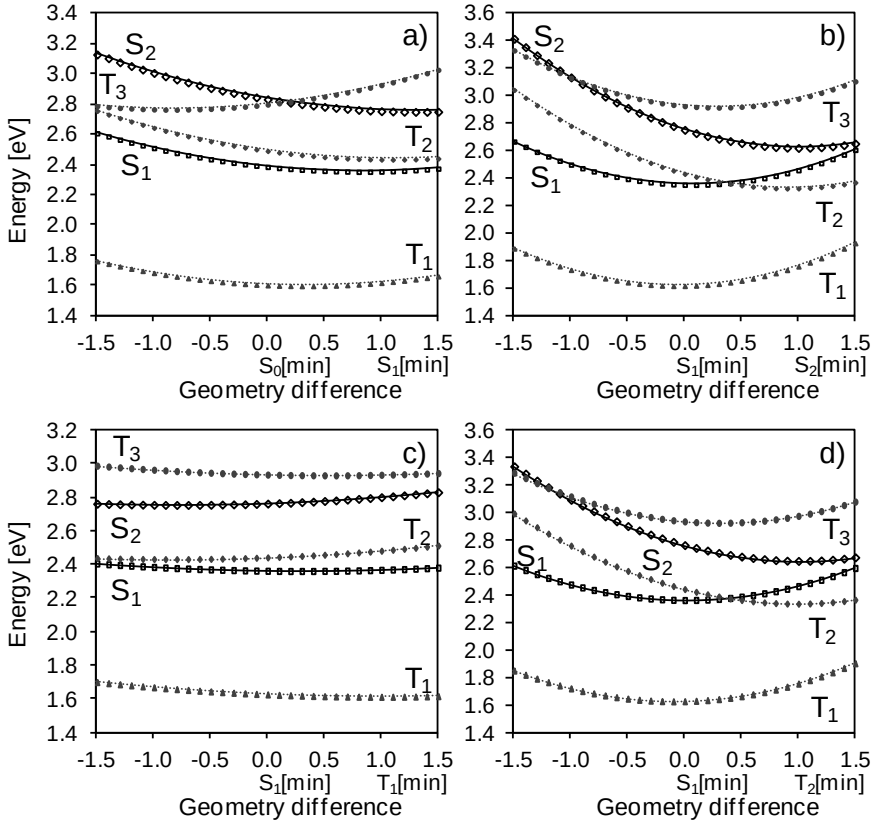

Fig. 41 DFT/MRCI excitation energy profiles along a linearly interpolated path between the low-lying singlet ($S_1(\pi_H \rightarrow \pi_L^*)$) and triplet ($T_1(\pi_H \rightarrow \pi_L^*)$ and $T_2(\pi_{H-1} \rightarrow \pi_L^*)$) state minima of oxonine.

The adiabatic energies of the $\pi \rightarrow \pi^*$ states vary in the X = O, S, Se series. The consequences for the photophysics are discussed in detail in Section

7.2.4. Here we present the most important features which determine the various relaxation channels after photoexcitation. Along the $S_0 \rightarrow S_1$ pathway (see see **Fig. 41** and **Fig. 42**) no crossing between the ground and the other electronic states is observed for oxonine and selenine. In oxonine, an energetically high-lying $S_2(\pi_{H-1}\rightarrow\pi_L^*)/T_3(n\rightarrow\pi_L^*)$ crossing is observed (**Fig. 41(a)**) which is not expected to compete with $S_n \dashrightarrow S_1$ IC (Kasha's rule [1]). The $S_1(\pi_H\rightarrow\pi_L^*)$ - $S_2(\pi_{H-1}\rightarrow\pi_L^*)$ adiabatic energy gap decreases along the series: X = O ΔE_{S1-S2} = 0.27 eV, X = S ΔE_{S1-S2} = 0.02 eV and X = Se ΔE_{S1-S2} = -0.04 eV. While for oxonine the $S_2(\pi_{H-1}\rightarrow\pi_L^*)$ state is adiabatically higher in energy (2.62 eV, see **Table 45**), in selenine the $S_2(\pi_{H-1}\rightarrow\pi_L^*)$ state is the adiabatic first singlet excited state (ΔE_{vac}^{ad} = 2.29 eV). A linear interpolation between the minima of the $S_1(\pi_H\rightarrow\pi_L^*)$ and $S_2(\pi_{H-1}\rightarrow\pi_L^*)$ states of selenine (see see **Fig. 42**) shows an energetically low-lying conical intersection between these states. Whereas, this same intersection is not reachable from the $S_1(\pi_H\rightarrow\pi_L^*)$ minimum of oxonine (**Fig. 41**(b)). In all cases, the $T_1(\pi_H\rightarrow\pi_L^*)$ and $T_2(\pi_{H-1}\rightarrow\pi_L^*)$ are located adiabatically below the $S_1(\pi_H\rightarrow\pi_L^*)$ state. The $T_2(\pi_{H-1}\rightarrow\pi_L^*)$ state of oxonine is located immediately below the $S_1(\pi_H\rightarrow\pi_L^*)$ by only 0.02 eV and should be considered quasidegenerate keeping in mind the uncertainties of the method ($\sim$ 0.2 eV).

7.2.2.2. Vacuum: n→π states.*

In some cases, geometrical relaxation may cause a reversal in the energetic order of the low-lying excited states. Hence, it is of interest to determine the adiabatic minima of the $S_3(n_{H-4}\rightarrow\pi^*)$ and $T_3(n_{H-4}\rightarrow\pi^*)$ states. In this subsection, we briefly describe the geometric and energetic behavior of these adiabatic $n\rightarrow\pi^*$ states in order to understand the heavy atom effects on the properties of these states.

Due to mixing with the lower lying states during optimization process it was not possible to find the $S_3(n\rightarrow\pi^*)$ minimum for oxonine and thionine (the same problem also arose in our study of thionine). Interestingly, we were able

to optimize a $S_3(n\rightarrow\pi^*)$ minimum for selenine. The optimization the $S_3(^1B_2)$ state at C_{2v} PES, yielded a first order saddle point with an imaginary frequency of *i*30 cm^{-1}. Upon geometry distortion along this imaginary mode, we found a C_2 symmetric minimum ($\Delta E_{(vac)}$ = 2.49 eV). This state has a slightly distorted *out-of-plane* geometry (see **Fig. 37(d)**) and a broadening of the <C-N-C central ring angle is observed (by 14° with respect to the S_0 geometry) which causes an elongation of the C-S bond by about 3 pm. This geometry relaxation contributes to a strong stabilization (by 0.62 eV) of the $S_3(n\rightarrow\pi^*)$ state with respect to the vertical electronic energy.

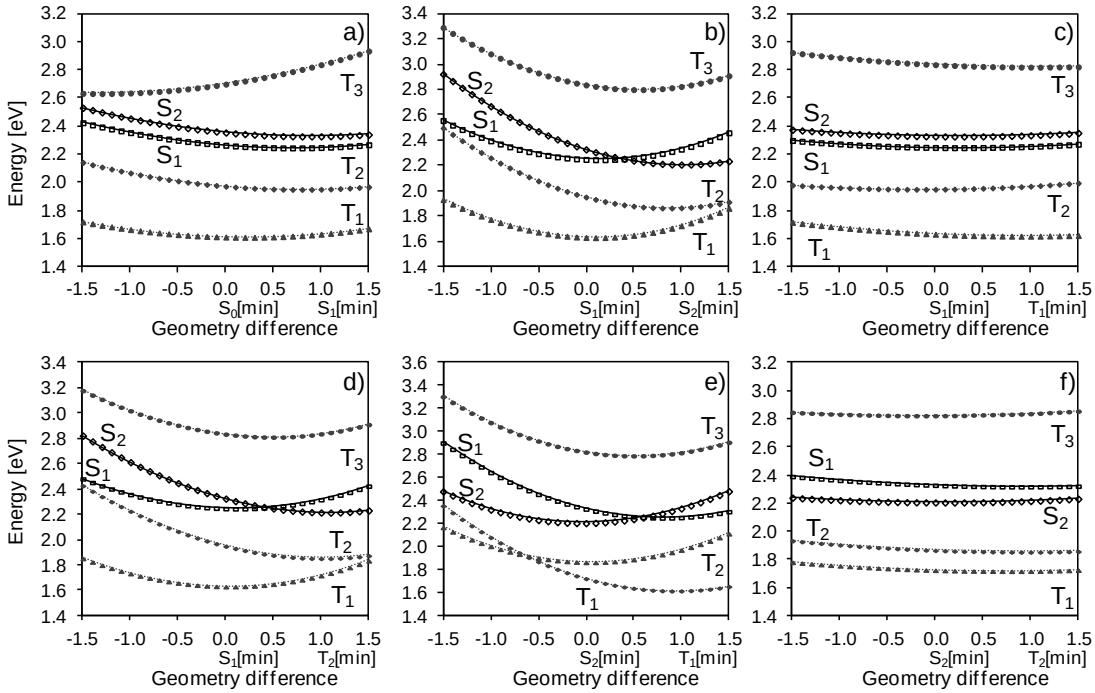

Fig. 42 DFT/MRCI excitation energy profiles along a linearly interpolated path between the low-lying singlet ($S_1(\pi_H\rightarrow\pi_L^*)$ and $S_2(\pi_{H-1}\rightarrow\pi_L^*)$) and triplet ($T_1(\pi_H\rightarrow\pi_L^*)$ and $T_2(\pi_{H-1}\rightarrow\pi_L^*)$) state minima of selenine.

The computed structure of the T_3 state of oxonine is a planar C_1 minimum and the electronic wave function corresponds to $n_{H-2}\rightarrow\pi_L^*$ transition, (**Fig. 36(f)**). The minor widening of the C-O bond (1 pm) reflects the lesser amount of electron density localized at the oxygen atom in the n_{H-2} MO compared to that of the central ring nitrogen atom where the <C-N-C angle is enlarged. At

this geometry point, the $T_3(n_{H-2}\rightarrow\pi_L^*)$ state has an adiabatic energy of 2.44 eV which correspond to a moderate stabilization of 0.36 eV. On the other hand, for selenine was not possible to localize a minimum for the $T_3(n\rightarrow\pi^*)$ excited state. The C_{2v} nuclear arrangement of the T_3 state is found to be a very flat saddle point at the TDDFT level. One imaginary frequency of $i28.35$ cm^{-1} is obtained for a B_2-symmetric normal mode which corresponds to a *butterfly out-of-plane* deformation of the tri-cyclic ring. However, a one-dimensional cut along this imaginary normal mode shows that at the DFT/MRCI level this planar structure is not favored and it corresponds to also to a first order saddle point where the energy difference between the energy of this stationary point and the lowest energy point calculated in the path is of 0.08 eV. At the TDDFT level this energy difference is negligible (3.72×10^{-4} eV) as expected. Deformation along this imaginary mode yielded a V-shaped structure. Subsequent optimization tests carried out with C_s and without symmetry constrains caused root flipping with the $T_1(\pi_H\rightarrow\pi_L^*)$ state yielded a planar structure. This brings to the light that the $T_3(n\rightarrow\pi^*)$ and $T_1(\pi_H\rightarrow\pi_L^*)$ state should be close lying and a conical intersection between these states should be nearby the $T_3(n\rightarrow\pi^*)$ minimum where TDDFT fails to optimize the required state. Moreover, when a strongly distorted V-shaped geometry was used in order to displace the state far from the $T_1(\pi_H\rightarrow\pi_L^*)$ state gave rise to triplet instabilities.

In Section **5.2.2.1.3**, it was already described that the nuclear arrangement of the $T_3(n\rightarrow\pi^*)$ state minimum of thionine was found to be characterized by V-shaped geometry and a strong energetic stabilization due to geometry relaxation (0.47 eV) pushed this state to be located nearly above (0.04 eV above) the $S_1(\pi_H\rightarrow\pi_L^*)$ state (see also **Table 45**). A planar stationary point on the TDDFT PES with C_{2v} symmetry was found for which the vibrational analysis indicated that this geometry was a saddle point ($i45$ cm^{-1}, B_2-symmetric shadow *butterfly* motion). The energy of this planar geometry (3.36 eV) is located slightly energetically above (0.05 eV) the V-shaped minimum.

The DFT/MRCI excitation energy behavior along the imaginary frequency motion also shows a first order saddle point where the planar geometry energy is also located 0.08 eV above the lowest energy point calculated (0.55 dimensionless coordinates). Taking into account the energetic and geometric resemblance of the $T_3(n\rightarrow\pi^*)$ state PESs of selenine and thionine, a qualitative picture on what could be the energetic position and geometrical characteristics of a possible $T_3(n\rightarrow\pi^*)$ minimum of selenine could be somehow analyzed. It could be expected that the $T_3(n\rightarrow\pi^*)$ adiabatic minimum of selenine also presents a V-shaped geometry for which the widening of the <C-S-C-C and <C-N-C-C dihedral angles should be greater due to the size of the selenium atom. As both C_{2v} planar $T_3(n\rightarrow\pi^*)$ states of thionine and selenine present an energetic stabilization from the ground states of ~ 0.42 - 0.45 eV and are located by ~ 0.02 - 0.03 eV below the $S_1(\pi_H\rightarrow\pi_L^*)$ state, it could be estimated that the adiabatic T_3 minimum of selenine should be energetically located in between (or below) the two low-lying singlet states (~ 2.20 - 2.24 eV) in vacuum. Nevertheless, it could be seen in **Fig. 41** and **Fig. 42** that (as found for thionine) these $n\rightarrow\pi^*$ states are not reachable from the two low-lying singlet state pathways and become inaccessible for the photophysical kinetics in vacuum for these dyes.

7.2.2.3. Estimated adiabatic excitation energies in water

Estimates of the adiabatic excitation energies in aqueous solution (ΔE_w^{ad}) calculated using **Eq 92** and **Eq 93** are presented in **Table 45**. The energy differences between the various electronic states allow us to draw a qualitative picture of the plausible decay channels in aqueous solution. The adiabatic $S_1(\pi_H\rightarrow\pi_L^*)$ excitation energy of oxonine of 2.21 eV agrees quite well with the experimental value estimated from the onset of the fluorescence emission band in acid aqueous solution (2.11 eV).[197] In aqueous solution the energy difference between the $S_1(\pi_H\rightarrow\pi_L^*)$ and $S_2(\pi_{H-1}\rightarrow\pi_L^*)$ states of oxonine increases ($\Delta E_{S1-S2} = 0.36$ eV) compared to vacuum. The adiabatic

S_1-S_2 energy gap of thionine increases slightly (0.09 eV), whereas the two states are nearly degenerate in selenine ($\Delta E_{S1\text{-}S2}$ = 0.01 eV). Thus, within the accuracy of the method, it is not possible to decide which of these states is lowest in energy and radiationless decay channels from both states should be considered for selenine in aqueous solution.

Our interest here is to determine which triplet states are energetically available from the initially excited singlet state in water. Hence, the energy differences between the various states of the singlet and triplet manifolds are analyzed. We find that the S_1-T_1 and S_1-T_2 adiabatic energy gaps change by less than 0.1 eV (in the case of thionine $\Delta E_{S1\text{-}T2}$ = 0.11 eV) in all the cases as compared to vacuum. These small shifts suggest that the singlet-triplet transition pathway is basically the same as in vacuum. However, a closer look at **Table 45** tells a different story. In oxonine there are two triplet states available for ISC from the S_1 state in vacuum, whereas in water the $S_1(\pi_H \rightarrow \pi_L^*)$ - $T_1(\pi_H \rightarrow \pi_L^*)$ is the only available channel (the T_2 state is located 0.09 eV above the S_1 state). In thionine, the T_1 and T_2 states are clearly below the bright S_1 state in aqueous solution, whereas the S_2 state now is substantially above the S_1 state. In selenine, the first two singlet excited states of selenine are adiabatically degenerate in water. Therefore, transitions from the $S_1(\pi_H \rightarrow \pi_L^*)$ and $S_2(\pi_{H-1} \rightarrow \pi_L^*)$ to the $T_1(\pi_H \rightarrow \pi_L^*)$ and $T_2(\pi_{H-1} \rightarrow \pi_L^*)$ states may all contribute to the ISC.

7.2.3. Direct and vibronic spin-orbit coupling

The rate determining-factors for efficient ISC involves not only the energy gap but also the strength of the spin-orbit coupling between a given pair of states. Herein, we discuss the heavy atom effects on the direct and vibronic spin-orbit coupling between the low-lying singlet and triplet states along the series of chromophores. The computed electronic SOMEs at the corresponding $S_{1,2}$ minima are compiled in **Table 46** and their numerical derivatives along the normal modes (∂SOMEs) are plotted in **Fig. 43** and **Fig. 44**.

The term "heavy-atom effect" refers to the influence of the of a substituent atom on molecular spin-orbit coupling that is caused by its large atomic number. The spin-orbit coupling is increased because the atomic spin-orbit coupling constant is proportional to $\sim Z^4$ which magnifies the contributions of the heavy atom. Thus, large changes in the direct electronic SOMEs are expected upon hetero-atom substitution X, by default, but the strength will be driven by the character and kind of transition. Indeed, from a close look to **Table 46** becomes evident that the substitution of X by selenium in the phenothiazinium ring can cause a rise of the SOMEs. Nevertheless, when going from X=O to X=S causes only a minor increase in the $S_2(\pi_{H-1}\rightarrow\pi_L^*)/T_3(n\rightarrow\pi^*)$ coupling while the $S_1(\pi_H\rightarrow\pi_L^*)/T_3(n\rightarrow\pi^*)$ coupling decreases. The latter trend could be related to the r^{-3}-dependence of the spin-orbit coupling Hamiltonian where the spin-orbit integrals between two MOs located in the same spatial region is conductive to larger matrix elements. The smaller localization of electron density at the X-atom at the n_{H-4} MO of oxonine compared to thionine and, at the same time, taking into account the shape of the π_H MO (which does not present an amplitude in this region) allows a slightly larger SOME of the $S_1(\pi_H\rightarrow\pi_L^*)/T_3(n\rightarrow\pi^*)$ pair in oxonine. Here there is also important to consider that the π_L^* MO also presents electron density distribution at X in both dyes, but more compact for X = O. In this same context, $S_1(\pi_H\rightarrow\pi_L^*)/T_3(n\rightarrow\pi^*)$ SOMEs are raised ($\sim 7\ cm^{-1}$) just because the heavier selenium atom which quenches the effect of the differences between the shapes of the MOs. On the other hand, the coupling of the $S_2(\pi_{H-1}\rightarrow\pi_L^*)$ and $T_3(n\rightarrow\pi_L^*)$ states significantly increases in the X = O, S, Se series (to above 40 cm^{-1}) promoted not only by the heavy atom effect but also because similarities in the amplitudes at the X-atom at the MOs (π_{H-1}, n and π_L) involved in the transitions.

As it expected from El-Sayed rules, larger matrix elements for the $S_{1,2}$ and the $T_3(n\rightarrow\pi_L^*)$ couplings compared to those between the low-lying singlet and triplet $\pi\rightarrow\pi^*$ states are found. The tabulated electronic SOMEs calculated

between the $S_1(\pi_H \rightarrow \pi_L^*)/T_1(\pi_H \rightarrow \pi_L^*)$ (B_1-symmetric) and $S_2(\pi_{H-1} \rightarrow \pi_L^*)/T_2(\pi_{H-1} \rightarrow \pi_L^*)$ (A_1-symmetric) pairs of states is symmetry forbidden at all of these C_{2v}-symmetric minima. For oxonine and thionine, the $S_1(\pi_H \rightarrow \pi_L^*)/T_2(\pi_{H-1} \rightarrow \pi_L^*)$ and $S_2(\pi_{H-1} \rightarrow \pi_L^*)/T_1(\pi_H \rightarrow \pi_L^*)$ SOMEs are negligible as may be expected for two states with similar character. Due to heavy atom effect, the coupling between these same states is increased in the case of selenine by one order of magnitude (to ~ 0.2 cm^{-1}) with respect to the corresponding SOMEs for oxonine and thionine.

Table 46 Spin-orbit matrix element (SOMEs, cm^{-1}) between low-lying singlet and triplet states at the corresponding adiabatic minimum geometry of the $S_1(\pi_H \rightarrow \pi_L^*)$ and $S_2(\pi_{H-1} \rightarrow \pi_L^*)$. The direction of the coupling *x*, *y* or *z* is given in parenthesis

SOMEs	Oxonine	Thionine	Selenine	
	$S_1(\pi_H \rightarrow \pi_L^*)$	$S_1(\pi_H \rightarrow \pi_L^*)$	$S_1(\pi_H \rightarrow \pi_L^*)$	$S_2(\pi_{H-1} \rightarrow \pi_L^*)$
$\langle S_0 \lvert \hat{H}_{SO} \rvert T_1(\pi_H \rightarrow \pi_L^*) \rangle$	0.01(y)	0.01(y)	0.10(y)	-0.03(y)
$\langle S_1(\pi_H \rightarrow \pi_L^*) \lvert \hat{H}_{SO} \rvert T_1(\pi_H \rightarrow \pi_L^*) \rangle$	-	-	-	-
$\langle S_1(\pi_H \rightarrow \pi_L^*) \lvert \hat{H}_{SO} \rvert T_2(\pi_{H-1} \rightarrow \pi_L^*) \rangle$	-0.01(y)	-0.08(y)	-0.23(y)	-0.19(y)
$\langle S_1(\pi_H \rightarrow \pi_L^*) \lvert \hat{H}_{SO} \rvert T_3(n \rightarrow \pi_L^*) \rangle$	-0.61(z)	0.39(z)	-6.99(z)	-6.52(z)
$\langle S_2(\pi_{H-1} \rightarrow \pi_L^*) \lvert \hat{H}_{SO} \rvert T_1(\pi_H \rightarrow \pi_L^*) \rangle$	0.00(y)	-0.02(y)	-0.18(y)	0.19(y)
$\langle S_2(\pi_{H-1} \rightarrow \pi_L^*) \lvert \hat{H}_{SO} \rvert T_2(\pi_{H-1} \rightarrow \pi_L$	-	-	-	-
$\langle S_2(\pi_{H-1} \rightarrow \pi_L^*) \lvert \hat{H}_{SO} \rvert T_3(n \rightarrow \pi_L^*) \rangle$	-3.04(x)	-9.90(x)	48.27(x)	-43.41(x)

The energy distribution of the excited states of these dyes suggest ISC pathways induced by vibronic spin-orbit coupling between π→π* states. The heavy atom effects on the spin-orbit coupling which contribute to accelerate these processes are less evident. A comparison of the component-averaged ∂SOMEs of the corresponding $S_{1,2}/T_{1,2}(\pi \rightarrow \pi^*)$ couplings calculated along the lowest 40 normal modes (v_1 to v_{40}) at the $S_{1,2}(\pi \rightarrow \pi^*)$ minima of oxonine, thionine and selenine is summarized in **Fig. 43** and **Fig. 44** (the vibronic coupling along the remaining normal modes ($72 > v_i > 40$) vanishes for all cases). Within the C_{2v} molecular point group, the A_2, B_1, and B_2 symmetric normal modes are active as promoting modes in accord to vibronic coupling selection rules. A full overview of the coupling vibrational normal modes

calculated at the $S_1(\pi_H \rightarrow \pi_L^*)$ minima of the X=O, S, Se series and at the $S_2(\pi_{H-1} \rightarrow \pi_L^*)$ of selenine and the values of the *∂*SOMEs are given in the SI (Section **7.4**). An increase in the electronic SOMEs that couples the $S_{1,2}(\pi \rightarrow \pi^*)/T_1(\pi_H \rightarrow \pi_L^*)$ and the $S_{1,2}(\pi \rightarrow \pi^*)/T_2(\pi_{H-1} \rightarrow \pi_L^*)$ state pairs could be vibronically induced depending on how the geometrical motion along the A_2 and B_2 *out-of-plane* normal modes allow an efficient interaction with the nearby $n \rightarrow \pi^*$ state. The *∂*SOMEs along the *in-plane* B_1-symmetric normal modes are nearly zero for the three dyes. However, also the extent of the mixing between the $\pi \rightarrow \pi^*$ and $n \rightarrow \pi^*$ states depends on the energy gap between those states. Typically, it is seen that the smaller the gap between $\pi \rightarrow \pi^*$ and $n \rightarrow \pi^*$ states, the larger the enhancement of the vibronic spin-orbit coupling. The magnitude of the calculated numerical *∂*SOMEs for each coupling could reflect this behavior and, therefore, it is analyzed in the following. The heavy atom effects on the vibronic coupling of the X=O, S, Se series of dyes are characterized not only by the magnitude of the *∂*SOMEs between the involved electronic states along a certain v_i, but also in the number of promoting modes which contribute with substantial *∂*SOMEs.

On the average, the magnitude of the *∂*SOMEs between the $S_1(\pi_H \rightarrow \pi_L^*)/T_2(\pi_{H-1} \rightarrow \pi_L^*)$ states is noticeably larger than for the $S_1(\pi_H \rightarrow \pi_L^*)/T_1(\pi_H \rightarrow \pi_L^*)$ pair as expected for all dyes, **Fig. 43**. It is evident that from the three dyes, selenine produces the larger *∂*SOMEs and a higher number of modes are able to contribute with substantial *∂*SOMEs. For the S_1/T_2 states of selenine, the largest *∂*SOME value of 11.94 cm^{-1} was obtained along the $v_{10}(B_2)$ = 290.6 cm^{-1} normal mode. This mode corresponds to a symmetric deformation of the ring-system including a pyramidalization of the nitrogen and selenium atoms of the central ring (see **Fig. 45**). For the S_1/T_2 pair, important the v_1, v_3, v_{11}, v_{18}, v_{20}, v_{21}, v_{23}, v_{24}, v_{29} and v_{30} modes shows significant *∂*SOMEs in the range of 6.91 -7.96 cm^{-1} (**Fig. 48** and **Table 51**). The *∂*SOMEs for the S_1/T_1 pair of selenine are lower than for the S_1/T_2 pair but comparatively larger than those computed for thionine ($S_{1,2}/T_{1,2}$ pairs).

Again, the ν_{10} = 290.6 cm^{-1} B_2-symmetric normal mode shows the largest ∂SOMEs between the S_1/T_1 pair (2.94 cm^{-1}). Other significant ∂SOMEs for this pair of states are in the range of 2.22 - 2.36 cm^{-1} and are found along the ν_7, ν_{18}, ν_{21} and ν_{29} modes.

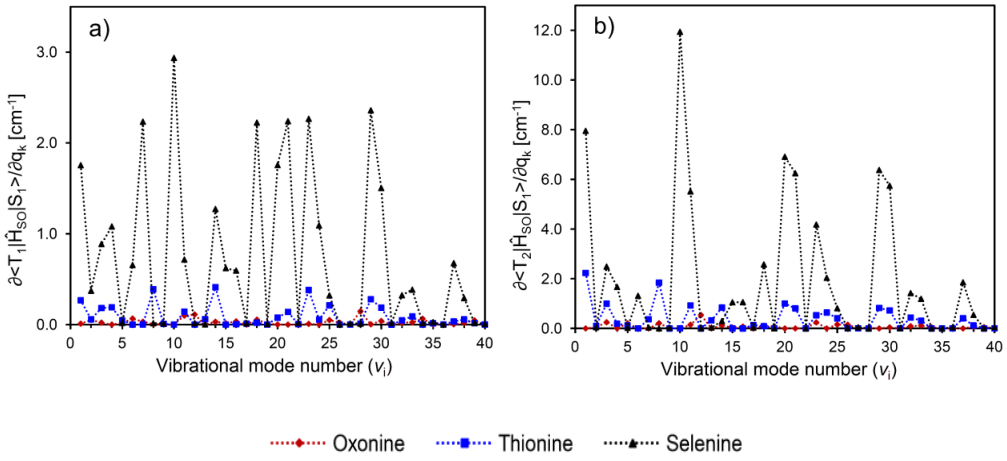

Fig. 43 Derivatives of the SOMEs (∂SOMEs) with respect to the corresponding (dimensionless) normal coordinates at the equilibrium geometry ν_i (1< i< 40) of the $S_1(\pi_H \rightarrow \pi_L^*)$ state.

Since radiationless decay channels to the $T_1(\pi_H \rightarrow \pi_L^*)$ and $T_2(\pi_{H-1} \rightarrow \pi_L^*)$ states are energetically available from the $S_2(\pi_{H-1} \rightarrow \pi_L^*)$ of selenine, we also analyzed the ∂SOMEs between them. A plot of the ∂SOMEs for the S_2/T_1 and S_2/T_2 pairs calculated at each vibrational mode is presented in **Fig. 44(c)**. In spite of the $T_2(\pi_{H-1} \rightarrow \pi_L^*)$ state is closer in energy to the $S_2(\pi_{H-1} \rightarrow \pi_L^*)$ state than to the $T_1(\pi_H \rightarrow \pi_L^*)$ in selenine, larger ∂SOMEs are found between the S_2/T_1 states because of the different MOs involved in each the transition. The calculated ∂SOMEs of 8.81 and 7.48 cm^{-1} are the largest for the S_2/T_1 pair promoted by the $\nu_{12}(B_2)$ = 315.2 cm^{-1} and $\nu_{21}(B_2)$ = 438.6 cm^{-1} modes.These modes are analogues of the ν_{10} and ν_{20} normal modes found at the $S_1(\pi_H \rightarrow \pi_L^*)$ minimum (**Fig. 49** and **Fig. 48**). The ν_{20}, ν_{29} and ν_{30} modes show also substantial contributions with ∂SOMEs above 6 cm^{-1} (**Fig. 44(c)**). The ∂SOMEs between the S_2/T_2 pair of states shows its larger value of only 2.85 cm^{-1} calculated along the $\nu_7(A_2)$ = 196.3 cm^{-1} mode. Lower ∂SOMEs

(0.33-1.93 cm^{-1}) can be found for the remaining coupling modes. The ν_{10} and ν_1 coupling modes calculated at the $S_1(\pi_H \rightarrow \pi_L^*)$ minimum of selenine (see **Fig. 45**) are analogues to the ν_8 and ν_1 normal modes of thionine (**Table 8** and **Fig. 20**).

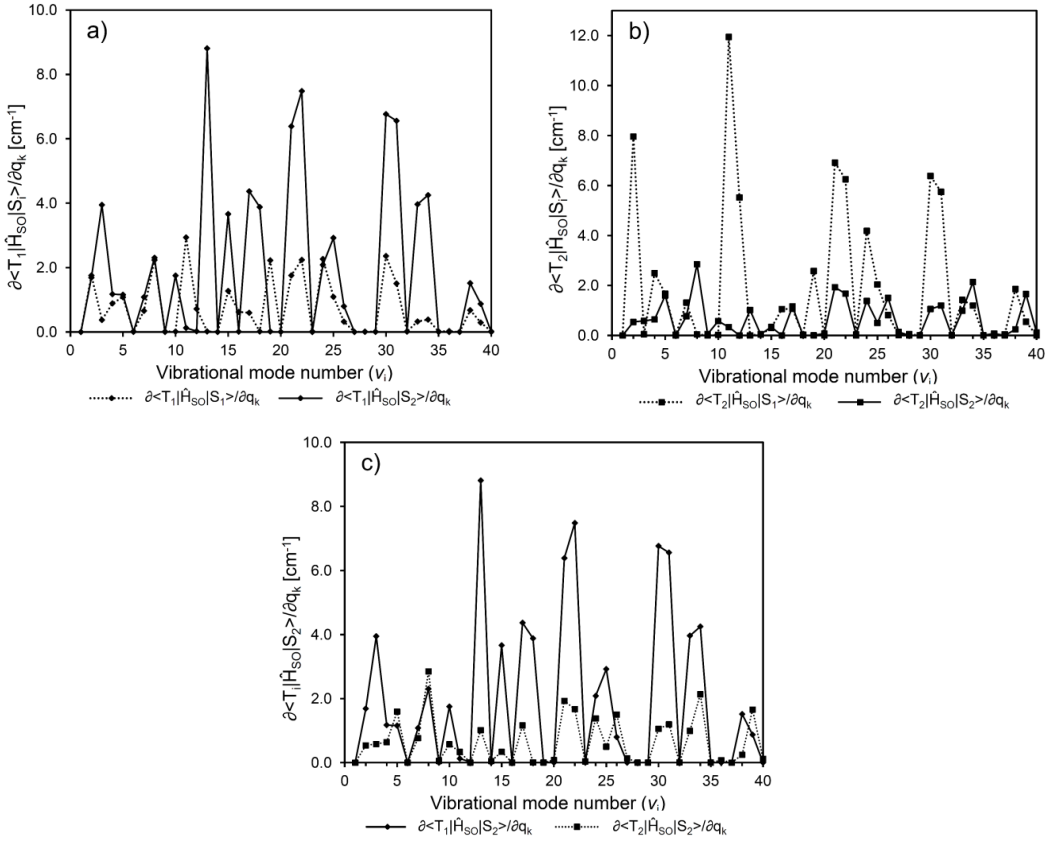

Fig. 44 Derivatives of the SOMEs (∂SOMEs) with respect to the corresponding (dimensionless) normal coordinates at the equilibrium geometry ν_i ($1 < i < 40$) of the $S_1(\pi_H \rightarrow \pi_L^*)$ and $S_2(\pi_{H-1} \rightarrow \pi_L^*)$ states of selenine.

In thionine, these modes also showed the large ∂SOMEs and are important for promoting modes for the $S_1(\pi_H \rightarrow \pi_L^*) \dashrightarrow T_2(\pi_{H-1} \rightarrow \pi_L^*)$ decay channel (∂SOMEs of 2.23 and 1.84 cm^{-1}). Other substantial ∂SOMEs originating from the ν_3, ν_{11}, ν_{14}, ν_{20}, ν_{21}, ν_{29} and ν_{30} modes were obtained (∂SOMEs 0.73 - 1.00 cm^{-1}) and the remaining active modes produce even lower ∂SOMEs in thionine. The S_1/T_1 ∂SOMEs are even smaller (below 0.41 cm^{-1}). In contrast, for oxonine the largest ∂SOMEs for the S_1/T_2 coupling is found to

be of only 0.54 cm^{-1} promoted by the $\nu_{12}(A_2)$ = 404.6 cm^{-1}. Other ten vibrational normal modes show very small vibronic contributions which fall in the range of 0.12 and 0.25 cm^{-1} (ν_3, ν_5, ν_8, ν_{11}, ν_{14}, ν_{18}, ν_{23}, ν_{25}, ν_{26} and ν_{33}, see **Table 51** and **Fig. 50**). The ∂SOMEs between the S_1/T_1 states of oxonine are negligible (below 0.15 cm^{-1}) and only three normal modes (ν_{11}, ν_{12} and ν_{28}) gave non-zero derivatives.

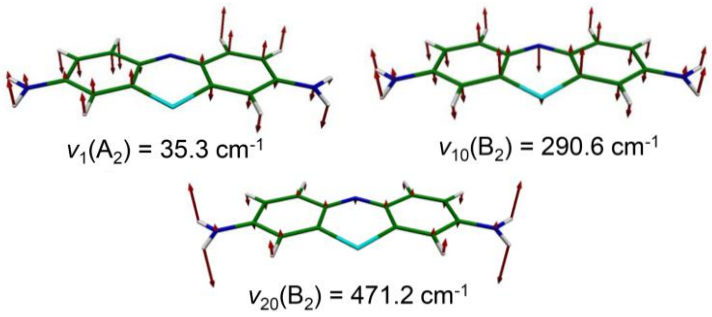

Fig. 45 Important vibrational coupling modes of selenine calculated at the $S_1(\pi_H \rightarrow \pi_L^*)$ minimum.

7.2.4. Photophysics: Radiationless vs Radiative Channel.

As has already pointed out in the previous sections, direct ISC channels like ($\pi \rightarrow \pi^*$) ⇝ ($n \rightarrow \pi^*$) are not accessible for relaxation purposes in these dyes. The case of thionine, however, has demonstrated how the triplet quantum yield may be promoted by vibronic coupling between $\pi\pi^*$ and $n\pi^*$ states, hence, indirectly causing the heavy-atom effect to become apparent in the photophysical kinetics. In the following, we discuss the kinetics of the possible concurrent deactivation processes of selenine and oxonine in vacuum and aqueous solution. Therefore, the implications of the replacement of the sulphur atom of thionine by selenium and oxygen are elucidated.

The ISC rate constants have been computed wherever possible and are listed in **Table 47**. A detailed overview of the estimated rate constants calculated within the time-independent and time-dependent approaches and different technical parameters can be found in the SI, Section **7.4**. For a better understanding of the photophysics, linearly interpolated pathways

connecting the excited state minima involved in the energetically plausible deactivation processes have been calculated in vacuum and are presented in **Fig. 41** and **Fig. 42**.

Table 47 Calculated (time-dependent) ISC rate constants k_{ISC}^{TD}(s^{-1}) and adiabatic excitation energy differences ΔE^{ad} (eV) between the corresponding electronic states.

Channel	Oxonine		Thionine		Selenine	
	ΔE^{ad}	k_{ISC}	ΔE^{ad}	k_{ISC}	ΔE^{ad}	k_{ISC}
		Vacuum				
$S_1(\pi_H\rightarrow\pi_L^*)\dashrightarrow T_1(\pi_H\rightarrow\pi_L^*)$	-0.74	2.55×10^{5}	-0.64	3.57×10^{6} [b]	-0.62	4.22×10^{7}
$S_1(\pi_H\rightarrow\pi_L^*)\dashrightarrow T_2(\pi_{H-1}\rightarrow\pi_L^*)$	-0.02	1.12×10^{8} [a]	-0.30	7.59×10^{8} [b]	-0.39	1.66×10^{10}
$S_2(\pi_{H-1}\rightarrow\pi_L^*)\dashrightarrow T_1(\pi_H\rightarrow\pi_L^*)$	-1.01	-	-0.66	$\sim10^{6}$ [c]	-0.58	1.06×10^{10}
$S_2(\pi_{H-1}\rightarrow\pi_L^*)\dashrightarrow T_2(\pi_{H-1}\rightarrow\pi_L^*)$	-0.29	-	-0.32	$\sim10^{6}$ [c]	-0.35	1.04×10^{9}
		Water[d]				
$S_1(\pi_H\rightarrow\pi_L^*)\dashrightarrow T_1(\pi_H\rightarrow\pi_L^*)$	-0.81	1.25×10^{5}	-0.68	2.52×10^{6} [b]	-0.68	2.59×10^{7}
$S_1(\pi_H\rightarrow\pi_L^*)\dashrightarrow T_2(\pi_{H-1}\rightarrow\pi_L^*)$	+0.09	4.49×10^{6} [a]	-0.21	1.07×10^{9} [b]	-0.32	2.60×10^{10}
$S_2(\pi_{H-1}\rightarrow\pi_L^*)\dashrightarrow T_1(\pi_H\rightarrow\pi_L^*)$	-1.17	-	-0.77	-	-0.69	4.65×10^{9}
$S_2(\pi_{H-1}\rightarrow\pi_L^*)\dashrightarrow T_2(\pi_{H-1}\rightarrow\pi_L^*)$	-0.27	-	-0.30	-	-0.33	1.58×10^{9}

[a]Rate computed at T = 298 K. [b]$k_{\mathrm{ISC}}^{\mathrm{TD}}$ from Section **5.2.5**. [c]$k_{\mathrm{ISC}}^{\mathrm{TI}}$ from Section **5.2.4.1**. [d]DFT/MRCI energy gaps calculated applying the spectroscopic hydration shifts to the adiabatic energies in vacuum using the OX^+3W, TH^+3W and SE^+3W models.

7.2.4.1. Vacuum

As stated in section **7.2.2**, oxonine has two possible ISC relaxation routes available: the $S_1 \dashrightarrow T_1$ and the $S_1 \dashrightarrow T_2$ channels. In thionine and selenine, the $S_2 \dashrightarrow T_1$ and $S_2 \dashrightarrow T_2$ channels are also energetically feasible. In order to be efficient, these channels should be faster than the radiative decay.

In oxonine, the nearly negligible ∂SOMEs computed for the $S_1(\pi_H\rightarrow\pi_L^*) \dashrightarrow T_{1,2}(\pi\rightarrow\pi^*)$ ISC channels (Table 5) results in very small computed rate constants: $k_{ISC}^{TD}(S_1\dashrightarrow T_1) = 2.55\times10^{5}\ s^{-1}$ and $k_{ISC}^{TD}(S_1\dashrightarrow T_2) = 1.12\times10^{8}\ s^{-1}$ (Table 6), respectively. The adiabatic minima of the S_1 and T_2 states are nearly degenerate (Figure 6(d)). Therefore, the density of acceptor vibrational levels is extremely low and Fermi's golden rule (which is the basis of our approach) is not strictly applicable. This may happen even if the path connecting the minima of the potential energy surfaces exhibits a small barrier, i. e. if it is a thermally activated processes. In

this case, it is important to take into account the population of higher vibrational levels of the $S_1(\pi_H \rightarrow \pi_L^*)$ state at room temperature. The energy difference between the adiabatic minimum of the $S_1(\pi_H \rightarrow \pi_L^*)$ state and the crossing point of the energy wells of the S_1 and T_2 states is approximately 207 cm^{-1} which is nearly k_BT at room temperature. The $S_0 \leftarrow S_1(\pi_H \rightarrow \pi_L^*)$ dipole transition is strong yielding a fluorescence rate constant of $k_F = 2.10 \times 10^8\ s^{-1}$ for oxonine. Hence, in vacuum the population transfer to the $T_2(\pi_{H-1} \rightarrow \pi_L^*)$ state from the $S_1(\pi_H \rightarrow \pi_L^*)$ is possible at ambient temperature. We conclude that in oxonine the $S_1(\pi_H \rightarrow \pi_L^*) \dashrightarrow T_2(\pi_{H-1} \rightarrow \pi_L^*)$ ISC channel may compete with the fluorescence decay in vacuum.

In oxonine, the nearly negligible ∂SOMEs computed for the $S_1(\pi_H \rightarrow \pi_L^*) \dashrightarrow T_{1,2}(\pi \rightarrow \pi^*)$ transitions (**Fig. 43**) results in small rate constants which are computed to be $k_{ISC}^{TD}(S_1 \dashrightarrow T_1) = 2.55 \times 10^5\ s^{-1}$ and $k_{ISC}^{TD}(S_1 \dashrightarrow T_2) = 1.12 \times 10^8\ s^{-1}$ (**Table 47**), respectively. The adiabatic minima of the S_1 and T_2 states are nearly degenerate (**Table 45**, **Fig. 41(d)**). Therefore, the density of acceptor vibrational levels is extremely low and Fermi's golden rule (which is the basis of our approach) is not strictly applicable. This may happen even if the path connecting the minima of the PESs exhibits a small barrier, *i. e.* if it is a thermally activated processes. In this case, it is important to take into account the population of higher vibrational levels of the $S_1(\pi_H \rightarrow \pi_L^*)$ state at room temperature. The energy difference between the adiabatic minimum of the $S_1(\pi_H \rightarrow \pi_L^*)$ state and the crossing point of the energy wells of the S_1 and T_2 states is approximately 207 cm^{-1} which is nearly k_BT at room temperature. The $S_0 \leftarrow S_1(\pi_H \rightarrow \pi_L^*)$ dipole transition is strong yielding a fluorescence rate constant of $k_F = 2.10 \times 10^8\ s^{-1}$ for oxonine. Hence, in vacuum the population transfer to the $T_2(\pi_{H-1} \rightarrow \pi_L^*)$ state from the $S_1(\pi_H \rightarrow \pi_L^*)$ is possible at ambient temperature. We conclude that in oxonine the $S_1(\pi_H \rightarrow \pi_L^*) \dashrightarrow T_2(\pi_{H-1} \rightarrow \pi_L^*)$ ISC channel may compete with the fluorescence decay in vacuum.

In thionine, the $S_1(\pi_H \rightarrow \pi_L^*)$ ⇝ $T_2(\pi_{H-1} \rightarrow \pi_L^*)$ ISC was reported to proceed with a rate constant of $k_{ISC}^{TD} \approx 3 \times 10^8$ s^{-1}, which was able to compete with the fluorescence from the $S_1(\pi_H \rightarrow \pi_L^*)$ state ($k_F \approx 1.7 \times 10^8$ s^{-1}) in vacuum (Section **5.2.4**). The other available ISC channels were computed to have rate constant which are two orders of magnitude smaller, hence, were not the dominating factors for the photophysics (**Table 47**). For instance, the ISC arising from the $S_2(\pi_{H-1} \rightarrow \pi_L^*)$ state (which is accessible via a low-lying conical intersection from the $S_1(\pi_H \rightarrow \pi_L^*)$ state) was found to be inefficient for thionine ($k_{ISC}^{TI} \sim 10^5$ - 10^6 s^{-1}) (Section **5.2.4.1**). The S_3 and $T_3(n_{H-4} \rightarrow \pi^*)$ states do not participate directly in the photophysics of thionine. Direct ISC involving these states is also not expected in selenine. However, though the $T_3(n_{H-4} \rightarrow \pi^*)$ state is not accessible from either the $S_1(\pi_H \rightarrow \pi_L^*)$ or $S_2(\pi_{H-1} \rightarrow \pi_L^*)$ minima of selenine (see **Fig. 42**), it affects the ISC by the vibronic coupling.

As mentioned above, an interesting observation in selenine is that the $S_2(\pi_{H-1} \rightarrow \pi_L^*)$ state is about 0.09 eV (**Table 42**) above the optically bright $S_1(\pi_H \rightarrow \pi_L^*)$ state in the vertical absorption spectrum, whereas the adiabatic minimum of S_2 is about 0.04 eV below that of the S_1 state (**Table 45**). This opens another possibility, besides ISC, for the radiationless relaxation of the photoexcited bright S_1 state, namely, IC to the S_2 state. **Fig. 42(b)** shows that the crossing point of the two singlet states is isoenergetic with the S_1 minimum of selenine. The vibronically induced $S_1(\pi_H \rightarrow \pi_L^*)$ ⇝ $T_2(\pi_{H-1} \rightarrow \pi_L^*)$ ISC is computed to have a large rate constant of $k_{ISC}^{TD} = 1.66 \times 10^{10}$ s^{-1}, whereas the population transfer to the $T_1(\pi_H \rightarrow \pi_L^*)$ state is nearly three orders of magnitude slower (**Table 47**). Thus, we expect two competing channels for radiationless relaxation from the $S_1(\pi_H \rightarrow \pi_L^*)$ state, namely, IC to the S_2 state and ISC to the T_2 state. After the S_2 state is populated, we expect that the $S_2(\pi_{H-1} \rightarrow \pi_L^*)$ ⇝ $T_1(\pi_H \rightarrow \pi_L^*)$ channel dominates the ISC with a rate constant of $k_{ISC}^{TD} = 1.06 \times 10^{10}$ s^{-1}. The ISC arising from the $S_2(\pi_{H-1} \rightarrow \pi_L^*)$ ⇝ $T_2(\pi_{H-1} \rightarrow \pi_L^*)$ channel is one order of magnitude slower

(k_{ISC}^{TD} = 1.04 × 10^9 s^{-1}). Therefore, we expect the following photophysical kinetics in vacuum. Population transfer from the $S_1(\pi_H \rightarrow \pi_L^*)$ state may occur to the $S_2(\pi_{H-1} \rightarrow \pi_L^*)$ (via IC) and the $T_2(\pi_{H-1} \rightarrow \pi_L^*)$ (via ISC) states, the latter is followed by IC to the $T_1(\pi_H \rightarrow \pi_L^*)$ state. The $S_2(\pi_{H-1} \rightarrow \pi_L^*)$ state depopulates directly to the lowest lying triplet state. The fluorescence decay from the $S_1(\pi_H \rightarrow \pi_L^*)$ state is computed to have a rate constant of k_F = 1.59 × 10^8 s^{-1}, and is effectively quenched by ISC and IC radiationless processes. Thus, of all the three dyes discussed in this section, we found selenine to be the most efficient triplet state photosensitizer in vacuum.

7.2.4.2. Water

As mentioned in Section **7.2.2.3**, we expect the photophysical kinetics of oxonine and selenine to be affected in different ways by solvation. Due to the fact that the $T_3(n_{H-4} \rightarrow \pi_L^*)$ state experiences a large blueshift in aqueous solution, the vibronic coupling and the indirect ISC rates are expected to decrease. However, a small decrease in the energy gap between a particular pair of π→π* states involved in a ISC channel may lead to a substantial increase in the associated rate constant.

In oxonine, the energy differences between the $S_1(\pi_H \rightarrow \pi_L^*)$ and $T_{1,2}(\pi \rightarrow \pi^*)$ states are increased when the hydration shifts are applied to the adiabatic energies in vacuum, see **Table 45** and **Table 47**. The ISC rate constants for the $S_1(\pi_H \rightarrow \pi_L^*)$ ⇝ $T_1(\pi_H \rightarrow \pi_L^*)$ channel in water are computed to be k_{ISC}^{TD} ~ 1.25 × 10^5 s^{-1} which is comparable to the isolated dye (**Table 47**). The $T_2(\pi_{H-1} \rightarrow \pi_L^*)$ state is no longer accessible from the $S_1(\pi_H \rightarrow \pi_L^*)$ state (ΔE_{S1-T2} ~ 0.1 eV). Thus, according to our calculations the deactivation via the $S_1(\pi_H \rightarrow \pi_L^*)$ ⇝ $T_2(\pi_{H-1} \rightarrow \pi_L^*)$ channel is not plausible for oxonine in water (k_{ISC}^{TD} ~ 4.49 × 10^6 s^{-1}). However, considering the precision of our approach it cannot be excluded. Nevertheless, our findings corroborate the observation

that oxonine is a very efficient fluorophore (calculated $k_F = 2.10 \times 10^8$ s^{-1}) in aqueous solution ($\phi_F = 1.00$).[198]

As expected, the $S_1(\pi_H \rightarrow \pi_L^*)$ ⇝ $T_1(\pi_H \rightarrow \pi_L^*)$ ISC rate constants of thionine ($k_{ISC}^{TD} \sim 10^6$ s^{-1}) and selenine ($k_{ISC}^{TD} \sim 10^7$ s^{-1}) are also unaffected by solvation and are very similar to those calculated in vacuum (**Table 47**). The ISC rate constant for the $S_1(\pi_H \rightarrow \pi_L^*)$ ⇝ $T_2(\pi_{H-1} \rightarrow \pi_L^*)$ channel for thionine has been determined to increase to $k_{ISC}^{TD} \sim 10^9$ s^{-1} (see **Table 9** and **Table 47**) and is faster than fluorescence ($k_F \sim 10^8$ s^{-1}) which can be explained by the decreased $\Delta E_{S1\text{-}T2}$ energy gap in water compared to vacuum. The same argument applies to the $S_1(\pi_H \rightarrow \pi_L^*)$ ⇝ $T_2(\pi_{H-1} \rightarrow \pi_L^*)$ channel, which is nearly two times faster in aqueous solution (see **Table 47**) than in isolated selenine. This ISC channel is expected to dominate the photophysics of selenine and effectively quenches fluorescence in aqueous solution as in thionine. The rate constants for the remaining S_2 ⇝ $T_{1,2}$ ISC channels are also computed to be higher ($k_{ISC}^{TD} \sim 10^9$ s^{-1}) than fluorescence ($k_F \sim 10^8$ s^{-1}).

Due to the heavy atom effect which is indirectly increasing the vibronic coupling between the π→π* electronic states, the radiationless transitions are accelerated in the series from X = O to X = Se. Within the limitations of the computational models used in this work, the qualitative picture obtained here is in very good agreement with the experimental data reported for oxonine and thionine. This validates our computational model and the conclusions derived therefrom, allowing us to classify selenine-based dyes to be very efficient triplet state photosensitizers.

7.3. Conclusions

New theoretical insights in the oxygen (oxonine, X = O) and selenium (selenine, X = Se) substitution on the photophysics of thionine (X = S) have been presented in this work. We have performed a systematic analysis of the electronic, energetic and structural properties of low-lying singlet/triplet excited states of isolated oxonine and selenine. Hydration effects were taken into account using models consisting of the dye and three water molecules (OXH^+3Wa and SEH^+3Wa) embedded in a COSMO environment. Moreover, due to the large spectroscopic solvent shifts found for the low-lying $n\rightarrow\pi^*$ excited states, we focused our attention on the ISC processes between the lowest-lying singlet and triplet $\pi\rightarrow\pi^*$ states.

The heavy atom effects on the series of dyes under investigation has consequences for the adiabatic energies of the excited states affecting the number of energetically available ISC channels. As the energy distribution of the excited states of these dyes suggests vibronic spin-orbit coupling induced ISC pathways between $\pi\rightarrow\pi^*$ states, the heavy atom effects on the direct spin-orbit coupling (which contribute to accelerate these processes) are less evident. In this work, we found that ISC is promoted by an enhanced vibronic spin-orbit coupling rather by direct coupling. From oxonine to selenine, the derivatives of the spin-orbit coupling matrix elements upon elongations along *out-of-plane* normal modes (∂SOMEs) increase, due to a more efficient mixing of the $\pi\rightarrow\pi^*$ and the low-lying states $n\rightarrow\pi^*$ excited states.

A detailed interpretation of the radiative and radiationless channels is presented both in vacuum and aqueous solution. After population of the $S_1(\pi_H\rightarrow\pi_L^*)$ excited state by irradiation with visible light, different decay pathways were found, whose rates depend on the heavy atom substitution (X = O, S, Se). Fluorescence is found to be the major relaxation channel for photoexcited oxonine ($k_F = 2.10 \times 10^8\ s^{-1}$) in aqueous environment. In thionine and selenine, it is the ISC decay which dominates the photophysical

kinetics. In **Chapter 5**, the $S_1(\pi_H \rightarrow \pi_L^*)$ ⇝ $T_2(\pi_{H-1} \rightarrow \pi_L^*)$ ISC channel was found to explain the efficient ISC decay of thionine, which is more efficient in water ($k_{ISC}^{TI} \sim 10^9 s^{-1}$) than in vacuum ($k_{ISC}^{TI} \sim 10^8\ s^{-1}$). This enhancement in the rate constant was due to the smaller adiabatic energy gap due to the solvent. Selenine has a more complex photophysics, where different trends for vacuum and aqueous solution have been found compared to thionine. In both environments the low-lying $S_1(\pi_H \rightarrow \pi_L^*)$ and $S_2(\pi_{H-1} \rightarrow \pi_L^*)$ excited states are found to be adiabatically isoenergetic and two triplet states $T_1(\pi_H \rightarrow \pi_L^*)$ and $T_2(\pi_{H-1} \rightarrow \pi_L^*)$ are energetically available for ISC. The population of the $S_2(\pi_{H-1} \rightarrow \pi_L^*)$ excited state is found to be energetically feasible via S_1 ⇝ S_2 IC, due to a conical intersection between their PESs. In vacuum, we found two fast El-Sayed forbidden ISC channels: $S_1(\pi_H \rightarrow \pi_L^*)$ ⇝ $T_2(\pi_{H-1} \rightarrow \pi_L^*)$ and $S_2(\pi_{H-1} \rightarrow \pi_L^*)$ ⇝ $T_1(\pi_H \rightarrow \pi_L^*)$ with computed rates in the order of $k_{ISC}^{TD} \sim 1 \times 10^{10}\ s^{-1}$, which is faster than fluorescence decay ($k_F = 1.59 \times 10^8\ s^{-1}$). The other, less efficient ISC channels were also found to be faster ($k_{ISC}^{TD} \sim 10^9\ s^{-1}$) than fluorescence. In aqueous solution, the energetic splitting of the $S_2(\pi_{H-1} \rightarrow \pi_L^*)$ and $T_1(\pi_H \rightarrow \pi_L^*)$ excited states is predicted to be larger than in vacuum. As a consequence, the $S_2(\pi_{H-1} \rightarrow \pi_L^*)$ ⇝ $T_1(\pi_H \rightarrow \pi_L^*)$ ISC rate is decreased to $k_{ISC}^{TD} \sim 10^9\ s^{-1}$ and is no longer a prominent channel. This suggests that the radiationless deactivation via $S_1(\pi_H \rightarrow \pi_L^*)$ ⇝ $T_2(\pi_{H-1} \rightarrow \pi_L^*)$ ISC dominates the population of the triplet manifold of selenine in aqueous solution ($k_{ISC}^{TD} = 2.60 \times 10^{10}\ s^{-1}$). Since all of these radiationless channels (IC and ISC) in selenine eventually lead to the efficient triplet population, we expect this chromophore to be the most efficient triplet photosensitizer of the molecules investigated here. The results obtained for oxonine and thionine agree well with experimental trends in aqueous solution validating our proposed models.

7.4. Supplementary information

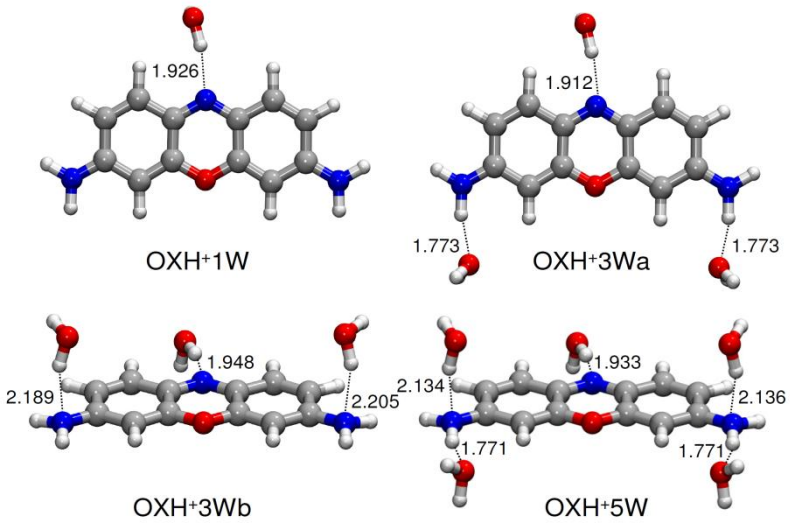

Fig. 46 Ground state minima of the hydrogen bonded complexes of oxonine embedded in COSMO and optimized at the B3LYP/SV(P) level of theory. Numbers indicate hydrogen bond lengths in Å.

Table 48 Oxonine: Comparison of the singlet and triplet vertical excitation energies (eV) in vacuum (OXH^+), solvation with COSMO (OXH^+C) and micro-hydration with one to five explicit water molecules (OXH^+1W - OXH^+5W) embedded in COSMO at the DFT/MRCI/SV(P) theoretical level.

Electronic state	Electronic structure[a]	OXONINE[b]					
		OXH^+	OXH^+C	OXH^+1W	OXH^+3Wa	OXH^+3Wb	OXH^+5W
$S_0(1^1A_1)$	(93) Ground state						
$S_1(1^1B_1)$	(82) $\pi_H \rightarrow \pi_L^*$	2.39(0.998)	2.33(1.016)	2.29(1.010)	2.25(1.026)	2.33(0.989)	2.27(1.001)
$S_2(2^1A_1)$	(80) $\pi_{H-1} \rightarrow \pi_L^*$	2.83(0.000)	2.83(0.000)	2.78(0.001)	2.78(0.002)	2.71(0.000)	2.71(0.000)
$S_3(1^1B_2)$	(80) $n_{H-4} \rightarrow \pi_L^*$	3.16(0.003)	3.37(0.003)	3.48(0.003)	3.60(0.002)	3.37(0.002)	3.39(0.002)
$S_4(3^1A_1)$	(48) $\pi_{H-2} \rightarrow \pi_L^*$ (25) $\pi_H \rightarrow \pi_L^*$ $\pi_H \rightarrow \pi_L^*$	3.64(0.028)	3.56(0.027)	3.49(0.029)	3.44(0.027)	3.55(0.032)	3.49(0.034)
$S_5(2^1B_1)$	(73) $\pi_{H-3} \rightarrow \pi_L^*$	3.64(0.015)	3.67(0.016)	3.61(0.019)	3.65(0.019)	3.51(0.022)	3.55(0.022)
$T_1(1^3B_1)$	(92) $\pi_H \rightarrow \pi_L^*$	1.61	1.52	1.45	1.40	1.52	1.47
$T_2(1^3A_1)$	(86) $\pi_{H-1} \rightarrow \pi_L^*$	2.49	2.49	2.45	2.46	2.37	2.38
$T_3(1^3B_2)$	(82) $n_{H-4} \rightarrow \pi_L^*$	2.80	3.03	3.17	3.30	3.05	3.08
$T_4(2^3A_1)$	(79) $\pi_{H-2} \rightarrow \pi_L^*$	3.13	3.11	3.09	3.08	3.11	3.07

[a]Dominant contributions of the various excited determinants at the DFT/MRCI/SV(P) level (percentage in parentheses). [b]The absorption oscillator strengths f(r) are shown in parentheses.

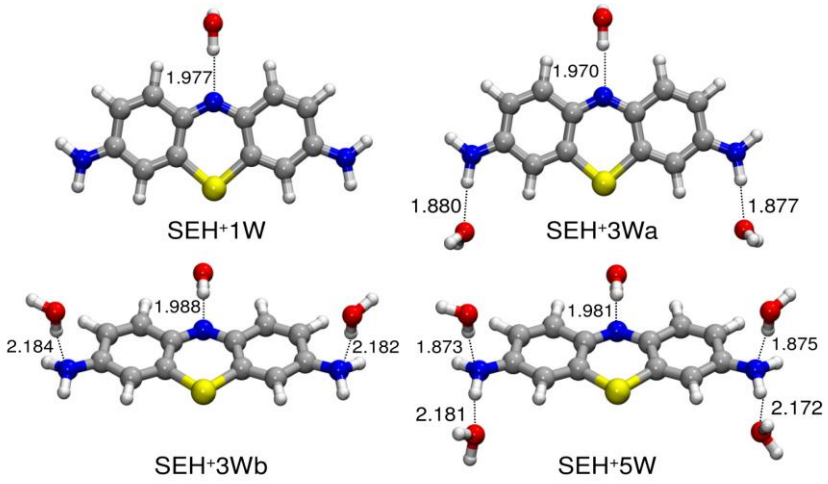

Fig. 47 Ground state minima of the hydrogen bonded complexes of selenine embedded in COSMO and optimized at the B3LYP/TZVP level of theory. Numbers indicate hydrogen bond lengths in Å.

Table 49 Selenine: Comparison of the singlet and triplet vertical excitation energies (eV) in vacuum (SEH^+), solvation with COSMO (SEH^+C) and micro-hydration with one to five explicit water molecules (SEH^+1W - SEH^+5W) embedded in COSMO at the DFT/MRCI/TZVP theoretical level.

Electronic state	Electronic structure[a]	SELENINE[b]					
		SEH^+	SEH^+C	SEH^+1W	SEH^+3Wa	SEH^+3Wb	SEH^+5W
$S_0(1^1A_1)$	(93) Ground state						
$S_1(1^1B_1)$	(80) $\pi_H \rightarrow \pi_L^*$	2.26(0.818)	2.21(0.840)	2.17(0.826)	2.14(0.858)	2.23(0.773)	2.18(0.813)
$S_2(2^1A_1)$	(82) $\pi_{H-1} \rightarrow \pi_L^*$	2.35(0.023)	2.32(0.018)	2.26(0.016)	2.28(0.013)	2.20(0.033)	2.21(0.028)
$S_3(1^1B_2)$	(77) $n_{H-4} \rightarrow \pi_L^*$	3.01(0.003)	3.21(0.003)	3.47(0.003)	3.50(0.003)	3.35(0.003)	3.40(0.003)
$S_4(3^1A_1)$	(52) $\pi_{H-2} \rightarrow \pi_L^*$						
	(21) $\pi_H \rightarrow \pi_L^*$ $\pi_H \rightarrow \pi_L^*$	3.51(0.012)	3.46(0.014)	3.41(0.015)	3.37(0.017)	3.35(0.015)	3.43(0.017)
$S_5(2^1B_1)$	(68) $\pi_{H-3} \rightarrow \pi_L^*$	3.50(0.009)	3.50(0.014)	3.44(0.018)	3.46(0.020)	3.47(0.014)	3.38(0.017)
$T_1(1^3B_1)$	(92) $\pi_H \rightarrow \pi_L^*$	1.61	1.53	1.48	1.43	1.58	1.52
$T_2(1^3A_1)$	(88) $\pi_{H-1} \rightarrow \pi_L^*$	1.97	1.95	1.89	1.92	1.80	1.83
$T_3(1^3B_2)$	(79) $n_{H-4} \rightarrow \pi_L^*$	2.69	2.90	3.18	3.22	3.05	3.10
$T_4(2^3A_1)$	(77) $\pi_{H-2} \rightarrow \pi_L^*$	3.10	3.09	3.07	3.05	3.17	3.07

[a]Dominant contributions of the various excited determinants at the DFT/MRCI/TZVP level (percentage in parentheses). [b]The absorption oscillator strengths f(r) are shown in parentheses.

Table 50 Adiabatic TD-DFT excitation energies (eV) in vacuum (ΔE_{vac}^{ad}). Oscillator strengths for emission at the excited-state minima are listed in parentheses.

State	Character	Oxonine[b]		Selenine[c]	
		DC[a]	ΔE_{vac}^{ad}	DC[a]	ΔE_{vac}^{ad}
$S_1(1^1B_1)$	$\pi_H \rightarrow \pi_L^*$	96	2.82 (0.588)	94	2.69 (0.526)
$S_2(2^1A_1)$	$\pi_{H-1} \rightarrow \pi_L^*$	99	2.77 (0.005)	98	2.47 (0.023)
$T_1(1^3B_1)$	$\pi_H \rightarrow \pi_L^*$	99	1.45	99	1.46
$T_2(1^3A_1)$	$\pi_{H-1} \rightarrow \pi_L^*$	97	2.17	98	1.75

[a]Percentage of the dominant contributions. Adiabatic energies computed relative to the ground state energy at the ground state geometry at the [b]TD-B3LYP/SV(P) and [c]TD-B3LYP/TZVP theoretical levels.

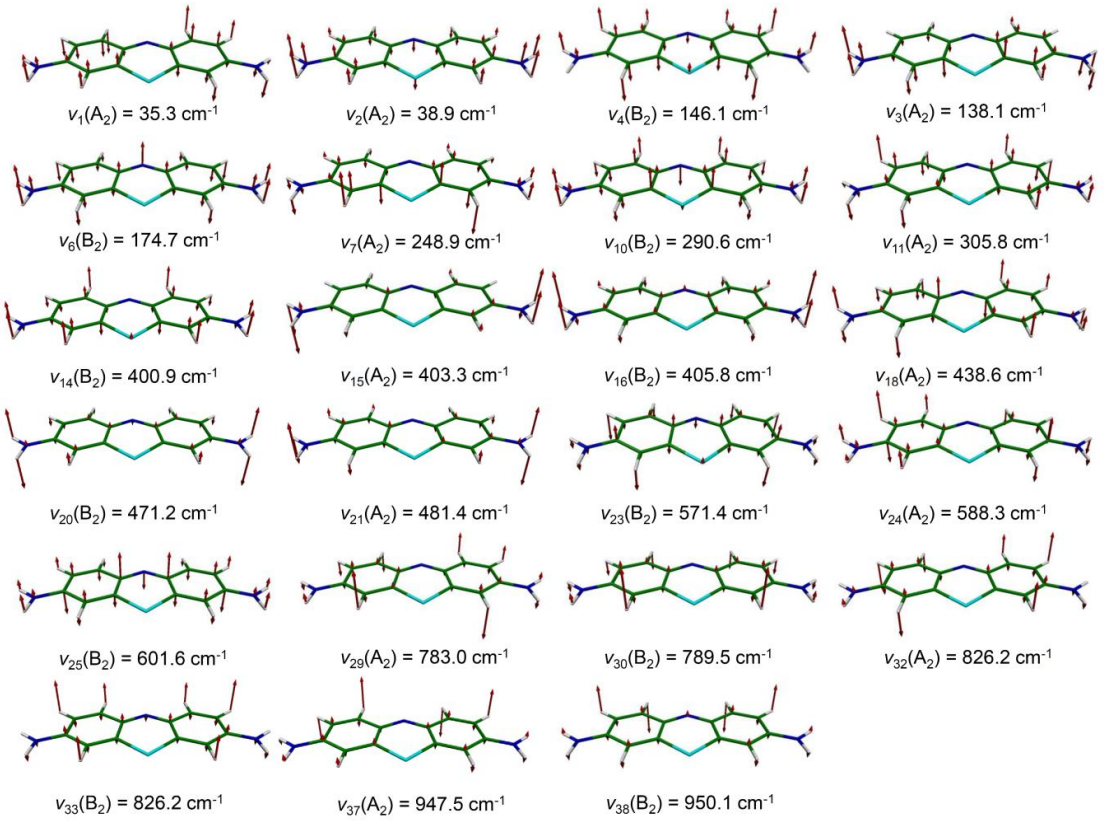

Fig. 48 Vibronic coupling promoting normal modes of selenine calculated at the $S_1(\pi_H \rightarrow \pi_L^*)$ minimum.

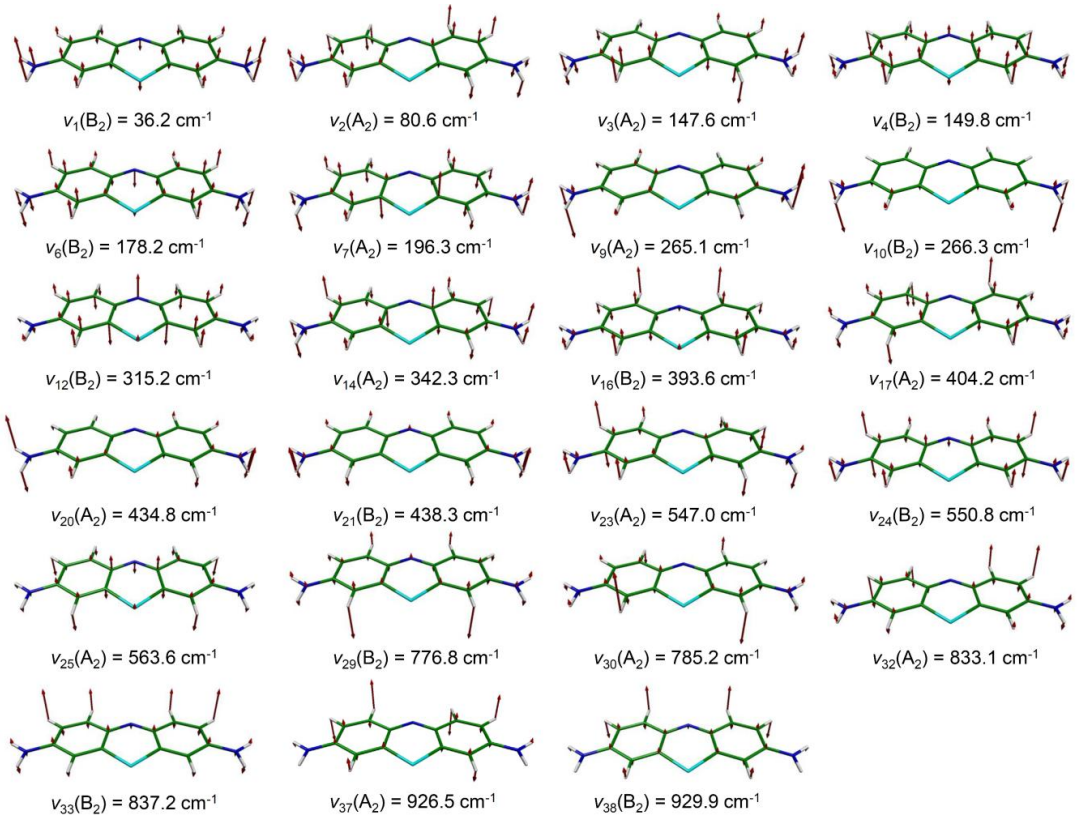

Fig. 49 Vibronic coupling promoting normal modes of selenine calculated at the $S_2(\pi_{H-1}\rightarrow\pi_L^*)$ minimum.

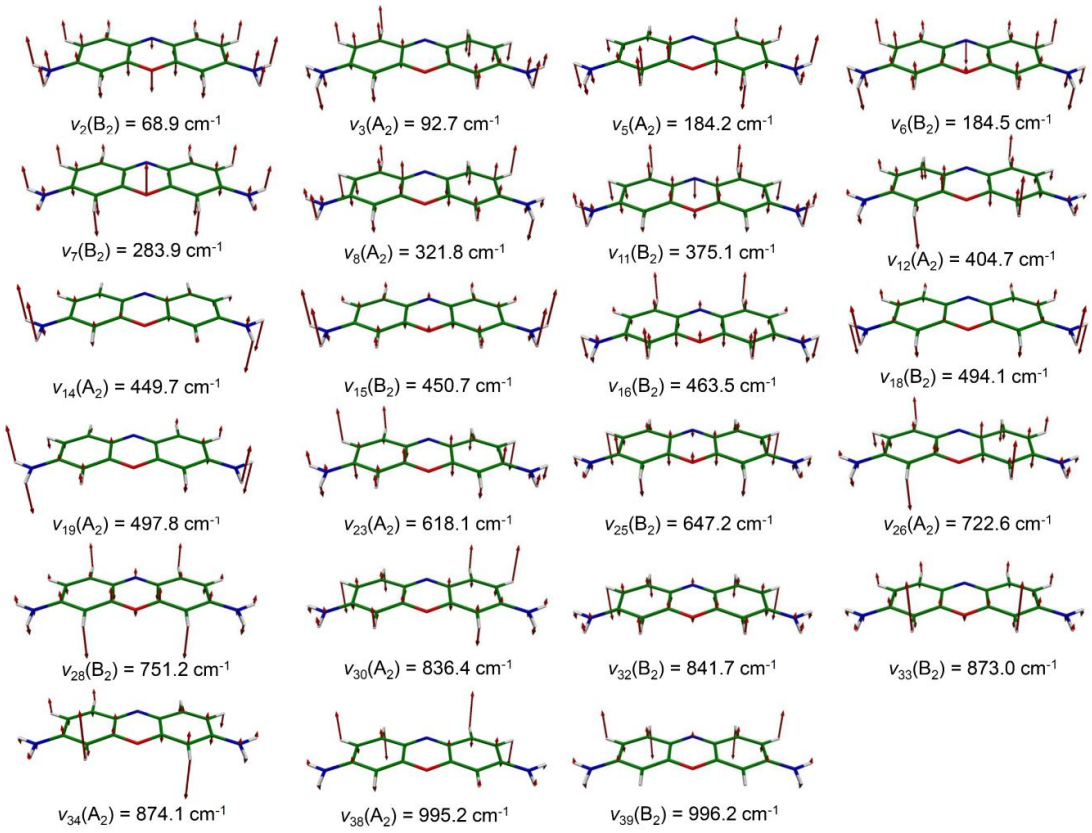

Fig. 50 Vibronic coupling promoting normal modes of oxonine calculated at the $S_1(\pi_H \rightarrow \pi_L^*)$ minimum.

Table 51 Derivatives of the SOMEs (∂SOMEs, cm^{-1}) with respect to the corresponding (dimensionless) normal coordinates at the equilibrium geometry of the $S_1(\pi_H \rightarrow \pi_L^*)$ and $S_2(\pi_{H-1} \rightarrow \pi_L^*)$ excited states.

Oxonine[a]			Thionine[b,c]			Selenine[b]					
$\nu_i(S_1)$	S_1-T_1	S_1-T_2	$\nu_i(S_1)$	S_1-T_1	S_1-T_2	$\nu_i(S_1)$	S_1-T_1	S_1-T_2	$\nu_i(S_2)$	S_2-T_1	S_2-T_2
68.95(B_2)	0.05	0.05	50.0(A_2)	0.27	2.23	35.3(A_2)	1.76	7.96	36.20(B_2)	1.69	0.54
92.73(A_2)	0.02	0.25	56.2(B_2)	0.06	0.11	38.9(B_2)	0.37	0.05	80.16(A_2)	3.95	0.58
184.21(A_2)	0.02	0.21	127.2(A_2)	0.18	1.00	138.1(A_2)	0.89	2.49	147.55(A_2)	1.17	0.64
184.54(B_2)	0.07	0.00	169.2(B_2)	0.19	0.19	146.1(B_2)	1.08	1.67	149.83(B_2)	1.16	1.60
283.90(B_2)	0.03	0.00	170.3(A_2)	0.05	0.12	174.7(B_2)	0.66	1.31	178.23(B_2)	1.08	0.77
321.83(A_2)	0.00	0.21	178.5(B_2)	0.00	0.37	242.9(A_2)	2.23	0.04	196.28(A_2)	2.30	2.85
375.05(B_2)	0.10	0.15	263.7(B_2)	0.39	1.84	290.6(B_2)	2.94	11.94	265.06(A_2)	1.75	0.57
404.65(A_2)	0.11	0.54	304.2(A_2)	0.14	0.93	305.8(A_2)	0.72	5.52	266.27(B_2)	0.13	0.33
449.70(A_2)	0.03	0.13	397.9(B_2)	0.06	0.33	400.9(B_2)	1.27	0.30	315.16(B_2)	8.81	1.02
450.67(B_2)	0.01	0.04	404.9(A_2)	0.41	0.84	403.3(A_2)	0.62	1.05	342.31(A_2)	3.66	0.34
463.46(B_2)	0.04	0.08	477.2(A_2)	0.01	0.14	405.8(B_2)	0.59	1.06	393.61(B_2)	4.37	1.16
494.12(B_2)	0.05	0.11	477.9(B_2)	0.02	0.09	438.6(A_2)	2.22	2.58	404.16(A_2)	3.88	0.01
497.84(A_2)	0.01	0.08	527.0(B_2)	0.08	1.00	471.2(B_2)	1.76	6.91	434.84(A_2)	6.39	1.93
618.09(A_2)	0.01	0.24	534.0(A_2)	0.14	0.81	481.4(A_2)	2.24	6.25	438.25(B_2)	7.48	1.67
647.19(B_2)	0.05	0.16	563.7(B_2)	0.38	0.53	571.4(B_2)	2.27	4.18	547.02(A_2)	2.09	1.38
722.64(A_2)	0.02	0.15	581.8(B_2)	0.06	0.64	588.3(A_2)	1.09	2.04	550.82(B_2)	2.92	0.50
751.19(B_2)	0.15	0.02	586.6(A_2)	0.21	0.41	601.6(B_2)	0.32	0.81	563.59(B_2)	0.80	1.50
836.36(A_2)	0.04	0.04	781.4(A_2)	0.28	0.83	783.0(A_2)	2.36	6.38	776.81(B_2)	6.76	1.06
841.68(B_2)	0.02	0.09	788.5(B_2)	0.19	0.73	789.5(B_2)	1.50	5.75	785.16(A_2)	6.56	1.20
872.96(B_2)	0.02	0.12	826.4(A_2)	0.05	0.44	826.2(A_2)	0.32	1.42	833.08(A_2)	3.96	0.99
874.07(A_2)	0.06	0.04	830.1(B_2)	0.09	0.32	829.0(B_2)	0.38	1.19	837.22(B_2)	4.25	2.13
995.20(A_2)	0.02	0.07	947.7(A_2)	0.03	0.41	947.5(A_2)	0.68	1.86	926.52(A_2)	1.52	0.24
996.21(B_2)	0.05	0.05	950.1(B_2)	0.06	0.12	950.1(B_2)	0.29	0.55	929.91(B_2)	0.87	1.65

Results calculated at the [a]DFT/MRCI/SV(P)//TD-B3LYP/SV(P) and [b]DFT/MRCI/TZVP//TD-B3LYP/TZVP theoretical levels.

Table 52 Calculated rate constants $k_{ISC}^{TI}(s^{-1})$ of oxonine for the $S_1 \rightsquigarrow T_{1(x,z)}$ channels within the time-independent approach. Other columns: adiabatic energy difference (ΔE^{ad}, eV), number of derivatives with respect of *out-of-plane* modes ($\#_{derivs}$), number of accepting modes ($\#_{acc}$), width of the search interval (η, cm^{-1}) and number of final state vibrational levels within the search interval ($\#_{v'}$)

Channel	ΔE^{ad}	$\#_{derivs}$	$\#_{acc}$	η	$\#_{v'}$	k_{ISC}^{TI}
$S_1 \rightsquigarrow T_{1x}$	0.74	12	25	0.01	5×10^{2}	8.29×10^{-1}
		12	25	0.1	5×10^{3}	2.28×10^{2}
		12	25	1	5×10^{4}	2.32×10^{2}
		12	25	10	5×10^{5}	7.65×10^{2}
		12	49	0.01	1×10^{4}	6.75×10^{2}
		12	49	0.1	1×10^{5}	1.47×10^{5}
		12	49	1	1×10^{6}	4.32×10^{5}
		12	49	10	1×10^{7}	7.05×10^{5}
		12	72	0.01	1×10^{6}	1.38×10^{3}
		12	72	0.1	1×10^{7}	1.69×10^{5}
	0.81[a]	12	25	0.01	1×10^{3}	8.64
		12	25	0.1	1×10^{4}	1.26×10^{1}
		12	25	1	1×10^{5}	9.11×10^{1}
		12	25	10	1×10^{6}	1.39×10^{3}
		12	49	0.01	4×10^{4}	1.14×10^{5}
		12	49	0.1	4×10^{5}	3.87×10^{5}
		12	49	1	4×10^{6}	5.57×10^{5}
		12	49	10	4×10^{7}	1.17×10^{6}
		12	72	0.01	5×10^{6}	1.15×10^{5}
$S_1 \rightsquigarrow T_{1z}$	0.74	11	25	0.01	3×10^{2}	2.77×10^{1}
		11	25	0.1	3×10^{3}	4.13
		11	25	1	3×10^{4}	2.74×10^{3}
		11	25	10	3×10^{5}	9.15×10^{2}
		11	49	0.01	7×10^{3}	6.14×10^{3}
		11	49	0.1	7×10^{4}	9.97×10^{4}
		11	49	1	7×10^{5}	1.72×10^{5}
		11	49	10	7×10^{6}	1.71×10^{5}
		11	72	0.01	2×10^{6}	7.26×10^{3}
	0.81[a]	11	25	0.01	8×10^{2}	1.46×10^{1}
		11	25	0.1	8×10^{3}	1.66×10^{2}
		11	25	1	8×10^{4}	6.24×10^{1}
		11	25	10	8×10^{5}	1.64×10^{2}
		11	49	0.01	8×10^{2}	1.46×10^{1}
		11	49	0.1	8×10^{3}	1.66×10^{2}
		11	49	1	8×10^{4}	6.24×10^{1}
		11	49	10	8×10^{5}	1.64×10^{2}

[a]Rate constants calculated: applying spectroscopic solvation shifts from models $OXH^{+}3Wa$

Table 53 Calculated rate constants $k_{ISC}^{TI}(s^{-1})$ of selenine for the $S_i \rightsquigarrow T_{i(x,z)}$ (i = 1,2) channels within the time-independent approach. Other columns: adiabatic energy difference (ΔE^{ad}, eV), number of derivatives with respect of *out-of-plane* modes ($\#_{derivs}$), number of accepting modes ($\#_{acc}$), width of the search interval (η, cm^{-1}) and number of final state vibrational levels within the search interval ($\#_{v'}$)

Channel	ΔE^{ad}	$\#_{derivs}$	$\#_{acc}$	η	$\#_{v'}$	k_{ISC}^{TI}
$S_1 \rightsquigarrow T_{1x}$	0.62	12	25	0.01	2×10^{3}	4.32×10^{4}
		12	25	0.1	2×10^{4}	1.92×10^{5}
		12	25	1	2×10^{5}	1.17×10^{6}
		12	25	10	2×10^{6}	4.37×10^{5}
		12	49	0.01	1×10^{5}	3.99×10^{6}
		12	49	0.1	1×10^{6}	8.50×10^{6}
		12	49	1	1×10^{7}	2.76×10^{7}
	0.68 [a]	12	25	0.01	5×10^{3}	8.84×10^{5}
		12	25	0.1	5×10^{4}	1.45×10^{5}
		12	25	1	5×10^{5}	3.29×10^{5}
		12	25	10	5×10^{6}	1.56×10^{6}
		12	49	0.01	3×10^{5}	3.41×10^{6}
		12	49	0.1	3×10^{6}	2.52×10^{6}
		12	49	1	3×10^{7}	7.04×10^{6}
$S_1 \rightsquigarrow T_{1z}$	0.62	11	25	0.01	2×10^{3}	2.87×10^{5}
		11	25	0.1	2×10^{4}	1.10×10^{5}
		11	25	1	2×10^{5}	9.52×10^{5}
		11	25	10	2×10^{6}	1.09×10^{6}
		11	49	0.01	7×10^{4}	4.08×10^{6}
		11	49	0.1	7×10^{5}	3.62×10^{6}
		11	49	1	7×10^{6}	8.36×10^{6}
		11	49	10	7×10^{7}	1.81×10^{7}
	0.68 [a]	11	25	0.01	3×10^{3}	1.26×10^{5}
		11	25	0.1	3×10^{4}	1.46×10^{5}
		11	25	1	3×10^{5}	1.53×10^{5}
		11	25	10	3×10^{6}	2.78×10^{5}
		11	49	0.01	2×10^{5}	6.54×10^{7}
		11	49	0.1	2×10^{6}	9.33×10^{6}
		11	49	1	2×10^{7}	4.17×10^{6}
$S_1 \rightsquigarrow T_{2x}$	0.39	11	25	0.01	5×10^{2}	9.16×10^{9}
		11	25	0.1	5×10^{3}	2.91×10^{9}
		11	25	1	5×10^{4}	5.85×10^{9}
		11	25	10	5×10^{5}	4.75×10^{9}
		11	49	0.01	4×10^{1}	7.61×10^{9}
		11	49	0.1	4×10^{2}	1.66×10^{9}
		11	49	1	4×10^{3}	5.12×10^{9}
		11	49	10	4×10^{4}	3.53×10^{9}
		11	72	0.01	3×10^{4}	9.58×10^{9}
		11	72	0.1	3×10^{5}	3.36×10^{9}
		11	72	1	3×10^{6}	5.93×10^{9}
		11	72	10	3×10^{7}	4.98×10^{9}
	0.32 [a]	11	25	0.01	2×10^{1}	3.04×10^{8}
		11	25	0.1	1×10^{2}	2.26×10^{9}
		11	25	1	1×10^{3}	3.07×10^{9}
		11	25	10	1×10^{4}	5.13×10^{9}
		11	49	0.01	9×10^{1}	3.11×10^{8}
		11	49	0.1	9×10^{2}	2.62×10^{9}

		11	49	1	9×10^{3}	5.86×10^{9}
		11	49	10	9×10^{4}	4.73×10^{9}
		11	72	0.01	4×10^{3}	4.28×10^{8}
		11	72	0.1	4×10^{4}	3.65×10^{9}
		11	72	1	4×10^{6}	5.32×10^{9}
		11	72	10	4×10^{5}	6.60×10^{9}
$S_1 \nrightarrow T_{2z}$	0.39	12	25	0.01	8×10^{1}	1.05×10^{8}
		12	25	0.1	6×10^{2}	5.34×10^{10}
		12	25	1	6×10^{3}	4.87×10^{9}
		12	25	10	6×10^{4}	1.12×10^{10}
		12	49	0.01	7×10^{2}	1.29×10^{8}
		12	49	0.1	7×10^{3}	5.36×10^{10}
		12	49	1	7×10^{4}	6.58×10^{9}
		12	49	10	7×10^{5}	1.16×10^{10}
		12	72	0.01	2×10^{4}	7.55×10^{9}
		12	72	0.1	2×10^{5}	5.50×10^{10}
		12	72	1	2×10^{6}	1.32×10^{10}
		12	72	10	2×10^{7}	8.04×10^{9}
	0.32 [a]	12	25	0.01	2×10^{1}	1.30×10^{7}
		12	25	0.1	2×10^{2}	6.71×10^{8}
		12	25	1	2×10^{3}	7.29×10^{9}
		12	25	10	2×10^{4}	7.22×10^{9}
		12	49	0.01	2×10^{2}	3.39×10^{8}
		12	49	0.1	1×10^{3}	9.25×10^{8}
		12	49	1	1×10^{4}	7.71×10^{9}
		12	49	10	1×10^{5}	8.20×10^{9}
		12	72	0.01	3×10^{3}	3.69×10^{9}
		12	72	0.1	3×10^{4}	3.06×10^{9}
		12	72	1	3×10^{5}	9.93×10^{9}
		12	72	10	3×10^{6}	1.14×10^{10}
$S_2 \nrightarrow T_{1x}$	0.58	11	25	0.01	2×10^{2}	1.05×10^{8}
		11	25	0.1	2×10^{3}	3.27×10^{8}
		11	25	1	2×10^{4}	6.78×10^{8}
		11	25	10	2×10^{5}	1.85×10^{9}
		11	49	0.01	2×10^{4}	1.04×10^{8}
		11	49	0.1	2×10^{5}	8.11×10^{8}
		11	49	1	2×10^{6}	1.11×10^{9}
	0.69 [a]	11	25	0.01	1×10^{3}	2.23×10^{7}
		11	25	0.1	9×10^{3}	6.34×10^{8}
		11	25	1	1×10^{5}	4.30×10^{8}
		11	25	10	1×10^{3}	2.23×10^{7}
		11	49	0.01	2×10^{5}	5.35×10^{8}
$S_2 \nrightarrow T_{1z}$	0.58	12	25	0.01	3×10^{2}	1.42×10^{8}
		12	25	0.1	3×10^{3}	1.29×10^{9}
		12	25	1	3×10^{4}	1.36×10^{9}
		12	25	10	3×10^{5}	2.85×10^{9}
		12	49	0.01	2×10^{3}	3.41×10^{8}
		12	49	0.1	2×10^{4}	5.76×10^{8}
		12	49	1	2×10^{5}	1.59×10^{9}
		12	49	10	2×10^{6}	3.07×10^{9}
	0.69 [a]	12	25	0.01	2×10^{3}	1.97×10^{7}
		12	25	0.1	2×10^{4}	3.59×10^{9}
		12	25	1	1×10^{5}	1.14×10^{9}
		12	25	10	1×10^{6}	9.26×10^{8}
		12	49	0.01	2×10^{4}	4.51×10^{8}

		12	49	0.1	2×10^{5}	4.35×10^{9}
		12	49	1	2×10^{6}	1.74×10^{9}
		12	49	10	2×10^{7}	1.44×10^{9}
$S_2 \rightsquigarrow T_{2x}$	0.35	12	25	0.01	2	5.18×10^{6}
		12	25	0.1	48	1.06×10^{6}
		12	25	1	4×10^{2}	3.99×10^{7}
		12	25	10	4×10^{3}	1.86×10^{8}
		12	25	100	4×10^{4}	4.70×10^{8}
		12	49	0.01	32	5.18×10^{6}
		12	49	0.1	2×10^{2}	2.13×10^{6}
		12	49	1	2×10^{3}	6.09×10^{8}
		12	49	10	2×10^{4}	2.61×10^{8}
		12	49	100	2×10^{5}	1.13×10^{8}
	0.33 [a]	12	25	0.01	1	1.51×10^{-3}
		12	25	0.1	17	1.31×10^{8}
		12	25	1	2×10^{2}	1.55×10^{8}
		12	25	10	2×10^{3}	1.05×10^{9}
		12	25	100	2×10^{4}	5.04×10^{8}
		12	49	0.01	5	1.51×10^{-3}
		12	49	0.1	1×10^{2}	1.38×10^{8}
		12	49	1	1×10^{3}	6.20×10^{8}
		12	49	10	1×10^{4}	1.09×10^{9}
		12	49	100	1×10^{5}	2.28×10^{8}
$S_2 \rightsquigarrow T_{2z}$	0.35	11	25	0.01	2	0.00
		11	25	0.1	25	3.09×10^{7}
		11	25	1	3×10^{4}	2.82×10^{7}
		11	25	10	3×10^{3}	7.68×10^{7}
		11	25	100	3×10^{4}	1.83×10^{8}
		11	49	0.01	21	3.27×10^{-7}
		11	49	0.1	2×10^{2}	4.17×10^{7}
		11	49	1	2×10^{3}	3.60×10^{8}
		11	49	10	2×10^{4}	2.29×10^{8}
		11	49	100	2×10^{5}	6.30×10^{8}
	0.33 [a]	11	25	0.01	2	1.64×10^{5}
		11	25	0.1	18	2.46×10^{6}
		11	25	1	2×10^{2}	4.02×10^{8}
		11	25	10	2×10^{3}	3.17×10^{8}
		11	49	0.01	5	2.45×10^{5}
		11	49	0.1	79	6.14×10^{6}
		11	49	1	8×10^{2}	4.07×10^{8}
		11	49	10	8×10^{3}	4.00×10^{8}

[a] Rate constants calculated: applying spectroscopic solvation shifts from models $SEH^{+}3Wa$

Table 54 Calculated rate constants $k_{ISC}^{TD}(s^{-1})$ of oxonine for the $S_1 \rightsquigarrow T_i$ (i = 1,2) channels within the time-dependent approach. Other columns: adiabatic energy difference (ΔE^{ad}, eV), time interval (t, fs), number of points ($\#_{points}$) and damping factor (η, cm^{-1})

Channel	ΔE^{ad}	η	t	$\#_{points}$	k_{ISC}^{TD}
Tests performed substituting the imaginary frequency at the S_1 state by v_1 = 316.86 cm^{-1}					
$S_1 \rightsquigarrow T_1$	0.74	10	30000	900000	2.01×10^{6}
		10	50000	1500000	8.18×10^{5}
	0.81[a]	10	30000	900000	1.05×10^{6}
		10	50000	1500000	1.33×10^{6}
$S_1 \rightsquigarrow T_2$	0.02[b]	10	30000	900000	1.43×10^{8}
		10	50000	1500000	1.42×10^{8}
	+0.09[a,b]	10	30000	900000	3.58×10^{6}
		10	50000	1500000	3.58×10^{6}
Tests performed substituting the imaginary frequency at the S_1 state by v_1 = 391.81 cm^{-1}					
$S_1 \rightsquigarrow T_1$	0.74	10	30000	900000	6.21×10^{4}
		10	100000	3000000	2.55×10^{5}
	0.81[a]	10	100000	3000000	1.25×10^{5}
		10	200000	6000000	1.30×10^{5}
$S_1 \rightsquigarrow T_2$	0.02[b]	10	30000	900000	1.11×10^{8}
		10	50000	1500000	1.12×10^{8}
	+0.09[a,b]	10	30000	900000	4.51×10^{6}
		10	50000	1500000	4.49×10^{6}
Tests performed substituting the imaginary frequency at the S_1 state by v_1 = 509.24 cm^{-1}					
$S_1 \rightsquigarrow T_1$	0.74	10	100000	3000000	1.65×10^{5}
		10	200000	6000000	1.01×10^{5}
	0.81[a]	10	30000	900000	2.53×10^{5}
		10	100000	3000000	5.07×10^{4}
		10	200000	6000000	7.33×10^{4}
$S_1 \rightsquigarrow T_2$	0.02[b]	10	30000	900000	1.39×10^{8}
		10	50000	1500000	1.40×10^{8}
	+0.09[a,b]	10	30000	900000	7.10×10^{6}
		10	50000	1500000	7.11×10^{6}
Tests performed substituting the imaginary frequency at the S_1 state by v_1 = 45 cm^{-1}					
$S_1 \rightsquigarrow T_1$	0.74	1	30000	900000	5.85×10^{5}
		1	50000	1500000	5.85×10^{5}
		1	500000	15000000	5.85×10^{5}
		10	30000	900000	8.95×10^{5}
		10	300000	9000000	8.95×10^{5}
		10	500000	15000000	8.95×10^{5}
	0.81[a]	1	30000	900000	1.59×10^{6}
		1	50000	1500000	1.59×10^{6}
		1	500000	15000000	1.59×10^{6}
		1	900000	27000000	1.59×10^{6}
		10	30000	900000	1.88×10^{6}
		10	50000	1500000	1.88×10^{6}
		10	500000	15000000	1.88×10^{6}
		10	900000	27000000	1.88×10^{6}

$S_1 \rightsquigarrow T_2$	0.02	1	30000	900000	1.58×10^{-1}
		1	500000	15000000	7.93×10^{-1}
		100	30000	900000	1.71×10^{5}
		100	50000	1500000	1.71×10^{5}
		100	900000	27000000	1.71×10^{5}
Tests performed substituting the imaginary frequency at the S_1 state by v_1 = 50 cm^{-1}					
$S_1 \rightsquigarrow T_1$	0.74	10	30000	900000	1.27×10^{6}
		10	100000	3000000	1.78×10^{5}
	0.81[a]	10	30000	900000	6.90×10^{5}
		10	50000	1500000	2.66×10^{6}
$S_1 \rightsquigarrow T_2$	0.02[b]	10	30000	900000	1.45×10^{7}
		10	50000	1500000	1.45×10^{7}
	+0.09[a,b]	10	30000	900000	4.70×10^{5}
		10	50000	1500000	4.71×10^{5}
Tests performed substituting the imaginary frequency at the S_1 state by v_1 = 55 cm^{-1}					
$S_1 \rightsquigarrow T_1$	0.74	10	30000	900000	1.22×10^{6}
		10	50000	1500000	6.73×10^{5}
	0.81[a]	10	30000	900000	1.51×10^{5}
		10	50000	1500000	5.54×10^{5}
$S_1 \rightsquigarrow T_2$	0.02[b]	10	30000	900000	1.72×10^{7}
		10	50000	1500000	1.71×10^{7}
	+0.09[a,b]	10	30000	900000	5.24×10^{5}
		10	50000	1500000	5.25×10^{5}
Tests performed substituting the imaginary frequency at the S_1 state by v_1 = 60 cm^{-1}					
$S_1 \rightsquigarrow T_1$	0.74	10	30000	900000	9.49×10^{5}
		10	50000	1500000	1.44×10^{6}
	0.81[a]	10	30000	900000	4.92×10^{6}
		10	50000	1500000	6.93×10^{6}
$S_1 \rightsquigarrow T_2$	0.02[b]	10	30000	900000	1.79×10^{7}
		10	50000	1500000	1.80×10^{7}
	+0.09[a,b]	10	30000	900000	5.88×10^{5}
		10	50000	1500000	5.90×10^{5}
Tests performed substituting the imaginary frequency at the S_1 state by v_1 = 65.430 cm^{-1}					
$S_1 \rightsquigarrow T_1$	0.74	10	30000	900000	7.84×10^{5}
		10	50000	1500000	7.79×10^{5}
	0.81[a]	10	30000	900000	9.03×10^{5}
		10	50000	1500000	1.46×10^{6}
$S_1 \rightsquigarrow T_2$	0.02[b]	10	30000	900000	1.84×10^{7}
		10	50000	1500000	1.85×10^{7}
	+0.09[a,b]	10	30000	900000	6.38×10^{5}
		10	50000	1500000	6.37×10^{5}

[a]Rate constants calculated: applying spectroscopic solvation shifts from models $OXH^{+}3Wa$. [b]Rate computed at 298K.

Table 55 Calculated rate constants $k_{ISC}^{TD}(s^{-1})$ of selenine for the $S_i \rightsquigarrow T_i$ (i = 1,2) channels within the time-dependent approach. Other columns: adiabatic energy difference (ΔE^{ad}, eV), time interval (t, fs), number of points ($\#_{points}$) and damping factor (η, cm^{-1})

Channel	ΔE^{ad}	η	t	$\#_{points}$	k_{ISC}^{TD},
$S_1 \rightsquigarrow T_1$	0.62	1	30000	900000	3.84×10^{7}
		1	50000	1500000	3.84×10^{7}
		1	100000	3000000	3.84×10^{7}
		1	300000	9000000	3.84×10^{7}
		1	500000	15000000	3.84×10^{7}
		1	900000	27000000	3.84×10^{7}
		10	30000	900000	4.22×10^{7}
		10	50000	1500000	4.22×10^{7}
		10	100000	3000000	4.22×10^{7}
		10	300000	9000000	4.22×10^{7}
		10	500000	15000000	4.22×10^{7}
		10	900000	27000000	4.22×10^{7}
		100	30000	900000	4.33×10^{7}
		100	50000	1500000	4.33×10^{7}
		100	100000	3000000	4.33×10^{7}
		100	300000	9000000	4.33×10^{7}
	0.68[a]	1	30000	900000	1.96×10^{7}
		1	50000	1500000	1.96×10^{7}
		1	100000	3000000	1.96×10^{7}
		1	300000	9000000	1.96×10^{7}
		1	500000	15000000	1.96×10^{7}
		1	900000	27000000	1.96×10^{7}
		10	30000	900000	2.59×10^{7}
		10	50000	1500000	2.59×10^{7}
		10	100000	3000000	2.59×10^{7}
		10	300000	9000000	2.59×10^{7}
		10	500000	15000000	2.59×10^{7}
		10	900000	27000000	2.59×10^{7}
$S_1 \rightsquigarrow T_2$	0.39	1	30000	900000	2.35×10^{10}
		1	50000	1500000	2.35×10^{10}
		1	100000	3000000	2.35×10^{10}
		1	300000	9000000	2.35×10^{10}
		1	500000	15000000	2.35×10^{10}
		1	900000	27000000	2.35×10^{10}
		10	30000	900000	1.66×10^{10}
		10	50000	1500000	1.66×10^{10}
		10	100000	3000000	1.66×10^{10}
		10	300000	9000000	1.66×10^{10}
		10	500000	15000000	1.66×10^{10}
		10	900000	27000000	1.66×10^{10}
		100	30000	900000	1.64×10^{10}
		100	50000	1500000	1.64×10^{10}
		100	100000	3000000	1.64×10^{10}
		100	300000	9000000	1.64×10^{10}
	0.32[a]	10	30000	900000	2.60×10^{10}
		10	50000	1500000	2.60×10^{10}
		10	100000	3000000	2.60×10^{10}
		10	300000	9000000	2.60×10^{10}
		10	500000	15000000	2.60×10^{10}

		10	900000	27000000	2.60×10^{10}
$S_2 \rightsquigarrow T_1$	0.58	1	30000	900000	9.93×10^{9}
		1	50000	1500000	9.93×10^{9}
		1	100000	3000000	9.93×10^{9}
		1	300000	9000000	9.93×10^{9}
		1	500000	15000000	9.93×10^{9}
		1	900000	27000000	9.93×10^{9}
		10	30000	900000	1.06×10^{10}
		10	50000	1500000	1.06×10^{10}
		10	100000	3000000	1.06×10^{10}
		10	300000	9000000	1.06×10^{10}
		10	500000	15000000	1.06×10^{10}
		100	30000	900000	1.02×10^{10}
		100	50000	1500000	1.02×10^{10}
		100	100000	3000000	1.02×10^{10}
		100	300000	9000000	1.02×10^{10}
	0.69[a]	10	30000	900000	4.65×10^{9}
		10	50000	1500000	4.65×10^{9}
		10	100000	3000000	4.65×10^{9}
		10	300000	9000000	4.65×10^{9}
		10	500000	15000000	4.65×10^{9}
		10	900000	27000000	4.65×10^{9}
$S_2 \rightsquigarrow T_2$	0.35	1	30000	900000	7.93×10^{8}
		1	50000	1500000	7.93×10^{8}
		1	100000	3000000	7.93×10^{8}
		1	300000	9000000	7.93×10^{8}
		1	500000	15000000	7.93×10^{8}
		1	900000	27000000	7.93×10^{8}
		10	30000	900000	1.04×10^{9}
		10	50000	1500000	1.04×10^{9}
		10	100000	3000000	1.04×10^{9}
		10	300000	9000000	1.04×10^{9}
		10	500000	15000000	1.04×10^{9}
		10	900000	27000000	1.04×10^{9}
		100	30000	900000	1.12×10^{9}
		100	50000	1500000	1.12×10^{9}
		100	100000	3000000	1.12×10^{9}
		100	300000	9000000	1.12×10^{9}
	0.33[a]	10	30000	900000	1.58×10^{9}
		10	50000	1500000	1.58×10^{9}
		10	100000	3000000	1.58×10^{9}
		10	300000	9000000	1.58×10^{9}
		10	500000	15000000	1.58×10^{9}

[a]Rate constants calculated: applying spectroscopic solvation shifts from models $SEH^{+}3Wa$

Chapter 8. General conclusions

This dissertation sheds more light in the understanding of the photophysical relaxation processes that take place in thionine and related compounds immediately after photoexcitation using of quantum chemical methods. These photosensitizers have been used for a variety of applications including energy conversion[15,16] and photodynamic therapy.[11,12] It has been recognized that the photodynamic action of thionine and its derivatives in the presence of oxygen proceeds efficiently by either involving direct excited-state reactions such as electron transfer and hydrogen abstraction[20,30] or by the formation of $^1O_2$.[31] Both mechanisms proceed via the triplet state of the dye. Before the development of this dissertation, it was not clear how intersystem crossing (ISC) leads to an efficient population of the triplet state its dependence on the environment.

In order to compete with other dissipation mechanisms that depopulate the first excited singlet state of thionine, the ISC have to be efficient. In **Chapter 5**, we had shed more light on the photophysics of thionine (TH^+). A complete description of the electronic structure is provided emphasizing on the possible ISC mechanisms that could promote the efficient population of the triplet manifold of thionine in vacuum and aqueous solution. Our results show the lowest excited singlet and triplet states are of $\pi\rightarrow\pi^*$ (S_1, S_2, T_1, T_2) and $n\rightarrow\pi^*$ (S_3, T_3) character. An efficient population transfer from the $S_1(\pi_H\rightarrow\pi_L^*)$ state to the $T_2(\pi_{H-1}\rightarrow\pi_L^*)$ state via this channel is confirmed. The calculated ISC rate constant for this channel is $k_{ISC} \approx 3.35 \times 10^8\ s^{-1}$, which can compete with the radiative depopulation of the $S_1(\pi_H\rightarrow\pi_L^*)$ state via fluorescence ($k_F \approx 1.66 \times 10^8\ s^{-1}$) in vacuum. Other ISC channels have been estimated to be less efficient ($k_{ISC} \approx 10^5 - 10^6\ s^{-1}$). Based on the computed ISC rate constants and excited-state hydration shifts, it is suggested that the efficient triplet quantum yield of thionine in water is primarily due to the

$S_1(\pi_H \rightarrow \pi_L^*) \rightsquigarrow T_2(\pi_{H-1} \rightarrow \pi_L^*)$ channel with a computed rate constant of the order of $k_{ISC} \approx 1.07 \times 10^9$ s^{-1} which is in good accord with the experimental finding ($k_{ISC} = 2.8 \times 10^9$ s^{-1}).[171]

In **Chapter 6**, the photophysics and electronic structure of the diprotonated (TH_2^{+2}) and neutral imine (T) forms of thionine in vacuum and taking into account hydration effects are studied. After the population of the T_1 state of TH^+, this state could undergo protonation and deprotonation reactions at neutral pH.[33-36] The protonation of the T_1 state of TH^+ was found to release more energy than its deprotonation. Furthermore, we have examined how does (de)protonation of TH^+ influences the triplet-triplet energy transfer from the T_1 state to molecular oxygen to form singlet oxygen. Our results show that the energy transfer of the T_1 state of TH_2^{2+} with $^3O_2$ to produce $^1O_2$ requires energy. These facts satisfactory explains the experimental observation of a much smaller efficiency of $^1O_2$ production for TH_2^{2+} than for TH^+.[34] In contrast, the energy transfer from the T_1 states of TH^+ and T to $^3O_2$ releases energy. On the other hand, we found that the protonation and deprotonation of thionine has remarkable effects on its electronic structure and ISC. In very acid aqueous solution (pH < 2) were TH_2^{2+} is present, the ISC proceeds with a rate constant of $k_{ISC} \sim 10^8$ s^{-1} which is four orders of magnitude than the calculated fluorescence decay ($k_F \sim 10^4$ s^{-1}). In basic aqueous solution (pH > 10) where T is present, a thermally activated ISC channel is more efficient ($k_{ISC} \sim 10^9$ s^{-1}) than fluorescence ($k_F \sim 10^7$ s^{-1}). According to these results, the protonation (or pH) effect in the population of the triplet manifold in aqueous solution show that ISC is more efficient for TH_2^{2+} and T than for TH^+.

In **Chapter 7**, the effects of substituting the intra-cyclic sulphur of thionine by oxygen and selenium on the ISC efficiencies is presented in vacuum and taking hydration effects into account. The ISC rate constants are considerably increased when going from O towards Se while the fluorescence rate

constants remain unchanged ($k_F \sim 10^8\ s^{-1}$). In oxonine the relaxation to the ground state after photoexcitation in water has been found to essentially proceed via fluorescence from the $S_1(\pi_H \rightarrow \pi_L^*)$ bright state ($k_F = 2.10 \times 10^8\ s^{-1}$), which is in agreement with the high experimental fluorescence quantum yield. Due to a much stronger vibronic spin-orbit coupling in selenine than in thionine, the ISC rate constant is increased from $k_{ISC} \sim 10^9\ s^{-1}$ in thionine to $k_{ISC} \sim 10^{10}\ s^{-1}$ in selenine. This suggests selenine - based dyes as very efficient triplet state photosensitizers. As the calculated excitation energy of the T_1 state of selenine is almost the same than for thionine, we expect this dye to be a more efficient $^1O_2$ photosensitizer than thionine.

References

[1] M. Kasha, Characterization of electronic transitions in complex molecules, Discuss. Faraday Soc., 1950, 9, 14.

[2] D. Wöll, S. Laimgruber, M. Galetskaya, J. Smirnova, W. Pfleiderer, B. Heinz, P. Gilch, U. E. Steiner, On the mechanism of intramolecular sensitization of photocleavage of the 2-(2-nitrophenyl)propoxycarbonyl (NPPOC) protecting group, J. Am. Chem. Soc., 2007, 129, 12148.

[3] J. J. Serrano-Perez, M. Merchán, L. Serrano-Andrés, Photoreactivity of furocoumarins and DNA in PUVA therapy: formation of psoralen-thymine adducts, J. Phys. Chem. B, 2008, 112, 14002.

[4] A. G. Griesbeck, M. Abe, S. Bondock, Selectivity control in electron spin inversion processes: regio- and stereochemistry of Paterno-Büchi photocycloadditions as a powerful tool for mapping intersystem crossing processes. Acc. Chem. Res., 2004, 37, 919.

[5] C. Neiß, P Saalfrank, Ab initio quantum chemical investigation of the first steps of the photocycle of phototropin: a model study. Photochem. Photobiol., 2003, 77, 101.

[6] S. Salzmann, M. R. Silva-Junior, W. Thiel, C. M. Marian, Influence of the LOV domain on low-lying excited states of flavin: a combined quantum mechanics/molecular-mechanics investigation. J. Phys. Chem. B, 2009, 113, 15610.

[7] J.J. Serrano-Perez, G. Olaso-Gonzales, M. Merchán, L. Serrano-Andrés, Singlet oxygen generation in PUVA therapy studied using electronic structure calculations, Chem. Phys., 2009, 360, 85.

[8] Y. N. Konan, R. Gurny, E. Allémann, State of the art in the delivery of photosensitizers for photodynamic therapy, J. Photochem. Photobiol. B, 2002, 66, 89.

[9] M. T. Jarvi, M. S. Patterson and B. C. Wilson, Insights into photodynamic therapy dosimetry: simultaneous singlet oxygen luminescence and photosensitizer photobleaching measurements. Biophys. J., 2012, 102, 661.

[10] M. C. DeRosa, R. J. Crutchley, Photosensitized singlet oxygen and its applications, Coord. Chem. Rev., 2002, 233-234, 351.

[11] J. P. Tardivo, A. Del Giglio, C. Santos de Oliveira, D. Santesso Gabrielli, H. Couto Junqueira, D. Batista Tadab, D. Severino, R. de Fatima Turchiello, M. S. Baptista, Methylene blue in photodynamic therapy: From basic

mechanisms to clinical applications, Photodiag. Photodyn. Ther., 2005, 2, 175.

[12] D. Gabrielli, E. Belisle, D. Severino, A. J. Kowaltowski, M. S. Baptista, Binding, aggregation and photochemical properties of methylene blue in mitochondrial suspensions, J. Photochem. Photobiol., 2004, 79, 227.

[13] T. Ohsaka, K. Tanaka, K. Tokuda, Electrocatalysis of poly(thionine)-modified electrodes for oxidation of reduced nicotinamide adenine dinucleotide, J. Chem. Soc., Chem. Commun., 1993, 222.

[14] K. Tanaka, S. Ikeda, N. Oyama, K. Tokuda, T. Ohsaka, Preparation of poly(thionine)-modified electrode and its application to an electrochemical detector for the flow-injection analysis of NADH, Anal. Sci., 1993, 9, 783.

[15] K. M. Gangotri, R. C. Meena, Use of reductant and photosensitizer in photogalvanic cells for solar energy conversion and storage: oxalic acid–methylene blue system, J. Photochem. Photobiol., 2001, 141.

[16] C. Lal, Use of mixed dyes in a photogalvanic cell for solar energy conversion and storage: EDTA-thionine-azur-B system, J. Power Sources, 2004, 164, 926.

[17] M. G. Neumann, M. R. Rodrigues, The mechanism of the photoinitiation of the polymerization of MMA by the thionine-triethanolamine system, Polymer, 1998, 39, 1657-1661.

[18] V. Svoboda, M. J. Cooney. C. Rippolz, B. Y. Liaw, In-situ characterization of electrochemical polymerization of methylene green on platinum electrodes, J. Electrochem. Soc., 2007, 154, D113.

[19] M. Wainwright, H. Mohr, W. H. Walker, Phenothiazinium derivatives for pathogen inactivation in blood products, J. Photochem. Photobiol. B, 2007, 86, 45.

[20] E. M. Tuite, J. M. Kelly, Photochemical reactions of methylene blue and analogues with DNA and other biological substrates, J. Photochem. Photobiol. B, 1993, 21, 103.

[21] M. Wainwright, D.A. Phoenix, J. Marland, D. R. A. Wareing, F.J. Bolton, A study of photobactericidal activity in the phenothiazinium series, FEMS Immunol. Med. Microbiol., 1997, 19, 75.

[22] M. Wainwright, The development of phenothiazinium photosensitisers, Photodiagn. Photodyn. Ther., 2005, 2, 263.

[23] D. A. Phoenix, Z. Sayed, S. Hussain, F. Harris, M. Wainwright, The phototoxicity of phenothiazinium derivatives against Escherichia coli and

Staphylococcus aureus, FEMS Immunol. Med. Microbiol., 2003, 39, 17.

[24] M. Wainwright, D. A. Phoenix, S. L. Laycock, D. R. Wareing, P. A Wright, Photobactericidal activity of phenothiazinium dyes against methicillin-resistant strains of Staphylococcus aureus, FEMS Microbiol. Lett., 1998, 160, 177.

[25] J. W. Foley, X. Song, T. N. Demidova, F. Jalil, M. R. Hamblin, Synthesis and properties of benzo[a]phenoxazinium chalcogen analogues as novel broad-spectrum antimicrobial photosensitizers, J. Med. Chem., 2006, 49, 5291.

[26] M. Wainwright, Photodynamic antimicrobial chemotherapy (PACT), J. Antimicrob. Chemother., 1998, 42, 13.

[27] J. P. Thurston, The chemotherapy of Plasmodium berghei. I. Resistance to drugs, Parasitology, 1953, 43, 246.

[28] C. Boda, B. Enanga, B. Courtioux, J. C. Breton, B. Bouteille, Trypanocidal activity of methylene blue. Evidence for in vitro efficacy and in vivo failure, Chemother., 2006, 52, 16.

[29] N. Kashef, G. R. S. Abadi, G. E. Djavid, Phototoxicity of phenothiazinium dyes against methicillin-resistant Staphylococcus aureus and multi-drug resistant Escherichia coli, Photodiag. Photodyn. Ther., 2012, 9, 1, 11.

[30] H. E. A. Kramer, A. Maute, Sensitized photooxygenation according to type I mechanism (radical mechanism) - part I. Flash photolysis experiments, Photochem. Photobiol., 1972, 15, 7.

[31] D. R. Kearns, Physical and chemical properties of singlet molecular oxygen, Chem. Rev., 1971, 71, 395.

[32] A. H. Cincotta, L. Cincotta, J. W. Foley, Novel benzophenothiazinium photosensitizers: preliminary in-vivo results. SPIE Proc., 1990, 1203, 202.

[33] H. Fischer, Light flash investigations on the fading out reaction of thionine with allylthiourea, Z. Phys. Chem. N. F., 1964, 43, 177.

[34] R. Bonneau, R. Pottier, O. Bagno, J. Joussot-Dubien, pH dependence of singlet oxygen production in aqueous solutions using thiazine dyes as photosensitizers, Photochem. Photobiol., 1975, 21, 159.

[35] R. Bonneau, D. S. Stevens, The protonation rate constants of the triplet state of thionine, Chem. Phys. Lett., 1972, 13, 376.

[36] R. Bonneau, J. Pereyre, Mechanism of photoreduction of thiazine dyes by EDTA studied by flash photolyisis - III Consequences of a newly found pK_T of thionine on the mechanism in basic solutions, Photochem. Photobiol., 1975, 21, 173.

[37] L. F. Epstein, F. Karush, E. Rabinowitch, A spectrophotometric study of thionine, J. Opt. Soc. Am., 1941, 31, 77.

[38] V. E. Nicotra, M. F. Mora, R. A. Iglesias, A. M. Baruzzi, Spectroscopic characterization of thionine species in different media, Dyes and Pigments, 2008, 76, 2, 315.

[39] E. G. Kelley, E. G. Miller, Reactions of dyes with cell substances II. The differential staining of nucleoprotein and mucin by thionine and similar dyes, J. Biol. Chem., 1935, 110, 119.

[40] S. Siegert, F. Vogeler, C. M. Marian, R. Weinkauf, Throwing light on dark states of a-oligothiophenes of chain lengths 2 to 6: radical anion photoelectron spectroscopy and excited-state theory, Phys. Chem. Chem. Phys., 2011,13, 10350.

[41] F. Vogeler; S. Siegert, C. M. Marian, R. Weinkauf, T_1/ T_2 State energies and electron affinities of small α,ω-diphenylpolyenes investigated by anion photodetachment photoelectron spectroscopy and Excited-State Theory, ChemPhysChem, 2011, 12, 1948.

[42] C. Brand, J. Küpper, D. W. Pratt, W. L. Meerts, D. Krügler, J. Tatchen, M. Schmitt, Vibronic coupling in indole: I. Theoretical description of the ^1L_a-^1L_b interaction and the electronic spectrum, Phys. Chem. Chem. Phys., 2010, 12, 4968.

[43] V. Rai-Constapel, M. Kleinschmidt , S. Salzmann, Luis Serrano-Andrés, Christel M. Marian, Thioxanthone: on the shape of the first absorption band, Phys. Chem. Chem. Phys., 2010,12, 9320.

[44] M. Etinski, C. M. Marian, Ab initio investigation of the methylation and hydration effects on the electronic spectra of uracil and thymine, Phys. Chem. Chem. Phys., 2010,12, 4915.

[45] M. Parac, M. Doerr, C. M. Marian, W. Thiel, QM/MM calculation of solvent effects on absorption spectra of guanine, J. Comput. Chem., 2010, 31, 90.

[46] T. Y. Ohulchanskyy; D. J. Donnelly; M. R. Detty, P. N. Prasad, Heteroatom substitution induced changes in excited-state photophysics and singlet oxygen generation in chalcogenoxanthylium dyes: Effect of sulfur and selenium substitutions, J. Phys. Chem. B, 2004, 108, 8668.

[47] M. R. Detty, P. N. Prasad, D. J. Donnelly, T. Ohulchanskyy, S. L. Gibson, R. Hilf, Synthesis, properties, and photodynamic properties in vitro of heavy-chalcogen analogues of tetramethylrosamine, Bioorg. Med. Chem., 2004, 12, 2537.

[48] L. Cincotta, J. W. Foley, A. H. Cincotta, Phototoxicity, redox behavior, and pharmacokinetics of benzophenoxazine analogues in EMT-6 murine sarcoma cells, Cancer Res., 1993, 53, 2571.

[49] F. Furche, R. Ahlrichs, Adiabatic time-dependent density functional methods for excited state properties, J. Chem. Phys., 2002, 117, 7433.

[50] A. Dreuw, M. Head-Gordon, Single-reference ab initio methods for the calculation of excited states of large molecules, Chem. Rev., 2005, 105, 4009.

[51] S. Grimme, M. Waletzke, A combination of Kohn-Sham density functional theory and multi-reference configuration interaction methods, J. Chem. Phys., 1999, 111, 5645.

[52] M. R. Silva-Junior, M. Schreiber, S. P. A. Sauer, W. Thiel, Benchmarks for electronically excited states: Time-dependent Density Functional Theory and Density Functional Theory Based Multireference Configuration Interaction, J. Chem. Phys., 2008, 129, 104103.

[53] M. C. Daza , M. Doerr , S. Salzmann , C. M. Marian, W. Thiel, Photophysics of phenalenone: quantum-mechanical investigation of singlet-triplet intersystem crossing, Phys. Chem. Chem. Phys., 2009,11, 1688.

[54] J. Tatchen, N. Gilka, C. M. Marian, Intersystem crossing driven by vibronic spin-orbit coupling: a case study on psoralen. Phys. Chem. Chem. Phys., 2007, 9, 5209.

[55] S. Perun, J. Tatchen, C. M. Marian, Singlet and triplet excited states and intersystem crossing in free-base porphyrin: TDDFT and DFT/MRCI study, ChemPhysChem, 2008, 9, 282.

[56] M. Etinski, J. Tatchen, C. M. Marian, Time-dependent approaches for the calculation of intersystem crossing rates, J. Chem. Phys., 2011, 134, 154105.

[57] M. Etinski, V. Rai-Constapel, C. M. Marian, Time-dependent approach to spin-vibronic coupling: Implementation and test results, submitted to J. Chem. Phys.

[58] M. Kleinschmidt, J. Tatchen, C. M. Marian, SPOCK.CI: A multireference spin-orbit configuration interaction method for large molecules, J. Chem. Phys., 2006, 124, 124101.

[59] M. Kleinschmidt, J. Tatchen, C. M. Marian, Spin-orbit coupling of DFT/MRCI wavefunctions: Method, test calculations, and application to thiophene, J. Comput. Chem., 2002, 23, 824.

[60] M. Kleinschmidt, C. M. Marian, Efficient generation of matrix elements for

one-electron spin-orbit operators, Chem. Phys., 2005, 311, 71.

[61] B. A. Heß, C. M. Marian, U. Wahlgren and O. Gropen, A mean-field spin-orbit method applicable to correlated wavefunctions, Chem. Phys. Lett., 1996, 251, 365.

[62] B. R. Henry, W. Siebrand, Organic Molecular Photophysics, vol. 1, John Wiley & Sons, London, 1973, p. 153; Spin-orbit coupling in aromatic hydrocarbons. Analysis of nonradiative transitions between singlet and triplet states in benzene and naphtalene. J. Chem. Phys., 1971, 54, 1072.

[63] S. K. Lower, M. A. El-Sayed, The triplet state and molecular electronic processes in organic molecules, Chem. Rev., 1966, 66, 199.

[64] C. M. Marian, Spin-orbit coupling in molecules, in Reviews in computational chemistry, ed. K. Lipkowitz and D. Boyd, Wiley-VCH, Weinheim, 2001, 17, 99.

[65] P. W. Atkins, R. S. Friedman, Molecular quantum mechanics, Third edition, Oxford University Press, Oxford, Great Britain, 1997.

[66] J. S. Binkley, J. A. Pople, W. J. Hehre, Self-consistent molecular orbital methods. 21. Small split-valence basis sets for first-row elements, J. Am. Chem. Soc., 1980, 102, 939.

[67] T. H. Dunning Jr., Gaussian basis sets for use in correlated molecular calculations. I. The atoms boron through neon and hydrogen, J. Chem. Phys., 1989, 90, 1007.

[68] A. Schaefer, H. Horn, R. Ahlrichs, Fully optimized contracted Gaussian-basis sets for atoms Li to Kr, J. Chem. Phys., 1992, 97, 2571.

[69] R. Parr, W. Yang, Density-functional theory of atoms and molecules, Oxford University Press, Oxford, 1989.

[70] D. Sholl, J. Steckel, Density Functional Theory: A Practical Introduction, John Wiley & Sons, Inc., New Jersey, United States of America, 2009

[71] M. van Faassen, K. Burke, Time-dependent density functional theory of high excitations: to infinity, and beyond, Phys. Chem. Chem. Phys., 2009, 11, 4437.

[72] L. O. Wagner, K. Burke, The role of exact conditions in TDDFT, To appear in: Time-dependent density functional theory, 2nd ed., edited by M. Marques, et al. (Springer, 201X).

[73] P. Geerlings, F. De Proft, W. Langenaeker, Conceptual Density Functional Theory, Chem. Rev., 2003, 103, 1793.

[74] P. Hohenberg, W. Kohn. Inhomogeneous electron gas. Phys. Rev., Phys. Rev., 1964, 136, B864.

[75] W. Kohn, Electronic structure of matter-wave functions and density functionals, Rev. Mod. Phys., 1998, 71, 1253.

[76] W. Kohn, L. Sham, Self-consistent equations including exchange and correlation effects, J. Phys. Rev. A, 1965, 140, 1133.

[77] M. Levy, Universal variational functionals of electron densities, first-order density matrices, and natural spin-orbitals and solution of the v-representability problem, Proc. Natl. Acad. Sci. U. S. A., 1979, 76, 6062.

[78] D. C. Langreth, Exchange-correlation energy of a metallic surface: Wave-vector analysis. II., J. P. Perdew, Phys. Rev. B, 1982, 26, 2810.

[79] J. Harris, R. O. Jones, The surface energy of a bounded electron gas, J. Phys. F: Metal Phys., 1974, 4, 1170.

[80] A. D. Becke, Density-functional exchange-energy approximation with correct asymptotic behavior, Phys. Rev. A, 1988, 38, 3098.

[81] C. Lee, W. Yang, R. G. Parr, Development of the Colle-Salvetti correlation-energy formula into a functional of the electron density, Phys. Rev. B, 1988, 37, 785.

[82] J. P. Perdew, K. Burke, M. Ernzerhof, Generalized gradient approximation made simple, Phys. Rev. Lett., 1996, 77, 3865.

[83] A. D. Becke, Density-functional thermochemistry. III. The role of exact exchange, J. Chem. Phys., 1993, 98, 5648.

[84] B. Miehlich, A. Savin, H. Stoll, H. Preuss, Results obtained with the correlation energy density functionals of Becke and Lee, Yang and Parr, Chem. Phys. Lett., 1989, 157, 200.

[85] R. Bauernschmitt, R. Ahlrichs, Treatment of electronic excitations within the adiabatic approximation of time dependent density functional theory, Chem. Phys. Lett., 1996, 256, 454.

[86] N. Gilka, C. M. Marian, Performance of the density functional theory/multireference configuration interaction method on electronic excitation of extended π-systems, J. Chem. Theory Comput. 2008, 4, 1501.

[87] C. M. Marian, The guanine tautomer puzzle: Quantum chemical investigation of ground and excited states, J. Phys. Chem. A, 2007, 111, 1545.

[88] C. M. Marian, D. Nolting, R. Weinkauf, The electronic spectrum of protonated adenine: Theory and experiment, Phys. Chem. Chem. Phys., 2005, 7, 3306.

[89] C. Neiss, P. Saalfrank, M. Parac, S. Grimme, Quantum chemical

calculation of excited states of flavin-related molecules, J. Phys. Chem. A, 2003, 107, 140.

[90] D. Nolting, C. M. Marian, R. Weinkauf, Protonation effect on the electronic spectrum of tryptophan in the gas phase, Phys. Chem. Chem. Phys., 2004, 6, 2633.

[91] K. A. Seefeld, C. Plutzer, D. Lowenich, T. Haber, R. Linder, K. Kleinermanns, J. Tatchen, C. M. Marian, Tautomers and electronic states of jet-cooled 2-aminopurine investigated by double resonance, Phys. Chem. Chem. Phys., 2005, 7, 3021.

[92] K. Tomić, J. Tatchen, C. M. Marian, Quantum chemical investigation of the electronic spectra of the keto, enol, and keto-imine tautomers of cytosine, J. Phys. Chem. A, 2005, 109, 8410.

[93] M. Schmitt, R. Brause, C. M. Marian, S. Salzmann, W. L. Meerts, Electronically excited states of tryptamine and its microhydrated complex, J. Chem. Phys., 2006, 125, 124309.

[94] A. B. J. Parusel, S. Grimme, DFT/MRCI calculations on the excited states of porphyrin, hydroporphyrins, tetrazaporphyrins and metalloporphyrins, J. Porphyrins Phthalocyanines, 2001, 5, 225.

[95] C. M. Marian, A new pathway for the rapid decay of electronically excited adenine, J. Chem. Phys., 2005, 122, 104314.

[96] C. M. Marian, F. Schneider, M. Kleinschmidt, and J. Tatchen, Electronic excitation and singlet-triplet coupling in uracil tautomers and uracil-water complexes, Eur. Phys. J. D, 2002, 20, 357.

[97] V. Rai-Constapel, S. Salzmann, C. M. Marian, Isolated and solvated thioxanthone: A photophysical study, J. Phys. Chem. A, 2011, 115, 8589.

[98] M. Etinski, T. Fleig, C. M. Marian, Intersystem crossing and characterization of dark states in the pyrimidine nucleobases uracil, thymine, and 1-methylthymine, J. Phys. Chem. A, 2009, 113, 11809.

[99] C. M. Marian, Spin-forbidden transitions in flavone, Spectrochim. Acta A, 2009, 73, 1.

[100] S. Salzmann, C. M. Marian, The photophysics of alloxazine: a quantum chemical investigation in vacuum and solution, Photochem. Photobiol. Sci., 2009, 8, 1655.

[101] M. Böhm, J. Tatchen, D. Krügler, K. Kleinermanns, M. G. D. Nix, T. A. LeGreve, T. S. Zwier, M. Schmitt, High-resolution and dispersed fluorescence examination of vibronic bands of tryptamine: Spectroscopic signatures for

L_a/L_b mixing near a conical intersection, J Phys Chem A., 2009, 113, 2456.

[102] D. Pfiffi, B. A. Bier, C. M. Marian, K. Schaper, C. A. M. Seidel, Diphenylhexatrienes as photoprotective agents for ultrasensitive fluorescence detection, J. Phys. Chem. A, 2010, 114, 4099.

[103] C. Diedrich, S. Grimme, Systematic investigation of modern quantum chemical methods to predict electronic circular dichroism spectra, J. Phys. Chem. A, 2003, 107, 2524.

[104] P. Elliott, F. Furche, K. Burke, in Reviews of Computational Chemistry, ed. K. B. Lipkowitz and T. R. Cundari, Wiley, Hoboken, NJ, 2009.

[105] S. Grimme, Calculation of electronic spectra of large molecules, Rev. Comp. Chem., 2004, 20, 153.

[106] E. K. U. Gross, W. Kohn, Time-dependent density functional theory, Adv. Quantum Chem., 1990, 21, 255.

[107] E. K. U. Gross, C. A. Ullrich, U. J. Gossmann in Density Functional Theory, p. 149, NATO ASI Series, E. K. U. Gross and R. M. Dreizler, eds., Plenum, New York, 1994.

[108] E. K. U. Gross, J. F. Dobson, M. Petersilka, Density Functional Theory II, in Topics in Current Chemistry Vol. 181, R. F. Nalewajski, ed., Springer, Berlin, Heidelberg, New York, 1996.

[109] E. Runge E. K. Gross, Density-functional theory for time-dependent systems, Phys. Rev. Lett., 1984, 52, 997.

[110] A. Castro, M. A. L. Marques, A. Rubio, Propagators for the time-dependent Kohn-Sham equations, J. Chem. Phys., 2004, 121, 3425.

[111] M. E. Casida, in Recent Advances in Density-Functional Methods, ed. D. P. Chong, World Scientific, Singapore, 1995, p. 155.

[112] A. Bhatia, Electron-He^+ P-wave elastic scattering and photoabsorption in two-electron systems, Phys. Rev. A, 2006, 73.

[113] P. Hessler, N. T. Maitra, K. Burke, Correlation in time-dependent density-functional theory, J. Chem. Phys., 2002, 117, 72.

[114] E. Gross, W. Kohn, Local density-functional theory of frequency-dependent linear response, Phys. Rev. Lett., 1985, 55, 2850.

[115] M. van Faassen, P. L. de Boeij, R. van Leeuwen, J. A. Berger, J. G. Snijders, Ultranonlocality in time-dependent current-density-functional theory: Application to conjugated polymers, Phys. Rev. Lett., 2002, 88, 186401.

[116] J. F. Dobson, M. J. Bünner, E. K. U. Gross, Time-dependent density functional theory beyond linear response: An exchange-correlation potential

with memory, Phys. Rev. Lett., 1997, 79, 1905.

[117] Y. Kurzweil, R. Baer, Time-dependent exchange-correlation current density functionals with memory, J. Chem. Phys., 2004, 121, 8731.

[118] S. Grimme, Density functional calculations with configuration interaction for the excited states of molecules, Chem. Phys. Lett., 1996, 259, 128.

[119] M. Waletzke, PhD thesis. Implementation und Anwendung von Multireferenz-DFT und -ab initio Methoden für groβe Moleküle, Universität Bonn, 2001.

[120] O. Christiansen, H. Koch, P. Jørgensen, The second-order approximate coupled cluster singles and doubles model CC2, Chem. Phys. Lett., 1995, 243, 409.

[121] G. D. Purvis III, R. J. Bartlett, A full coupled-cluster singles and doubles model: The inclusion of disconnected triples, J. Chem. Phys., 1982, 76, 1910.

[122] O. Christiansen, Coupled cluster theory with emphasis on selected new developments, Theor. Chim. Acta, 2006, 116, 106.

[123] A. Klamt, G. Schürmann, COSMO: a new approach to dielectric screening in solvents with explicit expressions for the screening energy and its gradient, J. Chem. Soc., Perkin Trans. 2, 1993, 799.

[124] A. Schäfer, A. Klamt, D. Sattel, J. C. W. Lohrenz, F. Eckert, COSMO Implementation in TURBOMOLE: Extension of an efficient quantum chemical code towards liquid systems, Phys. Chem. Chem. Phys., 2000, 2, 2187.

[125] N. J. Turro; V. Ramamurthy, J. C. Scaiano, Principles of molecular photochemisty. An introduction, University Science Books, Sausalito, USA.

[126] S. Salzmann, PhD thesis, Relaxation Processes in electronically excited states: Blue-Light Receptors and Related Compounds, Universität Düsseldorf, Germany, 2009.

[127] V. Vallet, L. Maron, C. Teichteil, J. -P. Flament, A two-step uncontracted determinantal effective Hamiltonian-based SO-CI method, J. Chem. Phys., 2000, 113, 1391.

[128] R. J. Buenker, A. B. Alekseyev, H. -P. Liebermann, R. Lingott, G. Hirsch, Comparison of spin-orbit configuration interaction methods employing relativistic effective core potentials for the calculation of zero-field splittings of heavy atoms with a $^2P^0$ ground state, J. Chem. Phys., 1998, 108, 3400.

[129] S. R. Langhoff, C. W. Kern, in Modern Theoretical Chemistry, ed. H. F. Schaefer III, Plenum, New York, 1977, pp. 381-437.

[130] J. Tatchen, C. M. Marian, Vibronic absorption, fluorescence, and

phosphorescence spectra of psoralen: a quantum chemical investigation, Phys. Chem. Chem. Phys., 2006, 8, 2133.

[131] W. Siebrand, Radiationless transitions in polyatomic molecules. II. triplet-ground-state transitions in aromatic hydrocarbons, J. Chem. Phys., 1967, 47, 2411.

[132] B. Soep, A. Kellmann, M. Martin, L. Lindqvist, Study of triplet quantum yields using a tunable dye laser, Chem. Phys. Lett., 1972, 13, 241.

[133] J. P. Heritage, A. Penzkofer, Relaxation dynamics of the first excited electronic single state of azulene in solution, Chem. Phys. Lett., 1976, 44, 76.

[134] E. P. Ippen, C. V. Shank, R. L. Woerner, Picosecond dynamics of azulene, Chem. Phys. Lett., 1977, 46, 20.

[135] G. Kavarnos, in Topics in Current Chemistry. Vol. 156, Photoinduced Electron Transfer I, Springer-Verlag, Berlin, Germany, 1990, 21.

[136] D. Rehm, A. Weller, Kinetics of fluorescence quenching by electron and H-atom transfer, Isr. J. Chem., 1970, 8, 259.

[137] S. Stenholm, K.-A. Suominen, Weisskopf-Wigner decay of excited oscillator states, Optics Express, 1998, 2, 378.

[138] V. F. Weisskopf, E. P. Wigner, Berechnung der natürlichen Linienbreite auf Grund der Diracschen Lichttheorie, Z. Phys., 1930, 63, 54.

[139] V. F. Weisskopf, E. P. Wigner, Über die natürliche Linienbreite in der Strahlung des harmonischen Oszillators, Z. Phys., 1930, 65, 18.

[140] R. Englman, J. Jortner, Energy gap law for radiationless transitions in large molecules, Mol. Phys., 1970, 18, 145.

[141] K. F. Freed, J. Jortner, Multiphonon processes in the nonradiative decay of large molecules, J. Chem. Phys., 1970, 52, 6272.

[142] R. A. Marcus, Nonadiabatic processes involving quantumlike and classicallike coordinates with applications to nonadiabatic electron transfers, J. Chem. Phys., 1984, 81, 4494.

[143] J. J. Cavaleri, K. Prater, R. M. Bowman, An investigation of the solvent dependence on the ultrafast intersystem crossing kinetics of xanthone, Chem. Phys. Lett., 1996, 259, 495.

[144] M. Etinski, C. M. Marian, Overruling the energy gap law: fast triplet formation in 6-azauracil, Phys. Chem. Chem. Phys., 2010, 12, 15665.

[145] A. Toniolo, M. Persico, A theoretical study of spectroscopy and predissociation dynamics in nitrosoalkanes, J. Chem. Phys., 2001, 115, 1817.

[146] A. Toniolo, M. Persico, Efficient calculation of Franck-Condon factors and

vibronic couplings in polyatomics, J. Comput. Chem., 2001, 22, 968.

[147] J. Tatchen, PhD Thesis. Spin-verbotene photophysikalische Prozesse in organischen Molekuelen: Entwicklung quantenchemischer Methoden und Anwendung aur Psoralene; Universität Düsseldorf, Germany, 2005.

[148] C. M. Marian, Spin-orbit coupling and intersystem crossing in molecules, WIREs Comput. Mol. Sci. 2012, 2, 187-203.

[149] F. Duschinsky, On the interpretation of electronic spectra of polyatomic molecules, Acta Physicochim. URSS, 1937, 7, 551.

[150] D. J. Tannor, Introduction to Quantum Mechanics: A Time-Dependent Perspective (University Science Books, 2006).

[151] M. Etinski, PhD thesis. Comparison between time-dependent and time-independent methods for the calculation of inter-system crossing rates: Application to uracil and its derivatives, Universität Düsseldorf, Germany, 2010.

[152] M. Etinsky, J. Tatchen, C. M. Marian, Thermal and solvent effects on the triplet formation in cinnoline. Phys. Chem. Chem. Phys., 2013, submitted.

[153] F. G. Mehler, Über die Entwicklung einer Funktion von beliebig vielen Variablen nach Laplaceschen Funktionen höherer Ordnung, J. reine angew. Math., 1866, 66, 161.

[154] J. J. Markham, Interaction of normal modes with electron traps, Rev. Mod. Phys. 1959, 31, 956.

[155] D. R. Kearns, Physical and chemical properties of singlet molecular oxygen, Chem. Rev., 1971, 71, 395.

[156] M. Michaelis, M. P. Schubert, S. Granick, Semiquinone radicals of the thiazines, J. Am. Chem. Soc., 1940, 62, 204.

[157] H. Eipper, M. H. Abdel-Kader, H. E. A. Kramer, Thionine triplet relaxation in pyridine: a completely time-resolved forster cycle, J. Photochem., 1985, 28, 3, 433.

[158] W. C. Lai, N. S. Dixit, R. A. Mackay, Formation of H aggregates of thionine dye in water, J. Phys. Chem., 1984, 88, 5364.

[159] G. N. Lewis, O. Goldschmid, T. T. Magel, J. Bigeleisen, Dimeric and other forms of methylene blue: absorption and fluorescence of the pure monomer, J. Am. Chem. Soc., 1943, 65, 6, 1150.

[160] E. Rabinowitch, L. F. Epstein, Polymerization of dyestuffs in solution. thionine and methylene blue, J. Am. Chem. Soc., 1941, 63, 69.

[161] M. Kasha, H. R. Rawls, M. Ashraf El-Bayoumi, The exciton model in

molecular spectroscopy, Pure Appl. Chem., 1965, Vol. 11, No. 3-4, pp. 371-392

[162] U. Sommer, H. E. A. Kramer, A theoretical treatment of the electronic states of thionine and related molecules, Photochem. Photobiol., 1971, 13, 387.

[163] P. Homem-de-Mello, B. Mennucci, J. Tomasi, A. B. F. da Silva, The effects of solvation in the theoretical spectra of cationic dyes, Theor. Chem. Acc., 2005, 113, 274.

[164] P. Homem-de-Mello, B. Mennucci, J. Tomasi, A. B. F. da Silva, Cationic dye dimers: A theoretical study, Theor. Chem. Acc., 2007, 118, 315.

[165] M. G. Neumann, M. J. Tiera, The use of basic dyes as photochemical probes, Química Nova, 1993, 16, 4, 280.

[166] S. Das, P. V. Kamat, Can H-aggregates serve as light-harvesting antennae? Triplet-triplet energy transfer between excited aggregates and monomer thionine in aerosol-OT solutions, J. Phys. Chem. B, 1999, 103, 209.

[167] G. R. Haugen, E. R. Hardwick, Ionic association in aqueous solutions of thionine, J. Phys. Chem., 1963, 67, 725.

[168] G. R. Haugen, E. R. Hardwick, Ionic association in solutions of thionine. II. Fluorescence and solvent effects, J. Phys. Chem., 1965, 69, 2988.

[169] M. D. Archer, M. I. C. Ferreira, G. Porter, C. J. Tredwell, Picosecond study of Stern-Volmer quenching of thionine by ferrous ions, Nouv. J. Chim., 1977, 1, 9.

[170] B. Patrick, P. V. Kamat, Photosensitization of Large-Bandgap Semiconductors. Charge Injection from Triplet Excited Thionine into ZnO Colloids, J. Phys. Chem., 1992, 96, 1423.

[171] U. Steiner, G. Winter, H. E. A. Kramer, Investigation of physical triplet quenching by electron donors, J. Phys. Chem., 1977, 81, 1104.

[172] M. Nemoto, H. Kokubun, M. Koizumi, Determination of S*-T transition probabilities of some xantene and thiazine dyes on the basis of T-energy transfer. II. Results in the aqueous solution, Bull. Chem. Soc. Japan, 1969, 42, 1223, 2464.

[173] Y. Usui, Determination of quantum yield of singlet oxygen formation by photosensitization, Chem. Lett., 1973, 743.

[174] E. Vogelmann, H. E. A. Kramer, Photochemical investigations of oxazine, thiazine and selenazine dyes. The reactivity of protolytic triplet forms in electron transfer reactions, Photochem. Photobiol., 1976, 23, 383.

[175] J. Faure, R. Bonneau, J. Joussot-Dubien, Etude en spectroscopie par eclair des colorants thiaziniques en solution aqueuse, Photochem. Photobiol., 1967, 6, 331.

[176] R. Bonneau, P. Fornier de Violet, J. Joussot-Dubien, Mechanism of photoreduction of thiazine dyes by EDTA studied by flash abstraction rate constant of the dyes in photolysis-II. pH dependence of electron their triplet state, Photochem. Photobiol., 1974, 19, 129.

[177] C. G. Hatchard, C. A. Parker, The photoreduction of thionine by ferrous sulphate, Trans. Faraday Soc., 1961,57, 1093.

[178] R. Bonneau, J. Joussot-Dubien, Mechanism of photoreduction of thiazine dyes by EDTA studied by flash-photolysis-I Photochem. Photobiol., 1973, 17, 313.

[179] M. Stubbs, P. M. J. McSheehy, J. R. Griffiths, C. L. Bashford, Causes and consequences of tumor acidity and implications for treatment, Mol. Med. Today, 2000, 6, 15.

[180] K N Solovyov, E A Borisevich, Intramolecular heavy-atom effect in the photophysics of organic molecules. Physics - Uspekhi, 2005, 48, 231.

[181] K. Hamanoue, T. Nakayama, I. Tsujimoto, S. Miki, K. Ushida, Further studies on the nature of the lowest excited triplet states of haloanthraquinones: Triplet-triplet absorption and phosphorescence spectra of the α-halo (1-bromo, 1-bromo-5-chloro, 1,5-dibromo, 1-bromo-8-chloro, 1,8-dibromo) and β-halo (2-bromo) compounds, J. Phys. Chem. ,1995, 99, 5802.

[182] M. Collet, M. Hoebeke, J. Piette, A. Jakobs, L. Lindqvist, A.V. de Vorst, Photosensitized generation of hydroxyl radical by eight new sulfur and selenium analogs of psoralen, J. Photochem. Photobiol. B, 1996, 35, 221.

[183] M. Wainwright, R. M. Giddens, Phenothiazinium photosensitisers: Choices in synthesis and application, Dyes Pigm. 2003, 57, 245.

[184] K. J. Mellish, R. D. Cox, D. I. Vernon, J. Griffiths, S. B. Brown, *In Vitro* photodynamic activity of a series of methylene blue analogues, Photochem. Photobiol. 2002, 75, 392.

[185] S. A. Gorman, A. L. Bell, J. Griffiths, D. Roberts, S. B. Brown, The synthesis and properties of unsymmetrical 3,7-diaminophenothiazin-5-ium iodide salts: potential photosensitisers for photodynamic therapy, Dyes Pigm. 2006, 71, 153.

[186] M. Wainwright, K. Meegan, C. Loughran, R. M. Giddens, Phenothiazinium

photosensitisers, part VI: photobactericidal asymmetric derivatives, Dyes Pigm. 2009, 82, 387.

[187] M. Wainwright, S. D. Brandt, A. Smith, A. Styles, K. Meegan, C. Loughran, Phenothiazinium photosensitisers VII: Novel substituted asymmetric *n*-benzylphenothiaziniums as photoantimicrobial agents, J. Photochem. Photobiol. 2010, 99, 74.

[188] M. Wainwright, A. Shah, K. Meegan, C. Loughran, A. Smith, N. Valli, N. Dempster, Phenothiazinium-fluoroquinolone drug conjugates, Int. J. Antimicrob. Agents 2010, 35, 405.

[189] M. A. Houghtaling, R. Perera, K. E. Owen, S. Wagner, R. J. Kuhn, H. Morrison, Photobiological properties of positively charged methylene violet analogs. Photochem. Photobiol. 2000, 71, 20.

[190] M. Wainwright, Photosensitisers in Biomedicine; John Wiley & Sons Ltd.: Chichester, UK, 2009.

[191] K. O'Riordan, O. E. Akilov, D. K. Chang, J. W. Foley, T. Hasan, Real-time fluorescence monitoring of phenothiazinium photosensitizers and their anti-mycobacterial photodynamic activity against Mycobacterium Bovis BCG in *in Vitro* and *in Vivo* models of localized infection, Photochem. Photobiol. Sci. 2007, 6, 1117.

[192] S. J. Wagner, A. Skripchenko, D. J. Donnelly, K. Ramaswamy, M. R. Detty, Chalcogenoxanthylium photosensitizers for the photodynamic purging of blood-borne viral and bacterial pathogens, Bioorg. Med. Chem., 2005, 13, 5927.

[193] S. L. Gibson, R. Hilf, D. J. Donnelly, M. R. Detty, Analogues of tetramethylrosamine as transport molecules for and inhibitors of P-glycoprotein-mediated multidrug resistance, Bioorg. Med. Chem., 2004, 12, 4625.

[194] J. J. Holt, M. K. Gannon, G. Tombline, T. A. McCarty, P. M. Page, F. V. Bright, M. R. Detty, A cationic chalcogenoxanthylium photosensitizer effective *in vitro* in chemosensitive and multidrug-resistant cells, Bioorg. Med. Chem. 2006, 14, 8635.

[195] R. E. McKnight, B. Onogul, S. R. Polasani, M. K. Gannon, M. R. Detty, Substituent control of DNA binding modes in a series of chalcogenoxanthylium photosensitizers as determined by isothermal titration calorimetry and topoisomerase I DNA Unwinding Assay, Bioorg. Med. Chem. 2008, 16, 10221.

[196] L. Michaelis, S. Granick, The oxidation-reduction equilibrium, over the

whole pH range, of oxonine and some related dyestuffs, J. Am. Chem. Soc., 1941, 63, 1636.

[197] E. Vogelmann, H. Schmidt, U. Steiner, H. E. A. Kramer, Photochemical investigations and ESR triplet spectra of oxazine, thiazine and selenazine dyes, Z. Phys. Chem. N. F., 1975, 94, 101.

[198] N. Gfeller, S. Megelski, G. Calzaferri, Transfer of electronic excitation energy between dye molecules in the channels of zeolite L, J. Phys. Chem. B, 1999, 103, 1250

[199] D. Creed, N. C. Fawcett, R. L. Thompson, Singlet and triplet reactivity in the photoreduction of oxonine(3,7-diaminophenoxazin-5-ium chloride) by iron (II), Photochem. Photobiol., 1991, 53, 5, 573.

[200] X. Song, D. S. Kassaye, J. W. Foley, 5,9-Diaminodibenzo[a,j]phenoxazinium Chloride: A rediscovered efficient long wavelength fluorescent dye, J. Fluoresc., 2008, 18, 513.

[201] F.P. Schafer, Dye Lasers, Springer, Berlin, 1990.

[202] R. Ahlrichs, M. Bär, H.-P. Baron, R. Bauernschmitt, S. Böcker, N. Crawford, P. Deglmann, M. Ehrig, K. Eichkorn, S. Elliott, F. Furche, F. Haase, M. Häser, C. Hättig, A. Hellweg, H. Horn, C. Huber, U. Huniar, M. Kattannek, A. Köhn, C. Kölmel, M. Kollwitz, K. May, P. Nava, C. Ochsenfeld, H. Öhm, H. Patzelt, D. Rappoport, O. Rubner, A. Schäfer, U. Schneider, M. Sierka, O. Treutler, B. Unterreiner, M. v. Arnim, F. Weigend, P. Weis, H. Weiss, Turbomole (vers. 6.1), Universität Karlsruhe, 2009.

[203] D. Jacquemin, V. Wathelet, E. A. Perpète, C. Adamo, Extensive TD-DFT benchmark: Singlet-excited states of organic molecules, J. Chem. Theory Comput., 2009, 5, 2420.

[204] C. Kind, M. Reiher, J. Neugebauer, SNF Version 2.2.1: A Program Package for Numerical Frequency Analyses, Universität Erlangen, 1999-2002.

[205] A. P. Scott, L. Radom, Harmonic vibrational frequencies: an evaluation of Hartree-Fock, Møller-Plesset, quadratic configuration interaction, density functional theory, and semiempirical scale factors, J. Phys. Chem., 1996, 100, 16502.

[206] A. Schäfer, C. Huber, R. Ahlrichs, Fully optimized contracted Gaussian basis sets of triple zeta valence quiality for atoms Li to Kr, J. Chem. Phys. 1994, 100, 5829.

[207] M. Schreiber, M. R. Silva-Junior, S. P. A. Sauer, W. Thiel, Benchmarks for

electronically excited states: CASPT2, CC2, CCSD and CC3, J. Chem. Phys., 2008, 128, 134110.

[208] P. A. M. Dirac, Quantum mechanics of many-electron systems, Proc. R. Soc. London, Ser. A., 1929, 123, 714.

[209] A. D. Becke, A new mixing of Hartree-Fock and local density-functional theories, J. Chem. Phys., 1993, 98, 1372.

[210] C. Reichardt, in Solvents and Solvent Effects in Organic Chemistry, Wiley-VCH, Weinheim, 1990.

[211] B. Schimmelpfennig, AMFI, an atomic spin-orbit integral program, University of Stockholm, 1996.

[212] S. R. Langhoff, C. W. Kern, in Modern theoretical chemistry, edited by H. F. Schaefer III Plenum, New York, 1977, Vol. 4, pp. 381.

[213] H. Ågren, O. Vahtras, B. Minaev, Response theory and calculations of spin-orbit coupling phenomena in molecules, Adv. Quantum Chem., 1996, 27, 71.

[214] H. E. Marr, J. M. Stewart, The crystal structure of methylene blue pentahydrate, Acta Cryst., 1973, B29, 847.

[215] H. E. A. Kramer, M. Hafner, M. Zügel, Bestimmung der Energie des Thionintripletts durch Triplett-Triplett-Energieübertragung, Z. Phys. Chem. N. F., 1969, 65, 276.

[216] H. E. A. Kramer, Bestimmung der Energie des Thionintripletts durch Triplett-Triplett-Energieübertragung, Z. Phys. Chem. N. F., 1969, 66, 73.

[217] S. Salzmann, J. Tatchen, C. M. Marian, The photophysics of flavins: What makes the difference between gas phase and aqueous solution?, J. Photochem. Photobiol. A, 2008, 198, 221.

[218] S. Salzmann, M. Kleinschmidt, J. Tatchen, R.Weinkauf, C. M. Marian, Excited states of thiophene: ring opening as deactivation mechanism, Phys. Chem. Chem. Phys., 2008, 10, 380.

[219] N. J. Turro, V. Ramamurthy, J. C. Scaiano, Principles of molecular photochemistry: an introduction, University Science Books, Sausalito, CA, 2009.

[220] A. A. Gorman, I. Hamblett, C. Lambert, B. Spencer, M. C. Standen, Identification of both preequilibrium and diffusion limits for reaction of singlet oxygen, $O_2(^1\Delta_g)$, with both physical and chemical quenchers: Variable-temperature, time-resolved infrared luminescence studies, J. Am. Chem. Soc., 1988, 110, 8053.

[221] A. F. Olea, F. Wilkinson, Singlet Oxygen Production from Excited Singlet and Triplet States of Anthracene Derivatives in Acetonitrile, J. Phys. Chem., 1995, 99, 4518.

[222] F. Wilkinson, D.J. McGarvey, A.F. Olea, Excited triplet state interactions with molecular oxygen: Influence of charge transfer on the bimolecular quenching rate constants and the yields of singlet oxygen ($O_2(^1\Delta_g)$) for substituted naphthalenes in various solvents, J. Phys. Chem., 1994, 98, 3762.

[223] D. J. McGarvey, P. G. Szekeres, F. Wilkinson, The efficiency of singlet oxygen generation by substituted naphthalenes in benzene. Evidence for the participation of charge-transfer interactions, Chem. Phys. Lett., 1992, 199, 314.

[224] L. M. Frutos, O. Castaño, A new algorithm for predicting triplet-triplet energy-transfer activated complex coordinate in terms of accurate potential-energy surfaces, J. Chem. Phys., 2005, 123, 104108.

[225] J. Qiang Wu, D. Baumann and U.E. Steiner, Interference of heavy-atom with magnetic spin effects in spin-correlated micellar radical pairs, Mol. Phys., 1995, 84, 981.